# Experimenteel-numeriek onderzoek naar de schademechanismen op micro- en mesoschaal in staalvezelversterkte textielcomposieten

# Mixed Experimental-Numerical Analysis of Micro-Meso Scale Damage Development in Steel Fiber Reinforced Textile Composites

Jana Faes

Promotoren: prof. dr. ir. W. Van Paepegem, dr. A. Rezaei
Proefschrift ingediend tot het behalen van de graad van
Doctor in de ingenieurswetenschappen: bouwkunde

UNIVERSITEIT
GENT

Vakgroep Materialen, Textiel en Chemische Proceskunde
Voorzitter: prof. dr. P. Kiekens
Faculteit Ingenieurswetenschappen en Architectuur
Academiejaar 2016 - 2017

ISBN 978-94-6355-030-7
NUR 971
Wettelijk depot: D/2017/10.500/65

**Promotors**:

Prof. dr. ir. Wim Van Paepegem
Ghent University
Faculty of Engineering and Architecture
Department of Materials, Textiles and Chemical Engineering

Dr. ir. Ali Rezaei
Ghent University
Faculty of Engineering and Architecture
Department of Materials, Textiles and Chemical Engineering

**Examination Committee:**

| | |
|---|---|
| Prof. Hendrik Van Landeghem (chairman) | Ghent University |
| Prof. Wim Van Paepegem | Ghent University |
| Dr. Ali Rezaei | Ghent University<br>& Katholieke Universiteit Leuven |
| Prof. Francisco Gilabert | Ghent University |
| Prof. Karen De Clerck | Ghent University |
| Prof. Wouter De Corte | Ghent University |
| Prof. Lincy Pyl | Free University of Brussels |
| Dr. Stijn De Pauw | NV Bekaert SA |

**Research Institute:**

Ghent University
Department of Materials, Textiles and Chemical Engineering
Technologiepark-Zwijnaarde 903
9052 Zwijnaarde, Belgium

# ACKNOWLEDGEMENTS

Ik wist toen ik aan mijn doctoraat begon dat het een uitdaging zou worden. Het moeilijke aan onderzoek, voor mij althans, is dat je per definitie niet weet wat de uitkomst van elke nieuwe stap zal zijn – anders zou het geen nuttige stap zijn. Je kan dus niet ver vooruit kijken, je kan niets plannen. Je kan alleen gedisciplineerd verder werken en blijven geloven dat het je ergens zal brengen. Een avontuur voor velen, iets gans anders voor mij, misschien net daarom dat het me ergens aansprak. Ik heb wel hard getwijfeld, en Wim, ik was er niet aan begonnen zonder jou als promotor. En ik had het niet tot een goed einde gebracht zonder jouw altijd positieve, oplossingsgerichte input. De manier waarop je de vakgroep leidt, zowel op wetenschappelijk als op menselijk vlak, heeft mij echt geïnspireerd en zal mij altijd bijblijven. Zeker op de cruciale momenten lijkt het soms alsof je met minstens vijf aan het werk bent. Het is onmogelijk je genoeg te bedanken voor alles wat je voor mij gedaan en betekend hebt, maar bij deze toch een poging: bedankt Wim, voor alles.

To my co promotor Ali – Dr. A, thanks for always being there and being you. You reminded me to build my research from a solid scientific base up, to study literature first, to start with simple cases, to benchmark models… In short, you made me the researcher I am today. Equally important to me were our talks about life, about politics, about the world, and our jokes that so few other people would be able to appreciate.

Ook onze vakgroepvoorzitter prof. Joris Degrieck zou ik willen bedanken voor het aangename kader waarin ik meer dan vier jaar heb mogen werken. Verder zou ik de collega's willen bedanken voor alle mooie momenten tijdens de koffiepauze, tijdens de occasionele uitjes in Gent, tijdens de jaarlijkse barbecue, tijdens recepties… Sommige collega's ook voor hun hulp bij het onderzoek. Stefan, bedankt voor de hulp bij het programmeren en het modelleren. Ives, Luc, Pascal, Klaas, bedankt om mij op weg te helpen in het labo. Martine, Line, Ilse, bedankt voor de hulp met alle administratieve problemen, en Roger, bedankt voor alle keren dat je mijn computer gedepanneerd hebt. Tom, ik heb zelden een betere match getroffen in mijn appreciatie voor orde en netheid en je bent ook gewoon een leuke peer. Ik kon me geen betere bureaugenoot wensen. Klaas, het was me een eer om in het kotje naast dat van jou te mogen zitten. Zoals je vast al hebt gezien sta ik scherper dan ooit, in voorbereiding voor ons jaarlijkse sportieve gebeuren begin april. Dus be there or be square.

Verder wil ik alle Nanoforce en SIM collega's van buiten de vakgroep bedanken voor de prettige samenwerking, en de zovele anderen die op een of andere manier hebben bijgedragen tot het tot stand komen van dit doctoraat. Met name Peter, bedankt voor de steun tijdens de laatste loodjes.

Tot slot wil ik mijn vrienden en familie bedanken. De vrienden van de kickerploeg, om mij te helpen mijn zinnen te verzetten op vrijdagavond. Tine en Lisa, mijn ex-homies, voor de bergwandelingen en voor alle keren dat we samen te veel eten hebben gemaakt. Michaël en Annie, om ons een fantastisch onderdak te geven tijdens mijn doctoraatsjaren en voor de gezellige etentjes. En Mahieu, om al meer dan 10 jaar mijn beste maat te zijn. Guy en Annemie, bedankt om ons altijd zo warm te ontvangen op de zovele gezellige zondagavonden. Bedankt aan Sigrid en Jitse, de twee mensen bij wie ik steeds mijn knorrige zelf kan zijn omdat je toch niet van zus kan veranderen. Moetie en poetie, jullie hebben me niet alleen alle kansen gegeven, maar ook een mooi voorbeeld van wat mogelijk is in het leven. Ik hoop het even goed te doen als jullie. En tot slot El Pistolero. Bedankt om er altijd en onvoorwaardelijk te zijn voor me, bedankt voor alles wat je gedaan hebt om mij de tijd te kopen die ik nodig had zonder me ooit op te jagen, bedankt om mijn teamie te willen zijn.

Jana Faes,
Augustus 2017

# SUMMARY

Structural composites are rapidly making their way in the automotive industry, in wind energy applications, in the aircraft industry, and in the world of advanced sports goods. Especially the search for lightweight solutions drives this evolution. Lighter sports equipment improves performances, lighter wind turbine blades increase the efficiency, and lighter automobile and aircraft components reduce the energy consumption. Especially in these latter fields, weight reductions have become essential in achieving the ever more stringent regulations on $CO_2$ emissions. Composites tend to behave fundamentally different from the classical materials, owing to their anisotropic nature. Introducing a composite material to a new market therefore usually requires new standards and a reinvention of the design flow. As these hurdles are being taken in more and more industries, the amount of applications grows exponentially.

The most commonly used advanced structural composite materials have glass or carbon fibers as reinforcement. The brittle nature of these fiber materials directly translates to a brittle behavior of the resulting composites. Impact, overloads and fatigue loads often cause cracks and delaminations that are hard to detect, because the damage is not visible at the surface of the composite part. At the same time, the damage often grows very suddenly, causing unexpected failure at a low strain level. This brittle behavior rules out some applications, and incites overly safe design dimensions in others. These cases would hence benefit from the development of a new class of tough composites. The recent developments in stainless steel fiber production technology are interesting in this context. A fiber diameter of 30 µm or less can be achieved nowadays, and the strain-to-failure can be tailored within a wide range through heat treatment. Moreover, the highly controlled production process outputs continuous fiber bundles with a constant quality and little to no fiber breakages, perfect to be woven into a reinforcement fabric. A fabric is easier to handle than unidirectional forms of reinforcement, which usually makes for a lower production cost. Other advantages over unidirectional composite laminates are the higher out-of-plane strength and stiffness and the lower risk of delaminations. Especially the latter is an interesting asset in acquiring a tougher composite.

The goal of this doctoral research is twofold. A first aim is to determine how and to what extent a textile of ductile stainless steel fibers can contribute in developing a tough composite material. Both the ductility of the fibers and the complexity of the reinforcement geometry are aspects to be taken into account in the investigation. A second aim is to develop a framework to simulate the mechanical behavior of ductile fiber textile composites through finite element modeling. These two goals are inseparably linked. Indeed, developing a strategy to model a composite material requires thorough knowledge of the mechanics that govern its behavior. Conversely,

a reliable numerical model will typically produce new insights about the material mechanics.

A fiber composite consists of a reinforcement phase and a matrix. In view of creating a tough composite, the ductile steel fiber textile reinforcement was combined with a ductile epoxy system that was especially developed to be used in wind turbine blades. A thorough mechanical characterization revealed, however, that the resulting composite does not reach the envisioned high failure strain. This finding directed the research towards understanding the damage mechanisms that are responsible for the early failure. Damage initiation and propagation are governed by stress and strain concentrations in the material. Therefore, a finite element model must be able to produce correct stress and strain distributions in order to be suited to study damage.

Amongst the existing finite element techniques for analyzing textile composites on the meso-scale, the RVE method is by far the most commonly used. The basic idea behind this technique is that the composite can be studied through an RVE, or a Representative Volume Element, subjected to periodic boundary conditions. Experimental validation on an RVE model showed that this method does not qualify to study damage in the composite material under study. The reason behind this inaptitude proved not to be the plastic nature of the composite components, but the geometry of the reinforcement. The RVE method is based on the assumption of perfect periodicity in the material structure, but these qualities are not found in the real reinforcement geometry. This discrepancy results in an incorrect localization of the stresses and strains in the finite element model.

To this day, there is no convention for measuring and quantifying the geometrical imperfections in a textile composite. This work hence presents a methodology to assess the geometrical variabilities on every length scale based on high resolution microscopic images of the polished edge of a composite laminate specimen. This non-destructive method was accompanied by the necessary tools to define the contours of fibers and yarns in an unbiased manner, and to calculate the (variability of) geometrical parameters. Moreover, owing to the high resolution of the images, it was possible to study and to automatically map the sub-mesoscopic inhomogeneity of the yarns. Finally, a semi-automatic conversion strategy was incorporated in the methodology to translate the microscopic images into a two-dimensional model in the Abaqus finite element software.

So far, two-dimensional modeling of textile composites was always limited to purely conceptual exercises – for instance, to show how a transversal yarn is locally pushed aside in the crimp region of a longitudinal yarn when the latter is loaded, and hence stretched. The concept of using a two-dimensional model to represent a real laminate specimen was never explored. This approach is thoroughly validated in this work, first with a conceptual numerical experiment, and later on with observations during a

tensile experiment. The experimental data were obtained by measuring the strain fields on the modeled edge of some of the laminates by using the DIC (Digital Image Correlation) technique. For other laminates, the edge was monitored for damage during the tensile test. Validation of the numerical result indicated that a two-dimensional modeling strategy is suited to represent a textile composite, as long as the internal structure is not too much disrupted by cracks. Damage propagation can hence not be predicted by a 2D model. This is in line with the experimental observations regarding the relation between the geometrical features that are visible on the edge of a laminate specimen on the one hand, and the strain and damage patterns on the other hand. The strain distributions and the initial damage pattern show a strong correlation with the geometry of the reinforcement on the specimen edge. The damage propagation, however, occurred very unpredictably with respect to the visible structure. The reason behind this phenomenon is that cracks can originate inside the laminate, and only travel to the edge at the very final moment.

A better insight in the damage mechanisms that govern the early failure of the steel fiber textile composite was acquired by studying the role of the matrix and the role of the fiber-matrix interface in more detail. Opposite to what was expected, a more brittle matrix seems to make for a tougher composite, while enhancing the interface strength embrittled the composite. Based on the damage morphology, a hypothesis was put forth on the reason why a ductile reinforcement and a ductile matrix do not necessarily lead to a tough composite. The fact that the steel fibers do not transfer their high ductility to the composite was attributed to their fixation in the transversal composite structure. Damage softens this interlock, which gives the ductile load-bearing yarns more room to strain. Therefore, the key to increasing the failure strain of the composite is to have as much distributed damage as possible before it starts to localize. A brittle matrix is very prone to develop an evenly distributed transversal crack pattern, and therefore leads to a tough composite. Enhancing the adhesion between fibers and matrix delays the initiation of damage on their interface. When a crack finally does originate, the global stress is high enough to cause a rapid propagation that leads to brittle failure.

# SAMENVATTING

Structurele composietmaterialen winnen steeds meer aan belang in de automobielindustrie, in de windenergiesector, in de luchtvaartindustrie, en in de markt van geavanceerde sportartikelen. Vooral de toenemende vraag naar lichtere componenten is de drijfveer achter deze evolutie. Lichtere sportartikelen zorgen voor verbeterde prestaties, lichtere windturbinebladen verhogen de efficiëntie, en lichtere onderdelen voor wagens en vliegtuigen verlagen de energieconsumptie. Vaak is een gewichtsreductie in die laatste sectoren zelfs onontbeerlijk voor het behalen van de steeds strengere normen wat betreft $CO_2$ uitstoot. De introductie van een composietmateriaal in een nieuwe markt vergt vaak een herziening van de normering en de ontwerpstrategieën, omdat deze materialen zich door hun anisotrope opbouw vaak fundamenteel anders gedragen dan klassieke materialen. Deze drempel raakt in meer en meer sectoren overwonnen, wat het aantal toepassingen in een stroomversnelling brengt.

De meest gangbare geavanceerde composietmaterialen zijn de glas- en koolstofvezelcomposieten. Het brosse karakter van de versterkingsvezels vertaalt zich bij deze composieten in een typisch bros schadegedrag. Schade kan hierbij ontstaan door een onvoorziene impactbelasting, maar ook door een eenmalige overbelasting of door vermoeiing. Vaak zijn beschadigingen bovendien moeilijk te detecteren, en als een beschadigd onderdeel verder belast wordt, leiden zelfs kleine scheurtjes of delaminaties vaak tot een abrupt falen. Het gevolg is dat de traditionele composieten voor bepaalde toepassingen sterk overgedimensioneerd moeten worden, of zelfs niet in aanmerking komen. Er is dus vraag naar taaiere composietmaterialen, en de recente ontwikkelingen in de productie van staalvezels kan in deze context interessant zijn. Het is tegenwoordig mogelijk om roestvaste stalen vezels te produceren met een diameter van 30 µm, en de breukrek van de vezels kan binnen brede grenzen aangepast worden door ze te temperen. Het stabiele productieproces zorgt bovendien voor continue vezelbundels met weinig tot geen defecten of vezelbreuken, die daardoor uitermate geschikt zijn om tot een weefsel verwerkt te worden. Weefselmatten zijn eenvoudiger te hanteren dan unidirectionele versterkingsvezels, wat de productiekosten drukt. De resulterende composieten zijn bovendien minder uitgesproken anisotroop en veelal minder gevoelig voor delaminaties dan hun unidirectionele tegenhanger. Vooral dat laatste voordeel is interessant bij de zoektocht naar een taaier composiet.

Twee doelstellingen werden vooropgesteld voor dit onderzoek. Een eerste betrachting is om na te gaan hoe een versterkingsweefsel van ductiele roestvast stalen vezels kan bijdragen tot de ontwikkeling van taaiere composieten. Meer specifiek moet hierbij de rol van zowel de ductiliteit van de vezels onderzocht worden, alsook de rol van de complexe versterkingsgeometrie. Een tweede doelstelling is om een

modelleringsstrategie uit te werken om het mechanisch gedrag van weefselcomposieten met ductiele vezels te simuleren met behulp van eindige elementen modellen. Deze doelstellingen zijn innig met elkaar verbonden. Het is immers niet mogelijk om een modelleringsstrategie uit te bouwen voor een composietmateriaal zonder kennis van de materiaalmechanica die het gedrag ervan bepaalt. Anderzijds draagt een goed numeriek model typisch bij aan het inzicht in het materiaalgedrag.

Een vezelversterkt composiet bestaat uit een vezelversterking en een matrix. Met het oog op een zo taai mogelijk eindresultaat werd een satijnweefsel van ductiele roestvaste staalvezels gecombineerd met een ductiel epoxysysteem dat speciaal ontwikkeld werd voor toepassingen in windturbinebladen. Een grondige mechanische karakterisering bracht echter aan het licht dat het composiet niet de beoogde, hoge breukrek bereikt. Deze bevinding dirigeerde het onderzoek in de richting van de schademechanismen die verantwoordelijk zijn voor het vroegtijdig falen. Scheurinitiatie en -propagatie worden bepaald door spannings- en rekconcentraties in het materiaal. Het spreekt dus voor zich dat een eindige elementen model een correcte voorspelling moet kunnen maken omtrent de spannings- en rekdistributies teneinde geschikt te zijn voor het bestuderen van schade.

Van alle bestaande technieken voor eindige elementen analyse van textielcomposieten op de meso-schaal wordt de RVE methode veruit het meest gebruikt. Bij deze methode wordt het composiet bestudeerd via een RVE, een Representatief Volume-Element, onderworpen aan periodische randvoorwaarden. Via experimentele validatie werd aangetoond dat deze techniek niet geschikt is om de schade te bestuderen in het composietmateriaal dat in dit werk onderzocht wordt. De reden hiervoor bleek niet te wijten aan het ductiele karakter van de componenten, maar aan de geometrie van de versterking. Deze wijkt sterk af van de perfect periodische structuur die de intrinsieke beginhypothese vormt van de RVE techniek, waardoor de spanningen en de rekken niet correct gelokaliseerd worden.

Tot op heden bestaat er geen eenduidige manier voor het meten en kwantificeren van geometrische imperfecties in een textielcomposiet. Daarom wordt in dit werk een methodologie vooropgesteld om de geometrische variabiliteit op elke lengteschaal in kaart te brengen, startend vanaf microscopische beelden van hoge resolutie, genomen van een gepolijste rand van een proefstuk. Deze niet-destructieve methode werd uitgebouwd met de nodige tools om de contouren van vezels en vezelbundels op een consequente manier te definiëren, en om de variabiliteit van geometrische parameters te kwantificeren. De hoge resolutie van de beelden liet bovendien toe om de sub-mesoscopische inhomogeniteit van de garenbundels op een geautomatiseerde manier in kaart te brengen. De methodologie werd ten slotte verder uitgebreid door een semiautomatische omzetting te voorzien van de microscopische beelden naar een tweedimensionaal model in de Abaqus eindige elementen software.

Tweedimensionale modellering van textielcomposieten werd in het verleden al vaker toegepast, maar dan steeds vanuit een puur conceptueel oogpunt – bijvoorbeeld om aan te tonen dat een dwarse garenbundel in de krimpzone weggeduwd wordt door een aangrenzende langse bundel als die laatste belast wordt en zich dus strekt. Het idee om een tweedimensionale representatie te maken van een reëel proefstuk werd nooit eerder onderzocht. In dit werk wordt deze aanpak grondig gevalideerd, eerst met een numeriek conceptueel experiment, en later met experimentele resultaten. Hiertoe werden bepaalde proefstukken geïnstrumenteerd voor DIC (Digital Image Correlation) metingen om zodoende de rekvelden op de gemodelleerde rand op te volgen tijdens een trekproef. Bij andere proefstukken werd de schade op de gemodelleerde rand in kaart gebracht tijdens het verloop van de trektest. Deze validatie toonde aan dat 2D modellering geschikt is om dit textielcomposiet te bestuderen, zolang de schade de interne geometrie niet verstoort. De scheurpropagatie kan dus niet met een 2D model voorspeld worden. Dit ligt in lijn met de experimentele observaties omtrent de relatie tussen de geometrie die aan de gepolijste rand van het proefstuk zichtbaar is enerzijds, en de rekvelden en schadefenomenen anderzijds. De rekvelden en het initiële scheurpatroon vertonen een sterke correlatie met de zichtbare versterkingsgeometrie. De schadepropagatie, daarentegen, bleek erg onvoorspelbaar op basis van de geometrie op de rand van het proefstuk. De reden hiervoor is dat scheuren inwendig in het proefstuk kunnen ontstaan, om pas bij het falen abrupt naar de gepolijste rand te propageren.

Om een beter inzicht te krijgen in de schademechanismen die verantwoordelijk zijn voor het voortijdige falen van het staalvezeltextielcomposiet werden de rol van de matrix en die van de adhesie tussen matrix en vezels nader onder de loep genomen. Tegen de verwachtingen in bleek een brossere matrix tot een taaier composiet te leiden, terwijl een verbetering in de adhesie tussen vezels en matrix net een verbrossing teweegbrengt in het composiet. Op basis van de schademorfologie werd een hypothese vooropgesteld die verklaart waarom een composiet dat is samengesteld uit ductiele verstevigingsvezels en een ductiele matrix niet noodzakelijk taai is. Meer bepaald werd gesteld dat de stalen vezels hun hoge breukrek niet kunnen overbrengen in het composiet omdat ze vastzitten in de brosse transversale structuur. Deze vergrendeling versoepelt naarmate de transversale structuur scheurt, waardoor de langse staalvezels ruimte krijgen om verder te rekken. Hoe meer verspreide scheuren er kunnen ontstaan in de transversale structuur vooraleer de rek lokaliseert in één ervan, hoe hoger de breukrek van het composiet dus zal zijn. Een brosse matrix heeft een sterke neiging tot scheuren, wat de taaiheid van het composiet ten goede komt. Een sterke hechting tussen vezels en matrix, daarentegen, verhindert in eerste instantie dat er scheuren ontstaan aan de interface tussen beide. Eens de interface uiteindelijk toch begeeft is de globale spanning zodanig hoog geworden dat de scheur snel propageert en daardoor meteen fataal wordt.

# CURRICULUM

Jana Faes was born on Januari 22, 1987 in Veurne, Belgium. In 2011 she received her Master of Science degree in Civil Engineering from Ghent University. During her master thesis work at the department of Materials Science and Engineering, she got acquainted with the fields of composite materials and she grew an interest in finite element modeling. This encouraged her to stay at the department to contribute to the research project Nanoforce. This project was proposed by a consortium of academic and industrial partners with the aim to find next generation steel polymer composites. The research work required close collaborations within the consortium, for instance with NV Bekaert SA, the industrial partner who supplied the steel fiber fabric reinforcement that is the subject of this doctoral thesis. Following these contacts, she started working at Bekaert NV SA in 2016, first as a mechanical design engineer, and later on as a modeling engineer. The work presented in this doctoral thesis was conducted under the guidance of Prof. dr. ir. Wim Van Paepegem and dr. ir. Ali Rezaei, and it was funded by SIM and IWT. Jana Faes is author of 3 publications in international journals of Science citation index (A1) and 1 publication in international conference proceedings.

# LIST OF PUBLICATIONS

**Publications in international journal of the Science Citation Index (A1)**

[1] **Jana Faes**, Ali Rezaei, Wim Van Paepegem, Joris Degrieck, "Influence of matrix toughness and interfacial strength on the toughness of epoxy composites with ductile steel fabric reinforcement", *Composite Interfaces*, vol. 22, pp. 779-793, 2015.

[2] **Jana Faes**, Ali Rezaei, Wim Van Paepegem, Joris Degrieck, "Accuracy of 2D FE models for prediction of crack initiation in nested textile composites with inhomogeneous intra-yarn fiber volume fractions", *Composite Structures*, vol. 140, pp. 11-20, 2016.

[3] Lode Daelemans, **Jana Faes**, Samir Allaoui, Gilles Hivet, Manuel Dierick, Luc Van Hoorebeke, Wim Van Paepegem, "Finite element simulation of the woven geometry and mechanical behaviour of a 3D woven dry fabric under tensile and shear loading using the digital element method", *Composites Science and Technology*, vol. 137, pp. 177-187, 2016.

**Publications in international conference proceedings (C1 – C3)**

[1] **Jana Faes**, Ali Rezaei, Wim Van Paepegem, Joris Degrieck, "Meso-scale analysis of ductile steel fabric/epoxy composites: numerical modeling and experimental validation", in *16th European conference on composite materials, Proceedings*, Sevilla, 2014.

# TABLE OF CONTENTS

# Chapter 1

## INTRODUCTION

*In this chapter, the current research work is first introduced and framed within the broader research context. Subsequently, a brief overview is given of the relevant prior research on stainless steel fiber polymer composites. Finally, the objectives and the outline of the dissertation are presented.*

## 1.1 INTRODUCTION AND BACKGROUND

A composite material is made of two or more constituent materials that can still be distinguished as separate entities in the finished structure [1]. The purpose is to combine constituents such that the resulting material has interesting characteristics. When it comes to fiber-reinforced polymers for mechanical applications, the quest is generally focused on maximizing performance, while keeping weight and volume to a minimum. The two aspects of performance that have been searched after the last decades are strength and stiffness. Consequently, the most commonly used composites excel in those areas in particular. Carbon and glass fiber reinforced polymers have made their way from one-off space and aircraft applications [2-4] to the higher-volume fields of automotive [5-7] and sports goods [8, 9]. This proves that they can compete with metals when a high strength and stiffness are required and the weight limitations are stringent.

One of the challenges when working with composite materials is that the highly anisotropic nature must be taken into account during the design process. Reusing the design of a metal part will often lead to unacceptable performance in the directions opposite to the main fiber direction, to unwanted secondary bending and torsions, and at the very least, to a suboptimal material use. Another aspect that inhibits the use of composites for some applications is the lack of toughness. Impact and fatigue loads often cause cracks and delaminations that are hard to detect, because the damage is not visible at the surface of the composite part [10, 11]. At the same time, the damage often grows very suddenly, causing unexpected brittle failure at a low strain level.

An opportunity to enhance the deformation capability of composites is to replace the traditional, brittle carbon or glass fibers by more ductile fibers. In this context, the recent developments in stainless steel fiber production technology are interesting. A fiber diameter of 30 μm or less can be achieved nowadays, and the strain-to-failure can be tailored within a wide range through heat treatment. Whereas the ductile polymeric and natural fibers often fall short when it comes to strength or stiffness, steel fibers can compete with glass fibers in this regard [12].

The highly controlled steel fiber production process outputs continuous fiber bundles with a constant quality and little to no fiber breakages, perfect to be woven into a reinforcement fabric. A fabric is easier to handle than unidirectional (UD) forms of reinforcement, which usually makes for a lower production cost. Other advantages over UD composite laminates are the higher out-of-plane strength and stiffness and the lower risk of delaminations. When properties in one preferred direction are crucial, however, textile reinforced composites cannot match the UD composites. Another drawback is the complex nature of the reinforcement architecture, which makes it more difficult to understand the mechanics of the composite behavior.

This research work aims to gain more insights in the behavior of polymer composites reinforced with a ductile steel fiber textile. The challenge is hence twofold. First, there is the novel aspect of continuous ductile fibers as a polymer reinforcement. The second challenge is in the added complexity of the woven reinforcement architecture.

## 1.2 CONTEXT OF THE RESEARCH

This research work was performed within the framework of Nanoforce – short for "next generation nano-engineered polymer hybrids". The Nanoforce program was proposed by a consortium of four academic research groups (UGent, KULeuven, UAntwerpen, and VUB), one research center (VITO), and three industrial companies (NV Bekaert SA, Arcelor Mittal/OCAS, and Recticel NV), and it was funded by the virtual research center SIM and the Flemish institute IWT.

The ultimate goal of the program was to develop steel/carbon nanotube polymer composites that are breakthrough structural materials when it comes to energy savings, optimal use of natural resources, life-cycle performance and recyclability. In order to achieve this, three SBO (Strategic Basic Research) projects were initially started within the Nanoforce program, each focusing on one aspect of the main, common goal (Figure 1-1).

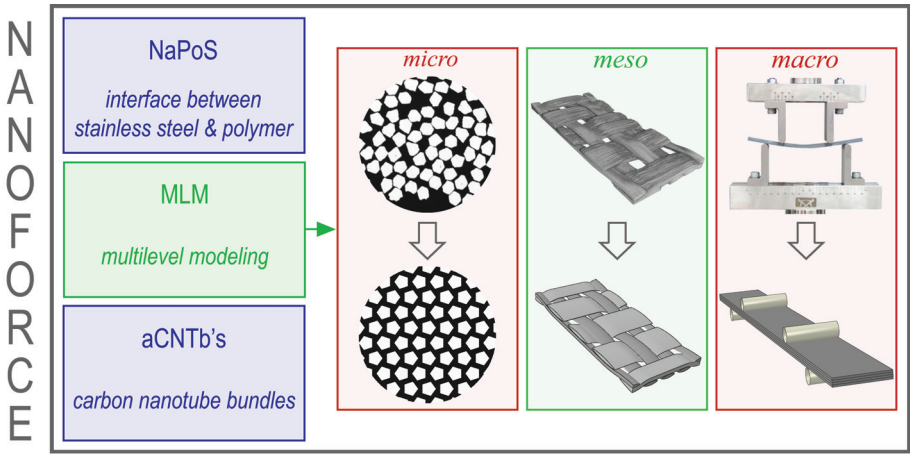


Figure 1-1: Position of the research within the framework of the Nanoforce program

The first SBO project, NaPoS, was about the optimization of the interaction between steel and polymers. The foundation of making two materials work as one is at the interface between them, so the results of the first project are crucial to the success of the program. The goal of the second project, MLM, was to develop and employ multiscale modeling techniques in order to gain insights into the mechanics of the

composite's behavior. A thorough understanding of the material mechanics drastically speeds up the development process of a new composite, and a proper model could allow to replace the expensive test campaigns partially by virtual specimen testing. The third project, aCNTb's, was about the development of the basic science and processing concepts for making aligned carbon nanotube bundles. With their exceptionally high specific stiffness and strength, carbon nanotubes could be an interesting addition to strengthen the interface and/or the matrix of an advanced composite material.

This research work was a part of the second project, MLM – short for multilevel modeling. The aim of multilevel modeling is twofold. One objective is to understand the mechanics on the scale that is represented in the model. Another goal is to predict the properties on the scale just above by homogenizing the model output. This exercise can hence be done on different length scales. The smallest length scale is the micro-scale. For a fiber-reinforced composite, this is the sub-yarn scale, or the scale of the fibers within the matrix. The largest scale is the macro-scale, or the scale of the composite laminates. In between micro and macro, there is the meso-scale, the scale on which the yarn architecture is represented when modeling textile composites. This is the scale that will be mainly addressed in this research work.

## 1.3 STATE OF THE ART

The current research was enriched by the valuable work that was done in parallel within the Nanoforce program. In particular the development of the steel-polymer interface modifications and the findings on unidirectional composites were codirecting this work. This parallel research will be summarized in the next section, along with other relevant research on stainless steel fiber polymer composites.

### 1.3.1 Stainless steel/polymer interface

The interface between fibers and matrix is crucial to the structural response of a composite [13]. Unfortunately, the mutual differences that make metals and polymers complementary in many ways also make for a low failure resistance of their bond. The adhesion between them is naturally low, and the large stiffness mismatch (ratio ±100) and the difference in thermal expansion (ratio ±10) give rise to stress concentrations at their interface. Without alterations, the interface between stainless steel and epoxy fails adhesively at around 10 MPa [14].

Adhesion is the amount of work that is needed to separate two surfaces. The many phenomena involved can all be accommodated in three main categories, i.e. mechanical interlocking, chemical bonding, and interdiffusion. The adhesion can be

improved through modifications in any of these categories, but addressing the chemistry of the interface has proven to be especially effective [15]. This can be achieved through the use of a coupling agent. A coupling agent, by definition, is a chemical compound that is able to react with two dissimilar materials, hence acting as a molecular bridge between them. For metal/polymer interfaces, the common choice is a silane-based coupling agent [16-18].

Silane treatments for the special case of a stainless steel/polymer interface have been developed within the framework of the Nanoforce program [14, 19-21]. Ghosh, Bertels, and coworkers [19] optimized the wet chemical deposition of APS (γ-aminopropyltriethoxysilan) on stainless steel, which resulted in a stainless steel/epoxy interfacial strength of 60 MPa, or about six times the native value. This value approaches the strength of the epoxy that was used, and consequently, the interface failure mode moved from adhesive failure to cohesive failure. Later on, another silane deposition method, i.e. atmospheric plasma chemical vapor deposition, was developed [14], two additional silanes, GPS and AEPTMS, were explored, and all systems were successfully transferred to stainless steel interfaces with polyamide and polyurethane [20].

Another possibility to increase the failure resistance of the stainless steel/polymer interface is to reduce the stiffness mismatch between them. Two strategies were explored within the framework of Nanoforce. The first idea was to strengthen the interphasial region of the coupling agent between the stainless steel and the polymer through nano-modifications. Two methods were explored by Bertels, but against all expectations, both of them had a negative effect on the interfacial strength [21]. The second idea was to apply nano-modifications to increase the stiffness of the polymer matrix, hence to reduce the mismatch with the stiffness of the stainless steel. Ghosh studied the effects of adding carbon nanotubes or organoclay CL30B to different polymer matrix systems, and found a successful combination in CL30B with epoxy [20].

### 1.3.2 Stainless steel/polymer composites

Steel as a composite reinforcement material is anything but new. Steel cords and wires have been used for many decades to strengthen rubber products [22-26], such as tires, pressure hoses and conveyor belts. Another big industry for reinforcing steel is the construction industry. The initial idea behind using reinforcement steel was to overcome the poor tensile strength of cement, masonry and concrete [27, 28]. Similarly as in the field of polymer composites, the focus is broadening as the general understanding of the material mechanics is improving, often with more attention for toughness [29-31], dynamic loading [32, 33] and post-fracture behavior [34, 35].

In polymer composites, steel (or any other metal) is not the conventional choice for the reinforcement phase. There are too many cheaper, lighter, or even stiffer options to choose from in the line of traditional fiber materials. The only way a metal reinforcement can compete in structural applications is when it can improve the toughness or the impact energy. Already in the 1970's, Wrzesien [36] and Ross et al. [37, 38] were exploring the potential of stainless steel wires as a hybrid reinforcement for ballistic impact applications of glass/polymer composites. More recent work on impact improvement was done by Ahmed [39], who also introduced stainless steel wires as an additional reinforcement in glass fiber/polymer composites. Most of the research on toughness improvement has been focused on short fibers. The extensive, fundamental work done by Wetherhold, Bagwell and others on short copper fiber polymer composites includes the influence of the shape [40-42] and the ductility [43] of the fibers on the toughness of the composite, and the role of the interface [44-47]. Long steel wire reinforcement as a toughness enhancer in polymer composites has been studied by Arikan et al. [48] and Samanci [49]. The reinforcement diameter ranged between 0.7 mm and 1.3 mm in these studies, and the volume fraction between 1.5% and 6%.

All in all, research on polymers reinforced with long ductile fibers was rather limited until recent developments in the stainless steel fiber production technique drastically reduced the achievable fiber diameter. Ultra-thin fibers cannot be handled separately, so they must be processed into a more manageable reinforcement fabric. Three different woven structures were produced to be studied within the framework of Nanoforce: a quasi-unidirectional (quasi-UD) weave (Figure 1-2.a), a basket weave (Figure 1-2.b), and a 4-harness satin weave (Figure 1-2.c). All three cloths were woven from the same stainless steel fibers, i.e. fibers with a diameter of 30 μm and a strain-to-failure of 19.5%. A weave consists of warp yarns and weft yarns, terms that relate to their different functions during the weaving process. The warp yarns are the fiber bundles that are held tight and in parallel to each other in the loom. The weft yarns are drawn back and forth in between two parallel layers of warp yarns, and then trapped between the warp layers as these cross over. In the quasi-UD weave on Figure 1-2.a, the weft yarns are called 'binder yarns', and they are made of PET fibers instead of stainless steel fibers. The idea behind this was to keep this reinforcement cloth as close as possible to a 'real' UD structure. The PET yarns are merely there to keep the warp yarns in place, they are not supposed to contribute to or interfere with the composite behavior.

Most of the research work done so far has been focused on quasi-UD polymer composite laminates. Allaer et al. [50] produced eight-layer unidirectional and cross-ply laminates with a ductile epoxy matrix for an extensive mechanical characterization. The tensile tests along the fiber direction of the UD laminates revealed a failure strain of about 19%, which is about as high as the failure strain of

the stainless steel fibers. This proves that the plastic potential of the ductile fibers can be fully retained in a ductile epoxy composite. Furthermore, the corresponding specific strength and stiffness values were found to be competitive compared to those of commercial E-glass/epoxy composites. The direction transverse to the load, however, exhibited low failure stress and strain values, and the failure surfaces clearly indicated a weak fiber-matrix interface. The importance of the interface regarding toughness was investigated by Callens et al. [51]. After treating the fiber surface with a silane coupling agent [20], transverse loading no longer caused pure adhesive debonding, but a mix between adhesive and cohesive failure. Improving the interface hence increased the transverse strength, and it was found to also increase the longitudinal toughness of the quasi-UD composite by about 20%. Callens et al. [52] also studied the influence of the matrix system on the toughness of the composite. Two different systems were considered, i.e. a brittle epoxy and a ductile thermoplastic. The quasi-UD composite with the ductile matrix was found to behave significantly more ductile along the loading direction than the one with the brittle matrix. None of the composites, however, reached the full failure strain of the fibers.

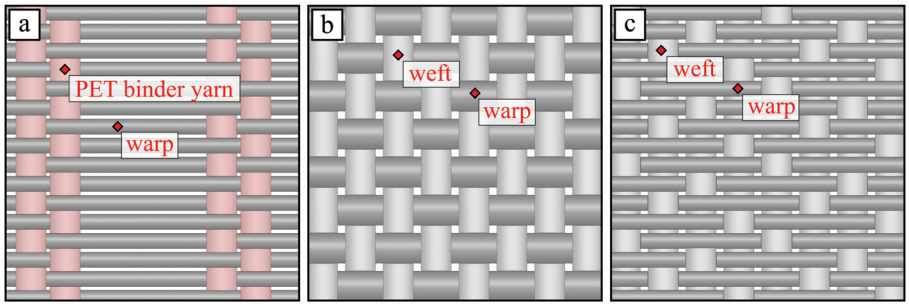


Figure 1-2: Different weave patterns: quasi-UD (a), basket (b), and 4-harness satin (c)

In the aforementioned works involving the quasi-UD weave [50-52], the first signs of damage were always reported to initiate on and around the binder yarns. A basket weave or a satin weave has a lot more transversal yarns, hence a lot more stress concentrators to induce damage. The influence of the reinforcement architecture on the toughness was studied by Callens et al. [53, 54] on composites with a polypropylene matrix system. All three weaves in Figure 1-2 were considered, but the results for the quasi-UD laminates were compromised by fiber misalignments. For the satin weave laminates, a strain-to-failure of 12.1% was found, while the basket weave laminates only made it up to 10.5%. The satin weaves also exhibited a higher stiffness than the basket weave. When it comes to the specific energy absorption of the laminates under an impact load, all three of the stainless steel fiber reinforcements outperformed the equivalent solutions known today [54]. The quasi-UD reinforcement proved to be up to twice as efficient as the 'real' woven reinforcements, which was in line with the trend reported in literature [55].

## 1.4 OBJECTIVES AND OUTLINE OF THE RESEARCH

The goal of this doctoral research is twofold. The first aim is to determine how and to what extent a textile of ductile stainless steel fibers can contribute in developing a tough composite material. The second aim is to develop a framework to simulate the mechanical behavior of ductile fiber textile composites through finite element modeling. These two objectives are inseparably linked. Indeed, developing a strategy to model a composite material requires thorough knowledge of the mechanics that govern its behavior. Conversely, a reliable numerical model will typically produce new insights about the material mechanics.

The objectives may seem well-defined, but they leave many questions unanswered. What aspects of the material behavior should be focused on? What is more crucial, the ductile nature of the reinforcement or its woven architecture? What is the right balance between experiments and numerical efforts in reaching the objectives? Every step taken in research is typically driven by the results and the findings of the previous one, and along the road, questions are answered while others arise. The natural course of this process is the reason why a chronological approach often works well for presenting a research work. The outline of this manuscript therefore roughly follows the chronology of the steps taken towards reaching the objectives stated above. This chronology is briefly explained and framed within the chapters in the next sections.

### 1.4.1 Chapter 2: Experimental characterization of the steel fiber textile reinforced epoxy laminates

A first step towards understanding the mechanics of a composite material and towards building a finite element model of its structure is to collect the necessary information about the constituents, and to characterize the geometry of the internal architecture. This work is reported on in Chapter 2. Additionally, the composite laminate production process is explained, and the laminates are subjected to static and cyclic testing for mechanical characterization. The mechanical characterization is not only key to understanding the material mechanics, it is also just as essential for the development of a reliable model as the geometrical characterization. First, because the experimental results are needed to validate the numerical outputs, and second, because the experiments may point towards issues or sensitivities that require special attention. Some aspects of the reality are inevitably lost when making the abstraction from a real material structure to a model, and knowledge of the concerns beforehand may help to decide which aspects must be represented. For the composite that is the subject of this work, the most notable experimental finding is the surprisingly low failure strain of the laminates. As achieving a high ductility is the rationale for this

composite material, aspects of damage initiation and propagation must be considered priorities when studying and modeling this material.

### 1.4.2 Chapter 3: Multiscale RVE analysis through finite element modeling

RVE (Representative Volume Element) modeling is the most commonly used strategy for meso-scale modeling of textile composites. The idea behind it is to consider the textile reinforcement as a periodic structure that can be represented by one periodic unit cell. A more thorough introduction on RVE modeling is the subject of the first section of Chapter 3. In the subsequent sections, an RVE model is elaborated in the finite element software Abaqus, and its outputs are validated against the experimental data that were obtained in Chapter 2. It was found that the elastic moduli are correctly predicted by the model, but that the stress and strain localizations within the structure are not in line with the experimental observations. The model is then further equipped with non-linear material models for the yarns and the matrix in an attempt to improve the quality of the localizations, yet without success. The chapter is concluded with the remark that the RVE model does not correctly predict the critical stress and strain locations within the composite laminates, and is therefore not suited to study damage.

### 1.4.3 Chapter 4: Experimental investigation on the geometric variabilities of the reinforcement, and on the relation between the internal geometry and the material mechanics

The most obvious shortcoming of RVE modeling is the intrinsic assumption of periodicity. The extent to which the real laminates diverge from this abstraction and the influence of the geometrical variabilities on the mechanical behavior is determined in Chapter 4. First, the 3D microscopic image stitching technique is presented. This technique was used to capture the edge of a laminate tensile specimen over its full length on high resolution microscopic images. Then, the necessary methodologies are established to quantify the geometrical variabilities in the reinforcement architecture. Finally, the laminates are subjected to tension, and the strain fields and the damage patterns on the laminate edge are compared to the internal geometry. These experiments indicate a strong relationship between the details of the geometry and the mechanics.

### 1.4.4 Chapter 5: Numerical evaluation of geometrical variabilities

The work presented in Chapter 4 revealed that the composite laminates under study exhibit strong variabilities on every aspect of the internal geometry, and that the mechanics strongly relate to the geometrical details. Based on these findings, a modeling strategy is proposed in which not the details of the geometry are sacrificed, but the dimension transverse to the loading direction. In the first section of Chapter 5, the proposed 2D modeling strategy is evaluated through a conceptual numerical exercise. Then, a methodology is presented for building a finite element model based on high resolution images of the edge of a laminate, and the results are validated against experimental data from Chapter 4. Finally, the model is developed further by implementing a sub-meso-scale detail, i.e. the inhomogeneity of the yarns. The chapter ends with the conclusion that a detailed 2D model is a valuable asset for studying the mechanics of the composite under study, yet that the working range is limited to the elastic regime. A 2D model can hence be useful when it comes to understanding damage initiation, but it cannot help explaining the mechanisms of damage propagation.

### 1.4.5 Chapter 6: Variation of the interfacial strength and the matrix ductility in search for the damage mechanisms

The 2D model presented in Chapter 5 was able to help understanding the internal mechanics up to the point of damage initiation. The final failure strain, however, also strongly depends on the way in which the damage propagates. In search for the damage mechanisms that govern the early failure of the composite, the role of the fiber/matrix interface and the matrix ductility are investigated experimentally in Chapter 6. Two variations on the original composite, differing in interfacial strength and matrix ductility, are presented in the first section. The influence of the interface and the matrix ductility on the mechanical response and the damage morphology are discussed in the second and third section, respectively. The results are rather unexpected, and Chapter 6 is concluded with a hypothesis on the fundamentals of damage propagation in ductile fiber textile composites.

## 1.5 REFERENCES

[1] Chawla KK. *Composite Materials: Science and Engineering*. 2 ed. New York: Springer Science + Business Media. 2012.

[2] Hardwick JG. *Cfrp rocket motor tubes wound with continuous pre-impregnated fibres*. Composites; 12: 41-47. 1981.

[3] Anderson BW. *The impact of carbon fibre composites on a military aircraft establishment*. Journal of Physics D: Applied Physics; 20: 311-314. 1987.

[4] Meyer RA. *Summary of panel discussion, challenges to researchers of carbon fibers and composites from the aerospace industry*. Carbon; 27: 765-766. 1989.

[5] Hufenbach W, Böhm R, Thieme M, Winkler A, Mäder E, Rausch J, et al. *Polypropylene/glass fibre 3D-textile reinforced composites for automotive applications*. Materials & Design; 32: 1468-1476. 2011.

[6] Sureshkumar M, Tamilselvam P, Kumaravelan R, Dharmalingam R. *Design, Fabrication, and Analysis of a Hybrid FIBER Composite Monoleaf Spring Using Carbon and E-Glass Fibers for Automotive Suspension Applications*. Mechanics of Composite Materials; 50: 115–122. 2014.

[7] Teixeira D, Giovanela M, Gonella LB, Crespo JS. *Influence of flow restriction on the microstructure and mechanical properties of long glass fiber-reinforced polyamide 6.6 composites for automotive applications*. Materials & Design; 47: 287-294. 2013.

[8] Liu TJ-C, Wu H-C. *Fiber direction and stacking sequence design for bicycle frame made of carbon/epoxy composite laminate*. Materials & Design; 31: 1971-1980. 2010.

[9] Cheong SK, Kang KW, Jeong SK. *Evaluation of the mechanical performance of golf shafts*. Engineering Failure Analysis; 13: 464-473. 2006.

[10] Kakei A, Epaarachchi JA, Islam M, Leng J, Rajic N. *Detection and characterisation of delamination damage propagation in Woven Glass Fibre Reinforced Polymer Composite using thermoelastic response mapping*. Composite Structures; 153: 442-450. 2016.

[11] Kersemans M, Martens A, Van Den Abeele K, Degrieck J, Zastavnik F, Pyl L, et al. *Detection and Localization of Delaminations in Thin Carbon Fiber Reinforced Composites with the Ultrasonic Polar Scan*. Journal of Nondestructive Evaluation; 33: 522-534. 2014.

[12] Mohammed L, Ansari MNM, Pua G, Jawaid M, Islam MS. *A Review on Natural Fiber Reinforced Polymer Composite and Its Applications*. International Journal of Polymer Science; 2015: 1-15. 2015.

[13] Banks-Sills L. *50th Anniversary Article: Review on Interface Fracture and Delamination of Composites*. Strain; 50: 98-110. 2014.

[14] Da Ponte G, Ghosh AK, Kakaroglou A, Van Hemelrijck D, Van Mele B, Verheyde B. *Adhesion Improvement between Epoxy and Stainless Steel Using a Silane Coupling Agent in an Atmospheric Plasma Process*. Plasma Processes and Polymers; 12: 347-361. 2015.

[15] Ochoa-Putman C, Vaidya UK. *Mechanisms of interfacial adhesion in metal–polymer composites – Effect of chemical treatment*. Composites Part A: Applied Science and Manufacturing; 42: 906-915. 2011.

[16] Honkanen M, Hoikkanen M, Vippola M, Vuorinen J, Lepistö T, Jussila P, et al. *Characterization of silane layers on modified stainless steel surfaces and related stainless steel–plastic hybrids*. Applied Surface Science; 257: 9335-9346. 2011.

[17] Vuori L, Hannula M, Lahtonen K, Jussila P, Ali-Löytty H, Hirsimäki M, et al. *Controlling the synergetic effects in (3-aminopropyl) trimethoxysilane*

*and (3-mercaptopropyl) trimethoxysilane coadsorption on stainless steel surfaces*. Applied Surface Science; 317: 856-866. 2014.

[18] Shokoohi S, Arefazar A, Khosrokhavar R. *Silane coupling agents in polymer-based reinforced composites: A review*. Journal of Reinforced Plastics and Composites; 27: 473-485. 2008.

[19] Ghosh AK, Bertels E, Goderis B, Smet M, Van Hemelrijck D, Van Mele B. *Optimisation of wet chemical silane deposition to improve the interfacial strength of stainless steel/epoxy*. Applied Surface Science; 324: 134-142. 2015.

[20] Ghosh AK. *The Interphase in Stainless Steel-Polymer Hybrids: Characterisation and Optimisation of Interfacial Interaction via Surface Treatment and Nano-modification of the Polymer*. [PhD Dissertation]. Brussels: Vrije Universiteit Brussel. Department of Materials and Chemistry - MACH. 2015.

[21] Bertels E. *Nano-Engineered Polymer-Steel Hybrids: Chemical and Physical Compatibilization*. [PhD dissertation]. Heverlee: KU Leuven. Department of Chemistry - Polymer Chemistry and Materials Division. 2015.

[22] Chandra AK, Mukhopadhyay R. *Studies of dynamic adhesion between steel cord and rubber using a new testing method*. Polymer Testing; 15: 13-34. 1996.

[23] Eiamnipon N, Nimdum P, Renard J, Kolitawong C. *Experimental investigation on high strain rate tensile behaviors of steel cord–rubber composite*. Composite Structures; 99: 1-7. 2013.

[24] Jamshidi M, Afshar F, Mohammadi N, Pourmahdian S. *Study on cord/rubber interface at elevated temperatures by H-pull test method*. Applied Surface Science; 249: 208-215. 2005.

[25] Shi X, Ma M, Lian C, Zhu D. *Investigation of the effects of adhesion promoters on the adhesion properties of rubbersteel cord by a new testing technique*. Journal of Applied Polymer Science; 131. 2014.

[26] Shi X, Ma M, Lian C, Zhu D. *Investigation on effects of dynamic fatigue frequency, temperature and number of cycles on the adhesion of rubber to steel cord by a new testing technique*. Polymer Testing; 32: 1145-1153. 2013.

[27] Taylor FW, Thompson SE, Feret R, Fuller WB, Newberry SB. *A treatise on concrete, plain and reinforced; materials, construction and design of concrete and reinforced concrete*. New York: J. Wiley & sons. 1905.

[28] Reid HA. *Concrete and Reinforced Concrete Construction*. New York: The M.C. Clark Publishing Co. 1907.

[29] Pirmohammad S, Bayat A. *Characterizing mixed mode I/III fracture toughness of asphalt concrete using asymmetric disc bend (ADB) specimen*. Construction and Building Materials; 120: 571-580. 2016.

[30] Wang Y, Hu X, Liang L, Zhu W. *Determination of tensile strength and fracture toughness of concrete using notched 3-p-b specimens*. Engineering Fracture Mechanics; 160: 67-77. 2016.

[31] Abdallah S, Fan M, Zhou X, Le Geyt S. *Anchorage Effects of Various Steel Fibre Architectures for Concrete Reinforcement*. International Journal of Concrete Structures and Materials; 10: 325-335. 2016.

[32] Srinivasan R, Suresh Babu S, Itti SV. *A study on performance of 3D RC frames with masonry in-fill under dynamic loading conditions*. KSCE Journal of Civil Engineering; 21: 322-328. 2016.

[33] Qu Y, Li X, Kong X, Zhang W, Wang X. *Numerical simulation on dynamic behavior of reinforced concrete beam with initial cracks subjected to air blast loading*. Engineering Structures; 128: 96-110. 2016.

[34] Van Tittelboom K, Wang J, Araújo M, Snoeck D, Gruyaert E, Debbaut B, et al. *Comparison of different approaches for self-healing concrete in a large-scale lab test*. Construction and Building Materials; 107: 125-137. 2016.

[35] Karaiskos G, Tsangouri E, Aggelis DG, Van Tittelboom K, De Belie N, Van Hemelrijck D. *Performance monitoring of large-scale autonomously healed concrete beams under four-point bending through multiple non-destructive testing methods*. Smart Materials and Structures; 25: 055003. 2016.

[36] Wrzesien A. *Improving the impact resistance of glass-fibre composites*. Composites; 3: 172-174. 1972.

[37] Ross CA, Cristescu N, Sierakowski RL. *Experimental studies on failure mechanisms of impacted composite plates*. Fibre Science and Technology; 9. 1976.

[38] Ross CA, Sierakowski RL. *Studies on the impact resistance of composite plates*. Composites; 4: 157-161. 1973.

[39] Ahmed T. *Hybrid Composite Structures: Multifunctionality through Metal Fibres*. [PhD dissertation]. Netherlands: TU Delft. Design and Production of Composite Structures. 2009.

[40] Wetherhold RC, Bös J. *Ductile reinforcements for enhancing fracture resistance in composite materials*. Theoretical and Applied Fracture Mechanics; 33: 83-91. 2000.

[41] Bagwell RM, Wetherhold RC. *Improvement in fracture toughness of an epoxy/copper composite through the use of various end shaped fibers*. Materials Science and Engineering: A; 361: 294-301. 2003.

[42] Bagwell RM, Wetherhold RC. *Fiber pullout behavior and impact toughness of short shaped copper fibers in thermoset matrices*. Composites Part A: Applied Science and Manufacturing; 36: 683-690. 2005.

[43] Wetherhold RC, Lee FK. *Shaped ductile fibers to improve the toughness of epoxy-matrix composites*. Composite Science and Technology; 61: 517-530. 2001.

[44] Zhu YT, Beyerlein IJ. *Bone-shaped short fiber composites - an overview*. Materials Science and Engineering: A; 326: 208-227. 2002.

[45] Tsai JH, Patra A, Wetherhold R. *Finite element simulation of shaped ductile fiber pullout using a mixed cohesive zone/friction interface model*. Composites Part A: Applied Science and Manufacturing; 36: 827-838. 2005.

[46] Wetherhold RC, Corjon M, Das PK. *Multiscale considerations for interface engineering to improve fracture toughness of ductile fiber/thermoset matrix composites*. Composites Science and Technology; 67: 2428-2437. 2007.

[47] Wetherhold RC, Das PK. *Oxidation of copper fiber surface to improve fracture toughness of Cu/epoxy composite*. Materials Science and Engineering: A; 460-461: 344-350. 2007.

[48] Arikan H, Avci A, Akdemir A. *Fracture behaviour of steel fibre reinforced polymer composite*. Polymer Testing; 23: 615-619. 2004.

[49] Samanci A. *Fracture behavior of woven steel fiber reinforced and sand particle filled polymer composites*. Construction and Building Materials; 26: 167-171. 2012.

[50] Allaer K, De Baere I, Lava P, Van Paepegem W, Degrieck J. *On the in-plane mechanical properties of stainless steel fibre reinforced ductile composites*. Composites Science and Technology; 100: 34-43. 2014.

[51] Callens MG, Gorbatikh L, Bertels E, Goderis B, Smet M, Verpoest I. *Tensile behaviour of stainless steel fibre/epoxy composites with modified adhesion*. Composites Part A: Applied Science and Manufacturing; 69: 208-218. 2015.

[52] Callens MG, Gorbatikh L, Verpoest I. *Ductile steel fibre composites with brittle and ductile matrices*. Composites Part A: Applied Science and Manufacturing; 61: 235-244. 2014.

[53] Callens MG, De Cuyper P, Gorbatikh L, Verpoest I. *Ductile steel fibre/polypropylene composites: influence of fibre architecture on the tensile behaviour*. In: A. Suleman PC, et al., editor. IV ECCOMAS Thematic Conference on the Mechanical Response of Composites. 2013.

[54] Callens MG, De Cuyper P, Gorbatikh L, Verpoest I. *Effect of fibre architecture on the tensile and impact behaviour of ductile stainless steel fibre polypropylene composites*. Composite Structures; 119: 528-533. 2015.

[55] Vallons K, Behaeghe A, Lomov SV, Verpoest I. *Impact and post-impact properties of a carbon fibre non-crimp fabric and a twill weave composite*. Composites Part A: Applied Science and Manufacturing; 41: 1019-1026. 2010.

# Chapter 2

## EXPERIMENTAL CHARACTERIZATION OF THE STEEL FIBER TEXTILE REINFORCED EPOXY LAMINATES

*The first part of this chapter briefly introduces the textile composite that is the subject of this research work. In the subsequent sections, the constituent materials are presented, and the laminate production process is explained. Finally, the experimental setup for mechanical testing of the composite laminates is presented, and the results of the mechanical characterization are discussed. These results include the elastic constants of the laminates and the strength properties under uniaxial static tensile loading, the strain field on the surface of the specimen, the damage morphology and propagation, and the behavior under cyclic loading.*

## 2.1 INTRODUCTION

The behavior and the properties of composites materials are generally not a as well known and documented as for many homogeneous materials. An important reason is the multitude of possibilities in combining different constituent materials, in different ratios, and with different internal structures, all of them composing different composites. Despite this wide variety and the resulting lack of listed properties, many of the more general mechanisms are well understood. Especially for UD laminates with brittle constituents, the current theories on laminate mechanics and failure [1] suffice to predict the mechanical response in a way that satisfies the designers' needs for many applications. For textile composites, analytical theories are not state of the art yet. The added complexity of the weave architecture makes it more difficult to understand the mechanics behind the observed behavior. The composite material that is the subject of this research work has the additional challenge of being composed of ductile materials. Therefore, a thorough characterization of the composite and its constituents is an essential start in understanding its behavior.

## 2.2 CONSTITUENT MATERIALS

### 2.2.1 Stainless steel fibers

The composite reinforcement that was used in this research is made from continuous 316L stainless steel fibers with a diameter of 30 μm. The fibers were manufactured by NV Bekaert S.A. by bundled drawing of stainless steel wires [2, 3]. The production process is illustrated schematically in Figure 2-1. Several copper-coated stainless steel wires are first bundled into a metal tube, which is then reduced in diameter via subsequent wire drawing steps. This drawing process hence transforms the initial wires into thin fibers that are embedded in a matrix of copper. Once the desired final fiber diameter has been obtained, the copper coating and the metal tube are dissolved in acid, resulting in individual long stainless steel fibers. In between drawing steps, the fiber bundle is annealed in order to obtain the deformability that is needed to achieve the large diameter reductions. After the drawing process, a final annealing treatment is performed in order to reach the desired fiber ductility. A failure strain of 19.5% was found in the single-fiber tensile experiments performed by the manufacturer. Specifications of the steel fibers as determined via static tensile testing can be found in Figure 2-2. All values reported are (based on) engineering stresses and strains.

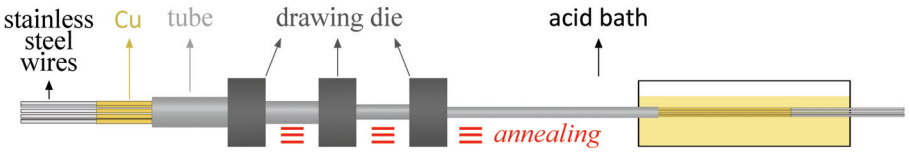


Figure 2-1: Schematic illustration of bundled wire drawing

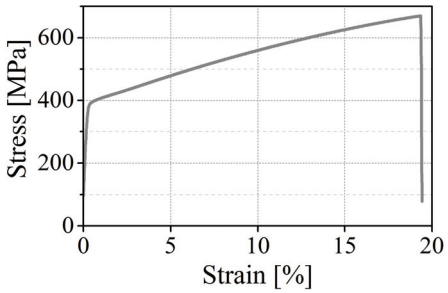


| Mechanical property | Value |
|---|---|
| Young's modulus [GPa] | 193 ± 6 |
| Yield strength [MPa] | 345 ± 13 |
| Tensile strength [MPa] | 667 ± 30 |
| Failure strain [%] | 19.5 ± 5.1 |

Figure 2-2: Stress-strain curve and mechanical properties (mean value ± standard deviation) of the individual stainless steel fibers as reported by NV Bekaert S.A.

Due to the production process, the fibers have an irregular, polygonal sectional shape and a rough surface, which was found to improve the adhesion to the matrix material of a fiber reinforced composite [4]. On the other hand, stress concentrations around the fiber vertices upon loading can be expected to advance debonding between fiber and matrix [5, 6]. Because of the irregular sectional shape of the fibers, their diameter is to be interpreted as an 'equivalent diameter', i.e. the diameter of an imaginary circle, of which the surface area is identical to the surface area of a cross section of the stainless steel fiber (Figure 2-3). Apart from serving as a composite reinforcement, stainless steel fibers are used in filter media, conductive plastics, electrically conductive or heat-resistant textiles, gas burner membranes or tubes, heating elements, or for electromagnetic interference (EMI) shielding and electrostatic discharge (ESD) applications.

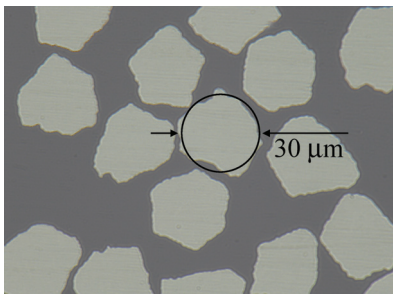


Figure 2-3: Equivalent diameter on a microscopic image of the steel fibers

### 2.2.2 Fabric reinforcement

Apart from a quasi-UD structure, two different woven textiles were produced with the stainless steel fibers, i.e. a basket weave and a 4-harness satin weave (cf. Figure 1-2). Based on the exploratory work by Callens et al. [7, 8], the 4-harness satin weave is selected as the most promising of both in view of developing a tough composite.

The warp yarns of the satin weave consist of 275 fibers and the weft yarns are composed of two warp yarns. The weave has two sides that look distinctly different: one is dominated by warp yarns (Figure 2-4.a), and the other by weft yarns (Figure 2-4.b). These sides will hence forward be addressed as 'warp side' and 'weft side', respectively. The fabric is loosely woven, with an areal density of 1455 g/m² and a thickness of 0.8 mm. As a result, the yarns are not very confined in the weave structure, so they are easily shifted upon handling. Translational shifting causes inhomogeneity in the overall fiber volume fraction in a composite part, while shear deformations of the fabric give rise to fiber misalignments. Therefore, the fabric must be handled with great care during composite production.

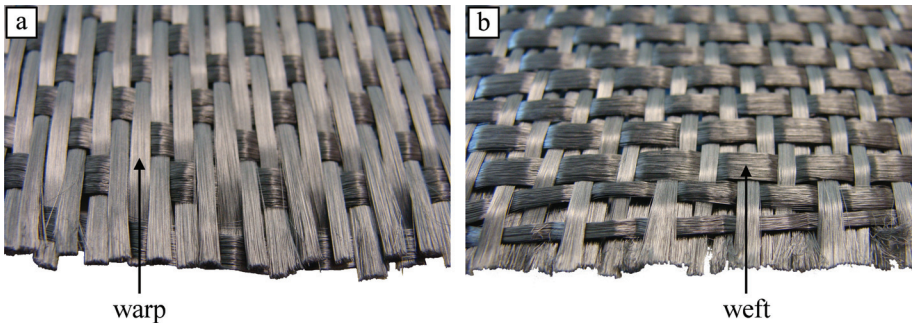


Figure 2-4: Warp side (a) and weft side (b) of the 4-harness satin weave

Due to its periodic structure, a fabric geometry can be represented by its simplest repeating unit cell (RUC). The simplest RUC is the smallest possible volume within the material structure that can be used to regenerate the macroscopic material with tessellation transformations only. The selection is not unique, because the position of the unit cell within the fabric structure can be chosen arbitrarily by shifting its bounding box. However, all possible selections are equivalent [9] and of equal size. Possible simplest RUC's for the 4-harness satin weave are illustrated on Figure 2-5.

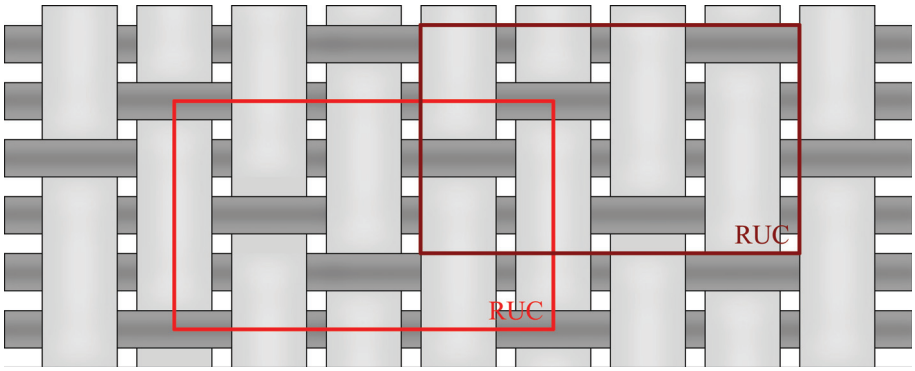


Figure 2-5: Possible RUC selections in the 4-harness satin weave

In principle, every yarn in the 4-harness satin weave should consist of the foreseen number of identical steel fibers, all of them with the mechanical properties as reported in Figure 2-2. In reality, however, fibers are often damaged, or even broken, during the weaving process [10]. Therefore, it is advisable to assess the properties of the weave experimentally, rather than to deduce them from the constituent fibers. The ASTM standards provide a method to measure the breaking force and elongation of a textile under tensile loading [11]. The tests were performed on five samples of fabric for both weave directions. An example of a weft-oriented fabric specimen is shown on Figure 2-6.a. On two additional fabric samples, the transversal yarns were removed manually from the gauge area after clamping, but before testing the fabric. Testing these samples hence comes down to testing the longitudinal yarns, as illustrated in Figure 2-6.b for a weft-oriented specimen. The samples were cut to a width containing 20 warp yarns, or 10 weft yarns. Therefore, the samples for both loading directions contained 5500 longitudinal fibers. The total length of the samples was 180 mm, with a gauge length of 100 mm.

The tests were performed on a servo-hydraulic INSTRON 8801 testing machine with an AlignPRO alignment fixture. The fabric was prestressed manually to 10 N, after which the alignment was checked with a self-levelling laser. The clamps of the machine are profiled with a fine dot pattern for grip, which indents the fabric. This patterned embossment was used after the test to ensure that there had been no slip in the clamps during the experiment. The tests were displacement-controlled with a constant crosshead speed of 2 mm/min. Force and displacement were given by the FastTrack 8800 digital controller with the same time sampling. For the ease of interpretation, the displacement values were converted to engineering strain by dividing them by the original gauge length. The fabric was monitored during the experiment with a Dino-Lite USB microscope in order to capture fiber failure.

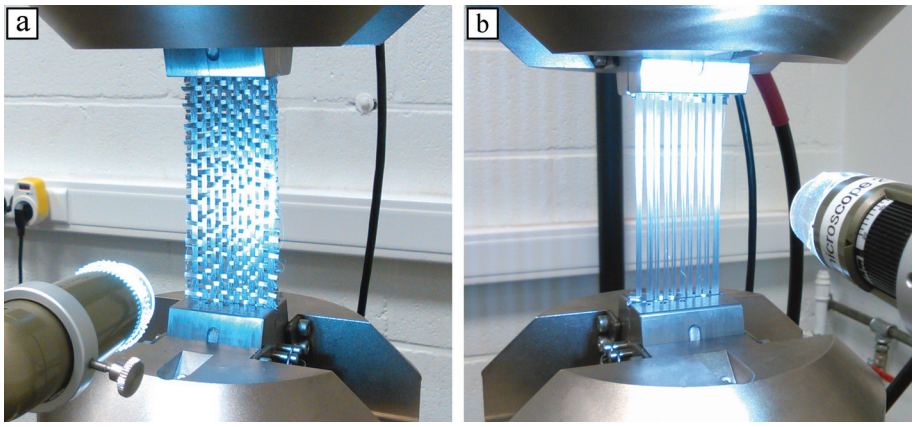


Figure 2-6: Experimental setup with a full fabric sample (a) and with a fabric sample containing only load-carrying yarns (b)

The resulting force-strain curves of both the complete fabric samples and the samples containing only the load-carrying yarns are shown in Figure 2-7.a for warp-oriented loading and on Figure 2-7.b for weft-oriented loading. Five frames from the microscopic movies are also shown with respect to their position on the force-strain graphs. These frames were correlated to the force-strain curve by tracing back the frame time to the FastTrack 8800 digital controller clock time. For comparison, a hypothetical upper limit is plotted in red along with the experimental curves. This hypothetical curve is calculated by multiplying the tensile force recorded for a single fiber by 5500, hence it would be obtained if all 5500 load-carrying fibers were strained in parallel at exactly the same rate. In a fabric configuration, this is never the case, because it is impossible to clamp the fabric without any statistical variation on the gauge lengths of the fibers. Despite these unavoidable variations, the experimentally obtained force-strain curves seem very reproducible. In the next paragraphs, the results will be discussed following the chronology of the experiments.

The initial part of the force-strain curve of a fabric holds an indication for the crimp of the load-carrying yarns. When a fabric is subjected to a displacement-controlled tensile test, the initially applied strain merely straightens the load-carrying yarns, and this straightening does not require a high force. The force-strain curves of the warp-oriented samples start rising almost immediately, while the weft-oriented samples can be strained up to about 1% before taking on tensile load. Therefore, the force-strain curves clearly indicate a higher crimp on the weft yarns than on the warp yarns. Both the full fabric samples and the samples containing only load-carrying yarns exhibit the same force-strain curves, which shows that the transversal yarns of the fabric have no influence on the tensile behavior. This finding was to be expected, except for the initial straightening behavior: if the transversal yarns are removed, there is nothing that keeps the longitudinal yarns from being straight. Nonetheless, the naked weft

yarns are just as undulated as the ones that are kept in place by transversal yarns, despite the prestress of 10 N. In other terms, the undulations – especially in the weft yarns – are present as permanent, plastic deformations. This finding will also help explaining the next stage of the force-strain behavior, which is the yield point of the samples.

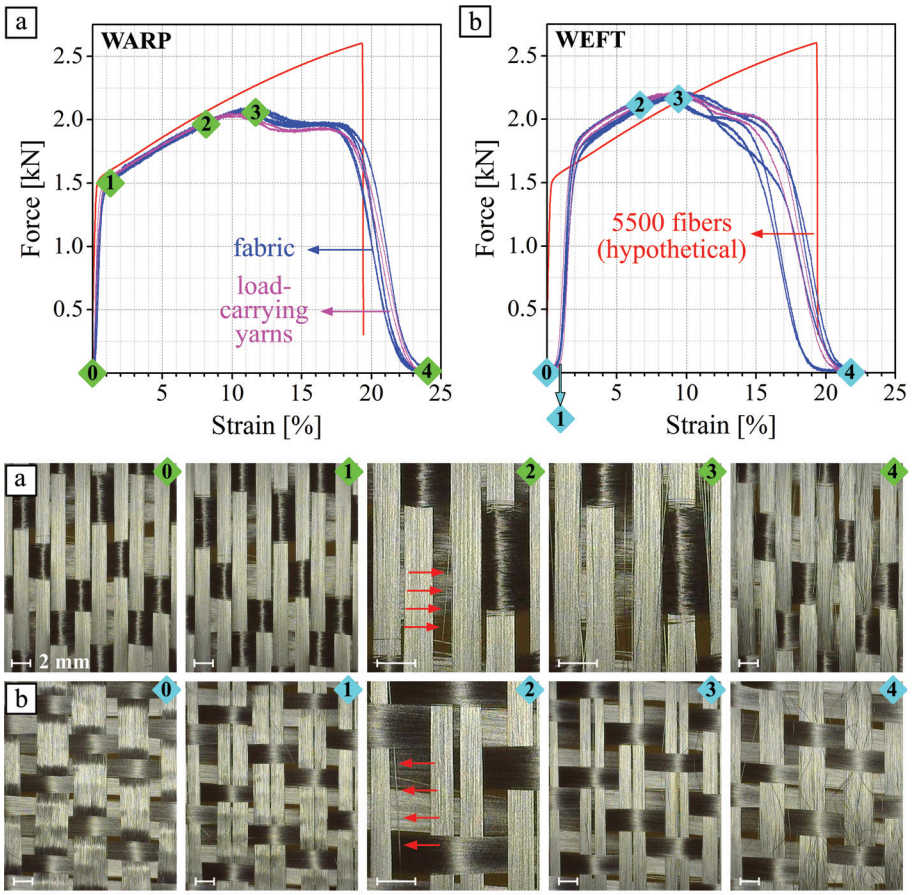


Figure 2-7: Force-strain curves of the dry fabric reinforcement (blue curves) and the load-carrying yarns (purple curves) loaded along the warp (a) and along the weft (b) direction, and corresponding microscopic images for the full fabric samples

The warp-oriented samples have almost the same yield force as the hypothetical curve. If there were large variations in gauge length between the fibers, the shortest ones would start yielding while the longest ones were still unloaded, and this would lower the measured yield force. Therefore, the high yield point, together with the good reproducibility of the experiments, indicates that the samples were clamped very evenly. An unexpected observation is made on the weft-oriented samples, as their

yield force is higher than the hypothetical upper limit. Any faults or inaccuracies regarding clamping can be ruled out to explain this finding, as these would only lower the measured yield strength. Inaccuracies on the single fiber data, hence on the hypothetical red curve, would still not explain why the yield point is higher in the weft direction than in the warp direction. The only remaining option is that the observed behavior is indeed physical, hence that the weft yarns have indeed a higher yield strength than the warp yarns. A difference in annealing treatment during fiber production cannot be the cause, because the distinction between warp and weft fibers was not made yet at that stage. A difference in cold working, however, is a very plausible explanation. During the weaving, the weft yarns are drawn back and forth in between two layers of parallel warp yarns at high speed, then trapped between the warp layers as these cross over, and then pushed back to tighten the weave. The weft fibers may have undergone plastic deformation, hence cold working, during this process. This would not only explain the higher yield strength and the plastically imprinted undulations, but also the lower failure strain of the weft-oriented samples.

The first signs of fiber breakage were observed before the maximum force was reached, regardless of the loading direction. The broken fibers are marked on the corresponding frames 2 on Figure 2-7. The fact that the force still increases beyond this point means that the few broken fibers are still more than compensated by the strain hardening of the remaining ones. When this is no longer the case, the force starts to drop. After that, fiber failures start succeeding each other rapidly under almost constant stress, before the fabric finally loses all of its load-bearing capacity.

### 2.2.3 Epoxy resin

Amongst the matrix systems that have been explored in combination with stainless steel fibers (cf. section 1.3.2), only one has been found capable of translating the full plastic potential of the fibers into the ductility of the composite material, i.e. the system used by Allaer et al. [12]. This matrix system is a low-viscosity resin system developed for vacuum infusion molding of wind turbine blades. It consists of the modified bisphenol-A resin EPIKOTE™ MGS™ RIMR 135 and the polyamine curing agent EPIKURE™ MGS™ RIMH 137. Both resin and harder were purchased from Momentive Specialty Chemicals, and they were mixed in a 100:30 weight ratio. The neat resin bulk material was characterized through mechanical testing on macro-scale specimens by Allaer et al. [12]. A summary of the behavior under static tensile loading is given in Figure 2-8. All values reported are (based on) engineering stresses and strains. A failure strain as high as 8% was reported for the neat epoxy. Due to size effects, the true failure strain of the resin pockets in the composite material could be even higher [13]. The product data sheet mentions an elongation at break between 8% and 16% [14].

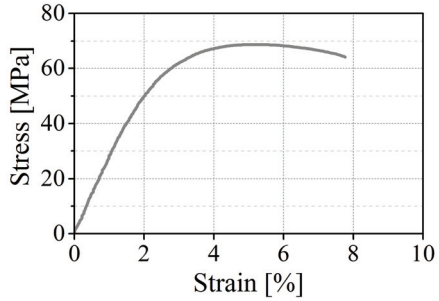


| Mechanical property | Value |
|---|---|
| Young's modulus [GPa] | 2.73 ± 0.02 |
| Yield strength [MPa] | 41.4 ± 2.4 |
| Tensile strength [MPa] | 66.1 ± 0.4 |
| Failure strain [%] | 8.24 ± 0.69 |

Figure 2-8: Stress-strain curve and mechanical properties (mean value ± standard deviation) under static tensile loading of the RIMR135/RIMH137 neat resin bulk material as reported by Allaer et al. [12]

## 2.3 PRODUCTION PROCESS OF SATIN WEAVE COMPOSITE

Composite plates with dimensions of 330 x 330 x 3 mm³ were produced using the vacuum assisted resin transfer molding (VA-RTM) technique (Figure 2-9.a). The mix of resin and hardener was degassed in a vacuum bell jar, after which it was drawn through a stack of dry fabric under vacuum pressure. Two symmetrical four-layer layup systems were considered, one with the warp side of the fabric outwards (Figure 2-9.b) and one with the weft side outwards (Figure 2-9.c). These layup systems will from now on be referred to as $[0°,90°]_{2S}^{warp}$ and $[0°,90°]_{2S}^{weft}$, respectively. All layers were aligned manually and with the same orientation. The plates were cured at 80°C

for 15h according to the manufacturer's data sheet. Microscopic inspection showed no sign of poor fiber impregnation or air entrapments. With a fabric thickness of 0.8 mm, the height of a four-layer stack is 3.2 mm at most. A fabric does not have an even profile, and the more the layers sink into the valleys of their neighbors, the more this lowers the stack thickness. The mold cavity was 3 mm high, and a mild pressure was needed to close the mold on four layers of fabric. An attempt to increase the fiber volume fraction by stacking five layers of fabric failed, because it was impossible to close the mold without damaging it.

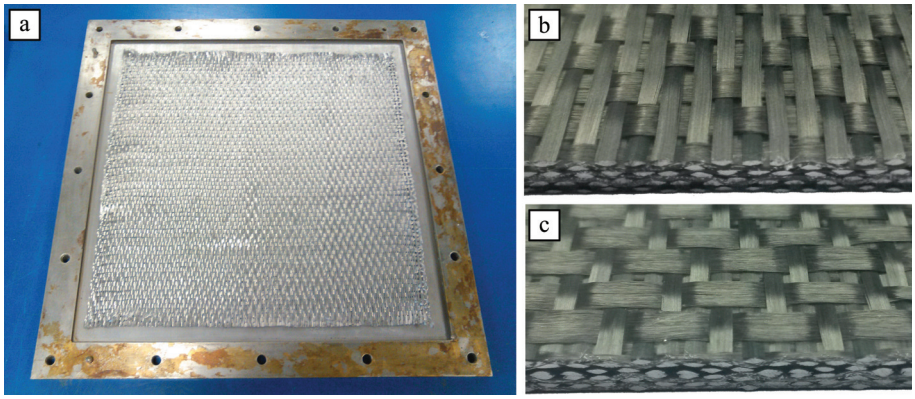


Figure 2-9: Mold for VA-RTM production (a), and the resulting stainless steel fiber/epoxy composite laminates with a $[0°,90°]_{2S}^{warp}$ layup system (a), and a $[0°,90°]_{2S}^{weft}$ layup system (b)

## 2.4 GEOMETRICAL CHARACTERIZATION

### 2.4.1 Dimensions of the fabric architecture

Micro-CT scans of a laminate slice of 25 x 25 x 3 mm³ were taken and the data were reconstructed using Volume Graphics software [15]. The geometrical characteristics were determined on the three perpendicular sectional views through the reconstructed sample. The yarn dimensions were determined by measuring width (Figure 2-10.a) and thickness (Figure 2-10.b) on the two available sectional views. This procedure was performed layer by layer, and on every yarn crossover. An analogous strategy was used to determine the RUC dimensions, which were then used to calculate the yarn spacing. The results of these measurements, including the standard deviations, are listed in Table 2-1. The number of measurements on which the result is based is mentioned between brackets for every parameter.

Table 2-1: Geometrical characteristics (mean value ± standard deviation) of the reinforcing fabric as measured using micro-CT data, with the number of measurements on which the result is based mentioned between brackets

| **Parameter (number of measurements)** | **warp** | **weft** |
|---|---|---|
| RUC dimension [mm] | 7.74 ± 0.23 (64) | 17.26 ± 0.39 (64) |
| Yarn thickness [mm] | 0.38 ± 0.05 (440) | 0.43 ± 0.06 (440) |
| Yarn width [mm] | 1.51 ± 0.12 (440) | 3.58 ± 0.39 (440) |
| Yarn spacing [mm] | 1.935 | 4.315 |

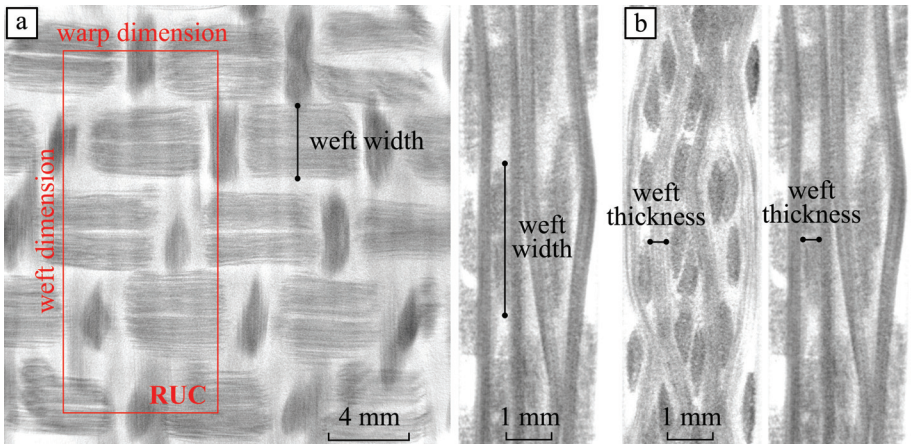


Figure 2-10: Geometrical characterization of the yarns using micro CT data: width (a) and thickness (b) measurements

## 2.4.2 Fiber volume fraction

A correct determination of the fiber volume fraction of a composite is very important, as this parameter corresponds directly with the mechanical properties. A quick assessment can be made using the plate thickness and the fabric and steel properties as provided by the manufacturer. The volume of fibers in one square meter of composite plate can be calculated from the areal density of the fabric $\rho^{A}_{fabric}$, the density of the steel $\rho_{steel}$, and the number of layers n as:

$$v_f = n\frac{\rho^{A}_{fabric}}{\rho_{steel}} = 4 \cdot \frac{1455\ g/m^2}{7990 \cdot 10^3\ g/m^3} = 0.7284 \cdot 10^{-3}\frac{m^3}{m^2} \quad (2\text{-}1)$$

The fiber volume fraction $V_f$ can now be calculated as the volume percentage of fibers in one square meter of composite plate material with a thickness of 3 mm:

$$V_f = \frac{0.7284 \cdot 10^{-3}\ m^3/m^2}{3 \cdot 10^{-3}\ m^3/m^2} = 24.28\% \tag{2-2}$$

A more accurate value can be achieved by directly measuring the volumetric contributions as specified in the ASTM D 792-08 standard [16]. For a voids-free composite, the fiber volume fraction $V_f$ can be expressed in terms of the density of the composite itself $\rho_c$, and the densities of the constituents, i.e. the fiber density $\rho_f$ and the matrix density $\rho_m$:

$$V_f = \frac{\rho_c - \rho_m}{\rho_f - \rho_m} \tag{2-3}$$

The densities of the constituent materials, as well as the density of the composite, can be determined using the principle of Archimedes. Small specimens of the steel fiber fabric, the neat epoxy and the composite material were selected. First, the dry mass m of these specimens was measured using an analytical balance, as illustrated schematically in Figure 2-11.a. Then, the specimens were submerged in demineralized water in order to measure their apparent mass $m_a$, as shown in Figure 2-11.b. The glass with the submerged specimen was de-aired in a bell jar before measuring. This was especially important for the fiber specimens, because a lot of air bubbles adhere to the fabric when it is submerged. These air bubbles exert a lifting force on the specimen, and therefore, they lower the measured value of $m_a$. The balance used for these measurements had a range up to 200 g and a resolution of 0.1 mg.

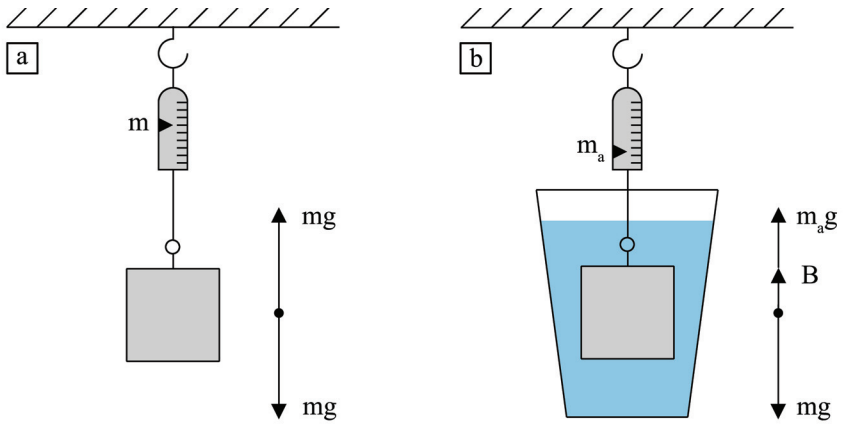


Figure 2-11: Measuring the dry weight (a) and the apparent weight (b) of the composite and its constituents

According to Archimedes' principle, a body submerged in water experiences an upward buoyant force B that equals the weight of the water that the object displaces:

$$B = v\rho_w g \tag{2-4}$$

In this, v is the volume of the specimen, g is the gravity constant, and $\rho_w = 0.9982\ g/cm^3$ is the density of demineralized water at a temperature of 20°C [17]. The force equilibrium on the submerged specimens can now be expressed as:

$$m_a g = mg - v\rho_w g \tag{2-5}$$

Rearranging this expression gives the volume of the specimens:

$$v = \frac{m_a - m}{\rho_w} \tag{2-6}$$

Now, the density of the specimens can be obtained from the measured mass values as:

$$\rho = \frac{m}{v} = \frac{m}{m_a - m} \cdot \rho_w \tag{2-7}$$

A summary of the measurements and calculations is given in Table 2-2. A fiber volume fraction of 25.61% was determined using this method.

Table 2-2: Mass measurements for the composite and its constituents and the calculated volume and density values

| **Parameter** | **Steel fiber fabric** | **Neat epoxy resin** | **Composite laminate** |
|---|---|---|---|
| Dry mass m [g] | 4.7305 | 9.6767 | 32.3766 |
| Apparent mass $m_a$ [g] | 4.1454 | 2.2104 | 21.2919 |
| Volume v [cm³] | 0.5862 | 8.4816 | 11.1047 |
| Density ρ [g/cm³] | 8.0704 | 1.1409 | 2.9156 |
| Fiber volume fraction $V_f$ [%] | | | **25.61** |

A notion of the directional fiber distribution can be achieved by calculating the number of steel fibers along each of the principal directions in the fabric RUC. Along the warp direction, there are four yarns of each 275 fibers over a length of 7.74 mm. Therefore, the total amount of warp fibers per mm equals 142. The four weft yarns each contain 550 fibers, and they are spread over a length of 17.26 mm. The amount of weft fibers per mm thus equals 127. This means that the warp direction accounts for 52.7% of the fiber volume fraction.

## 2.5 MECHANICAL CHARACTERIZATION

Two types of experiment were performed in order to characterize the tensile behavior of the composite laminates. The mechanical properties, as well as the strain distribution on the specimen surface and the damage propagation on the laminate edge were investigated by statically loading the specimens until failure. Additionally, hysteresis tests were performed in order to obtain the evolution of the permanent deformation and the stiffness as a function of the loading history.

### 2.5.1 Specimen selection

The response of the composite under static tensile loading was tested in accordance with the ASTM standard D3039/D3039M [18]. Four different rectangular specimen types were considered for the static tests, which will be designated with an 'S'. Their specifications are given in Table 2-3. The first two types are standard size coupons, both with the warp side of the fabric directed outwards. The first type, S-warp-A, is loaded along the warp direction, the second type, S-weft-A, along the weft direction. The third specimen type, S-weft-B, was introduced to assess the influence of the layup system on the mechanical properties. The fourth type, S-weft-AL, was introduced to ensure that the coupon size does not affect the mechanical response. The ASTM standard D6856/D6856M recommends a specimen width of at least two repeating units of the reinforcing fabric structure [19]. Due to the large unit cell dimension along the warp yarns in the 4-harness satin weave, this recommendation is not met in the standard size coupons for weft-oriented loading (cf. Table 2-3). The reason why the standard specimens were not chosen wider is because this would also require them to be sufficiently longer, in order to minimize bending stresses caused by minor grip eccentricities. The total length of the specimens is, however, limited to 300 mm by the plate dimensions. The standard specimen size was hence chosen in favor of having the ideal proportionality in dimensions, while the S-weft-AL specimens were designed to include two unit cells.

The hysteresis experiments were performed on two specimen types, which are designated with an 'H'. One type is reserved for loading along the warp yarns (H-warp-B), and one for loading along the weft yarns (H-weft-B). Specifications of these specimen types are also summarized in Table 2-3.

Every set of the static experiments was repeated five times, the hysteresis tests were performed three times. No end tabs were used, as preliminary testing had proven them unnecessary. All results reported in this work refer to coupons that failed in the mid-section of the gauge area, sufficiently far away from the clamps.

Table 2-3: Specimen types for characterization of the tensile behavior of the composite laminate

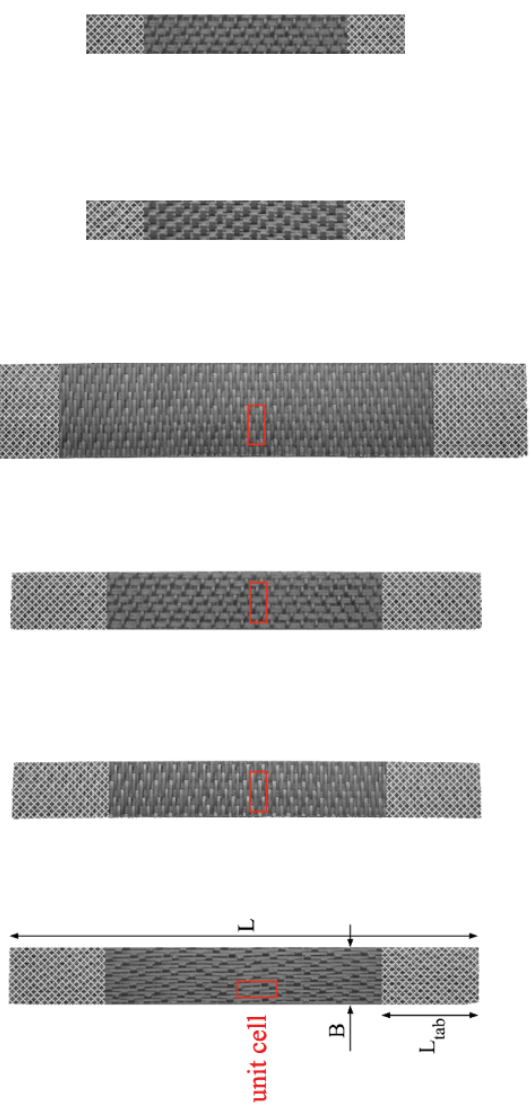


| | S-warp-A | S-weft-A | S-weft-B | S-weft-AL | H-warp-B | H-weft-B |
|---|---|---|---|---|---|---|
| **System** | $[0°,90°]_{2S}^{warp}$ | $[90°,0°]_{2S}^{warp}$ | $[90°,0°]_{2S}^{weft}$ | $[90°,0°]_{2S}^{warp}$ | $[0°,90°]_{2S}^{weft}$ | $[90°,0°]_{2S}^{weft}$ |
| **Layup** | A (warp out) | A (warp out) | B (weft out) | A (warp out) | B (weft out) | B (weft out) |
| **Loading** | along warp | along weft | along weft | along weft | along warp | along weft |
| **L [mm]** | 250 | 250 | 250 | 300 | 165 | 165 |
| **B [mm]** | 30 | 30 | 30 | 50 | 20 | 20 |
| **$L_{tab}$ [mm]** | 50 | 50 | 50 | 50 | 30 | 30 |

### 2.5.2 Test setup, instrumentation and data acquisition

The coupons intended for static tensile experiments were equipped with two strain gauges with a resistance of 350 Ω and a maximum strain of 5% in order to measure local strains in the gauge area in both principal directions, as shown in Figure 2-12.a. The resistance wire of the strain gauge covers an area of 3 x 7 mm², so the measurement made by a strain gauge is the average longitudinal strain over this region. This is an important note, because the surface strains in fabric reinforced composites are typically non-uniform. In order to get a view on the full-field surface displacements and deformations, the specimens were additionally instrumented with Digital Image Correlation (DIC) [20, 21]. The principle behind this technique is to monitor a speckle pattern (Figure 2-12.b) on the specimen surface during loading and to calculate the full surface strain fields afterwards by correlating the consecutive images. Pictures of the speckled specimen surface were taken every second by a 2 mega-pixel 8-bit CCD AVT Stingray F-201 B1/1.8" camera, and all post processing was performed with the MatchID software application [22]. The camera setup was calibrated in order to account for intrinsic and extrinsic parameters during the image correlation process. In addition to providing a view on the surface strain distribution, the DIC results can be used to verify the strain gauge measurements. To this end, the DIC longitudinal strain map was averaged out over the same 3 x 7 mm² working area as the strain gauge and on the same position. The damage propagation was monitored during loading at 15 frames per second with a Dino-Lite AM4113T USB microscope, which was positioned on a polished edge of the coupon (Figure 2-12.b). The hysteresis coupons were equipped with a longitudinal strain gauge of the same type as the ones used for the static experiments.

All tests were performed on a servo-hydraulic INSTRON 8801 testing machine with an AlignPRO alignment fixture and a load cell of 50 kN. The tests were displacement-controlled with a constant crosshead speed of 2 mm/min. Force and displacement were given by the FastTrack 8800 digital controller with the same time sampling. Strain gauge measurements were acquired synchronously using Labview data acquisition software, while the DIC measurements were synchronized manually during post processing. The static tensile specimens were loaded continuously until failure. The hysteresis specimens were subjected to loading-unloading with an amplitude increase of 5 MPa per cycle.

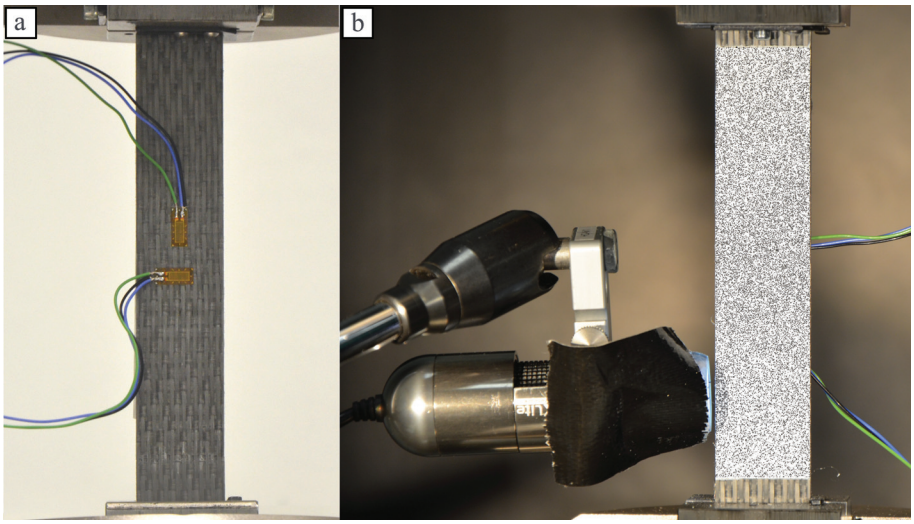


Figure 2-12: Instrumentation on the tensile experiments: strain gauges (a), the speckle pattern for DIC, and the USB microscope for online recording of damage events (b)

### 2.5.3 Stress-strain relation

The static tensile stress-strain curves as recorded by the longitudinal strain gauges are shown in Figure 2-13, along with the curves that were obtained by averaging the DIC results over the strain gauge area. The strain obtained via the strain gauges is the engineering strain, while the strain measured with DIC is the true strain. The stress on the ordinate axis is the engineering value for both cases. The difference between true strain and engineering strain should not be relevant at the low strain level at hand, and indeed, the match between the measurements via strain gauges and DIC is very good. The DIC strain distributions will be discussed in more detail in a later section.

Four different regimes can be identified on the graphs in Figure 2-13, as indicated in blue. The initial response of all specimen types seems linear up to a strain of about 0.4%. The second regime is characterized by an increasingly fast drop in stiffness, until the stress-strain curves are almost horizontal. The third regime is the horizontal plateau, during which the composite can be strained further under almost constant stress. For the weft-oriented specimens, this is the final stage. The warp-oriented specimens exhibit a fourth regime in the form of a downward slope. The difference in the final stage of the stress-strain curves comes from the difference in failure mode between the loading directions.

In the warp-oriented specimens, one crack opens up over the full specimen section at one point. This crack does not cause rupture, because it is still bridged by the warp yarns, as illustrated in Figure 2-14.a. As soon as the fibers are being pulled out, the

stress starts dropping drastically. This is reflected in the fourth regime, i.e. the downward slope on the stress-strain curves. The recorded strain tends to decrease a little during this regime, even though the crosshead displacement keeps increasing at the same constant rate of 2 mm/min. This is because the strain localizes in the failing section. The rest of the specimen – including the section monitored by the longitudinal strain gauge – is relieved from stress, and therefore, the elastic part of the strain is relieved as well. When loading is applied along the weft direction, a very different failure mode is observed, as shown in Figure 2-14.b. Unlike the warp yarns, the weft yarns do not bridge the crack. Instead, they all break at the same time, causing brittle failure of the composite. This most probably relates to the weft fibers being about 20% less ductile than the warp fibers. Another factor could be the more undulated path of the weft yarns. Yarns are much more likely to ravel out in those sections where they are straight, while curves in the yarn path will cause local bending, which promotes a localized fracture of the yarn.

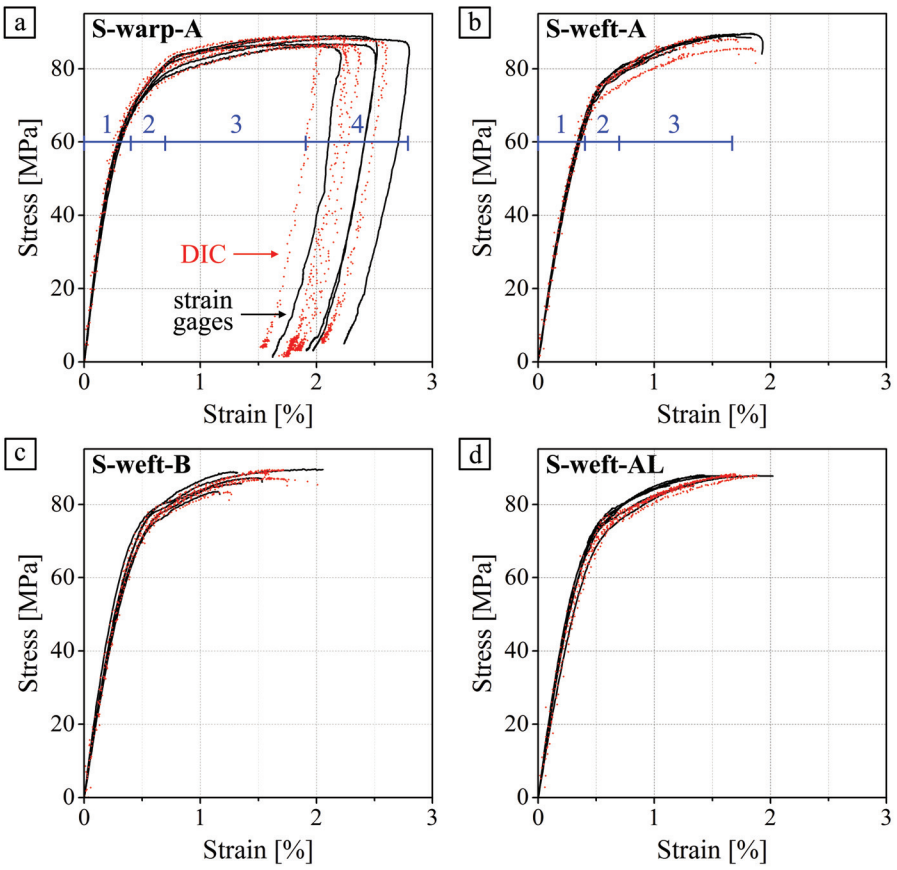


Figure 2-13: Stress-strain response measured with strain gauges and DIC for the laminates of types S-warp-A (a), S-weft-A (b), S-weft-B (c), and S-weft-AL (d)

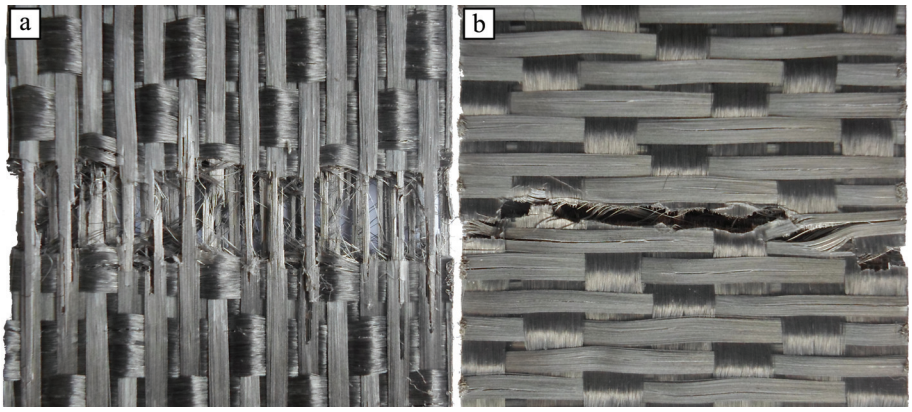


Figure 2-14: Failure of a warp-oriented (S-warp-A) specimen with bridging warp yarns (a), and fracture with broken weft yarns in a weft-oriented (S-weft-A) specimen (b)

### 2.5.4 Mechanical properties

The ASTM D3039/D3039M standard [18] recommends to extract the elastic constants from the stress-strain curves in the region between 0.1% and 0.3% strain. This suggestion aims at avoiding the initial part of the curve, while still remaining in the elastic region. The applicability of this recommendation was first checked by determining the elastic limit for this material. The methodology and the results of this assessment are shown in Figure 2-15. For every data point $(\varepsilon, \sigma)$ on the stress-strain curve, a least squares linear regression fit was made through the data point at hand and the 9 subsequent ones (Figure 2-15.a). The longitudinal stiffness E of the data point can then be calculated as the slope of the linear regression line (Figure 2-15.b). This value can be expressed in terms of the variance and covariance of the 10 data points:

$$E = \frac{\mathrm{Cov}(\varepsilon, \sigma)}{\mathrm{Var}(\varepsilon)} \tag{2-8}$$

As is clear from Figure 2-15.b, there is no clear region of constant stiffness, neither for warp-oriented loading, nor for weft-oriented loading. Any properties determined for this material will hence strongly depend on the strain region over which they are calculated. Therefore, they should not be interpreted as intrinsic material parameters. As a compromise between measuring only the initial behavior and still keeping enough data points for calculations to minimize the influence of noise, the region between 0% and 0.15% strain was chosen for determination of the elastic constants.

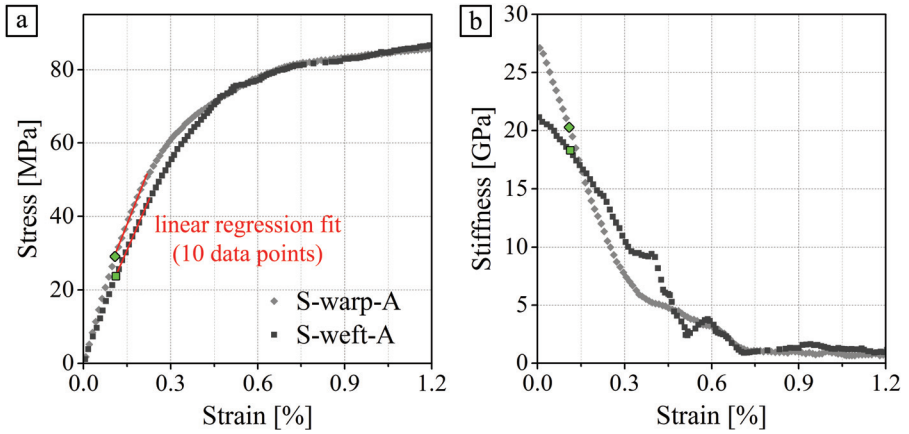


Figure 2-15: Determination of the elastic limit: linear regression fit through 10 subsequent data points on the stress-strain curve (a), of which the slope is taken as the instantaneous stiffness (b) for the data point under consideration (marked in green)

The mechanical characteristics are listed in Table 2-4 for specimen types S-warp-A and S-weft-A, and in Table 2-5 for specimen types S-weft-B and S-weft-AL. The properties are termed according to their orientation with respect to the fabric reinforcement, with the warp direction as the first, and the weft direction as the second direction. The yield point was calculated as the 0.1% offset value, and the ultimate values for stress and strain are the maximum values recorded. All mechanical properties were calculated based on the strain gauge data.

The degree of orthotropy of the composite laminates can be evaluated by comparing the first two specimen types, S-warp-A and S-weft-A, as these types only differ in loading direction. The stiffness along the warp yarns is 25% higher than along the weft yarns. This can partly be explained by the slightly higher fiber volume fraction along the warp direction, and partly by the yarn undulations. The load-carrying yarns contribute most to the stiffness when they are aligned with the load, so the stronger the undulations, the more they lower the stiffness. Weft yarns are typically more undulated than warp yarns, and the fact that the weft yarns are twice as wide as the warp yarns further contributes to the difference. Indeed, the wide weft yarns must undulate much more and much more steeply to be woven around the narrow warp yarns than vice versa. The Poisson's ratios are low in both directions, which is not unusual for a textile composite [23, 24]. The elastic properties are in reasonable agreement with the orthotropic compliance tensor symmetry condition:

$$\frac{\nu_{12}}{E_{11}} = \frac{\nu_{21}}{E_{22}} \tag{2-9}$$

Table 2-4: Mechanical properties (mean value ± standard deviation) of steel fabric reinforced epoxy laminates: S-warp-A and S-weft-A specimens

| | **S-warp-A** | **S-weft-A** |
|---|---|---|
| ***System*** | $[0°,90°]_{2S}^{warp}$ | $[90°,0°]_{2S}^{warp}$ |
| ***Layup*** | warp out | warp out |
| ***Loading*** | along warp | along weft |
| ***Dimension*** | standard | standard |
| **Mechanical property** | **Value ± SD** | **Value ± SD** |
| Young's modulus $E_{11}$ and $E_{22}$ [GPa] | 25.7 ± 0.8 | 20.4 ± 0.7 |
| Poisson's ratio $\nu_{12}$ and $\nu_{21}$ [-] | 0.110 ± 0.014 | 0.086 ± 0.039 |
| Yield strength $\sigma_{Y,11}$ and $\sigma_{Y,22}$ [MPa] | 64.6 ± 0.8 | 68.0 ± 1.6 |
| Yield strain $\varepsilon_{Y,11}$ and $\varepsilon_{Y,22}$ [%] | 0.352 ± 0.008 | 0.434 ± 0.012 |
| Ultimate strength $\sigma_{ult,11}$ and $\sigma_{ult,22}$ [MPa] | 87.8 ± 1.2 | 88.0 ± 1.9 |
| Ultimate strain $\varepsilon_{ult,11}$ and $\varepsilon_{ult,22}$ [%] | 2.399 ± 0.314 | 1.655 ± 0.255 |

Table 2-5: Mechanical properties (mean value ± standard deviation) of steel fabric reinforced epoxy laminates: S-weft-B and S-weft-AL specimens

| | **S-weft-B** | **S-weft-AL** |
|---|---|---|
| ***System*** | $[90°,0°]_{2S}^{weft}$ | $[90°,0°]_{2S}^{warp}$ |
| ***Layup*** | weft out | warp out |
| ***Loading*** | along weft | along weft |
| ***Dimension*** | standard | large |
| **Mechanical property** | **Value ± SD** | **Value ± SD** |
| Young's modulus $E_{22}$ [GPa] | 20.6 ± 1.6 | 20.8 ± 1.3 |
| Poisson ratio $\nu_{21}$ [-] | 0.094 ± 0.016 | 0.035 ± 0.019 |
| Yield strength $\sigma_{Y,0.1\%,22}$ [MPa] | 66.0 ± 3.8 | 67.0 ± 1.1 |
| Yield strain $\varepsilon_{Y,0.1\%,22}$ [%] | 0.421 ± 0.023 | 0.422 ± 0.020 |
| Ultimate tensile strength $\sigma_{ult,22}$ [MPa] | 86.0 ± 3.1 | 86.9 ± 1.3 |
| Ultimate tensile strain $\varepsilon_{ult,22}$ [%] | 1.693 ± 0.630 | 1.504 ± 0.301 |

The influence of the layup system on the mechanical properties can be evaluated by comparing the results for the S-weft-A and S-weft-B specimens, and the effect of the specimen dimensions can be assessed by comparing the results for the S-weft-A specimens to those for the S-weft-AL specimens. A Student's t-test with a significance level of 5% was performed on the results. This test indicates that nor the layup system,

nor the specimen size have an effect on the static tensile behavior. One exception is the Poisson's ratio: the measured values are significantly smaller for the large S-weft-AL type. The specimens of types S-weft-A and S-weft-AL are intrinsically the same composite material; some coupons even come from the same plate. Therefore, this difference must be an artifact, caused either by the force introduction or by the strain gauge measurements. A proper force introduction produces a uniform stress field over the gauge area of the test coupon. A non-uniform stress would cause a non-uniform strain, hence this should be detectable on the DIC surface strain fields. Figure 2-16 shows both the longitudinal and the transversal surface strain at a global tensile strain of 1.2%. The strain fields are clearly patterned, but they are uniformly distributed over the specimen width, with equivalent values on both specimen types. This means that the difference in Poisson's ratio is most likely due to the strain gauge measurements. The strain gauges that were used provide the average strain over a 3 by 7 mm² region, while the unit cell measures 7.74 by 17.26 mm². Therefore, the strain gauges were probably too small compared to the fabric unit cell to make a sufficiently accurate measurement of the small Poisson's ratios. The resolution of the DIC technique is also insufficient to verify the Poisson's ratio at the low global strains that govern the linear regime.

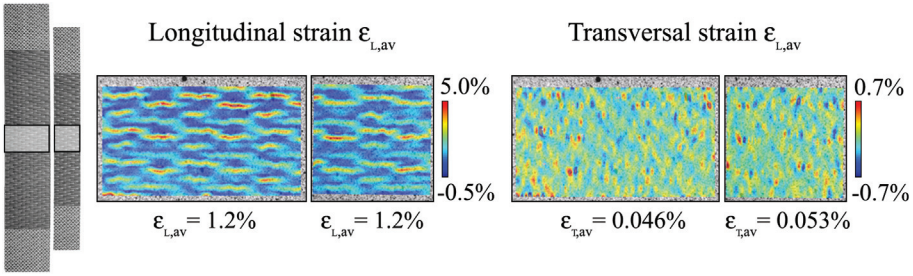


Figure 2-16: Longitudinal and transversal DIC surface strain fields in the standard size (S-weft-A) specimen and the large (S-weft-AL) specimen

The most notable of all mechanical properties is the failure strain of the composite. The idea behind using a ductile steel fiber reinforcement in combination with a ductile matrix material was to obtain a ductile composite material. However, the failure strain of the composite does not even reach up to that of the matrix material. The large difference in ductility between the warp and weft direction of the laminates indicates that the textile architecture plays a very important role in the strain that can be achieved before failure, and therefore, in the damage mechanisms that proceed final rupture of the composite. The investigation of the strain distribution and the microscopically observed damage on the laminate edges in the next sections may help understanding the role of the internal composite structure.

### 2.5.5 Surface strain fields

Fabric-reinforced composites have a structured internal geometry, which causes a corresponding inhomogeneous stress and strain distribution upon loading. When a laminate specimen is subjected to tension, the load-carrying yarns have a tendency to straighten up, pushing the transversal yarns aside. On the specimen surface, the transversal yarns are bent outwards, causing tension on their central section at the laminate surface, as illustrated on Figure 2-17. The stronger the crimp, the stronger this effect.

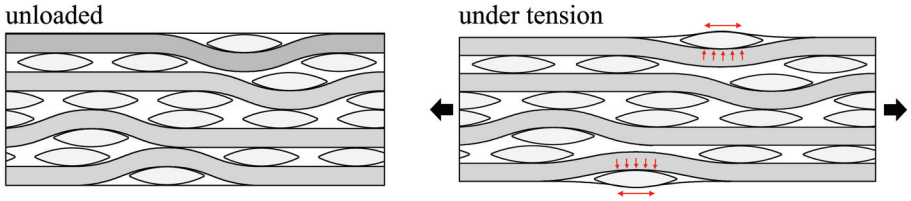


Figure 2-17: Principle behind the patterned strain distribution on the surface of a textile composite laminate

Figure 2-18 shows the longitudinal strain fields on the surface of three different types of specimen, and for four different global strain levels. The strain patterns clearly correspond to the underlying textile structure according to the principles explained in Figure 2-17. The strain distribution is relatively uniform at low strains, but as the global strain is increased, the strain fields becomes more and more patterned. The severity of the strain concentrations is often expressed by means of the strain concentration factor, a parameter that is calculated by dividing the highest local strain value by the global strain. At a global strain of 0.4%, the concentration factor amounts to about 2 for the weft-oriented specimens on Figure 2-18.b-c, while at a strain of 1.6%, the concentration factor has grown to 3. The strain concentrations are much less severe in the warp-oriented specimen on Figure 2-18.a, which is the result of the smaller crimp of the warp yarns. At the highest strain level, some spots could not be correlated by the MatchID software. This is due to small cracks on the specimen surface that interrupt the speckle pattern. As could be expected, these cracks can be found where the local strains reach their peak values, i.e. in the center of the transversal yarns. The nature and the position of damage in the inside layers is analyzed in the next section.

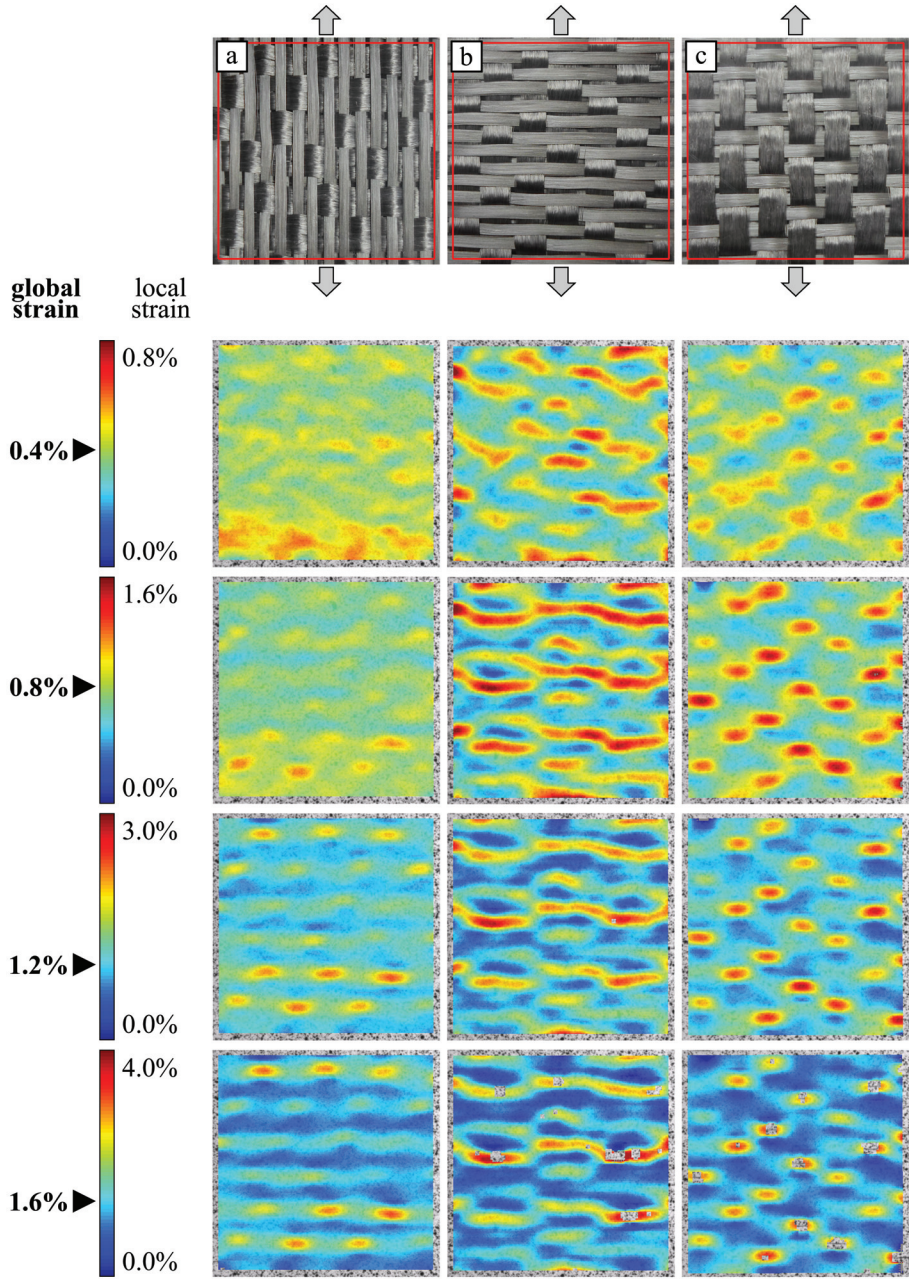


Figure 2-18: Longitudinal strain fields obtained through DIC on the surface of an S-warp-A (a), an S-weft-A (b), and an S-weft-B (c) specimen for 4 global strain levels

### 2.5.6 Damage morphology and crack propagation

The frames from the microscopic movies made by the Dino-Lite USB microscope can be correlated to the stress-strain curve by tracing back the frame time to the FastTrack 8800 digital controller clock time. Due to this, the video recordings can give a view on the propagation of damage, as well as on the damage morphology. A selection of frames is shown on Figure 2-19.a for a specimen loaded along the warp yarns, and on Figure 2-19.b for a specimen loaded along the weft yarns. The position of the frames is indicated on the corresponding stress-strain curves. The frames 0 are the reference frames, depicting the edges in their unloaded state. Due to the limited resolution of the images, it is necessary to compare later frames to these reference images to distinguish any signs of damage with confidence. This is illustrated more clearly through the enlargements in Figure 2-19.a. The frames 1 are the frames on which damage was first observed. This damage prevails in the form of transversal cracks through the non-loadbearing yarns. For clarity, crack initiations are marked with arrows on Figure 2-19. The subsequent frames show the evolution of the existing cracks and the initiation of new ones.

Some typical features are observed in the crack morphology, independent of the loading direction:

- Cracks always originate inside the transversal yarns, never in the matrix pockets.
- The crack planes are perpendicular to the loading direction.
- Cracks span the full height of the yarns. If a cracked yarn has an immediate neighbor, the crack usually extends over both yarns.
- Cracks seem to prefer the yarn center over the yarn edges.
- Both the inner and outer layers of the laminate seem equally prone to transversal damage.
- Other types of damage, such as delamination of the load-bearing yarns, were not observed on the microscopic movies. Even in the last frame on Figure 2-19.b, the load-bearing yarns are still attached to the surrounding material structure on both sides of the wide (fatal) crack.

The first crack is typically observed between 1.2% and 1.3% strain for both loading directions. As is clear from Figure 2-19, this strain level lies in the regime of nearly-constant stress on the stress-strain curves, far beyond the initial deflection from quasi-linearity. This means either that the cracks initiate earlier than observed with the Dino-Lite microscope, or that other phenomena, like nonlinear elasticity or plasticity, are responsible for the strongly nonlinear behavior. The hysteresis experiments that are the subject of the next sections will show to what extent the nonlinear behavior is due to permanent changes in the material structure.

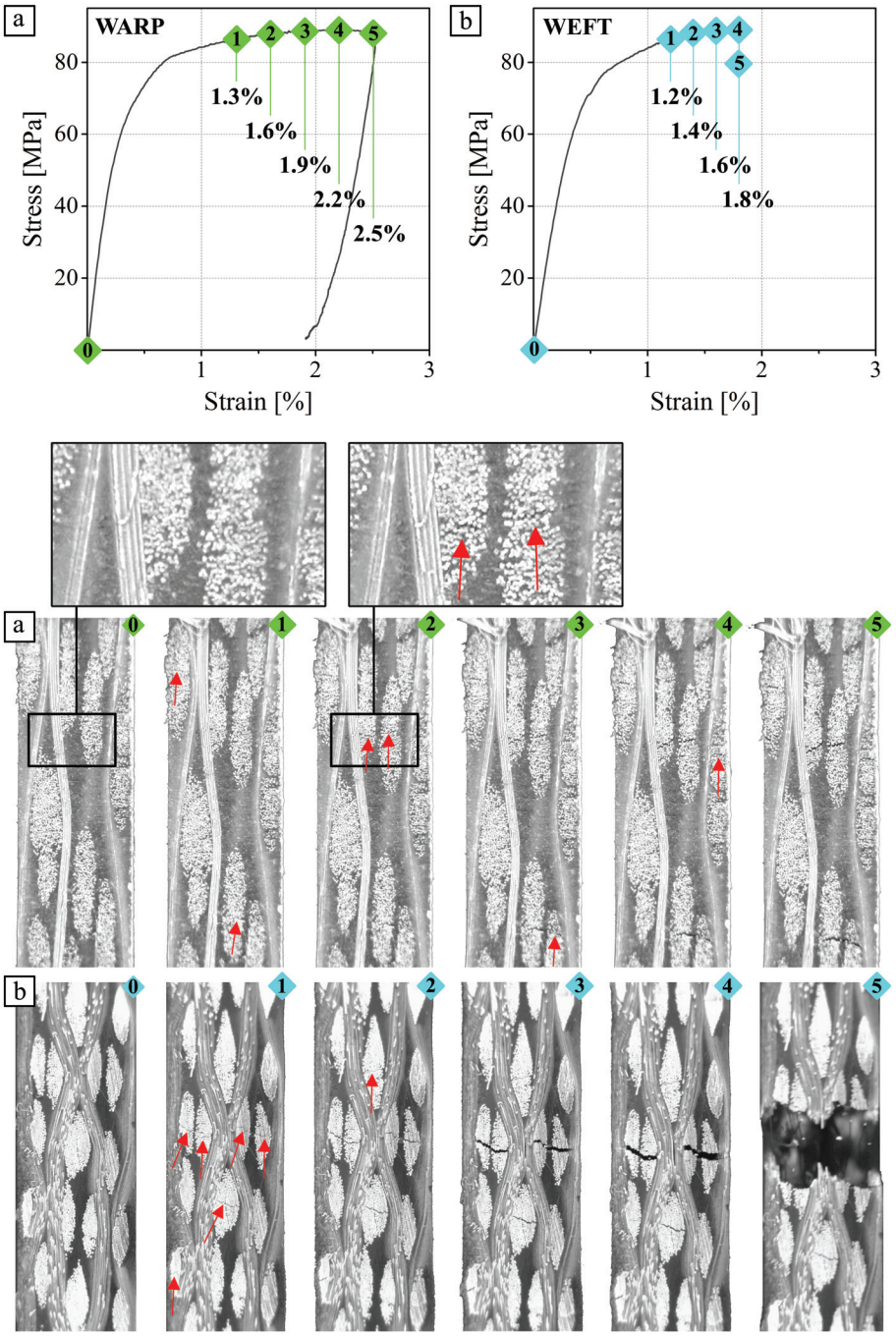


Figure 2-19: Evolution of damage on the polished edge of a warp-oriented (a) and a weft-oriented (b) composite specimen during the tensile experiment

### 2.5.7 Hysteresis

The response of the composite material to tensile loading-unloading was obtained by performing hysteresis experiments. The amplitude of the first loading cycle was 20 MPa. After that, the load was increased by 5 MPa on every cycle up to the final tensile stress of 80 MPa for the warp-oriented specimens, and up to 75 MPa for the weft-oriented specimens. The hysteresis curves are depicted on Figure 2-20.a. For comparison, the static stress-strain curves, which envelope the hysteresis loops, are plotted on the same graphs.

The amount of permanent deformation as a function of the stress on Figure 2-20.b was calculated by taking the residual strain after every loading cycle as a function of the stress amplitude of the cycle. These results show that permanent deformations start to build up at a very low stress level, with a similar evolution in both loading directions.

The evolution of the longitudinal stiffness on Figure 2-20.c was assessed by calculating the slope of the ascending part of every hysteresis loop. If the average loop slopes were taken in this case, the obtained stiffness evolution would not be a reflection of the intrinsic material behavior. Therefore, the strain that was achieved in the first loop was taken as the strain range over which the E-modulus was calculated for all loops using a least squares linear regression fit. This way, the largest possible strain region was selected, while still performing the same processing on all loops. The results on Figure 2-20.c show no significant decrease in stiffness during the hysteresis experiment. Note that the stiffness values are much larger than the ones obtained earlier from the static tensile experiments. The elastic properties mentioned in section 2.5.4 were calculated over a strain region between 0% and 0.15%, while the strain range for the E-moduli in Figure 2-20.c was only about 0.06%. As mentioned before, the calculated stiffness values strongly depend on the chosen strain range, because the stress-strain curves of the composites do not have a strictly linear initial part.

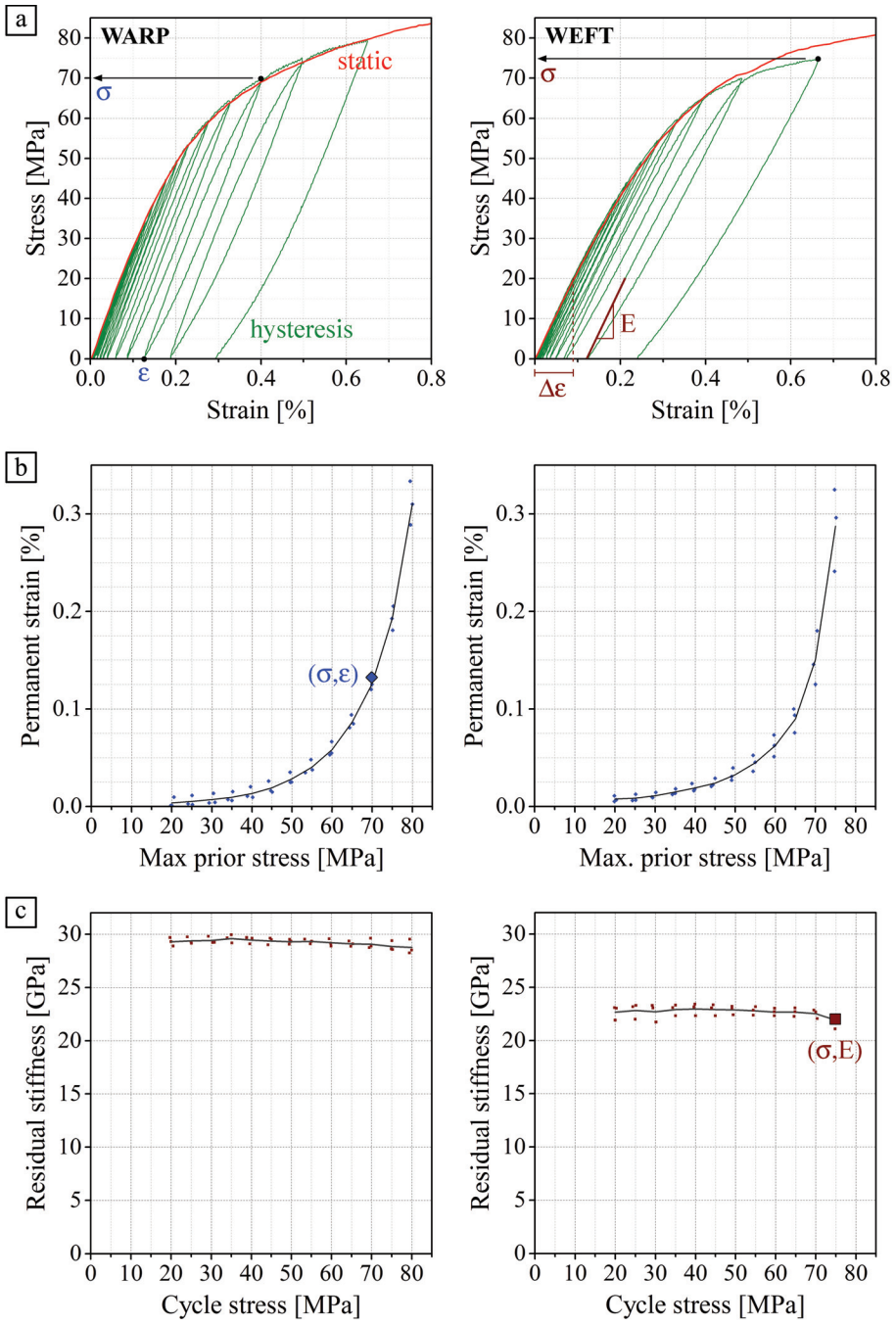


Figure 2-20: Stress-strain curve (a), permanent strain as a function of maximum prior tensile stress (b), and residual stiffness as a function of the cycle stress (c), resulting from hysteresis experiments along warp and weft direction

## 2.6 CONCLUSIONS

In this chapter, the composite under study was first introduced through its constituents and the production process. Then, the geometry of the internal structure and the mechanical behavior were characterized. The differences in yarn architecture between warp and weft yarns were found to translate into a different behavior of the composite along the corresponding loading directions. For the stiffness of the composite, a 25% higher value was recorded along the warp direction. This difference was attributed to the somewhat higher volume fraction along this direction, combined with the smaller undulations of the warp yarns. An even more notable difference was the difference in ductility along both directions. A crack caused by weft-oriented loading localizes suddenly and causes rather brittle failure at about 1.6% strain. Warp-oriented loading, on the other hand, causes a crack that opens up slowly, while the warp fibers that bridge the crack are continuously being pulled out. Even along the warp direction, however, the strain-to-failure is limited to about 2.4%. With an epoxy that can reach over 8% strain and fibers that stretch up to 19.5%, the achieved failure strain of 2.4% even means an embrittlement of the epoxy.

The idea behind using ductile steel fibers as a reinforcement material in a ductile epoxy was to realize a composite material that could undergo large strains before losing structural integrity. The results of the tensile tests clearly show that the ductile potential of the constituents is not matched in the composite material. The difference in failure mechanism between both loading directions indicates that the textile architecture is of great significance for the toughness of the composite. Therefore, the next chapter will study the role of the reinforcement architecture in the composite mechanics by means of finite element modeling.

## 2.7 REFERENCES

[1] Herakovich CT. *Mechanics Of Fibrous Composites*. New York: John Wiley & Son. 1997.

[2] NV Bekaert S.A. *Metal fiber production & products*. Available from: http://www.bekaert.com/en/products-and-applications/our-core-competences-1/steel-wire-transformation/metal-fiber-production-products. 2014.

[3] De Bondt S, Decrop J. *Bundle drawn stainless steel fibers*. Assigned to N.V. Bekaert S.A. US 7166174 B2. 2007.

[4] Vandewalle S. *Steel fiber reinforced composites.* Assigned to N.V. Bekaert S.A. US 2014/0045400 A1. 2014.

[5] Sabuncuoglu B. *On the high stress concentrations in steel fiber composites under transverse loading*. Journal of Reinforced Plastics and Composites; 33: 1941-1953. 2014.

[6] Sabuncuoglu B, Orlova S, Gorbatikh L, Lomov SV, Verpoest I. *Micro-scale finite element analysis of stress concentrations in steel fiber composites under transverse loading*. Journal of Composite Materials. 2014.

[7] Callens MG, De Cuyper P, Gorbatikh L, Verpoest I. *Ductile steel fibre/polypropylene composites: influence of fibre architecture on the tensile behaviour*. In: A. Suleman PC, et al., editor. IV ECCOMAS Thematic Conference on the Mechanical Response of Composites. 2013.

[8] Callens MG, De Cuyper P, Gorbatikh L, Verpoest I. *Effect of fibre architecture on the tensile and impact behaviour of ductile stainless steel fibre polypropylene composites*. Composite Structures; 119: 528-533. 2015.

[9] Xia Z, Zhou C, Yong Q, Wang X. *On selection of repeated unit cell model and application of unified periodic boundary conditions in micro-mechanical analysis of composites*. International Journal of Solids and Structures; 43: 266-278. 2006.

[10] Adanur S. *Handbook of weaving*. Boca Raton, Florida, US: CRC Press 2000. 2000.

[11] ASTM Standard. D5035. *Standard Test Method For Breaking Force and Elongation of Textile Fabrics (Strip Method)*. West Conshohocken, PA: ASTM International; DOI: 10.1520/D5035-11. Available from: www.astm.org. 2003.

[12] Allaer K, De Baere I, Lava P, Van Paepegem W, Degrieck J. *On the in-plane mechanical properties of stainless steel fibre reinforced ductile composites*. Composites Science and Technology; 100: 34-43. 2014.

[13] Hobbiebrunken T, Fiedler B, Hojo M, Tanaka M. *Experimental determination of the true epoxy resin strength using micro-scaled specimens*. Composites Part A: Applied Science and Manufacturing; 38: 814-818. 2007.

[14] Momentive Specialty Chemicals Inc. *Technical Data Sheet EPIKOTE RIMR 135/ EPIKURE RIMH 137*. Available from: http://www.momentivespecialtychemicals.com/Products/TechnicalDataSheet.aspx?id=8246. 2006.

[15] Volume Graphics GmbH. *Volume Graphics viewer myVGL*. Available from: http://www.volumegraphics.com/en/products/myvgl/. 2015.

[16] ASTM Standard. D792. *Standard Test Methods for Density and Specific Gravity (Relative Density) of Plastics by Displacement*. West Conshohocken, PA: ASTM International; DOI: 10.1520/D0792. Available from: www.astm.org. 2013.

[17] The Engineering Toolbox. *Density and specific weight of water at temperatures 0 - 100 °C*. Available from: http://www.engineeringtoolbox.com/water-density-specific-weight-d_595.html.

[18] ASTM Standard. D3039/D3039M. *Standard Test Method for Tensile Properties of Polymer Matrix Composite Materials*. West Conshohocken, PA: ASTM International; DOI: 10.1520/D3039_D3039M-14. Available from: www.astm.org. 2014.

[19] ASTM Standard. D6856/D6856M. *Standard Guide for Testing Fabric-Reinforced Textile Composite Materials*. West Conshohocken, PA: ASTM

International; DOI: 10.1520/D6856_D6856M-03R08E01. Available from: www.astm.org. 2008.

[20] Pinto M, Gupta S, Shukla A. *Study of implosion of carbon/epoxy composite hollow cylinders using 3-D Digital Image Correlation*. Composite Structures; 119: 272-286. 2015.

[21] Pazmino J, Carvelli V, Lomov SV, Van Mieghem B, Lava P. *3D digital image correlation measurements during shaping of a non-crimp 3D orthogonal woven E-glass reinforcement*. International Journal of Material Forming; 7: 439-446. 2013.

[22] MatchID. *MatchID software*. Available from: http://www.matchid.org/. 2015.

[23] De Baere I, Van Paepegem W, Degrieck J, Sol H, Van Hemelrijck D, Petreli A. *Comparison of different identification techniques for measurement of quasi-zero Poisson's ratio of fabric-reinforced laminates*. Composites Part A: Applied Science and Manufacturing; 38: 2047-2054. 2007.

[24] De Baere I, Van Paepegem W, Degrieck J. *On the nonlinear evolution of the Poisson's ratio under quasi-static loading for a carbon fabric-reinforced thermoplastic. Part I: Influence of the transverse strain sensor*. Polymer Testing; 28: 196-203. 2009.

# Chapter 3

## MULTISCALE RVE ANALYSIS THROUGH FINITE ELEMENT MODELING

*In this chapter, the strategy of RVE analysis is applied to study the mechanics of the steel fiber textile reinforced epoxy laminates. As will be explained in the first section, the RVE approach serves two goals, homogenization and localization. Homogenization of the elastic properties of the laminates from the micro to the meso level, and then from the meso to the macro level, respectively, will be performed in sections two and three. In section four, the numerical stress and strain localizations within the textile structure will be compared to the experimental findings. The meso-scale RVE model is further elaborated by adding material non-linearity in section five, and finally, the conclusion on the suitability of the RVE approach to study the mechanics of the ductile textile reinforced epoxy laminates is formulated in section six.*

## 3.1 INTRODUCTION ON MULTISCALE RVE ANALYSIS

To explain about RVE analysis, one must first introduce the broader research field of micromechanics. Micromechanics studies heterogeneous materials based on the properties and the geometry of their constituents. The technique was originally developed with the focus on micro-scale inclusions [1-6], but nowadays, it is used to tackle multiscale problems in composite mechanics [7, 8]. The first goal in micromechanics is to assess the local stresses and strains within the heterogeneous material structure for a given global stress or strain load, a task that was termed *localization* by Suquet [9]. The second goal is to predict the global response of the heterogeneous material based on the properties and the geometry of the constituents, a task known as *homogenization*.

Most micromechanical methods are based on the assumption that the heterogeneous material structure can be studied on a sub-volume that contains all the necessary geometrical information. This sub-volume is termed an RVE, short for Representative Volume Element. The first micromechanical methods were analytical methods. Famous examples are the theories by Voigt [10] and Reuss [11], the Hashin-Shtrikman bounds [4, 12, 13], and the Mori-Tanaka method [14]. Later on, numerical approaches came to dominate the field of micromechanics. A particularly popular numerical method is to study the RVE through finite element analysis (FEA). This is the approach that will be applied in the current chapter.

Many inhomogeneous materials are multiscale materials, and analyzing them requires a multiscale analysis. In the case of textile composites, three length scales can be discerned, as illustrated on Figure 3-1. The largest scale is the macro scale, or the laminate level. The properties on this level are the ones that are typically requested for design purposes. Finding these properties requires homogenization from the scale below, i.e. the meso-scale. A meso-scale RVE represents the textile architecture, and will therefore also provide the stress and strain localizations within the textile structure. On the meso-scale, the yarns are considered as homogeneous entities, even though they consist of fibers and matrix. Acquiring the properties of these yarns requires to homogenize them from the micro-scale. This task can be performed analytically through one of the countless analytical homogenization theories, or it can be done by homogenizing the results of a micro-scale RVE model. In the current chapter, the full multiscale analysis will be performed, and hence RVE models will be built on two length scales, i.e. on the micro-scale and on the meso-scale.

The choice of an appropriate RVE is usually the first step into an RVE analysis, and this is straightforward in some, but not in all cases. A thorough discussion on the RVE selection is the subject of the first part of this section. Studying an RVE means to subject it to a global stress or strain field, and to then analyze its response. When

applying a global stress or strain, it is crucial to consider the proper boundary conditions. As the RVE represents the larger material structure, it must behave as if it were still attached to the surrounding material. An in-depth discussion on boundary conditions is the subject of the second part of this section. The third part reflects on the use of symmetries within the RVE to save on calculation time. In the final part of this section, the two tasks of micromechanics, localization and homogenization, are elaborated starting from the results of a finite element RVE analysis.

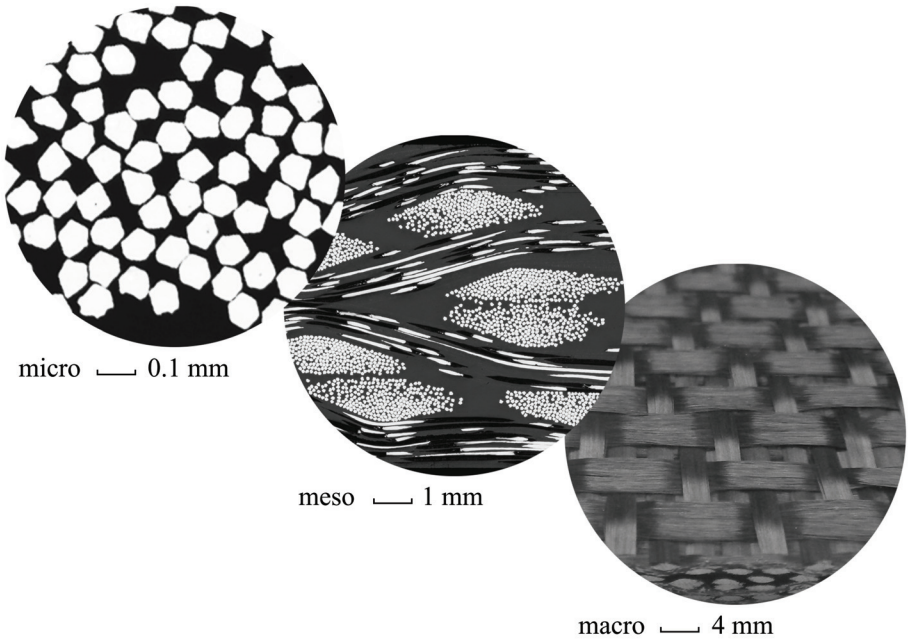


Figure 3-1: Length scales in textile-reinforced composites

### 3.1.1 Selection of the RVE

The selection of a volume element that best represents the material structure is usually an important first step into an RVE analysis. The choice is not unambiguous, and the selection strategy depends on the characteristics of the material structure, the length scale to be studied, the requested properties or behavior, and the required accuracy. One of the first formal definitions was proposed by Hill [15], who stated that an RVE is 1) structurally entirely typical of the composite material on average and 2) contains a sufficient number of inclusions such that the apparent moduli are independent of the RVE boundary displacements or tractions. Note that this definition specifically refers to ‘inclusions’ – an attestation of the original focus of micromechanics towards the micro-scale. Also apparent is that Hill’s early formulation is especially mindful of the homogenization, and less of the localization task. It is known now that for

homogenization purposes, a correct fiber volume fraction alone suffices in some cases to come to reasonable results, whereas localizations are usually very sensitive towards details of the geometry [16, 17].

The micro-scale image in Figure 3-1 clearly illustrates how the distribution of fiber filaments in a yarn of a textile composite is usually at random. When looking at such **non-periodic microstructures**, it is clear that a countless number of different distribution samples (or realizations) could be generated, even for a given sample size. The individual responses of those realizations will in general not comport, but their average will converge to the microstructure's response [18]. Within this concept, defining the number of realizations of a given sample size that would lead to a sufficiently accurate average response is termed *average response technique* [19]. This approach is illustrated in Figure 3-2.a. The realizations are in this case – strictly speaking – not RVE's, since they display scatter in their response. Zohdi [20] pointed out that for the average response technique to come to a solution, a certain minimum sample size is needed. Samples that are too small with respect to the microstructure will indeed not produce meaningful responses. Figure 3-2.a also shows a second strategy, the *sample enlargement technique* [19]. This strategy comes down to enlarging the sample size stepwise, up to the point where two consecutive responses lie within chosen tolerance limits. This technique does define an RVE in the strict sense of Hill's definition.

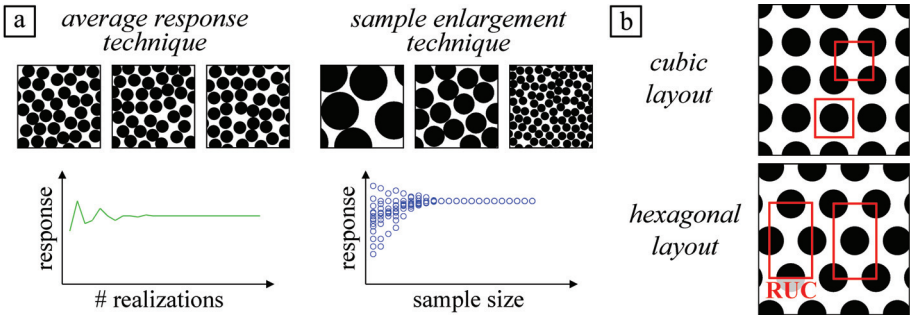


Figure 3-2: RVE selection strategies for non-periodic material structures (a) and well-known idealizations into regular fiber arrangements

The rather cumbersome RVE selection procedures in non-periodic microstructures has prompted many researchers to introduce an idealized regular packing when analyzing the microstructure of fiber-reinforced composites. Two popular packing systems are the well-known cubic and hexagonal layouts, as shown in Figure 3-2.b. The cubic layout is relatively easy when it comes to the interpretation of geometrical symmetries and the implementation of the boundary conditions. In turn, the hexagonal layout preserves the transverse isotropy that can be found in the majority of real unidirectional reinforced composite materials.

The assumption of a regular packing idealizes the micro-scale of a fiber composite as being a **periodic structure**. The yarn architecture that defines the meso-scale of a textile composite as well is usually considered to be periodic. In this type of structure, the role of RVE can usually be taken up by the Repeating Unit Cell (RUC), i.e. the smallest possible sub-volume that could be used to regenerate the material structure using nothing but tessellation transformations. Figure 3-2.b shows how the position of the RUC within the composite structure can be chosen arbitrarily by shifting its bounding box. The selection is hence not unique, but all possible selections are equivalent [21]. A rare counterexample on when the RUC cannot function as an RVE is bifurcation behavior [19]. For instance, a single unit cell subjected to a compressive load will usually not show the same buckling resistance as an assembly of multiple unit cells.

### 3.1.2 Periodic boundary conditions

Mathematically, RVE analysis comes down to applying a certain global stress or strain to the RVE through boundary conditions, and then solving the resultant boundary value problem. The applied boundary conditions should correspond with the actual boundary conditions on the RVE, hence they should reflect the periodicity of the RVE within the composite. The degree to which this requirement is met is decisive for the accuracy of the obtained solution.

A mathematically exact formulation for imposing periodic boundary conditions can be realized by coupling the displacements or the tractions of nodes on opposite sides of the RVE. The basic node-coupling scheme for periodic boundary conditions of a full RVE can be found in literature in a variety of formulations [22-25]. A particularly elegant one was given by Xia, Zhang et al. [26], starting from the asymptotically expanded macroscopic displacement field $u_i(x_1, x_2, x_3)$ on a heterogeneous microstructure [9]:

$$u_i(x_1, x_2, x_3) = \bar{\varepsilon}_{ik} x_k + u_i^*(x_1, x_2, x_3) \tag{3-1}$$

In this equation, $\bar{\varepsilon}_{ik}$ is the global strain tensor, so the first term on the right hand side represents a linear displacement field. The second term on the right hand side represents the periodic part of the displacement components from one RVE to another. This term is generally unknown. However, due to its periodic nature, it has equal values on every $j^{th}$ pair of nodes on opposite sides of the RVE, $u_i^{j-}$ and $u_i^{j+}$. This insight allows for the elimination of the unknown term by linking the opposite RVE sides into periodic displacement-difference boundary conditions:

$$u_i^{j+} - u_i^{j-} = \bar{\varepsilon}_{ik}\left(x_k^{j+} - x_k^{j-}\right) = \bar{\varepsilon}_{ik}\,\Delta x_k^j \tag{3-2}$$

The displacement field proposed in Equation (3-1) meets the displacement continuity condition, but can in general not guarantee traction continuity. Xia et al. [21] proved that if a displacement-based finite element method is used, introducing Equation (3-2) as periodic boundary conditions on an RVE will lead to a unique solution. Following this theorem, proof was given that this unique solution will also meet the traction boundary conditions. Crucial in the argumentation was that the displacement-based finite element method uses the variational principle of minimum total potential energy. In general, variational calculus aims to find the stationary value of a functional by solving the Euler-Lagrange equations. The boundary conditions that result when no restrictions are imposed on the boundary values are called natural boundary conditions. When minimizing the potential energy, the Euler equations are the equilibrium equations of elasticity and the natural boundary conditions are the surface tractions. Therefore, the surface tractions are satisfied automatically as a part of the variational process. According to Li [27], imposing them explicitly may even prevent the strain energy from reaching its minimum in the solution space.

Prior to the availability of computational tools, 'plane-remains-plane' conditions were often used at the boundaries of the RVE. These homogeneous displacement conditions are equivalent to periodic boundary conditions, provided that the RVE shows reflectional symmetry and is subjected to deformations corresponding to a macroscopic direct strain only. In any other analysis, these conditions over-constrain the RVE and cause the predicted elastic moduli to be too high. This can easily be seen when considering the minimal strain energy principle. If the actual boundary conditions would minimize the energy, then every other assumed displacement boundary condition will by definition produce more energy. While homogeneous displacement boundary conditions provide an upper bound for the calculated elastic moduli, lower bounds can be attained by applying homogeneous traction boundary conditions. Proof of this statement has been provided by many researchers [3, 9, 20, 28-30], and it is the computational equivalent of the famous Voigt and Reuss bounds.

### 3.1.3 Note on the use of symmetries

In a periodic material structure, the RUC usually defines the RVE. In that case, the RVE shows by definition *translational symmetry* in every direction. The RVE may show additional symmetries, as illustrated on a 2D hexagonal fiber-matrix system in Figure 3-3. Two *reflectional symmetry* axes (Figure 3-3.b) bisect the RVE, and each allows dividing the model by half. Finally, employing the *rotational symmetry* (Figure 3-3.c) leads to the smallest possible model for this microstructure, this is 1/8 of the RVE. This 1/8 model was termed the 'unit cell' by Li and coworkers [31-34].

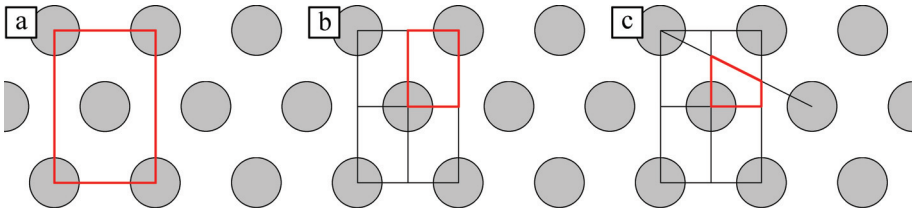


Figure 3-3: RVE (a), quarter model obtained by using two reflectional symmetries (b) and 1/8 model (the 'unit cell') obtained by employing the rotational symmetry (c)

Provided that the used symmetries are known, the unit cell contains the same information as the full RVE and hence allows for the same analyses at a lower calculation cost. This gain, however, comes at a price, since the periodic boundary conditions obviously need reconsidering. Li [31] stated as follows. Every geometrical symmetry transformation can be described by a mapping, say S, of a point (y, z) to its image (y', z') in the same plane:

$$S : (y, z) \rightarrow (y', z') \tag{3-3}$$

As an example, Figure 3-4.a illustrates the reflectional symmetry transformation about the y-axis, $\Sigma_y$, which maps a point (y, z) to its image (y, -z):

$$S : (y, z) \rightarrow (y, -z) \tag{3-4}$$

A general loading combination can be resolved into a symmetric and an antisymmetric part with respect to the geometrical symmetry transformation. When a macroscopic stress tensor $\bar{\boldsymbol{\sigma}}$, or a macroscopic strain tensor $\bar{\boldsymbol{\varepsilon}}$ are treated as loads, then the mapping of their values at a point (y, z) to its image (y', z') can be described as:

$$S : \bar{\boldsymbol{\sigma}}|_{(y,z)} \rightarrow \bar{\boldsymbol{\sigma}}|_{(y',z')} \quad \text{or} \quad S : \bar{\boldsymbol{\varepsilon}}|_{(y,z)} \rightarrow \bar{\boldsymbol{\varepsilon}}|_{(y',z')} \tag{3-5}$$

In the example given in Figure 3-4, loading components $\bar{\varepsilon}_x$, $\bar{\varepsilon}_y$, $\bar{\varepsilon}_z$ (Figure 3-4.b) and $\bar{\gamma}_{xy}$ are symmetrical about the y-axis, whereas $\bar{\gamma}_{xz}$ and $\bar{\gamma}_{yz}$ (Figure 3-4.c) are antisymmetrical:

$$\text{Symmetrical with respect to } \Sigma_y: \begin{cases} \bar{\varepsilon}_x|_{(y,z)} = \bar{\varepsilon}_x|_{(y,-z)} \\ \bar{\varepsilon}_y|_{(y,z)} = \bar{\varepsilon}_y|_{(y,-z)} \\ \bar{\varepsilon}_z|_{(y,z)} = \bar{\varepsilon}_z|_{(y,-z)} \\ \bar{\gamma}_{xy}|_{(y,z)} = \bar{\gamma}_{xy}|_{(y,-z)} \end{cases} \tag{3-6}$$

$$\text{Antisymmetrical with respect to } \Sigma_y: \begin{cases} \bar{\gamma}_{xz}|_{(y,z)} = -\bar{\gamma}_{xz}|_{(y,-z)} \\ \bar{\gamma}_{yz}|_{(y,z)} = -\bar{\gamma}_{yz}|_{(y,-z)} \end{cases}$$

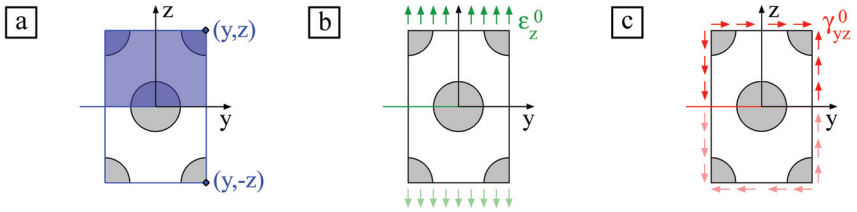


Figure 3-4: Geometrical reflectional symmetry about the y-axis (a) and the corresponding mapping of the loading components: $\bar{\varepsilon}_z$ maps symmetrically (b), while $\bar{\gamma}_{yz}$ maps antisymmetrically (c)

The responses, i.e. the microscopic stress tensor $\boldsymbol{\sigma}$, the microscopic strain tensor $\boldsymbol{\varepsilon}$, and the displacements u, will show the same symmetry as the loading:

$$\begin{aligned} S : \boldsymbol{\sigma}|_{(y,z)} &\rightarrow \boldsymbol{\sigma}|_{(y',z')} \\ S : \boldsymbol{\varepsilon}|_{(y,z)} &\rightarrow \boldsymbol{\varepsilon}|_{(y',z')} \\ S : u|_{(y,z)} &\rightarrow u|_{(y',z')} \end{aligned} \tag{3-7}$$

Loadings with a different nature of symmetry (symmetric or antisymmetric) require different boundary conditions, and hence, a separate analysis. In fully elastic problems, superposition of results is valid and every possible loading combination can be simulated. In case of failure or plasticity, superposition is of course no longer an option. Furthermore, when geometrical deformations in the material become large, geometrical symmetry will be destroyed by antisymmetric deformations. In these cases, geometrical symmetries should not be employed. Another restriction on the use of reflectional or rotational symmetries plays when one is interested in geometrical irregularities of local imperfections such as debonding or microcracks. Though the solution strategy proposed by Li [31] is straightforward, the practical implementation is far from intuitive, and this is all the more true as the number of used symmetries increases. Indeed, every symmetry corresponds to different sets of symmetrical and antisymmetrical loading components, which all require a different set of boundary conditions. It can be concluded that using symmetries within the RVE to reduce the model size comes at a price, and that making this balance should be the first exercise when attacking an RVE analysis.

### 3.1.4 Localization and homogenization

As mentioned in the very beginning of this chapter, an RVE analysis serves two goals, i.e. localization and homogenization. The localization task is finished as soon as the finite element analysis finishes, as the local stresses $\sigma_{ij}$ and the local strains $\varepsilon_{ij}$ in the RVE are readily available from the finite element solution. The homogenization task – to determine the homogenized properties of the RVE – requires to deduce the relationship between global stresses $\bar{\sigma}_{ij}$ and global strains $\bar{\varepsilon}_{ij}$ from the finite element

analysis results. In an elastic analysis, the relation between stress and strain is given by Hooke's law. If material orthotropy is assumed, the stiffness tensor holds nine independent stiffness constants $C_{ij}$:

$$\begin{bmatrix}\bar{\sigma}_{11}\\ \bar{\sigma}_{22}\\ \bar{\sigma}_{33}\\ \bar{\tau}_{12}\\ \bar{\tau}_{13}\\ \bar{\tau}_{23}\end{bmatrix} = \begin{bmatrix}C_{11} & C_{12} & C_{13} & 0 & 0 & 0\\ C_{12} & C_{22} & C_{23} & 0 & 0 & 0\\ C_{13} & C_{23} & C_{33} & 0 & 0 & 0\\ 0 & 0 & 0 & C_{44} & 0 & 0\\ 0 & 0 & 0 & 0 & C_{55} & 0\\ 0 & 0 & 0 & 0 & 0 & C_{66}\end{bmatrix}\begin{bmatrix}\bar{\varepsilon}_{11}\\ \bar{\varepsilon}_{22}\\ \bar{\varepsilon}_{33}\\ \bar{\gamma}_{12}\\ \bar{\gamma}_{13}\\ \bar{\gamma}_{23}\end{bmatrix} \tag{3-8}$$

The global strains $\bar{\varepsilon}_{ij}$ are applied as load to the model and are hence known, and the global stresses $\bar{\sigma}_{ij}$ can be calculated from the analysis results by averaging the local stresses over the total volume V of the RVE:

$$\bar{\sigma}_{ij} = \frac{1}{V}\int_V \sigma_{ij}\, dV \tag{3-9}$$

The tensor in Equation (3-8) is an underdetermined linear system, as there are only six equations for nine unknown stiffness constants. This can be overcome by applying three different sets of global strains $\bar{\varepsilon}_{ij}^{A}, \bar{\varepsilon}_{ij}^{B}$, and $\bar{\varepsilon}_{ij}^{C}$ in three different analyses. Three analyses suffice to make the system fully determined, provided that the three chosen global strain vectors are linearly independent. Often, the first two normal strain components are applied separately in analyses A and B, and the third normal strain component is combined with the three shear components in analysis C:

$$\begin{cases}\bar{\varepsilon}_{11}^{A} = 1\\ \bar{\varepsilon}_{22}^{A} = 0\\ \bar{\varepsilon}_{33}^{A} = 0\\ \bar{\gamma}_{12}^{A} = \bar{\gamma}_{13}^{A} = \bar{\gamma}_{23}^{A} = 0\end{cases} \overset{(3\text{-}8)}{\Longrightarrow} \begin{cases}\bar{\sigma}_{11}^{A} = C_{11}\\ \bar{\sigma}_{22}^{A} = C_{12}\\ \bar{\sigma}_{33}^{A} = C_{13}\\ \bar{\tau}_{12}^{A} = \bar{\tau}_{13}^{A} = \bar{\tau}_{23}^{A} = 0\end{cases}$$

$$\begin{cases}\bar{\varepsilon}_{11}^{B} = 0\\ \bar{\varepsilon}_{22}^{B} = 1\\ \bar{\varepsilon}_{33}^{B} = 0\\ \bar{\gamma}_{12}^{B} = \bar{\gamma}_{13}^{B} = \bar{\gamma}_{23}^{B} = 0\end{cases} \overset{(3\text{-}8)}{\Longrightarrow} \begin{cases}\bar{\sigma}_{11}^{B} = C_{12}\\ \bar{\sigma}_{22}^{B} = C_{22}\\ \bar{\sigma}_{33}^{B} = C_{23}\\ \bar{\tau}_{12}^{B} = \bar{\tau}_{13}^{B} = \bar{\tau}_{23}^{B} = 0\end{cases} \tag{3-10}$$

$$\begin{cases}\bar{\varepsilon}_{11}^{C} = 0\\ \bar{\varepsilon}_{22}^{C} = 0\\ \bar{\varepsilon}_{33}^{C} = 1\\ \bar{\gamma}_{12}^{C} = 1\\ \bar{\gamma}_{13}^{C} = 1\\ \bar{\gamma}_{23}^{C} = 1\end{cases} \overset{(3\text{-}8)}{\Longrightarrow} \begin{cases}\bar{\sigma}_{11}^{C} = C_{13}\\ \bar{\sigma}_{22}^{C} = C_{23}\\ \bar{\sigma}_{33}^{C} = C_{33}\\ \bar{\tau}_{12}^{C} = C_{44}\\ \bar{\tau}_{13}^{C} = C_{55}\\ \bar{\tau}_{23}^{C} = C_{66}\end{cases}$$

## 3.2 MICRO TO MESO HOMOGENIZATION: THE ELASTIC CONSTANTS OF THE YARNS

On the meso-scale, the yarns are considered homogeneous entities. The mechanical properties of these yarn entities can be obtained by considering the scale below, i.e. the micro-scale. The link between both scales in the stainless steel fiber textile composite is illustrated in Figure 3-5.

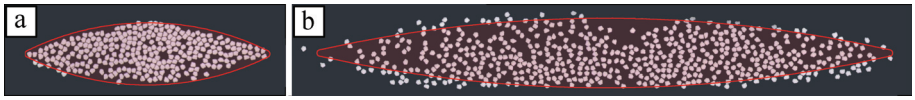


Figure 3-5: Microscopic image of the fibers (micro-scale) and the idealized yarn shapes (meso-scale) for a warp yarn (a) and a weft yarn (b)

If the fibers are randomly distributed in the yarns, i.e. with equal probability density in all directions of the plane, the yarns can be considered transversely isotropic. If the yarn's longitudinal direction is taken to be the 1-direction, the relation between average stress $\bar{\sigma}_{ij}$ and average strain $\bar{\varepsilon}_{ij}$ can be expressed in terms of five elastic constants as:

$$\begin{bmatrix} \bar{\varepsilon}_{11} \\ \bar{\varepsilon}_{22} \\ \bar{\varepsilon}_{33} \\ \bar{\gamma}_{12} \\ \bar{\gamma}_{13} \\ \bar{\gamma}_{23} \end{bmatrix} = \begin{bmatrix} \frac{1}{E_{11}} & -\frac{\nu_{21}}{E_{22}} & -\frac{\nu_{21}}{E_{22}} & 0 & 0 & 0 \\ -\frac{\nu_{12}}{E_{11}} & \frac{1}{E_{22}} & -\frac{\nu_{23}}{E_{22}} & 0 & 0 & 0 \\ -\frac{\nu_{12}}{E_{11}} & -\frac{\nu_{23}}{E_{22}} & \frac{1}{E_{22}} & 0 & 0 & 0 \\ 0 & 0 & 0 & \frac{1}{G_{12}} & 0 & 0 \\ 0 & 0 & 0 & 0 & \frac{1}{G_{12}} & 0 \\ 0 & 0 & 0 & 0 & 0 & \frac{2(1+\nu_{23})}{E_{22}} \end{bmatrix} \begin{bmatrix} \bar{\sigma}_{11} \\ \bar{\sigma}_{22} \\ \bar{\sigma}_{33} \\ \bar{\tau}_{12} \\ \bar{\tau}_{13} \\ \bar{\tau}_{23} \end{bmatrix} \tag{3-11}$$

The homogenized elastic constants can be deduced through analytical methods or through a numerical approach. Both strategies require the fiber volume fraction within the idealized yarn as input. This value can be calculated as:

$$V_f = \frac{n \cdot A_f}{A} \tag{3-12}$$

In this, n is the total amount of fibers in the yarn, $A_f$ is the cross section of one fiber, and A is the cross section of the idealized yarn. In order to determine the sectional area A, an idealized shape must be chosen for the yarn cross sections. Based on the

CT-images, a lenticular idealization with a rounding radius of 20 µm on the edges was chosen, as shown on Figure 3-6. The dimensions were determined in the previous chapter and can be found in Table 2-1, as well as on Figure 3-6. The sectional areas can be calculated as 0.39887 mm² and 1.06663 mm², for the idealized warp and weft yarn, respectively. Now, Equation (3-12) can be evaluated as:

$$V_{f,warp} = \frac{275 \cdot (0.015^2\pi)\ mm^2}{0.39887\ mm^2} = 48.7342\%$$
$$V_{f,weft} = \frac{550 \cdot (0.015^2\pi)\ mm^2}{1.06663\ mm^2} = 36.4486\% \quad (3\text{-}13)$$

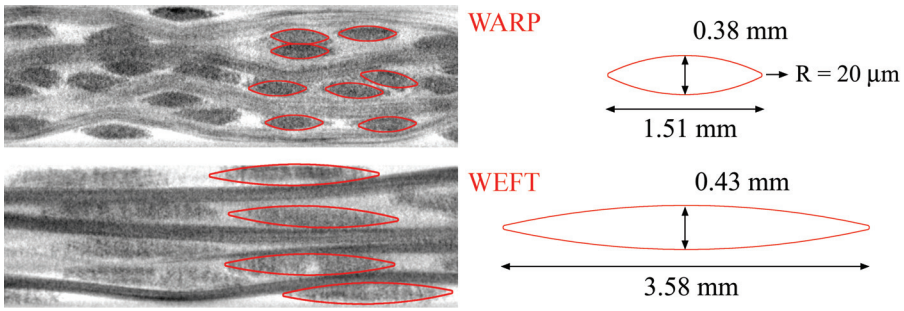


Figure 3-6: Cross section dimensions of the warp and weft yarns idealizations

### 3.2.1 Analytical homogenization methods

The foundations of the field of analytical homogenization are the phenomenological models proposed by Voigt [10] and Reuss [11]. These models disregard the fiber packing by simplifying the composite as a two-volume entity, as shown on Figure 3-7. The Voigt model assumes an iso-strain condition of the constituents with respect to loading along the fiber direction. As the constituents are loaded in parallel, the average force is the sum of the forces over fibers and matrix. The force equilibrium can be expressed in terms of the longitudinal stress and the area on which the stress is applied:

$$\bar{\sigma}_{11} A = \sigma_{11}^{f} n A_f + \sigma_{11}^{m} A_m \quad (3\text{-}14)$$

Substituting Equation (3-12) in (3-14) leads to:

$$\bar{\sigma}_{11} = \sigma_{11}^{f} V_f + \sigma_{11}^{m} V_m \quad (3\text{-}15)$$

The matrix is often assumed isotropic and the fibers transversely isotropic. If the Poisson's effect is neglected and if the iso-strain condition is taken into account, this expression can be further developed to give the longitudinal modulus of the composite $E_{11}$ as a function of the moduli and the volume fractions of the constituents:

$$E_{11} = E_{11}^{f} V_f + E^m V_m \tag{3-16}$$

The Poisson's ratio $\nu_{12}$ according to Voigt has the same form – known as the rule of mixtures – as the longitudinal modulus:

$$\nu_{12} = \nu_{12}^{f} V_f + \nu^m V_m \tag{3-17}$$

The Reuss model starts from an iso-stress assumption under transverse loading. In this serial system, the total transversal deformation of the two-volume entity is the sum of the deformations of the constituents:

$$\bar{\varepsilon}_{22} L = \varepsilon_{22}^{f} L_f + \varepsilon_{22}^{m} L_m \tag{3-18}$$

The dimensions of the fiber and matrix sub-volumes, $L_f$ and $L_m$, are proportional to the volume fractions, $V_f$ and $V_m$. Therefore, Equation (3-18) can be expressed as:

$$\bar{\varepsilon}_{22} = \varepsilon_{22}^{f} V_f + \varepsilon_{22}^{m} V_m \tag{3-19}$$

If the Poisson's strain is neglected and the iso-stress assumption is considered, this expression can be written to give the transversal modulus $E_{22}$ as a function of the moduli and the volume fractions of the constituents:

$$\frac{1}{E_{22}} = \frac{V_f}{E_{22}^{f}} + \frac{V_m}{E^m} \tag{3-20}$$

Similarly, the shear modulus $G_{12}$ can be deduced by assuming equal shear stress in fibers and matrix:

$$\frac{1}{G_{12}} = \frac{V_f}{G_{12}^{f}} + \frac{V_m}{G^m} \tag{3-21}$$

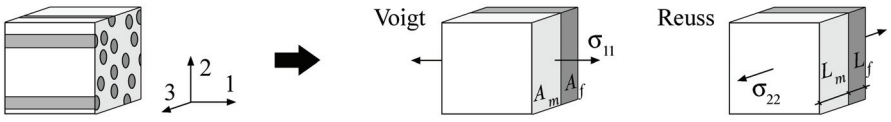


Figure 3-7: Principle of the Voigt and Reuss model for analytical homogenization of unidirectionally reinforced composites

The Voigt solutions are considered sufficiently accurate for design purposes, while the Reuss solutions are generally known not to be. The cause of the latter is in the simplification of the composite geometry into a serial system and the iso-stress assumption that is based on it. This abstraction is too far from the reality of a real composite under transverse loading. For this reason, semi-empirical methods usually only provide an alternative for $E_{22}$, $G_{12}$ and $G_{23}$, while for $E_{11}$ and $\nu_{12}$, Voigt's rule

of mixtures is adopted. This is the case for the two semi-empirical models that will be considered here, the Halpin-Tsai model and the Chamis model.

The Halpin-Tsai model [35], a user-friendly form with engineering approximations of the "self-consistent micromechanics method" by Hill [1], states that the property P of a composite can be expressed in terms of the corresponding property of the matrix $P_m$ and the fibers $P_f$ using the following generalized relationships:

$$P = P_m \frac{1 + \zeta \eta V_f}{1 - \eta V_f} \qquad \eta = \frac{\frac{P_f}{P_m} - 1}{\frac{P_f}{P_m} + \zeta} \tag{3-22}$$

It is clear from the expression for P that $P \to P_m$ if $V_f \to 0$. The function $\eta$ is such that $P \to P_f$ for $V_f \to 1$. The parameter $\zeta$ depends on the reinforcement geometry and on the loading conditions. For unidirectional, continuous fibers, $\zeta$ is usually taken as 2 and 1, respectively, for the calculation of $E_{22}$ and $G_{12}$. The value of $\zeta$ for $E_{11}$ and $\nu_{12}$ is such that the Halpin-Tsai expression can be rewritten as the Voigt solution.

The Chamis model [36] is probably the most used semi-empirical model. It is generally trusted, it provides all the elastic constants and it does not depend on empirical parameters. Chamis's solutions for $E_{11}$ and $\nu_{12}$ are the same as the Voigt solutions. The other constants can be expressed as:

$$\begin{aligned}
E_{22} = E_{33} &= \frac{E^m}{1 - \sqrt{V_f}\left(1 - \frac{E^m}{E_{22}^f}\right)} \\
G_{12} = G_{13} &= \frac{G^m}{1 - \sqrt{V_f}\left(1 - \frac{G^m}{G_{12}^f}\right)} \\
G_{23} &= \frac{G^m}{1 - \sqrt{V_f}\left(1 - \frac{G^m}{G_{23}^f}\right)} \\
\nu_{23} &= \frac{E_{22}}{2G_{23}} - 1
\end{aligned} \tag{3-23}$$

The proposed analytical homogenization methods foresee the option of transversely isotropic fibers, which is indeed crucial when dealing with carbon fibers. For the case of stainless steel fibers, the elastic properties are considered isotropic. As a result, there is no distinction between the predicted shear moduli $G_{12}$ ( = $G_{13}$) and $G_{23}$. The elastic constants of the constituents are listed in Table 3-1 and the predictions for the elastic constants of the composite warp and weft yarn are listed in Table 3-2.

Table 3-1: Elastic constants of the steel fibers and the epoxy matrix

| **Elastic constant** | **Steel fibers[(a)]** | **Epoxy matrix[(b)]** |
|---|---|---|
| $E\ [\mathrm{MPa}]$ | 193000 | 2731 |
| $\nu\ [-]$ | 0.300 | 0.369 |
| $G = \frac{E}{2(1+\nu)}\ [\mathrm{MPa}]$ | 74231 | 997 |

[(a)] Data obtained from NV Bekaert S.A.
[(b)] Data obtained from Allaer et al. [37]

Table 3-2: Constitutive properties of warp and weft yarns according to the analytical homogenization models by Halpin-Tsai and Chamis

| **Elastic constant** | **warp** | | **weft** | |
|---|---|---|---|---|
| | *Halpin-Tsai* | *Chamis* | *Halpin-Tsai* | *Chamis* |
| $E_{11}\ [\mathrm{MPa}]$ | 95457 | 95457 | 72081 | 72081 |
| $E_{22} = E_{33}\ [\mathrm{MPa}]$ | 9915.9 | 8759.4 | 7131.8 | 6746.3 |
| $\nu_{12} = \nu_{13}\ [-]$ | 0.335 | 0.335 | 0.344 | 0.344 |
| $\nu_{23}\ [-]$ | | 0.367 | | 0.368 |
| $G_{12} = G_{13}\ [\mathrm{MPa}]$ | 2798.1 | 3204.3 | 2094.5 | 2466.6 |
| $G_{23}\ [\mathrm{MPa}]$ | | 3204.3 | | 2466.6 |

### 3.2.2 Numerical homogenization approach

In the numerical homogenization approach, the elastic constants of the yarns are deduced from the known properties of the constituents through the analysis of an RVE of the microstructure. Unlike the analytical values, the solutions of this method depend on the fiber geometry and the fiber packing, because these features define the RVE geometry. This leaves the opportunity to assess the effect of the angularity of the steel fiber cross section on the elastic constants. Three different fiber cross sections will be considered – round, hexagonal and pentagonal, and two different regular fiber packing systems – square and hexagonal. Additionally, the influence of an interphase between fibers and matrix will be assessed by adding a cohesive layer around the fibers. The RVE configurations that will be analyzed are depicted in Figure 3-8. Possible symmetries are not exploited, because the added complexity would not be justified, considering the very reasonable calculation times for the finite element models.

The fiber dimensions in the models are chosen such that their cross sectional area corresponds to an equivalent fiber diameter of 30 µm (cf. Figure 2-3). The in-plane dimensions of the RVE are calculated as a function of the fiber volume fraction of the yarns (cf. Equation (3-13)). The length of the RVE along the fibers is irrelevant to the results and is therefore limited to 1 µm in order to reduce the calculation time.

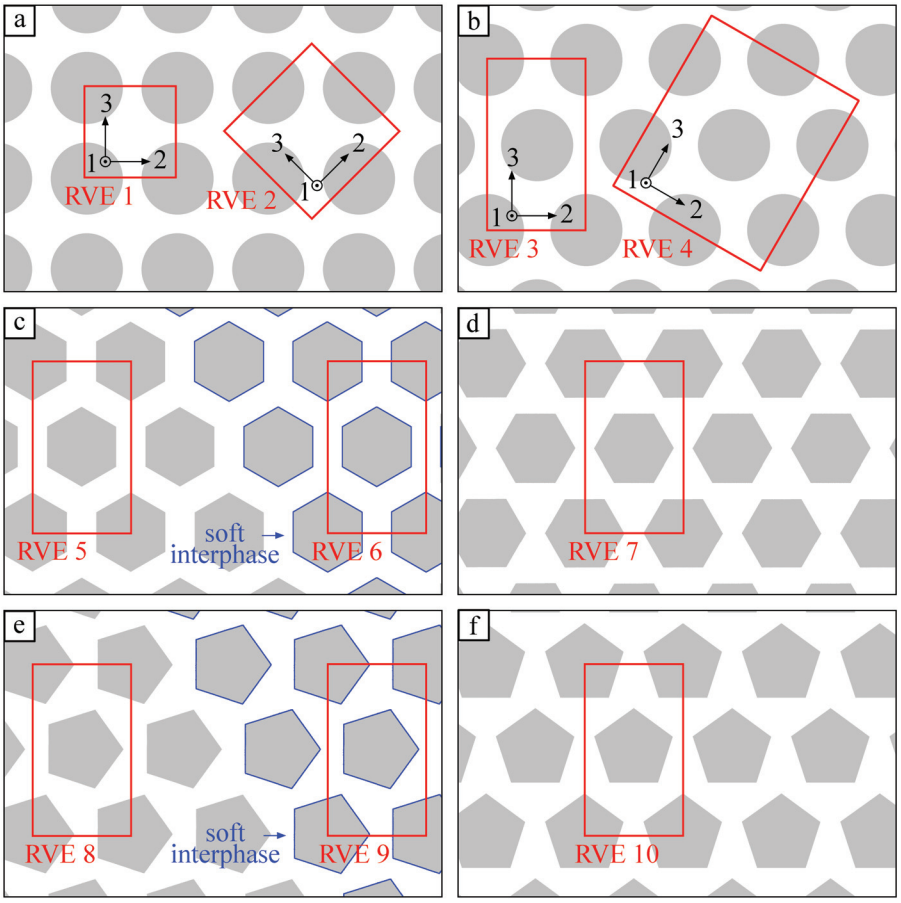


Figure 3-8: RVE's considered for numerical homogenization of the elastic constants, assuming circular fibers in a square (a) and hexagonal (b) packing, a hexagonal packing of hexagonal fibers, with fibers aligned side-to-side (c) and with fibers positioned tip-to-tip (d), and a hexagonal packing of pentagonal fibers with the fibers pointing right (e) and with the fibers pointing up (f)

The RVE's are all one-part models, in which the fibers and the matrix are by default perfectly bonded sections. As was mentioned in section 2.2.1, the angular shape of the fibers increases the stress concentrations on the fiber-matrix interface upon transverse loading, which in turn advances interface debonding. Numerical research by

Sabuncuoglu [38] on this topic has revealed that the stress concentrations on the interface can be mitigated by introducing a *soft interphase*, i.e. a layer around the fibers with a stiffness lower than that of the matrix. The influence of such an interphase was assessed by explicitly modeling it in RVE 6 and RVE 9 through the introduction of a layer of cohesive elements around the fibers.

Cohesive elements are special-purpose elements in the Abaqus finite element software that are designed to model adhesive joints and interfaces. In the case they represent a very thin (or even zero-thickness) interface, their behavior is usually modeled with a traction-separation response. Two regimes can be discerned in this response: the initial linear elastic regime, and the progressive damage regime, as illustrated in Figure 3-9. Both tractions and separations are considered to have three components, i.e. one normal to the interface (designated with 'n'), and two along both in-plane directions (designated with 's' and 't').

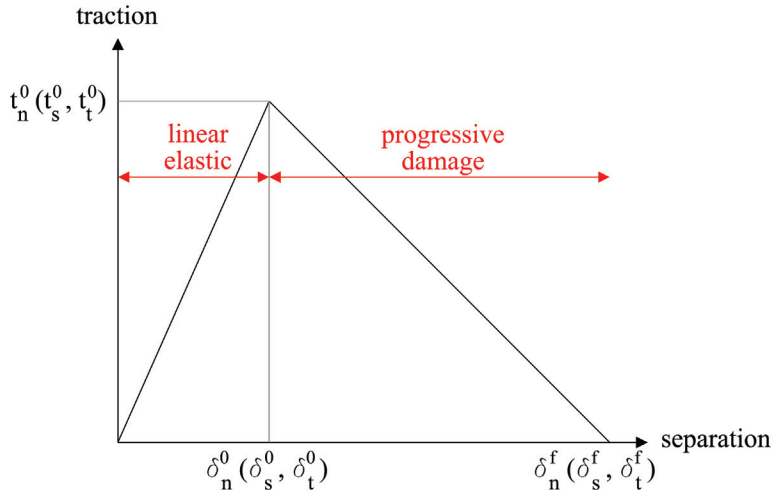


Figure 3-9: Typical traction-separation response

The initial elastic behavior of the cohesive layer can be defined through a constitutive matrix that relates the three nominal stress components (or tractions) under consideration to the three corresponding nominal strain components:

$$\begin{bmatrix} t_n \\ t_s \\ t_t \end{bmatrix} = \begin{bmatrix} E_{nn} & E_{ns} & E_{nt} \\ E_{ns} & E_{ss} & E_{st} \\ E_{nt} & E_{st} & E_{tt} \end{bmatrix} \begin{bmatrix} \varepsilon_n \\ \varepsilon_s \\ \varepsilon_t \end{bmatrix} \tag{3-24}$$

The elasticity matrix for a fully coupled behavior has 6 independent terms. Uncoupled behavior only depends on 3 constants, as the off-diagonal terms can be set to zero in that case.

Note that the constitutive law in Equation (3-24) defines the relation between stresses (or tractions) and strains, whereas the response in Figure 3-9 is expressed in terms of tractions and separations. The reason why Figure 3-9 is not defined through strains is that cohesive elements are typically implemented as a flat layer, with zero thickness across the interface. Any definition of strain across or along the interface requires a certain thickness to relate the displacements to, and therefore, it is not possible to define strain in the strict sense of the term. This obstacle is bypassed in Abaqus by assigning a virtual 'constitutive' thickness to the cohesive elements. The constitutive thickness is 1 by default, and hence in that case, the nominal strain across the interface is equal to the interface separation.

For the conceptual analysis of the influence of a soft interphase, the constitutive thickness was set to 0.1 μm, and the constitutive behavior was characterized by a stiffness that is ten times lower than that of the matrix:

$$\begin{bmatrix} t_n \\ t_s \\ t_t \end{bmatrix} = \frac{E}{(1+\upsilon)(1-2\upsilon)} \begin{bmatrix} 1-\upsilon & 0 & 0 \\ 0 & (1-2\upsilon)/2 & 0 \\ 0 & 0 & (1-2\upsilon)/2 \end{bmatrix} \begin{bmatrix} \varepsilon_n \\ \varepsilon_s \\ \varepsilon_t \end{bmatrix} = \begin{bmatrix} 480.4\ \text{MPa} & 0 & 0 \\ 0 & 99.7\ \text{MPa} & 0 \\ 0 & 0 & 99.7\ \text{MPa} \end{bmatrix} \tag{3-25}$$

With the chosen properties, the cohesive layer can be interpreted as an interphase around the fibers along and across which the separations under a certain stress field will be the same as those in a 0.1 μm thick layer of material which is ten times more compliant than the matrix.

In typical interface applications, the stiffness is usually chosen very high, so as to mimic a perfect initial bonding. The end of the linear elastic regime is then detected with a damage initiation criterion, defined in terms of either the stress or the strain components. Subsequently, the damage grows progressively and the stiffness of the element decreases accordingly. The damage evolution can be defined in terms of the separation, or in terms of the total energy dissipation. In the current application of a soft interphase, damage is not incorporated.

The models were meshed in Abaqus using C3D8R and COH3D8 finite elements with a characteristic element size of 0.5 μm. For models RVE 5 to 10, for instance, this comes down to a mesh of about 38000 elements. This refinement is much finer than needed to reach convergence on the homogenized properties, but it is necessary to come to accurate results for the stress concentrations around the angular fibers. The reduced integration of the elements should not compromise the accuracy in these simulations, as the analysis is geometrically linear with little bending, and the material

properties are elastic. Moreover, the mesh is very refined and only contains well-shaped, hexahedral elements.

Because the RVE geometries intrinsically only have two dimensions, the models can be meshed using a sweeping operation along the fiber direction. This operation results in a periodic mesh, which is suited for the application of periodic boundary conditions by coupling nodes on opposite sides of the RVE. Rigorous practice of the node-coupling scheme as proposed in section 3.1.2 leads to redundant boundary conditions on the edges and the corners of the RVE. Abaqus cannot handle overconstraints, and therefore, the redundant information was eliminated beforehand as suggested by Li and coworkers [33, 34]. The periodic boundary conditions for three linearly independent load cases were implemented directly into the Abaqus input files of the models. The resulting stress distributions were read from the output data bases and averaged out over the RVE volume through Python scripting, and the homogenized elastic properties were calculated as described in section 3.1.4. The results are reported in Table 3-3 with respect to the axes systems shown on Figure 3-8. The stress distribution in the RVE that result from a global strain of 0.2% along the 2-direction are shown in Figure 3-10.

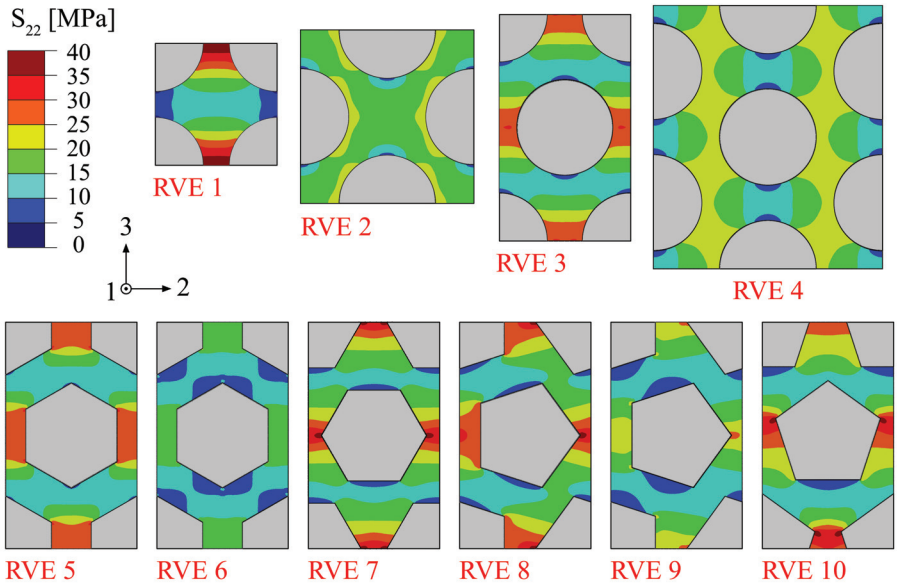


Figure 3-10: Distribution of the $S_{22}$ stress component in the RVE's at a global strain of 0.2% along the 2-direction

The first two RVE's under consideration represent the same system of cylindrical fibers in a square packing (Figure 3-8.a). Both of them are genuine RUC's – they can both be used to reconstruct the material structure using tessellations only – but they are 45° apart. The first RVE is the smallest possible repeating unit cell, hence this is the *simplest* RUC. This first RVE has its axes along the direction with the smallest inter-fiber distances, and the second one has its axes along the diagonals, where the fibers are the furthest apart. The result is that RVE 1 has a much larger transversal stiffness than RVE 2, which illustrates that the square packing is not a transversely isotropic system. The next two RVE's represent cylindrical fibers in a hexagonal packing (Figure 3-8.b). Similarly as with the previous two RVE's, they both represent the same material structure, only they have a different size and they are 45° apart. Rotating the RVE principal directions has no effect on the properties in this system. This transverse isotropy is the reason why the hexagonal packing is generally preferred over the square packing to represent a random fiber distribution.

In reality, the cross section of the steel fibers is not round, but angular in shape, mostly hexagonal or pentagonal. RVE's 5 to 7 represent hexagonal fibers in a hexagonal packing (Figure 3-8.c-d). The angularity of the fiber cross section seems to increase the stiffness of the RVE, especially in the transverse direction. The difference between RVE 5 and RVE 7 is the orientation of the fibers within the packing. This as well seems to influence the transversal properties, with higher values for the configuration in which the fibers are aligned edge to edge (RVE 5). As expected, the soft interphase around the fibers in RVE 6 relieves the stress peaks on the fiber-matrix interface (Figure 3-10) and knocks down the transversal properties, while leaving the longitudinal stiffness intact. Note that the effect of the soft interphase is quite strong, considering its properties and the according interpretation that was explained earlier in this section. RVE's 8 to 10 represent pentagonal fibers in a hexagonal packing (Figure 3-8.e-f). These pentagonal fibers are even more angular than the hexagonal ones, which translates into an even higher transversal stiffness. Due to the mismatch between the pentagonal fiber shapes and the hexagonal packing system, it is no longer possible to stack the fibers corner-to-corner or edge-to-edge, and the RVE becomes slightly anisotropic.

When comparing results in Table 3-2 and Table 3-3, it is clear that the predictions for the transversal properties are higher when an analytical approach is used than when a numerical homogenization is applied. The predictions on the longitudinal stiffness, however, are very similar.

Table 3-3: Elastic constants of warp and weft yarns for ten RVE's

| *Fiber packing* | Square | Hexagonal | | | | | | | | |
|---|---|---|---|---|---|---|---|---|---|---|
| *Fiber shape* | Circular | | Hexagonal | | | | Pentagonal | | | |
| *Fiber orient.* | 0° | | 0° | | 30° | | 0° | | 18° | |
| *Interface* | Perfect bonding | | Perfect | Weak | Perfect | | Perfect | Weak | Perfect | |
| **Constant** | **RVE 1** | **RVE 2** | **RVE 3** | **RVE 4** | **RVE 5** | **RVE 6** | **RVE 7** | **RVE 8** | **RVE 9** | **RVE 10** |
| **WARP YARN** | | | | | | | | | | |
| $E_{11}$ [MPa] | 95444 | 95444 | 95444 | 95444 | 95462 | 95461 | 95462 | 95462 | 95462 | 95462 |
| $E_{22}$ [MPa] | 9997.9 | 6641.8 | 7940.5 | 7940.6 | 8344.7 | 5883.5 | 8036.9 | 8359.2 | 6891.6 | 8420.3 |
| $E_{33}$ [MPa] | 9997.9 | 6641.8 | 7940.6 | 7940.6 | 8344.7 | 5883.7 | 8037.0 | 8330.8 | 6877.1 | 8357.3 |
| $\nu_{12}$ [–] | 0.331 | 0.331 | 0.331 | 0.331 | 0.331 | 0.333 | 0.331 | 0.331 | 0.332 | 0.331 |
| $\nu_{13}$ [–] | 0.331 | 0.331 | 0.331 | 0.331 | 0.331 | 0.333 | 0.331 | 0.331 | 0.332 | 0.331 |
| $\nu_{23}$ [–] | 0.369 | 0.581 | 0.459 | 0.495 | 0.472 | 0.403 | 0.495 | 0. 476 | 0.431 | 0. 475 |
| $G_{12}$ [MPa] | 2855.6 | 2855.6 | 2800.8 | 2800.8 | 2850.0 | 2456.9 | 2922.5 | 2948.1 | 2714.4 | 2948.3 |
| $G_{13}$ [MPa] | 2855.6 | 2855.6 | 2800.7 | 2800.8 | 2849.8 | 2456.9 | 2922.5 | 2938.1 | 2706.9 | 2956.1 |
| $G_{23}$ [MPa] | 2100.9 | 3652.1 | 2656.3 | 2656.4 | 2835.5 | 2096.0 | 2688.1 | 2860.5 | 2418.1 | 2836.9 |
| **WEFT YARN** | | | | | | | | | | |
| $E_{11}$ [MPa] | 72073 | 72073 | 72073 | 72073 | 72073 | 72085 | 72086 | 72086 | 72085 | 72086 |
| $E_{22}$ [MPa] | 6869.3 | 5317.0 | 5927.7 | 5927.7 | 6116.6 | 4933.4 | 5972.4 | 6122.7 | 4967.7 | 6140.7 |
| $E_{33}$ [MPa] | 6869.2 | 5317.0 | 5927.7 | 5927.7 | 6116.6 | 4933.5 | 5972.4 | 6130.9 | 4971.7 | 6132.7 |
| $\nu_{12}$ [–] | 0.340 | 0.340 | 0.340 | 0.340 | 0.340 | 0. 342 | 0.340 | 0.340 | 0. 342 | 0.340 |
| $\nu_{13}$ [–] | 0.340 | 0.340 | 0.340 | 0.340 | 0.340 | 0. 342 | 0.340 | 0.340 | 0. 342 | 0.340 |
| $\nu_{23}$ [–] | 0.446 | 0.571 | 0.522 | 0.522 | 0.508 | 0. 457 | 0.521 | 0.509 | 0. 453 | 0.509 |
| $G_{12}$ [MPa] | 2103.0 | 2103.0 | 2094.6 | 2094.5 | 2127.5 | 1924.0 | 2142.0 | 2167.5 | 1954.2 | 2166.9 |
| $G_{13}$ [MPa] | 2103.0 | 2103.0 | 2094.5 | 2094.5 | 2127.5 | 1924.0 | 2142.0 | 2166.8 | 1953.9 | 2167.6 |
| $G_{23}$ [MPa] | 1691.8 | 2374.8 | 1947.9 | 1947.8 | 2027.6 | 1693.4 | 1963.7 | 2033.2 | 1709.9 | 2029.0 |

On microscopic images of the cross sections of the yarns, it is not obvious to select a dominant packing system. In Figure 3-11, for instance, there are certain regions in which RVE 5 can be discerned, i.e. hexagonal fibers in a close-packed arrangement. Most of the yarns, however, are pentagonal. In the denser region, their shape is such that the sides of neighboring yarns are aligned – a result of the bundle drawing production process. In regions with a low fiber volume fraction, the fibers are no longer in their original spot within the fiber bundle, and they are no longer aligned side by side. As a compromise, the analyses to come will be performed with elastic properties taken as the average of RVE5, RVE7, RVE8, and RVE10. The transverse moduli $E_{22}$ and $E_{33}$ and the shear moduli $G_{12}$ and $G_{13}$ were averaged out to make the material perfectly transversely isotropic. The properties are listed in Table 3-4.

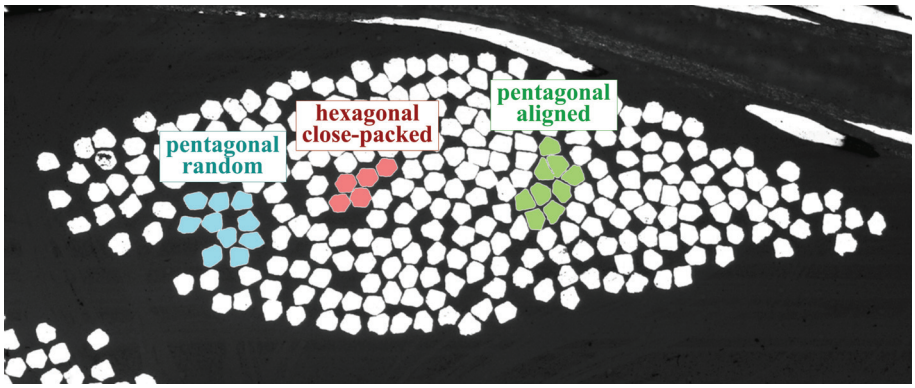


Figure 3-11: Fiber packing systems in a warp yarn

Table 3-4: Elastic constants of the warp and weft yarns as the average values of 4 packing systems, obtained through numerical homogenization

| **Elastic constant** | **warp** | **weft** |
|---|---|---|
| $E_{11}$ [MPa] | 95462 | 72083 |
| $E_{22}$ [MPa] | 8278.9 | 6088.1 |
| $E_{33}$ [MPa] | 8278.9 | 6088.1 |
| $\nu_{12}$ [−] | 0.331 | 0.340 |
| $\nu_{13}$ [−] | 0.331 | 0.340 |
| $\nu_{23}$ [−] | 0.480 | 0.512 |
| $G_{12}$ [MPa] | 2916.9 | 2146.5 |
| $G_{13}$ [MPa] | 2916.9 | 2146.5 |
| $G_{23}$ [MPa] | 2805.2 | 2013.4 |

## 3.3 MESO TO MACRO HOMOGENIZATION: THE ELASTIC CONSTANTS OF A COMPOSITE LAMINATE

The elastic constants of the composite laminate were determined experimentally in Chapter 2. These constants can also be obtained numerically, by homogenizing the properties from the meso-scale to the macro-scale. To this end, a meso-scale RVE finite element model will be constructed and analyzed in this section.

### 3.3.1 Finite element RVE model

The geometry of the meso-scale RVE was designed based on the geometrical characterization of the internal material structure of the composite as described in section 2.4.1. The yarn cross sections were represented by the lenticular idealizations that were proposed in Figure 3-6. The construction of the centerline is illustrated in Figure 3-12 for the case of a weft yarn. First, the cross sections of the warp yarns were positioned in the bounding box of the RVE. Then, two parallel lines were fit in between the warp yarns. As these lines represent the edges of the weft yarn when it is sectioned through its center, they are 0.43 mm apart. The centerline of the weft yarn, finally, is the line in between both parallel edges. In the model geometry, a thin layer of matrix, 5 µm in thickness, was kept in between the yarns for meshing feasibility. In order for the RVE to be a periodic unit cell, half this distance must be kept between the RVE side and the yarns as well. Adding the inter-yarn distances to the thicknesses of the yarns brings the height of the RVE to 0.82 mm. Since the composite laminates have four layers of fabric over a plate thickness of 3 mm, a real layer is only 0.75 mm thick. The reason for this difference in thickness is that the real laminates have layer nesting, a phenomenon that is not accounted for in an RVE model.

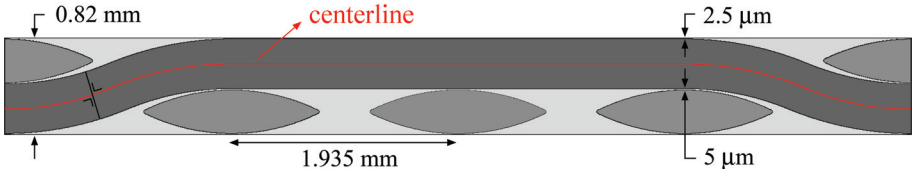


Figure 3-12: Determination of the yarn centerline

All entities were built in CATIA® as separate parts. The yarn entities were constructed by sweeping their cross section along their centerline. In order to obtain a constant sectional area over the whole length of the yarns, the cross section was kept perpendicular to the centerline throughout the sweeping operation. An RVE of the yarn architecture as captured through X-ray tomography and the corresponding finite element representation are shown side by side in Figure 3-13. Once the yarn parts

were built, the matrix part was created by subtracting the yarn volumes from the RVE bounding box.

The yarn meshes were generated using the same sweeping operation as was used to create the geometry. Therefore, these meshes are periodic – they have corresponding nodes on opposite sides of the RVE. The complex matrix part can only be meshed in Abaqus using the free meshing technique, which does not produce a periodic mesh. As a result, the RVE mesh will not be directly suited for the application of periodic boundary conditions through a node-coupling scheme. As will be explained in detail in the next section, this issue will be solved by using the ORAS software to make the PBC's. When it comes to the mesh, this solution imposes the restriction that no second-order finite elements may be used. Therefore, the yarns were meshed with first-order hexahedrons with a reduced integration scheme (C3D8R), and the matrix was discretized using first-order tetrahedrons (C3D4), both to an element size of maximum 0.1 mm. In the matrix pockets, the element size decreases down to 0.5 µm.

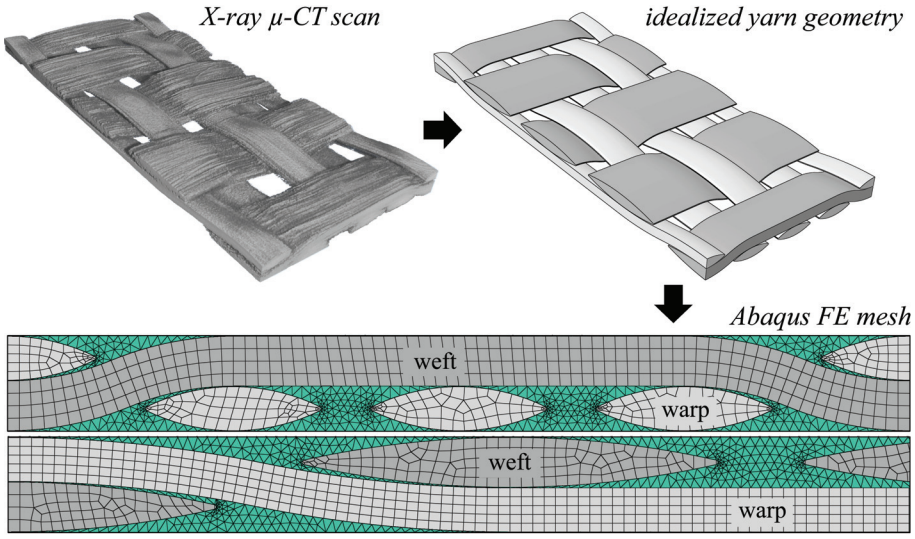


Figure 3-13: Construction of the finite element RVE model: from an X-ray µ-CT scan of the yarn architecture to an idealized geometrical representation of the yarns, to a meshed finite element model in Abaqus

### 3.3.2 Periodic boundary conditions

Because the matrix mesh is non-periodical, it is not possible to make a one-on-one coupling between nodes on opposite sides of the RVE. An adapted node-coupling strategy for this type of mesh was developed by Jacques [39] and implemented as the ORAS software application. The program creates a virtual grid on the faces of the RVE, as illustrated on Figure 3-14. The mesh nodes $p_i$ in every grid section are tied

to one new reference node p in that section, which is the centroid of the mesh nodes. This way, the grid sections k and k* on opposite sides of the RVE can be coupled through their reference nodes p and p* through a basic node-coupling scheme.

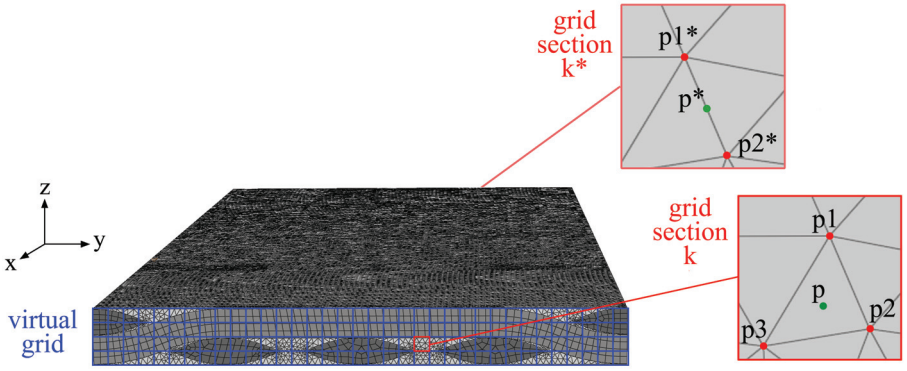


Figure 3-14: Working principle of the ORAS software application

The choice of the grid size has a few implications. The nodes in every section are tied to the reference node by a multiple point constraint (MPC) that fixed all six degrees of freedom. Therefore, all the nodes in one grid section will remain on one plane during the analysis. The larger the grid size, the more nodes every grid section contains, and the larger the leverage on the nodes. A large grid size will hence decrease the accuracy of the results. On the other hand, if the grid size is chosen small compared to the average element size, it may occur that a grid section k contains nodes, while the corresponding grid section k* on the other side of the RVE is empty. In that case, the nodes in grid section k are called 'floating nodes'. This problem is solved by joining every floating node with another section on the same side of the RVE, being the section which contains the node closest to the floating node. This operation takes computation time, so the grid size should not be chosen overly small compared to the element size. The grid size that was used for the RVE model at hand was 0.01 mm.

### 3.3.3 Homogenization results

Three FE analyses were performed in view of finding the homogenized elastic constants of the RVE, corresponding to the three linearly independent load cases as proposed in Equation (3-10), with the global axes system as in Figure 3-14. Geometrical non-linearity was not accounted for during the analyses. The obtained elastic constants are listed in Table 3-5, again according to the axes system on Figure 3-14, i.e. with the x-axis and the y-axis oriented along the warp and the weft direction, respectively.

Table 3-5: Homogenized elastic constants of the meso-scale RVE

| **Elastic constant** | **Homogenized value** |
|---|---|
| $E_{11}$ [MPa] | 25909 |
| $E_{22}$ [MPa] | 19139 |
| $E_{33}$ [MPa] | 5630 |
| $\nu_{12}$ [−] | 0.130 |
| $\nu_{13}$ [−] | 0.488 |
| $\nu_{23}$ [−] | 0.525 |
| $G_{12}$ [MPa] | 1695 |
| $G_{13}$ [MPa] | 1544 |
| $G_{23}$ [MPa] | 1611 |

The homogenized stiffness moduli $E_{11}$ and $E_{22}$ and the Poisson's ratio $\nu_{12}$ in Table 3-5 compare well to the experimentally obtained values that are reported in Table 2-4 and Table 2-5 ($E_{11} = 25.7 \pm 0.8$ GPa and $\upsilon_{12} = 0.110 \pm 0.014$ based on S-warp-A, and $E_{22} = 20.4 \pm 0.7$ GPa and $\upsilon_{12} = 0.086 \pm 0.039$ based on S-weft-A). Nevertheless, some considerations are in order on this comparison. First, it was argued in section 2.5.4 that the experimentally obtained elastic constants strongly depend on the strain range over which they are calculated, because there is no linear initial part to the stress-strain relation of the composite laminates under tension. The E-modulus, for instance, was found to decrease with increasing strain range. The reported E-moduli were calculated between 0% and 0.15% strain, hence they underestimate the very initial stiffness of the material. The FE analyses, on the other hand, do not account for non-linear material behavior, nor for geometrical non-linearity. Therefore, the homogenized values in Table 3-5 represent the very initial response of the material. Following this argumentation, the numerical stiffness values should be higher than the experimental ones. A second consideration is that the RVE model has a lower overall fiber volume fraction than the real composite material. As explained in section 3.3.1, the measured fiber architecture does not fit within the designated RVE bounding box, because the model does not account for layer nesting. This issue was handled by increasing the RVE thickness artificially by 0.07 mm, which lowers the overall volume fraction. According to this argumentation, the numerical stiffness values should be lower than the experimental ones. Considering the good agreement between numerical and experimental results, the effects of the issues that were just mentioned seem to balance out each other.

## 3.4 STRESSES AND STRAINS IN THE MESO-SCALE RVE MODEL VERSUS EXPERIMENTAL OBSERVATIONS

The RVE model will be further evaluated by comparing the stress and strain distributions within the model to the experimental results of Chapter 2. Two validations will be performed. First, the longitudinal surface strain will be compared to the DIC results (section 2.5.5), and second, the correlation between the stresses within the transversal yarns and the observed transversal cracks (section 2.5.6) will be investigated.

The experiments will be simulated by subjecting the RVE model to tension along both loading directions. Two types of boundary conditions will be considered: complete periodic boundary conditions (complete PBC's) and in-plane periodic boundary conditions (in-plane PBC's). The complete PBC's are the full periodic boundary conditions, which make the RVE behave as if it were part of an infinite stack of plies. Therefore, this abstraction will be more realistic as the number of plies in the composite is larger, and as the ply under consideration is further away from the laminate surface. The second type of boundary conditions, in-plane PBC's, is obtained by releasing the constraints in the out-of-plane direction, hence to simulate a single-ply laminate. This abstraction will be more realistic as the number of plies is smaller, and as the ply under study is closer to the laminate surface. The boundary conditions within the real 4-layer laminate should be in between both simulations, with the inner plies closer resembling the infinite stack simulations and the outer plies tending more towards the single-ply-conditions.

### 3.4.1 Numerical surface strain distribution versus DIC surface strain fields

A comparison between the numerical and experimental surface strains is given in Figure 3-15 for three different cases. The S-warp-A case in Figure 3-15.a is a specimen loaded along the warp direction, and with a stacking system that has the warp-dominated side of the fabric directed outwards. The S-weft-A case in Figure 3-15.b has the same stacking system, but the load is applied along the weft direction. The S-weft-B case in Figure 3-15.c is loaded along the weft yarns, and has the stacking system with the weft-dominated side of the textile directed outwards. All three cases have a symmetrical stacking system, whereas periodic boundary conditions can only represent either a single ply, or an infinite ply with all layers stacked in the same direction. In principle, single-ply-simulations (in-plane PBC's) are the most appropriate choice when the region of interest is the surface of a composite laminate. The strain distributions obtained from infinite-stack-simulations (complete PBC's) are reported as well in Figure 3-15, merely to assess the impact of the boundary

conditions. The numerical results are reported at a global strain level of 0.2%. As the yarns and the matrix are assigned with purely elastic material models, results at a higher global strain level would not be physical. The DIC surface strain patterns are not visible yet at such a low global strain. Therefore, the experimental results are shown at the global strain for which the patterns are most clear, which is 1.2%. As is clear from Figure 2-18, the shape of the patterns does not depend on the global strain level. For the ease of comparison, all longitudinal strains are expressed in terms of the strain concentration factor (SCF), i.e., the local strain value divided by the global strain level.

A fundamental difference can be seen in Figure 3-15 between the DIC strain patterns and the numerical strain distributions. The DIC strain typically concentrates around the centers of the transversal yarns, where those yarns appear on the surface. This effect is most clear in the specimens that have the load-bearing yarns directed outwards, i.e. S-warp-A (Figure 3-15.a) and S-weft-B (Figure 3-15.c). In the numerical pattern obtained with in-plane PBC's, the peaks are located at the edges of the transversal yarns. This difference becomes even more pronounced when complete PBC's are applied. When it comes to the quantitative validation, it is clear that the numerical model with in-plane PBC's overestimates the strain concentration factor. It was experimentally observed that the SCF increases with an increasing global strain. Nevertheless, the numerical values for the SCF at 0.2% strain are already higher than the experimental values at 1.2% global strain. It can be argued that in-plane PBC's, which make the RVE behave as a single ply, are less confining to the out-of-plane deformations – and hence to the surface strains – than the real 4-layer laminate structure. However, the model with complete PBC's, which should be too confining in the out-of-plane direction, also outputs rather high strain concentration factors.

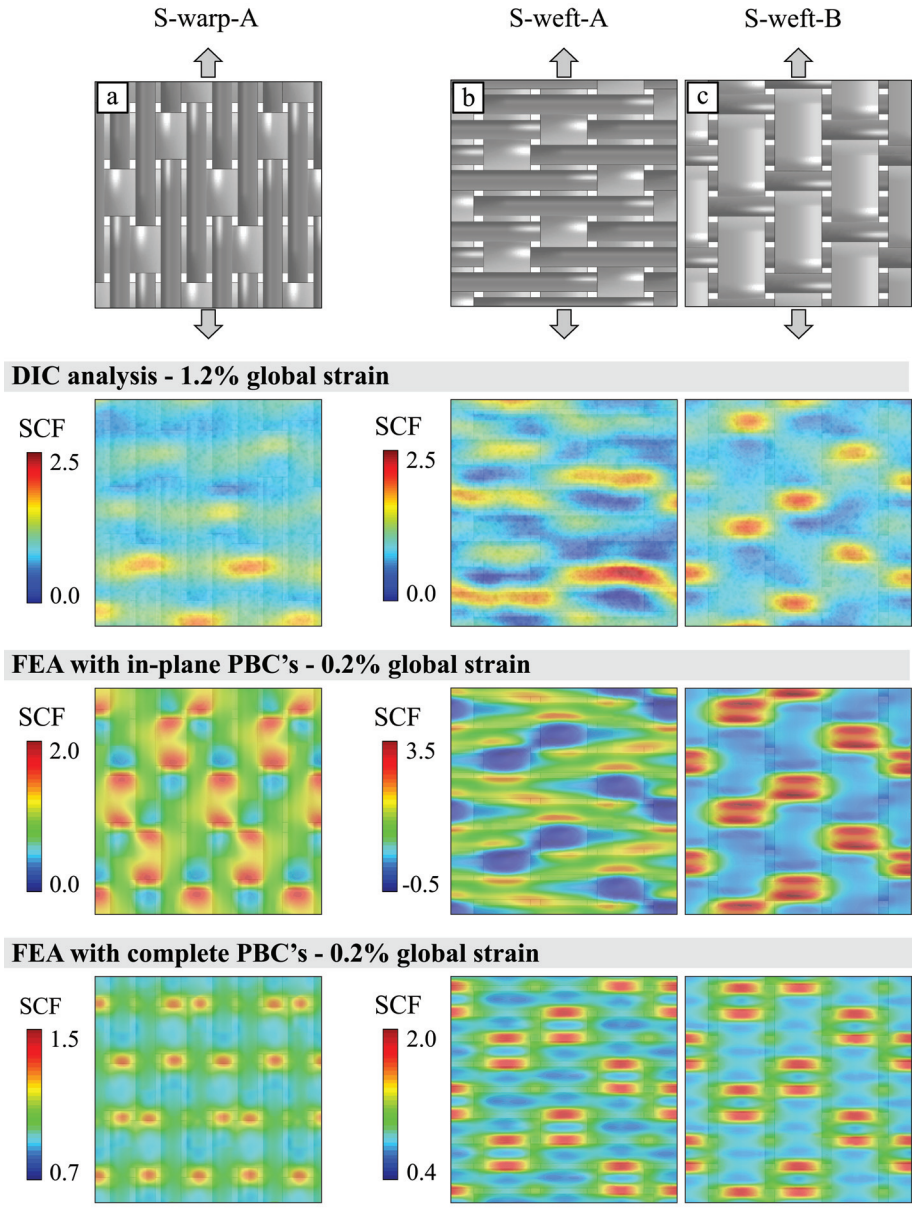


Figure 3-15: Comparison between the experimental and the numerical strain concentration factor (SCF) at the surface of an S-warp-A (a), an S-weft-A (b), and an S-weft-B (c) specimen

### 3.4.2 Numerical stress distribution versus observed damage

Damage was observed in the composite laminates in the form of cracks in the transversal yarns. This type of damage is known as inter-fiber fracture, and amongst the many attempts to predict this type of damage, the physically sound criteria that were developed by Puck [40] are generally considered the most reliable ones. Puck basically modified the Coulomb-Mohr theory on brittle fracture of isotropic materials for the application on UD composites. The fracture hypothesis that underlies Puck's criteria is hence the well-known hypothesis posed by Mohr: *Fracture is governed by the stresses on the fracture plane.* Puck discerned three stresses on the fracture plane, being the normal stress $\sigma_n$, the transversal shear stress $\tau_{nt}$, and the longitudinal shear stress $\tau_{n1}$. Their relation to the stresses $S_{ij}$ in the yarn's local coordinate system is clear from Figure 3-16.

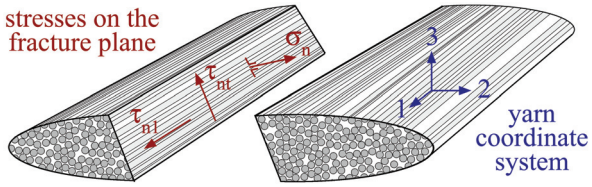


Figure 3-16: Puck's hypothesis on inter-fiber fracture in fiber composites

Puck's principle is simple, but the interpretation and the implementation are usually not, mainly because the location and the orientation of the fracture plane are not known a priori. In this specific case, i.e. the steel fiber fabric reinforced composite laminates subjected to static tension, the cracks were found to run more or less perpendicular to the loading direction. Therefore, the fracture surface will be assumed parallel to the (1,3)-plane in Figure 3-16, hence the stresses on the fracture plane can be identified as:

$$\begin{aligned} \sigma_n &= S_{22} \\ \tau_{n1} &= S_{12} \\ \tau_{nt} &= S_{23} \end{aligned} \tag{3-26}$$

The stresses $S_{22}$, $S_{12}$ and $S_{23}$ are direct outputs from an FE analysis. Their distributions over the transversal yarns are shown on Figure 3-17 for both loading directions at a global strain of 0.2%, and with both complete PBC's and in-plane PBC's.

In order to decide which locations within the transversal yarns are most prone to inter-fiber fracture, the combined action of the stresses must be evaluated. Puck visualized this problem by introducing the Master Fracture Body (MFB), a surface in the $(\sigma_n, \tau_{n1}, \tau_{nt})$ space that envelopes all the stress combinations that do not lead to

fracture. If the normal stress $\sigma_n$ on the fracture plane is known to be positive (tensile), Puck's suggestion for the fracture condition reads:

$$\left(\frac{\tau_{n\psi}}{R^A_{\perp\psi}}\right)^2 + 2\cdot\frac{p^t_{\perp\psi}\cdot\sigma_n}{R^A_{\perp\psi}} + \left(1 - 2\cdot\frac{p^t_{\perp\psi}\cdot R^{At}_{\perp}}{R^A_{\perp\psi}}\right)\frac{\sigma_n^2}{\left(R^{At}_{\perp}\right)^2} = 1 \qquad (3\text{-}27)$$

In this, $\tau_{n\psi}$ is the resultant of the shear stresses $\tau_{n1}$ and $\tau_{nt}$, $R^A_{\perp\psi}$ and $R^{At}_{\perp}$ are the resistances of the fracture plane against the stresses $\tau_{n\psi}$ and $\sigma_n$, respectively, and $p^t_{\perp\psi}$ is the inclination angle of the fracture surface at the intersection with the $(\sigma_n, \tau_{n\psi})$-plane at $\sigma_n = 0$. Determination of the experimental parameters $R^A_{\perp\psi}$, $R^{At}_{\perp}$ and $p^t_{\perp\psi}$ is a challenging task, even for UD laminates. Measuring these values for the composite yarns would be even more difficult, as it would require to produce and test specimens with the exact same fiber volume fraction as the real composite yarns. This incites to go back to a more pragmatic approach. As all three stress components have a strictly positive contribution to Equation (3-27), it should be possible to at least locate the positions within the transversal yarns where their combined effect is most critical. Considering the results of the four simulations in Figure 3-17:

- In an infinite stack, loaded along the warp yarns (Figure 3-17.a), both the normal stress $S_{22}$ $(= \sigma_n)$ and the transversal shear stress $S_{23}$ $(= \tau_{nt})$ are concentrated in the crimp region, around the edges of the transversal yarns. Stress $S_{23}$ has comparable peaks next to the crimp regions, central to the yarn, but these peaks are not supported by other stresses and will hence not be as critical. The longitudinal shear stress $S_{12}$ $(= \tau_{n1})$ is negligible in value.
- Interpretation is less straightforward in the single ply model, loaded along the warp yarns (Figure 3-17.b). The normal stress $S_{22}$, which is by far the highest in value, reaches its maximum in the crimp region, near the edges of the transversal yarns. It is supported by the shear stresses in this region, especially at the very edges of the yarns. The shear stresses both have other local extremes, but these do in general not coincide, and they are not supported by the normal stress.
- The infinite stack model with loading along the weft yarns (Figure 3-17.c), clearly predicts damage in the crimp regions, on the edges of the transversal yarns. The normal stress $S_{22}$ is the highest component; the longitudinal shear stress $S_{12}$ is negligible. The overall stress level is about two times higher than in the models loaded along the warp yarns.
- If loading along the weft direction is applied to a single ply (Figure 3-17.d), the peak location of the normal stress $S_{22}$ shifts towards the yarn center, while the highest transversal shear stress $S_{23}$ remains most elevated on the yarn edges. The longitudinal shear $S_{12}$ is less in value, but supports the other stresses around the yarn edges in the crimp region.

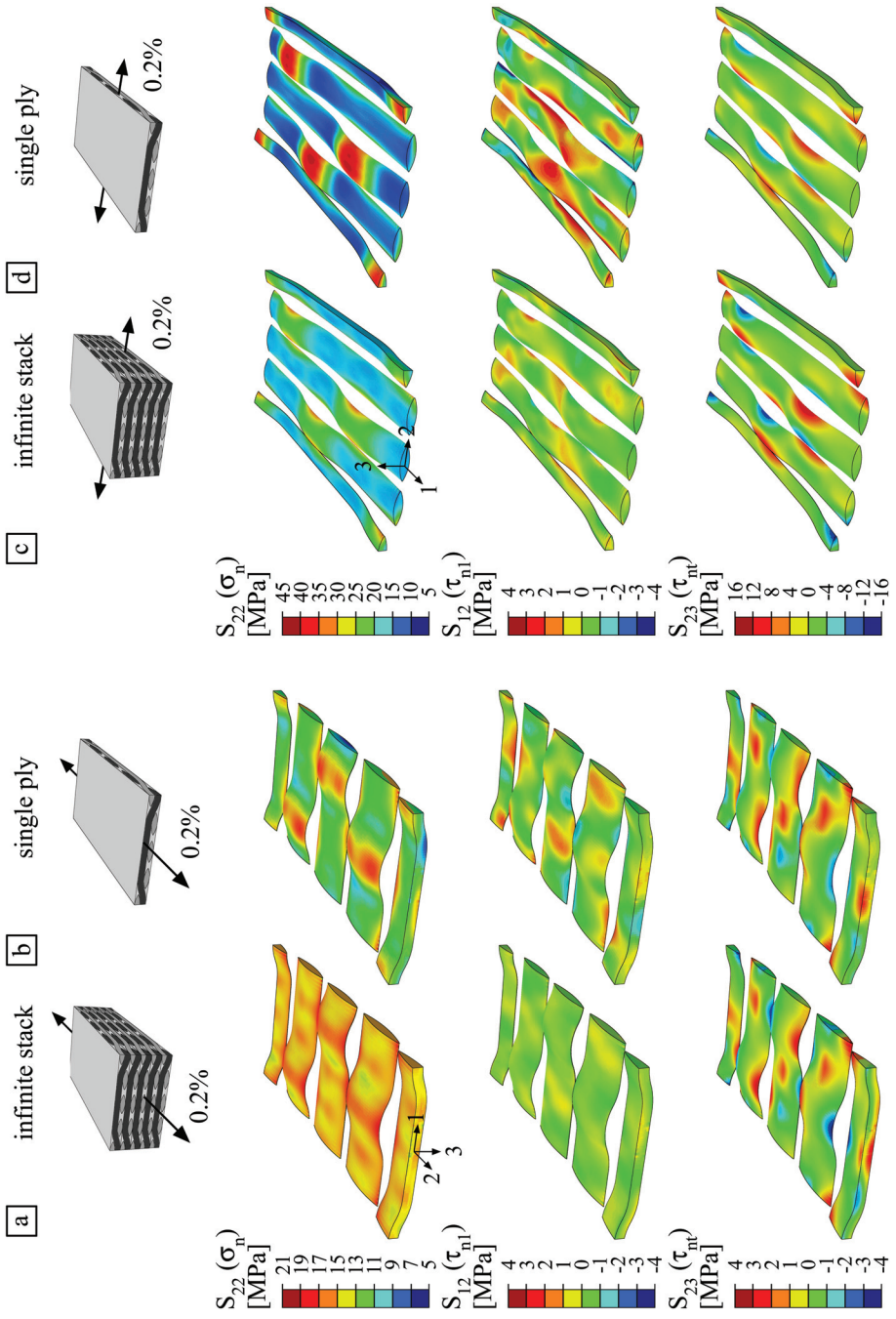


Figure 3-17: Stress in the transversal yarns at a global strain of 0.2% for loading of an infinitely thick laminate (a) and a single ply (b) along the warp yarns, and for loading of an infinitely thick laminate (c) and a single ply (d) along the weft yarns

In conclusion, the numerical stress values predict fracture in the crimp region, around the yarn edges, regardless of the loading directions or the boundary conditions. This is not in line with the observations, which showed that many cracks run through the centers of the transversal yarns. Considering the overall stress level, there is a significant difference between the loading directions. This is unexpected, because the initiation of cracks was observed at about the same strain level for both specimen orientations.

### 3.4.3 Evaluation of the numerical stresses and strains

None of the validations – surface strain fields and crack locations – indicate an agreement between the numerical results and the experimental observations, nor for the stress and strain distributions, nor for their values. Two shortcomings of the RVE model come to mind for explaining this poor agreement:

1. The lack of material non-linearity.
   The real composite laminates have a severely non-linear response, but the simulations were performed with purely elastic material models for both yarns and matrix. As a result, the numerical output is only valid up to a global strain of about 0.2%. The experimental data that was used for both validations, on the other hand, corresponded to a global strain of 1.2%.
2. The inadequate representation of the internal geometry.
   On the macro-scale, the RVE does not account for geometrical effects such as layer nesting, ply shifts and laminate thickness. The importance of these features to the damage behavior has yet been pointed out, both in experimental [41, 42] and numerical studies [43]. On the meso-scale, the yarns are assumed to have perfectly lenticular cross sections, and geometrical imperfections or variations in shape along the yarn path are disregarded in the model. Finally, on the micro-scale, the yarns are considered homogeneous entities in the RVE model. In reality, the fiber volume fraction always shows some variation over the yarn's cross section. Regions with a higher fiber volume fraction have a higher stiffness and will hence attract more stress. Therefore, taking this effect into account could have a strong impact on the stress and strain distributions within the yarns.

The first issue, material non-linearity, will be addressed in the next sections. The other issue is an intrinsic limitation of RVE modeling.

## 3.5 NON-LINEAR MATERIAL BEHAVIOR

Two plastic material responses can be expected in steel-fiber reinforced epoxy: (1) plastic deformations in the yarns along the fiber direction, and (2) isotropic plasticity in the matrix pockets. When strained along the fiber direction, the yarns are a parallel system of fibers and matrix. Therefore, the yarns will start deforming plastically as soon as either fibers or matrix reach their respective yield strain. Additional to the two plastic responses, fracture of the transversal yarns can be identified as a third non-linear material behavior.

In the next sections, plasticity models will be presented for the two plastic responses, and their effect on the stress distribution within the transversal yarns – hence on the predicted fracture locations – will be discussed.

### 3.5.1 Plasticity model for the yarns

#### 3.5.1.a Description

For a plasticity model to fully describe the mechanical response of a material, it requires a yield criterion, a flow rule, and a hardening law. The yield criterion decides which stress states will cause the material to yield, the flow rule defines the direction of the plastic flow, and the hardening rule defines the resilience against further plastic deformations. A comprehensive explanation on the theory of plasticity and its numerical implementation can be found in the works by Dunne et al. [44], and by de Souza Neto et al. [45].

Composite yarns are a typical example of a transversely isotropic material. If the longitudinal direction is chosen as the 1-direction, the elastic law can be expressed as:

$$\begin{bmatrix}\sigma_{11}\\ \sigma_{22}\\ \sigma_{33}\\ \sigma_{12}\\ \sigma_{13}\\ \sigma_{23}\end{bmatrix} = \begin{bmatrix} C_{11} & C_{12} & C_{12} & 0 & 0 & 0 \\ C_{12} & C_{22} & C_{23} & 0 & 0 & 0 \\ C_{12} & C_{23} & C_{22} & 0 & 0 & 0 \\ 0 & 0 & 0 & C_{44} & 0 & 0 \\ 0 & 0 & 0 & 0 & C_{44} & 0 \\ 0 & 0 & 0 & 0 & 0 & \frac{1}{2}(C_{22}-C_{23}) \end{bmatrix} \begin{bmatrix}\varepsilon_{11}\\ \varepsilon_{22}\\ \varepsilon_{33}\\ \gamma_{12}\\ \gamma_{13}\\ \gamma_{23}\end{bmatrix} \tag{3-28}$$

When it comes to the non-linear response, the yarns can be expected to behave plastically along the fiber direction. Transversal loading of the yarns, on the other hand, will cause fracture, rather than plastic deformation. The simplest possible yield criterion that represents this constitutive decoupling of the 1-direction expresses that yielding occurs when the longitudinal stress $\sigma_{11}$ reaches the yield strength $\sigma_y$:

$$f = \sigma_{11} - \sigma_y \tag{3-29}$$

This criterion only deals with tensile yielding, not with compressive yielding. Its range of applications is hence strictly limited to tensile load cases in which occasional local longitudinal compressive stresses remain within the elastic region.

When the tensile loading continues after the yield point has been reached, the material will undergo plastic deformations. The increment of the plastic strain tensor $\Delta\boldsymbol{\varepsilon}^p$ is defined by the flow rule, usually in terms of the plastic multiplier $\gamma$ and a flow potential g:

$$\Delta\boldsymbol{\varepsilon}^p = \Delta\gamma \frac{\partial g}{\partial \boldsymbol{\sigma}} \tag{3-30}$$

The magnitude of the plastic strain increment is hence defined by $\Delta\gamma$, while the flow tensor $\frac{\partial g}{\partial \boldsymbol{\sigma}}$ defines the direction of the plastic flow. For pressure-independent materials, the yield function is usually chosen as the flow potential. This hypothesis is termed the normality hypothesis, because it assumes the plastic flow to be perpendicular to the yield surface. A flow rule that corresponds to the normality hypothesis is termed an 'associated flow rule'. In this case, the normality hypothesis leads to a plastic strain tensor with only one non-zero term:

$$\Delta\varepsilon_{11}^p = \Delta\gamma \tag{3-31}$$

Note that Equation (3-31) implies that plastic deformations do not conserve volume, so the incompressibility condition that is valid for e.g. most metal plasticity models is not met in this case.

As the plastic strain increases, the material hardens, which causes the yield surface to expand. Linear isotropic hardening will be assumed, but more sophisticated hardening laws could as easily be implemented. The hardening law is expressed in terms of the hardening modulus H and the initial yield strength $\sigma_{y0}$:

$$\sigma_y\left(\varepsilon_{11}^p\right) = \sigma_{y0} + H\varepsilon_{11}^p \tag{3-32}$$

The hardening parameters of the yarns were calculated based on the experimental stress-strain curves of fibers and matrix, as shown in Figure 3-18. These curves are based on engineering stresses and strains, whereas the input for a constitutive law should be based on true values. The difference between both, however, is negligible for the low strain level that is considered here. When loaded along the fiber direction, the yarns can be regarded as an iso-strain system of fibers and matrix. If for a certain strain level $\varepsilon$, the stress in the fibers $\sigma_f$ and the stress in the matrix $\sigma_m$ are known, then the stress in a yarn $\sigma_{yarn}$ with a fiber volume fraction $V_f$ can be calculated as:

$$\sigma_{yarn} = \sigma_f V_f + \sigma_m (1 - V_f) \quad (3\text{-}33)$$

The yarn will start to yield when the fibers reach their yield strain, i.e. at point 1 in Figure 3-18. The furthest point on the stress-strain curve of the yarn is point 2 in Figure 3-18, i.e. the ultimate point on the stress-strain curve of the matrix. The yarns do not lose integrity yet at point 2, as the fibers will still bridge the matrix cracks. The reason why this is the end point of the curve is because a plasticity model does not suffice to simulate the behavior of the composite beyond this point. Linear interpolation between points 1 and 2 completes the linear hardening law, with parameter H calculated from Equation (3-32). All hardening parameters are summarized in Table 3-6.

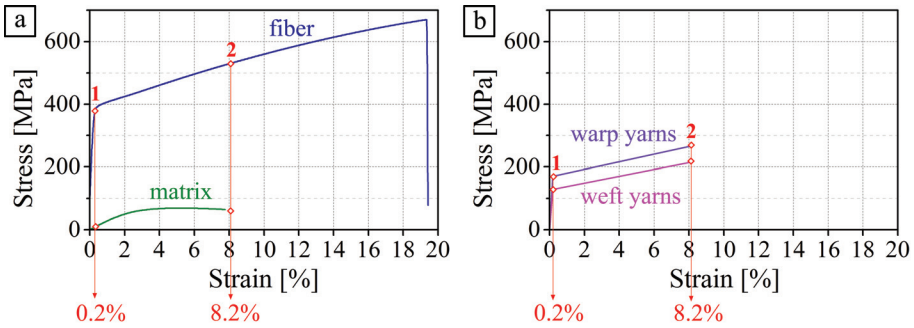


Figure 3-18: Non-linear response of the steel fibers and the epoxy matrix (a), and the calculated hardening curves of the yarns (b)

Table 3-6: Linear hardening data for the warp and weft yarn

| | | **Warp yarns** | | **Weft yarns** | |
|---|---|---|---|---|---|
| **$V_f$ [%]** | | 48.7342 | | 36.4486 | |
| **H [MPa]** | | 1216.82 | | 1106.79 | |
| Point | ε [%] | $\varepsilon_p$ [%] | σ [MPa] | $\varepsilon_p$ [%] | σ [MPa] |
| 1 | 0.18 | 0.00 | 170.64 | 0.00 | 128.85 |
| 2 | 8.24 | 7.96 | 267.49 | 7.94 | 216.72 |

### 3.5.1.b Implementation

The plasticity model was implemented as a user material for implicit analysis (UMAT) in Abaqus. This subroutine must update two tensors: the stress and the consistent tangent operator. The stress tensor at the end of the increment is calculated based on the strain increment, and on the stresses, the strains, and the yield strength at the beginning of the increment. The consistent tangent operator is the tangent

stiffness matrix or material Jacobian, which determines the incremental strain tensor that will be attempted in the next time step. As a result, the consistent tangent operator is responsible for convergence, but it does not influence the accuracy of the solution.

The stress update was implemented using the return mapping strategy. This strategy comes down to calculating a trial stress at the end of the increment as if there were no plastic strain in the current increment, and then returning the stress to the yield surface through a plastic correction. The trial stress can be expressed as:

$$\boldsymbol{\sigma}_{\mathbf{n+1}}^{\mathbf{tr}} = \boldsymbol{\sigma}_{\mathbf{n}} + \mathbf{C}\Delta\boldsymbol{\varepsilon}_{\mathbf{n+1}} \tag{3-34}$$

Using the trial stress defined above, a trial evaluation of the yield surface can be made:

$$f_{n+1}^{tr} = \sigma_{11,n+1}^{tr} - \left(\sigma_{y0} + H\varepsilon_{11,n}^{p}\right) \tag{3-35}$$

An expression for the plastic strain increment $\Delta\varepsilon_{11,n+1}^{p}$ can now be obtained by evaluating the consistency condition at the end of the increment:

$$\begin{aligned} &\sigma_{11,n+1} - \left(\sigma_{y0} + H\varepsilon_{11,n+1}^{p}\right) = 0 \\ &\quad \Leftrightarrow \sigma_{11,n+1}^{tr} - C_{11}\Delta\varepsilon_{11,n+1}^{p} - \sigma_{y0} - H\left(\varepsilon_{11,n}^{p} + \Delta\varepsilon_{11,n+1}^{p}\right) = 0 \\ &\quad \Leftrightarrow f_{n+1}^{tr} - C_{11}\Delta\varepsilon_{11,n+1}^{p} - H\Delta\varepsilon_{11,n+1}^{p} = 0 \\ &\quad \Leftrightarrow \Delta\varepsilon_{11,n+1}^{p} = \frac{f_{n+1}^{tr}}{C_{11} + H} \end{aligned} \tag{3-36}$$

Now the stress can be updated with a plastic correction that returns the trial stress to the yield surface:

$$\boldsymbol{\sigma}_{\mathbf{n+1}} = \boldsymbol{\sigma}_{\mathbf{n+1}}^{\mathbf{tr}} - \mathbf{C}\Delta\boldsymbol{\varepsilon}_{\mathbf{n+1}}^{\mathbf{p}} \tag{3-37}$$

The consistent tangent operator $\mathbf{D}^{ep}$ provides the tangent relation between stress and strain during the increment. An expression for the stress increment $\Delta\boldsymbol{\sigma}_{n+1}$ is not readily available, but $\mathbf{D}^{ep}$ can be rewritten in terms of the stress at the end of the increment $\boldsymbol{\sigma}_{n+1}$:

$$\mathbf{D}^{ep} = \frac{d\Delta\boldsymbol{\sigma}_{n+1}}{d\Delta\boldsymbol{\varepsilon}_{n+1}} = \frac{d(\boldsymbol{\sigma}_{n+1} - \boldsymbol{\sigma}_{n})}{d\Delta\boldsymbol{\varepsilon}_{n+1}} = \frac{d\boldsymbol{\sigma}_{n+1}}{d\Delta\boldsymbol{\varepsilon}_{n+1}} \tag{3-38}$$

This 4th order tensor can be expressed in the same form as Hooke's law in Equation (3-28), i.e. with a Voight notation for the stress and strain tensors:

$$\begin{bmatrix} d\sigma_{11} \\ d\sigma_{22} \\ d\sigma_{33} \\ d\sigma_{12} \\ d\sigma_{13} \\ d\sigma_{23} \end{bmatrix} = \begin{bmatrix} D^{ep}_{1111} & D^{ep}_{1122} & D^{ep}_{1133} & D^{ep}_{1112} & D^{ep}_{1113} & D^{ep}_{1123} \\ D^{ep}_{2211} & D^{ep}_{2222} & D^{ep}_{2233} & D^{ep}_{2212} & D^{ep}_{2213} & D^{ep}_{2223} \\ D^{ep}_{3311} & D^{ep}_{3322} & D^{ep}_{3333} & D^{ep}_{3312} & D^{ep}_{3313} & D^{ep}_{3323} \\ D^{ep}_{1211} & D^{ep}_{1222} & D^{ep}_{1233} & D^{ep}_{1212} & D^{ep}_{1213} & D^{ep}_{1223} \\ D^{ep}_{1311} & D^{ep}_{1322} & D^{ep}_{1333} & D^{ep}_{1312} & D^{ep}_{1313} & D^{ep}_{1323} \\ D^{ep}_{2311} & D^{ep}_{2322} & D^{ep}_{2333} & D^{ep}_{2312} & D^{ep}_{2313} & D^{ep}_{2323} \end{bmatrix} \begin{bmatrix} d\Delta\varepsilon^{tr}_{11} \\ d\Delta\varepsilon^{tr}_{22} \\ d\Delta\varepsilon^{tr}_{33} \\ d\Delta\gamma^{tr}_{12} \\ d\Delta\gamma^{tr}_{13} \\ d\Delta\gamma^{tr}_{23} \end{bmatrix} \tag{3-39}$$

The consistent tangent operator will be calculated term by term. Subscripts denoting incremental notations will be omitted for conciseness. All variables are evaluated at the end of the step, unless specified otherwise. The stress in the numerator $\boldsymbol{\sigma}_{n+1}$ can be elaborated to its components in accordance with Equation (3-37):

$$\begin{aligned}
\sigma_{11} &= \sigma^{tr}_{11} - C_{11}\Delta\varepsilon^{p}_{11} = \sigma_{11,n} + C_{11}\Delta\varepsilon_{11} + C_{12}\Delta\varepsilon_{22} + C_{12}\Delta\varepsilon_{33} - C_{11}\Delta\varepsilon^{p}_{11} \\
\sigma_{22} &= \sigma^{tr}_{22} - C_{12}\Delta\varepsilon^{p}_{11} \\
&= \sigma_{22,n} + C_{12}\Delta\varepsilon_{11} + C_{22}\Delta\varepsilon_{22} + C_{23}\Delta\varepsilon_{33} - C_{12}\Delta\varepsilon^{p}_{11} \\
\sigma_{33} &= \sigma^{tr}_{33} - C_{12}\Delta\varepsilon^{p}_{11} \\
&= \sigma_{33,n} + C_{12}\Delta\varepsilon_{11} + C_{23}\Delta\varepsilon_{22} + C_{22}\Delta\varepsilon_{33} - C_{12}\Delta\varepsilon^{p}_{11} \\
\sigma_{12} &= \sigma^{tr}_{12} = \sigma_{12,n} + C_{44}\Delta\gamma_{12} \\
\sigma_{13} &= \sigma^{tr}_{13} = \sigma_{13,n} + C_{44}\Delta\gamma_{13} \\
\sigma_{23} &= \sigma^{tr}_{23} = \sigma_{23,n} + \frac{1}{2}(C_{22} - C_{23})\Delta\gamma_{23}
\end{aligned} \tag{3-40}$$

The stress components are functions of the strain tensor $\Delta\boldsymbol{\varepsilon}$ directly, and through the plastic strain increment $\Delta\varepsilon^{p}_{11}$:

$$\begin{aligned}
\frac{d\Delta\varepsilon^{p}_{11}}{d\Delta\boldsymbol{\varepsilon}} &= \frac{d}{d\Delta\boldsymbol{\varepsilon}}\left(\frac{f^{tr}_{n+1}}{C_{11} + H}\right) \\
&= \frac{d}{d\Delta\boldsymbol{\varepsilon}}\left(\frac{\sigma_{11,n} + C_{11}\Delta\varepsilon_{11} + C_{12}\Delta\varepsilon_{22} + C_{12}\Delta\varepsilon_{33} - \sigma_{y0} - H\varepsilon^{p}_{11,n}}{C_{11} + H}\right)
\end{aligned} \tag{3-41}$$

This derivative can be elaborated term-by-term as:

$$\Rightarrow \begin{cases} \dfrac{d\Delta\varepsilon^{p}_{11}}{d\Delta\varepsilon_{11}} = \dfrac{C_{11}}{C_{11} + H} \\ \dfrac{d\Delta\varepsilon^{p}_{11}}{d\Delta\varepsilon_{22}} = \dfrac{d\Delta\varepsilon^{p}_{11}}{d\Delta\varepsilon_{33}} = \dfrac{C_{12}}{C_{11} + H} \\ \dfrac{d\Delta\varepsilon^{p}_{11}}{d\Delta\varepsilon_{12}} = \dfrac{d\Delta\varepsilon^{p}_{11}}{d\Delta\varepsilon_{13}} = \dfrac{d\Delta\varepsilon^{p}_{11}}{d\Delta\varepsilon_{23}} = 0 \end{cases} \tag{3-42}$$

Every row of the consistent tangent operator is then found by differentiating the corresponding stress component in Equation (3-40) to all components of the strain increment, with the aid of Equation (3-42). With the zero-terms omitted, the components of the tangent stiffness operator are:

$$
\begin{aligned}
D^{ep}_{1111} &= \frac{\partial \sigma_{11}}{\partial \Delta \varepsilon_{11}} = C_{11} - C_{11}\frac{C_{11}}{C_{11}+H} = \frac{C_{11}H}{C_{11}+H} \\
D^{ep}_{1122} &= \frac{\partial \sigma_{11}}{\partial \Delta \varepsilon_{22}} = C_{12} - C_{11}\frac{C_{12}}{C_{11}+H} = \frac{C_{12}H}{C_{11}+H} \\
D^{ep}_{1133} &= \frac{\partial \sigma_{11}}{\partial \Delta \varepsilon_{33}} = C_{12} - C_{11}\frac{C_{12}}{C_{11}+H} = \frac{C_{12}H}{C_{11}+H} \\
D^{ep}_{2211} &= \frac{\partial \sigma_{22}}{\partial \Delta \varepsilon_{11}} = C_{12} - C_{12}\frac{C_{11}H}{C_{11}+H} = \frac{C_{12}H}{C_{11}+H} \\
D^{ep}_{2222} &= \frac{\partial \sigma_{22}}{\partial \Delta \varepsilon_{22}} = C_{22} - C_{12}\frac{C_{12}H}{C_{11}+H} = \frac{C_{11}C_{22}+C_{22}H-C_{12}^2}{C_{11}+H} \\
D^{ep}_{2233} &= \frac{\partial \sigma_{22}}{\partial \Delta \varepsilon_{33}} = C_{23} - C_{12}\frac{C_{12}H}{C_{11}+H} = \frac{C_{11}C_{23}+C_{23}H-C_{12}^2}{C_{11}+H} \\
D^{ep}_{3311} &= \frac{\partial \sigma_{33}}{\partial \Delta \varepsilon_{11}} = C_{12} - C_{12}\frac{C_{11}H}{C_{11}+H} = \frac{C_{12}H}{C_{11}+H} \\
D^{ep}_{3322} &= \frac{\partial \sigma_{33}}{\partial \Delta \varepsilon_{22}} = C_{23} - C_{12}\frac{C_{12}H}{C_{11}+H} = \frac{C_{11}C_{23}+C_{23}H-C_{12}^2}{C_{11}+H} \\
D^{ep}_{3333} &= \frac{\partial \sigma_{33}}{\partial \Delta \varepsilon_{33}} = C_{22} - C_{12}\frac{C_{12}H}{C_{11}+H} = \frac{C_{11}C_{22}+C_{22}H-C_{12}^2}{C_{11}+H} \\
D^{ep}_{1212} &= \frac{\partial \sigma_{12}}{\partial \Delta \gamma_{12}} = C_{44} \\
D^{ep}_{1313} &= \frac{\partial \sigma_{13}}{\partial \Delta \gamma_{13}} = C_{44} \\
D^{ep}_{2323} &= \frac{\partial \sigma_{23}}{\partial \Delta \gamma_{23}} = \frac{1}{2}(C_{22} - C_{23})
\end{aligned}
\tag{3-43}
$$

Fundamental testing of the UMAT on one-element models indicates that the subroutine produces the intended material behavior for the elementary load cases of simple tension or shear, as shown on Figure 3-19.a. If the model is meshed with more than one element, however, Abaqus returns an erroneous stress state. This is illustrated in Figure 3-19.b for the case of simple shear loading in the (1,2)-plane. The stress $S_{22}$ due to shear loading $\gamma_{12}$ is correctly returned as zero in the one-element model, but it takes a spurious non-zero pattern in the eight-element mesh. This problem emanates from an improper suggestion by Abaqus for the incremental strain tensor in those

nodes that are not directly controlled by the boundary conditions, which causes the solver to converge to an imbalanced solution. Abaqus calculates the incremental strain tensor to be attempted in the next time step based on the tangent stiffness operator, hence the nature of the problem may point towards a mistake in Equation (3-43) or in its implementation. Nevertheless, no errors could be found in the equations, nor in the fortran code that defines the UMAT.

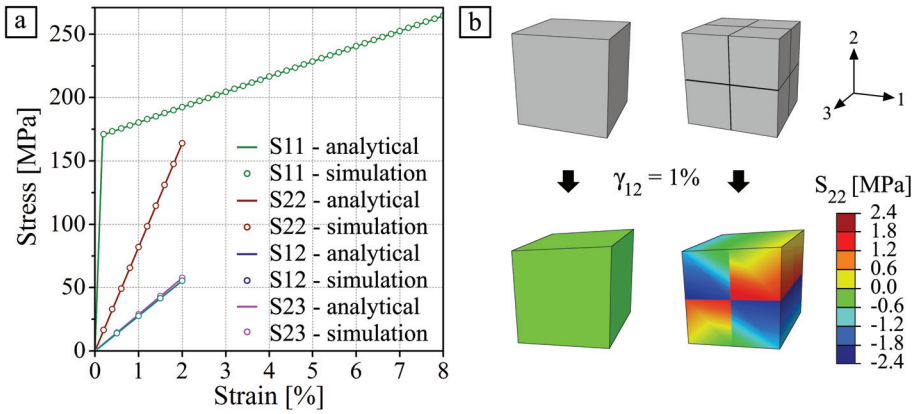


Figure 3-19: Comparison between output from one-element model and analytical data (a) and erroneous stress state in models with more than one element (b)

The problem illustrated in Figure 3-19.b is an often-encountered issue when solving non-linear material models with an implicit solution scheme. The strong anisotropy of the proposed model, along with the fact that the incompressibility condition is not met, only add to the challenge of making it run properly in Abaqus/Standard. One way to address this problem would be to translate the whole model from Abaqus/Standard to Abaqus/Explicit, as an explicit time integration scheme does not typically pose problems when confronted with material plasticity. The concept of this solution is straightforward, but the implementation would be cumbersome. Especially the translation of the periodic boundary conditions would almost certainly cause difficulties. At this point, it is by no means sure that the RVE model will yield reliable outputs for stresses and strains once the material non-linearity is taken into account. Therefore, the intended material behavior for the yarns will initially be approximated by the classical metal plasticity model that is readily available in Abaqus.

The metal plasticity model in Abaqus uses the Von Mises yield criterion. This criterion is also known as $J_2$ plasticity, because the Von Mises effective stress $\sigma_e$ can be expressed using the second stress invariant $J_2$:

$$f = \sigma_e - \sigma_y = \sqrt{3J_2} - \sigma_y = \left(\frac{3}{2}\mathbf{s}:\mathbf{s}\right)^{\frac{1}{2}} - \sigma_y \tag{3-44}$$

In this, $\sigma_y$ is the yield stress under simple tension, and $\mathbf{s}$ is the deviatoric stress tensor. The deviatoric stress tensor is the part of the stress that causes a body to distort – the other part being the hydrostatic stress p, which causes a body to change in volume. Every stress tensor can be expressed as the sum of its deviatoric and its hydrostaic part as:

$$\boldsymbol{\sigma} = \mathbf{s} + \mathrm{p}\mathbf{I} = \mathbf{s} + \frac{1}{3}\mathrm{Tr}(\boldsymbol{\sigma})\mathbf{I} \tag{3-45}$$

The Von Mises criterion was developed based on the theory that metal plasticity is caused by crystallographic slip. This microscopic phenomenon (1) is independent of the hydrostatic pressure, (2) is usually assumed to be isotropic, and (3) does not lead to volume changes. The first characteristic is directly incorporated in the yield criterion, as Equation (3-44) is a function of the deviatoric stress. The second characteristic is ensured because the yield criterion only depends on the stress through an invariant. The third characteristic, the incompressibility, induces that the equivalent plastic strain rate $\Delta\mathrm{p}$ is deviatoric by nature:

$$\Delta\mathrm{p} = \sqrt{\frac{2}{3}\Delta\boldsymbol{\varepsilon}^{\mathbf{p}} : \Delta\boldsymbol{\varepsilon}^{\mathbf{p}}} \tag{3-46}$$

This, in turn, makes that the associative flow rule can be written as:

$$\Delta\boldsymbol{\varepsilon}^{\mathrm{p}} = \Delta\gamma\frac{\partial \mathrm{f}}{\partial\boldsymbol{\sigma}} = \frac{3}{2}\Delta\mathrm{p}\frac{\mathbf{s}}{\sigma_{\mathrm{e}}} \tag{3-47}$$

Isotropic hardening can be entered in Abaqus as a table containing the true effective yield stress as a function of the true effective plastic strain. The data in Table 3-6 are based on engineering (rather than true) values, but they are suited as input for the built-in classical metal plasticity model in Abaqus for this low-strain application.

Uniaxial loading along the fiber direction reduces the Von Mises yield criterion to the criterion proposed in Equation (3-29), and the built-in flow rule in Equation (3-47) will produce the same plastic strain along the loading direction as the one proposed in Equation (3-31). When it comes to the plastic strain in the lateral directions, Equation (3-47) includes a plastic Poisson's effect, whereas the originally intended behavior did not foresee plasticity along the transverse directions. Any stress component other than the direct stress along the fibers will contribute to the yield in the Von Mises model, so these components make the built-in yield condition and the according plastic flow diverge further from the intended behavior. Uniaxial loading of the laminate will cause a stress in the load-bearing yarns that is predominantly longitudinal. Therefore, the built-in material model should be able to capture the plasticity in those yarns with an accuracy that suffices to evaluate whether plastic

phenomena can be responsible for the poor accuracy of the stress and strain localizations within the RVE model.

### 3.5.2 Plasticity model for the matrix

#### 3.5.2.a Description

The non-linear response of epoxies is known to be pressure-dependent, with typically a higher yield strength in compression than in tension. This response was found to be best represented by a parabolic yield criterion [46-48], which was first defined by Tschoegl [49] as:

$$\begin{aligned} f &= 6J_2 + 2(\sigma_c - \sigma_t)I_1 - 2\sigma_c\sigma_t \\ &= 3\mathbf{s}:\mathbf{s} + 6(\sigma_c - \sigma_t)p - 2\sigma_c\sigma_t \\ &= 0 \end{aligned} \tag{3-48}$$

In these formulas, $\sigma_c$ and $\sigma_t$ are the compressive and tensile yield strengths, respectively. The first equation is written in terms of the stress invariants $J_2$ and $I_1$, and the second one is written in terms of the deviatoric stress tensor $\mathbf{s}$ and the hydrostatic stress p.

Equation (3-48) lends itself perfectly for a separate treatment of the deviatoric and the hydrostatic part of the stress. This approach will prove to be very useful when implementing the plasticity model, because it will simplify the mathematics and enhance the readability. All this is a consequence of the plasticity model being symmetric about the hydrostatic axis. More specifically, the yield criterion can be visualized as a parabolic surface in the three-dimensional principal stress space, with the hydrostatic axis as the symmetry axis. Note that the symmetry does not mean that the criterion is pressure independent. In comparison: yield surfaces that are independent of the hydrostatic pressure are parallel to the hydrostatic axis. The Von Mises yield surface, for instance, is cylindrical, and the Tresca yield surface is a hexagonal prism.

For pressure-dependent materials, an associated flow rule often leads to non-physical results. In the specific case of the parabolic yield surface in equation (3-48), it leads to positive volumetric strains under hydrostatic pressure [50, 51]. Therefore, a non-associated flow potential was used instead, as suggested by Haufe et al. [52]:

$$\begin{aligned} g &= 3J_2 + \frac{1}{9}\alpha {I_1}^2 \\ &= \frac{3}{2}\mathbf{s}:\mathbf{s} + \alpha p^2 \end{aligned} \tag{3-49}$$

The flow parameter α controls the plastic volumetric flow, and it correlates to the plastic Poisson's ratio $\nu_p$ under uniaxial loading as:

$$\alpha = \frac{9}{2}\left(\frac{1-2\nu_p}{1+\nu_p}\right) \tag{3-50}$$

The flow potential is now fully defined, and the increment of the plastic strain tensor $\Delta\boldsymbol{\varepsilon}^p$ can be expressed through the non-associative flow rule:

$$\Delta\boldsymbol{\varepsilon}^p = \Delta\gamma\frac{\partial g}{\partial\boldsymbol{\sigma}} = \Delta\gamma\left(3\mathbf{s} + \frac{2}{3}\alpha p\mathbf{I}\right) \tag{3-51}$$

Based on this equation, the deviatoric component of the plastic strain tensor $\Delta\boldsymbol{\varepsilon}_\mathbf{d}^\mathbf{p}$ and the volumetric elastic strain $\Delta\varepsilon_v^p$ can be written as:

$$\begin{aligned}\Delta\boldsymbol{\varepsilon}_\mathbf{d}^\mathbf{p} &= 3\Delta\gamma\mathbf{s}\\ \Delta\varepsilon_v^p &\equiv \mathrm{Tr}(\varepsilon^p) = 2\Delta\gamma\alpha p\end{aligned} \tag{3-52}$$

Both the tensile and the compressive strength are parameters in the yield criterion in Equation (3-48), so both can be provided with a hardening law. The hardening rules were obtained by making a curve fit to data obtained from uniaxial tensile and compressive tests, according to the following exponential expressions:

$$\begin{aligned}\sigma_t(p) &= A_t + B_t\exp\left(\frac{p}{r_t}\right) + C_t\exp\left(\frac{p}{s_t}\right)\\ \sigma_c(p) &= A_c + B_c\exp\left(\frac{p}{r_c}\right) + C_c\exp\left(\frac{p}{s_c}\right)\end{aligned} \tag{3-53}$$

The experimental stress-strain curves for the RIMR 135/ RIMH 137 epoxy system under uniaxial tension and compression are shown in Figure 3-20.a. Figure 3-20.b shows the same experimental data as a function of the plastic strain, and the fitted hardening rules. The hardening parameters are summarized in Table 3-7.

The hardening rules in Equation (3-53) are functions of the equivalent plastic strain p, which can be defined as:

$$p = \sqrt{\frac{1}{1+2\nu_p^2}}\sqrt{\boldsymbol{\varepsilon}^\mathbf{p}:\boldsymbol{\varepsilon}^\mathbf{p}} \stackrel{\text{def}}{=} \sqrt{k}\sqrt{\boldsymbol{\varepsilon}^\mathbf{p}:\boldsymbol{\varepsilon}^\mathbf{p}} \tag{3-54}$$

In this, the plastic Poisson's ratio $\nu_p$ is the ratio between the plastic transverse strain and the plastic longitudinal strain in a uniaxial tensile test. For a pressure-independent material, the plastic Poisson's ratio must equal 0.5, and consequently, the parameter k must equal 2/3, in order to enforce $\varepsilon_e^p = \varepsilon_{11}^p$ under uniaxial loading without volume

changes. In the case of Von Mises plasticity, for instance, Equation (3-54) reduces to the definition for p that was mentioned in Equation (3-46) of the previous section. In the most general case, however, the plastic Poisson's ratio can vary during the hardening process between the values 0.3 and 0.5. Guild at al. [53] established that $\nu_p$ tends to converge to a value of about 0.3, and that this convergence is quite rapid. Therefore, they assumed a constant value of 0.32 for numerical simulations.

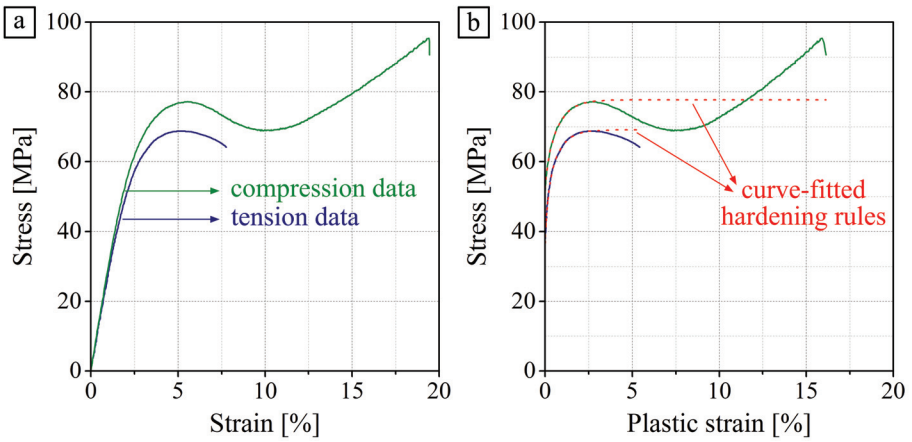


Figure 3-20: Experimental stress-strain curves under uniaxial loading (a) and the curve-fitted hardening functions (b)

Table 3-7: Hardening data for uniaxial tension and compression of the epoxy

| **Parameter** | | **Parameter** | |
|---|---|---|---|
| $A_t$ [MPa] | 69.11530 | $A_c$ [MPa] | 77.73117 |
| $B_t$ [MPa] | -11.15738 | $B_c$ [MPa] | -21.74434 |
| $C_t$ [MPa] | -1.27e-3 | $C_c$ [MPa] | -7.17e-3 |
| $r_t$ [-] | -21.97078 | $r_c$ [-] | -3.98718 |
| $s_t$ [-] | -6.38e-3 | $s_c$ [-] | -9.96e-4 |

Now that a yield criterion, a flow rule, and a hardening rule are defined, the plasticity model is ready to be implemented as a user material for implicit analysis (UMAT) in Abaqus. The implementation will be performed under the assumption of small deformations, and only the initial hardening will be accounted for, not the softening that is seen at higher strain levels. The material model will also not account for the rate- and temperature-dependency that is typical for the non-linear response of epoxies. These assumptions are justified because the model will be applied to study

the behavior of the laminates under monotonic displacement-controlled tensile loading up to relatively small strain levels, and in controlled atmospheric conditions.

### 3.5.2.b Implementation

Similarly as for the yarn plasticity model, the subroutine for the matrix plasticity model must update two tensors, i.e. the stress tensor and the consistent tangent operator. The rest of this section will be dedicated to the elaboration of these two updates. This task was guided by the work by Melro [50], who implemented a plasticity model with the same yield criterion and flow rule, only with a linear hardening rule rather than an exponential one.

The update for the stress tensor is elaborated first. Analogously as for the yarn plasticity model, the stress is updated through a return mapping algorithm, which returns the trial stress $\boldsymbol{\sigma}_{\mathbf{n+1}}^{\mathbf{tr}}$ to the yield surface by applying a plastic correction $\mathbf{C}\Delta\boldsymbol{\varepsilon}_{\mathbf{n+1}}^{\mathbf{p}}$:

$$\boldsymbol{\sigma}_{\mathbf{n+1}} = \boldsymbol{\sigma}_{\mathbf{n+1}}^{\mathbf{tr}} - \mathbf{C}\Delta\boldsymbol{\varepsilon}_{\mathbf{n+1}}^{\mathbf{p}} \tag{3-55}$$

It was mentioned earlier in this section that the symmetry of the plasticity model about the hydrostatic axis can be employed to simplify the mathematics through a separate treatment of the hydrostatic and the deviatoric stress. In that case, it is convenient to express Hooke's law in terms of the bulk modulus K and the shear modulus G:

$$\boldsymbol{\sigma} = 2\mathrm{G}\boldsymbol{\varepsilon}_{\mathbf{d}}^{\mathbf{e}} + \mathrm{K}\varepsilon_{\mathrm{v}}^{\mathrm{e}}\mathbf{I} \tag{3-56}$$

In this relation, $\boldsymbol{\varepsilon}_{\mathbf{d}}^{\mathbf{e}} \equiv \boldsymbol{\varepsilon}^{\mathbf{e}} - \frac{1}{3}\varepsilon_{\mathrm{v}}^{\mathrm{e}}\mathbf{I}$ is the deviatoric component of the elastic strain tensor, and $\varepsilon_{\mathrm{v}}^{\mathrm{e}} \equiv \mathrm{Tr}(\varepsilon^{\mathrm{e}})$ is the volumetric elastic strain.

The plastic correction term can be elaborated by substituting the increment of plastic strain tensor $\Delta\boldsymbol{\varepsilon}^{\mathrm{p}}$ from Equation (3-51), and applying Hooke's law in Equation (3-56):

$$\boldsymbol{\sigma}_{\mathbf{n+1}} = \boldsymbol{\sigma}_{\mathbf{n+1}}^{\mathbf{tr}} - 6\mathrm{G}\Delta\gamma\mathbf{s}_{\boldsymbol{n+1}} - 2\mathrm{K}\alpha\Delta\gamma\mathrm{p}_{n+1}\mathbf{I} \tag{3-57}$$

This expression can be explicitly solved for the deviatoric and the hydrostatic stress as:

$$\begin{aligned}\mathbf{s}_{\mathbf{n+1}} &= \frac{\mathbf{s}_{\mathbf{n+1}}^{\mathbf{tr}}}{1 + 6\mathrm{G}\Delta\gamma} \overset{\text{def}}{=} \frac{\mathbf{s}_{\mathbf{n+1}}^{\mathbf{tr}}}{\varsigma_{\mathrm{s}}} \\ \mathrm{p}_{\mathrm{n+1}} &= \frac{\mathrm{p}_{\mathrm{n+1}}^{\mathrm{tr}}}{1 + 2\mathrm{K}\alpha\Delta\gamma} \overset{\text{def}}{=} \frac{\mathrm{p}_{\mathrm{n+1}}^{\mathrm{tr}}}{\varsigma_{\mathrm{p}}}\end{aligned} \tag{3-58}$$

The parameters $\varsigma_{\mathrm{s}}$ and $\varsigma_{\mathrm{p}}$ in the denominators were introduced to allow a more concise notation for the formulas to come. Note that they are both linear functions of

$\Delta\gamma$, and hence that the stress can be updated by using Equation (3-58) as soon as $\Delta\gamma$ is found.

The equivalent plastic strain increment $\Delta p$ can be calculated by applying the definition in Equation (3-54) to the formula in (3-51), and by again substituting with Equation (3-58) in order to get an expression in terms of trial stresses. The subscript 'n+1' will be omitted from now on for conciseness:

$$\begin{aligned}\Delta p &= \sqrt{k}\sqrt{\Delta\boldsymbol{\varepsilon}^{\mathbf{p}}:\Delta\boldsymbol{\varepsilon}^{\mathbf{p}}}\\ &= \sqrt{k}\Delta\gamma\sqrt{9\frac{\mathbf{s}^{\mathbf{tr}}:\mathbf{s}^{\mathbf{tr}}}{\varsigma_s{}^2}+\frac{4}{3}\alpha^2\frac{(p^{tr})^2}{\varsigma_p{}^2}}\\ &= \sqrt{k}\Delta\gamma\sqrt{18\frac{J_2^{tr}}{\varsigma_s{}^2}+\frac{4}{27}\alpha^2\frac{(I_1^{tr})^2}{\varsigma_p{}^2}}\\ &\overset{\text{def}}{=} \sqrt{kA}\Delta\gamma\end{aligned} \tag{3-59}$$

The parameter A is introduced for the conciseness of the equations to come. The formulation in terms of the trial stress invariants $J_2^{tr}$ and $I_1^{tr}$ is the most convenient one for implementation, because it does not involve any tensor operations.

The yield surface in Equation (3-48) can be evaluated through substitution with Equation (3-58):

$$\begin{aligned}f &= 3\frac{\mathbf{s}^{\mathbf{tr}}:\mathbf{s}^{\mathbf{tr}}}{\varsigma_s{}^2}+6(\sigma_c-\sigma_t)\frac{p^{tr}}{\varsigma_p}-2\sigma_c\sigma_t\\ &= 6\frac{J_2^{tr}}{\varsigma_s{}^2}+2(\sigma_c-\sigma_t)\frac{I_1^{tr}}{\varsigma_p}-2\sigma_c\sigma_t\end{aligned} \tag{3-60}$$

Equation (3-60) depends on $\Delta\gamma$ through parameters $\varsigma_s$ and $\varsigma_p$. Furthermore, f depends on the strength parameters $\sigma_c(p)$ and $\sigma_t(p)$, with p in turn dependent on $\Delta\gamma$. Therefore, a Newton-Raphson iteration scheme can be set up to find the value of $\Delta\gamma$ that makes f equal to zero. The stress tensor $\boldsymbol{\sigma}_{\mathbf{n+1}}$ that is calculated with this value of $\Delta\gamma$ will hence correspond to the stress state that lies on the yield surface.

A Newton-Raphson iteration starts with an initial guess for $\Delta\gamma$ and then finds an improved value through:

$$\Delta\gamma_{n+1} = \Delta\gamma_n - \frac{f(\Delta\gamma_n)}{\frac{\partial f(\Delta\gamma_n)}{\partial\Delta\gamma}} \tag{3-61}$$

After every iteration, the yield surface in Equation (3-60) is re-evaluated with the new-found value for $\Delta\gamma$. The process is terminated once f lies within a predefined window around zero.

The derivative of the yield surface to $\Delta\gamma$ in Equation (3-60) can be elaborated as:

$$\begin{aligned}\frac{\partial f}{\partial \Delta\gamma} &= 6J_2^{tr}\frac{\partial}{\partial \Delta\gamma}\left(\frac{1}{\varsigma_s{}^2}\right) + 2I_1^{tr}(\sigma_c-\sigma_t)\frac{\partial}{\partial \Delta\gamma}\left(\frac{1}{\varsigma_p}\right) + 2\frac{I_1^{tr}}{\varsigma_p}\left(\frac{\partial \sigma_c}{\partial \Delta\gamma}-\frac{\partial \sigma_t}{\partial \Delta\gamma}\right)\\ &\quad - 2\sigma_c\frac{\partial \sigma_t}{\partial \Delta\gamma} - 2\sigma_t\frac{\partial \sigma_c}{\partial \Delta\gamma}\\ &= -12\frac{J_2^{tr}}{\varsigma_s{}^3}\frac{\partial \varsigma_s}{\partial \Delta\gamma} - 2\frac{I_1^{tr}}{\varsigma_p{}^2}(\sigma_c-\sigma_t)\frac{\partial \varsigma_p}{\partial \Delta\gamma} + 2\frac{I_1^{tr}}{\varsigma_p}\left(\frac{\partial \sigma_c}{\partial \Delta\gamma}-\frac{\partial \sigma_t}{\partial \Delta\gamma}\right)\\ &\quad - 2\sigma_c\frac{\partial \sigma_t}{\partial \Delta\gamma} - 2\sigma_t\frac{\partial \sigma_c}{\partial \Delta\gamma}\end{aligned} \tag{3-62}$$

The derivatives of the parameters $\varsigma_s$ and $\varsigma_p$ to $\Delta\gamma$ can be easily calculated from Equation (3-58):

$$\begin{aligned}\frac{\partial \varsigma_s}{\partial \Delta\gamma} &= 6G\\ \frac{\partial \varsigma_p}{\partial \Delta\gamma} &= 2K\alpha\end{aligned} \tag{3-63}$$

The derivatives of the strength parameters to $\Delta\gamma$ can be calculated by using the chain rule on Equation (3-53):

$$\begin{aligned}\frac{\partial \sigma_t}{\partial \Delta\gamma} &= \frac{\partial \sigma_t}{\partial p}\frac{\partial p}{\partial \Delta\gamma} = \left[\frac{B_t}{r_t}\exp\left(\frac{p}{r_t}\right) + \frac{C_t}{s_t}\exp\left(\frac{p}{s_t}\right)\right]\frac{\partial p}{\partial \Delta\gamma}\\ \frac{\partial \sigma_c}{\partial \Delta\gamma} &= \frac{\partial \sigma_c}{\partial p}\frac{\partial p}{\partial \Delta\gamma} = \left[\frac{B_c}{r_c}\exp\left(\frac{p}{r_c}\right) + \frac{C_t}{s_c}\exp\left(\frac{p}{s_c}\right)\right]\frac{\partial p}{\partial \Delta\gamma}\end{aligned} \tag{3-64}$$

The derivative of the equivalent plastic strain to $\Delta\gamma$, finally, can be calculated from Equation (3-59):

$$\begin{aligned}\frac{\partial p}{\partial \Delta\gamma} \equiv \frac{\partial p_{n+1}}{\partial \Delta\gamma} &= \frac{\partial p_n}{\partial \Delta\gamma} + \frac{\partial \Delta p_{n+1}}{\partial \Delta\gamma} = \frac{\partial \Delta p_{n+1}}{\partial \Delta\gamma}\\ &= \sqrt{kA} + \sqrt{\frac{k}{A}}\frac{\Delta\gamma}{2}\frac{\partial}{\partial \Delta\gamma}\left(18\frac{J_2^{tr}}{\varsigma_s{}^2} + \frac{4}{27}\alpha^2\frac{(p^{tr})^2}{\varsigma_p{}^2}\right)\\ &= \sqrt{kA} + \sqrt{\frac{k}{A}}\frac{\Delta\gamma}{2}\left(18J_2^{tr}\frac{\partial}{\partial \Delta\gamma}\left(\frac{1}{\varsigma_s{}^2}\right) + \frac{4}{27}\alpha^2(p^{tr})^2\frac{\partial}{\partial \Delta\gamma}\left(\frac{1}{\varsigma_p{}^2}\right)\right)\end{aligned} \tag{3-65}$$

Once the Newton-Raphson iteration has converged, the solution for $\Delta\gamma$ is used to update the stress tensor through Equation (3-58).

The second update that needs to be specified is the consistent tangent operator $\mathbf{D}^{ep}$. By definition, this tensor defines the relationship between the stress and strain increments $\Delta\boldsymbol{\sigma}_{n+1}$ and $\Delta\boldsymbol{\varepsilon}_{n+1}$, but it can be rewritten in terms of the stress at the end of the increment $\boldsymbol{\sigma}_{n+1}$ and the trial strain at the end of the increment $\boldsymbol{\varepsilon}^{\mathbf{tr}}_{\mathbf{n+1}}$:

$$\begin{aligned}\mathbf{D^{ep}} = \frac{d\Delta\boldsymbol{\sigma}_{n+1}}{d\Delta\boldsymbol{\varepsilon}_{n+1}} = \frac{d(\boldsymbol{\sigma}_{n+1}-\boldsymbol{\sigma}_n)}{d\Delta\boldsymbol{\varepsilon}_{n+1}} = \frac{d\boldsymbol{\sigma}_{n+1}}{d\Delta\boldsymbol{\varepsilon}_{n+1}} = \frac{d\boldsymbol{\sigma}_{n+1}}{d\boldsymbol{\varepsilon}^{\mathbf{tr}}_{\mathbf{n+1}}}\frac{d\boldsymbol{\varepsilon}^{\mathbf{tr}}_{\mathbf{n+1}}}{d\Delta\boldsymbol{\varepsilon}_{n+1}} \\ = \frac{d\boldsymbol{\sigma}_{n+1}}{d\boldsymbol{\varepsilon}^{\mathbf{tr}}_{\mathbf{n+1}}}\frac{d(\boldsymbol{\varepsilon}_{\mathbf{n}}+d\Delta\boldsymbol{\varepsilon}_{n+1})}{d\Delta\boldsymbol{\varepsilon}_{n+1}} = \frac{d\boldsymbol{\sigma}_{n+1}}{d\boldsymbol{\varepsilon}^{\mathbf{tr}}_{\mathbf{n+1}}} = \frac{d\mathbf{s}_{n+1}+dp_{n+1}\mathbf{I}}{d\boldsymbol{\varepsilon}^{\mathbf{tr}}_{\mathbf{n+1}}}\end{aligned} \tag{3-66}$$

In what follows, the consistent tangent operator will be deduced by working towards the last expression in Equation (3-66). The subscript 'n+1' will be omitted from now on for conciseness.

The derivatives of $\mathbf{s}$ and p can be calculated from Equation (3-58) as:

$$\begin{aligned}d\mathbf{s} &= \frac{d\mathbf{s}^{\mathbf{tr}}}{\varsigma_s} - \frac{6G\mathbf{s}^{\mathbf{tr}}d\Delta\gamma}{\varsigma_s{}^2} \\ dp &= \frac{dp^{tr}}{\varsigma_p} - \frac{2K\alpha p^{tr}d\Delta\gamma}{\varsigma_p{}^2}\end{aligned} \tag{3-67}$$

The derivative $d\Delta\gamma$ in these formulas can be obtained by differentiating the yield surface in Equation (3-60):

$$\begin{aligned}&d\left(6\frac{J_2^{tr}}{\varsigma_s{}^2} + 2(\sigma_c-\sigma_t)\frac{I_1^{tr}}{\varsigma_p} - 2\sigma_c\sigma_t\right) = 0 \\ \Leftrightarrow\ &\frac{6dJ_2^{tr}}{\varsigma_s{}^2} - \frac{72GJ_2^{tr}}{\varsigma_s{}^3}d\Delta\gamma + \frac{2\left(\frac{\partial\sigma_c}{\partial\Delta\gamma}-\frac{\partial\sigma_t}{\partial\Delta\gamma}\right)I_1^{tr}}{\varsigma_p}d\Delta\gamma + \frac{2(\sigma_c-\sigma_t)dI_1^{tr}}{\varsigma_p} \\ &\quad - \frac{4(\sigma_c-\sigma_t)I_1^{tr}K\alpha}{\varsigma_p^2}d\Delta\gamma - 2\left(\sigma_t\frac{\partial\sigma_c}{\partial\Delta\gamma}+\sigma_c\frac{\partial\sigma_t}{\partial\Delta\gamma}\right)d\Delta\gamma = 0\end{aligned} \tag{3-68}$$

Now, the terms containing $d\Delta\gamma$ can be separated:

$$\begin{aligned}d\Delta\gamma\Bigg[&\frac{72GJ_2^{tr}}{\varsigma_s{}^3} - \frac{2I_1^{tr}}{\varsigma_p}\left(\frac{\partial\sigma_c}{\partial\Delta\gamma}-\frac{\partial\sigma_t}{\partial\Delta\gamma}\right) + \frac{4(\sigma_c-\sigma_t)I_1^{tr}K\alpha}{\varsigma_p^2} \\ &+ 2\left(\sigma_t\frac{\partial\sigma_c}{\partial\Delta\gamma}+\sigma_c\frac{\partial\sigma_t}{\partial\Delta\gamma}\right)\Bigg] = \frac{6dJ_2^{tr}}{\varsigma_s{}^2} + \frac{2(\sigma_c-\sigma_t)dI_1^{tr}}{\varsigma_p}\end{aligned} \tag{3-69}$$

The terms between square brackets do not contain any derivatives, hence they are all constant during a given time increment. In fact, the expression between square brackets is the derivative of the yield condition to $\mathrm{d}\Delta\gamma$; it can be obtained by substituting Equation (3-63) in Equation (3-62). Therefore, it is readily available from the earlier calculations, and Equation (3-69) can be rewritten as:

$$\mathrm{d}\Delta\gamma = \frac{1}{\frac{\partial f}{\partial \Delta\gamma}}\left(\frac{6\mathrm{d}J_2^{tr}}{\varsigma_s^{\,2}} + \frac{2(\sigma_c - \sigma_t)\mathrm{d}I_1^{tr}}{\varsigma_p}\right) \overset{\text{def}}{=} \frac{1}{\eta}\left(\frac{6\mathrm{d}J_2^{tr}}{\varsigma_s^{\,2}} + \frac{2(\sigma_c - \sigma_t)\mathrm{d}I_1^{tr}}{\varsigma_p}\right) \tag{3-70}$$

The derivatives of the stress invariants in this formula can be obtained in terms of the deviatoric and the volumetric strain as:

$$\begin{aligned} \mathrm{d}J_2^{tr} &= \mathrm{d}\left(\frac{1}{2}\mathbf{s^{tr}}:\mathbf{s^{tr}}\right) = \mathbf{s^{tr}}:\mathrm{d}\mathbf{s^{tr}} = \mathbf{s^{tr}}:2\mathrm{G}\mathrm{d}\boldsymbol{\varepsilon}_{\mathbf{d}}^{\mathbf{tr}} = 2\mathrm{G}\mathbf{s^{tr}}:\mathrm{d}\boldsymbol{\varepsilon^{tr}} \\ \mathrm{d}I_1^{tr} &= \mathrm{d}\big(\mathrm{Tr}(\boldsymbol{\sigma})\big) = \mathrm{Tr}(\mathrm{d}\boldsymbol{\sigma}) = 3\mathrm{K}\mathrm{d}\varepsilon_v^{tr} = 3\mathrm{K}\,\mathbf{I}:\mathrm{d}\boldsymbol{\varepsilon^{tr}} \end{aligned} \tag{3-71}$$

Equation (3-70) can be rephrased by substituting Equation (3-71):

$$\mathrm{d}\Delta\gamma = \frac{1}{\eta}\left(\frac{12\mathrm{G}}{\varsigma_s^{\,2}}\mathbf{s^{tr}}:\mathrm{d}\boldsymbol{\varepsilon^{tr}} + \frac{6\mathrm{K}(\sigma_c - \sigma_t)}{\varsigma_p}\mathbf{I}:\mathrm{d}\boldsymbol{\varepsilon^{tr}}\right) \tag{3-72}$$

Now, the derivative of $\mathbf{s}$ in Equation (3-67) can be calculated by substituting $\mathrm{d}\Delta\gamma$ with Equation (3-72):

$$\begin{aligned} \mathrm{d}\mathbf{s} &= \frac{\mathrm{d}\mathbf{s^{tr}}}{\varsigma_s} - \frac{6\mathrm{G}\mathbf{s^{tr}}}{\varsigma_s^{\,2}}\frac{1}{\eta}\left(\frac{12\mathrm{G}}{\varsigma_s^{\,2}}\mathbf{s^{tr}}:\mathrm{d}\boldsymbol{\varepsilon^{tr}} + \frac{6\mathrm{K}(\sigma_c - \sigma_t)}{\varsigma_p}\mathbf{I}:\mathrm{d}\boldsymbol{\varepsilon^{tr}}\right) \\ \Leftrightarrow\ \mathrm{d}\mathbf{s} &= \frac{2\mathrm{G}\mathrm{d}\boldsymbol{\varepsilon}_{\mathbf{d}}^{\mathbf{tr}}}{\varsigma_s} - \frac{72\mathrm{G}^2\mathbf{s^{tr}}}{\eta\varsigma_s^{\,4}}(\mathbf{s^{tr}}:\mathrm{d}\boldsymbol{\varepsilon^{tr}}) - \frac{36\mathrm{K}\mathrm{G}(\sigma_c - \sigma_t)\mathbf{s^{tr}}}{\eta\varsigma_p\varsigma_s^{\,2}}(\mathbf{I}:\mathrm{d}\boldsymbol{\varepsilon^{tr}}) \\ \Leftrightarrow\ \mathrm{d}\mathbf{s} &= \frac{2\mathrm{G}}{\varsigma_s}\mathrm{d}\boldsymbol{\varepsilon^{tr}} - \frac{72\mathrm{G}^2\mathbf{s^{tr}}}{\eta\varsigma_s^{\,4}}(\mathbf{s^{tr}}:\mathrm{d}\boldsymbol{\varepsilon^{tr}}) \\ &\quad - \left[\frac{36\mathrm{K}\mathrm{G}(\sigma_c - \sigma_t)\mathbf{s^{tr}}}{\eta\varsigma_p\varsigma_s^{\,2}} + \frac{2\mathrm{G}\mathbf{I}}{3\varsigma_s}\right](\mathbf{I}:\mathrm{d}\boldsymbol{\varepsilon^{tr}}) \end{aligned} \tag{3-73}$$

The derivative of p can be obtained in a similar manner:

$$\begin{aligned} \mathrm{d}p &= \frac{\mathrm{d}p^{tr}}{\varsigma_p} - \frac{2\mathrm{K}\alpha p^{tr}}{\varsigma_p^{\,2}}\frac{1}{\eta}\left(\frac{12\mathrm{G}}{\varsigma_s^{\,2}}\mathbf{s^{tr}}:\mathrm{d}\boldsymbol{\varepsilon^{tr}} + \frac{6\mathrm{K}(\sigma_c - \sigma_t)}{\varsigma_p}\mathbf{I}:\mathrm{d}\boldsymbol{\varepsilon^{tr}}\right) \\ \Leftrightarrow\ \mathrm{d}p &= \frac{\mathrm{K}}{\varsigma_p}(\mathbf{I}:\mathrm{d}\boldsymbol{\varepsilon^{tr}}) - \frac{24\mathrm{K}\mathrm{G}\alpha p^{tr}}{\eta\varsigma_s^{\,2}\varsigma_p^{\,2}}(\mathbf{s^{tr}}:\mathrm{d}\boldsymbol{\varepsilon^{tr}}) - \frac{12\mathrm{K}^2\alpha(\sigma_c - \sigma_t)p^{tr}}{\eta\varsigma_p^{\,3}}(\mathbf{I}:\mathrm{d}\boldsymbol{\varepsilon^{tr}}) \end{aligned} \tag{3-74}$$

$$\Leftrightarrow \mathrm{dp} = \left[\frac{\mathrm{K}}{\varsigma_\mathrm{p}} - \frac{12\mathrm{K}^2\alpha(\sigma_\mathrm{c}-\sigma_\mathrm{t})\mathrm{p}^{\mathrm{tr}}}{\eta{\varsigma_\mathrm{p}}^3}\right](\mathbf{I}\colon \mathrm{d}\boldsymbol{\varepsilon}^{\mathbf{tr}}) - \frac{24\mathrm{KG}\alpha\mathrm{p}^{\mathrm{tr}}}{\eta{\varsigma_\mathrm{s}}^2{\varsigma_\mathrm{p}}^2}(\mathbf{s}^{\mathbf{tr}}\colon \mathrm{d}\boldsymbol{\varepsilon}^{\mathbf{tr}})$$

First, five constants $\omega, \psi, \beta, \chi$ and $\rho$ are introduced in order to allow a more concise notation:

$$\omega = \frac{\mathrm{K}}{\varsigma_\mathrm{p}} - \frac{12\mathrm{K}^2\alpha(\sigma_\mathrm{c}-\sigma_\mathrm{t})\mathrm{p}^{\mathrm{tr}}}{\eta\varsigma_\mathrm{p}^3} \qquad \rho = \frac{36\mathrm{KG}(\sigma_\mathrm{c}-\sigma_\mathrm{t})}{\eta\varsigma_\mathrm{p}\varsigma_\mathrm{s}^2}$$
$$\psi = \frac{24\mathrm{KG}\alpha\mathrm{p}^{\mathrm{tr}}}{\eta{\varsigma_\mathrm{s}}^2\varsigma_\mathrm{p}^2} \qquad \beta = \frac{2\mathrm{G}}{\varsigma_\mathrm{s}} \qquad \chi = \frac{72\mathrm{G}^2}{\eta{\varsigma_\mathrm{s}}^4} \tag{3-75}$$

Equations (3-73) and (3-74) can now be combined to write the relation between incremental stress and strain:

$$\mathrm{d}\mathbf{s} + \mathrm{dp}\mathbf{I} = \left[\omega - \frac{\beta}{3}\right]\mathbf{I}(\mathbf{I}\colon \mathrm{d}\boldsymbol{\varepsilon}^{\mathbf{tr}}) - \psi\mathbf{I}(\mathbf{s}^{\mathbf{tr}}\colon \mathrm{d}\boldsymbol{\varepsilon}^{\mathbf{tr}}) + \beta\mathrm{d}\boldsymbol{\varepsilon}^{\mathbf{tr}} - \chi\mathbf{s}^{\mathbf{tr}}(\mathbf{s}^{\mathbf{tr}}\colon \mathrm{d}\boldsymbol{\varepsilon}^{\mathbf{tr}}) - \rho\mathbf{s}^{\mathbf{tr}}(\mathbf{I}\colon \mathrm{d}\boldsymbol{\varepsilon}^{\mathbf{tr}}) \tag{3-76}$$

The 4th order consistent tangent operator $\mathbf{D}^{\mathrm{ep}}$ that is indirectly defined through Equation (3-76) can be written in the same apprehensive matrix notation as Equation (3-39) by adopting the Voight notation for the stress and strain tensors, rather than the tensor notation:

$$\mathbf{D}^{\mathbf{ep}} = \left(\omega - \frac{\beta}{3}\right)\begin{bmatrix}1&1&1&0&0&0\\1&1&1&0&0&0\\1&1&1&0&0&0\\0&0&0&0&0&0\\0&0&0&0&0&0\\0&0&0&0&0&0\end{bmatrix}$$
$$-\psi\begin{bmatrix}s_{11}^{tr}&s_{22}^{tr}&s_{33}^{tr}&s_{12}^{tr}&s_{13}^{tr}&s_{23}^{tr}\\s_{11}^{tr}&s_{22}^{tr}&s_{33}^{tr}&s_{12}^{tr}&s_{13}^{tr}&s_{23}^{tr}\\s_{11}^{tr}&s_{22}^{tr}&s_{33}^{tr}&s_{12}^{tr}&s_{13}^{tr}&s_{23}^{tr}\\0&0&0&0&0&0\\0&0&0&0&0&0\\0&0&0&0&0&0\end{bmatrix} + \beta\begin{bmatrix}1&0&0&0&0&0\\0&1&0&0&0&0\\0&0&1&0&0&0\\0&0&0&\frac{1}{2}&0&0\\0&0&0&0&\frac{1}{2}&0\\0&0&0&0&0&\frac{1}{2}\end{bmatrix} \tag{3-77}$$

$$-\chi\begin{bmatrix} s_{11}^{tr}s_{11}^{tr} & s_{11}^{tr}s_{22}^{tr} & s_{11}^{tr}s_{33}^{tr} & s_{11}^{tr}s_{12}^{tr} & s_{11}^{tr}s_{13}^{tr} & s_{11}^{tr}s_{23}^{tr} \\ s_{22}^{tr}s_{11}^{tr} & s_{22}^{tr}s_{22}^{tr} & s_{22}^{tr}s_{33}^{tr} & s_{22}^{tr}s_{12}^{tr} & s_{22}^{tr}s_{13}^{tr} & s_{22}^{tr}s_{23}^{tr} \\ s_{33}^{tr}s_{11}^{tr} & s_{33}^{tr}s_{22}^{tr} & s_{33}^{tr}s_{33}^{tr} & s_{33}^{tr}s_{12}^{tr} & s_{33}^{tr}s_{13}^{tr} & s_{33}^{tr}s_{23}^{tr} \\ s_{12}^{tr}s_{11}^{tr} & s_{12}^{tr}s_{22}^{tr} & s_{12}^{tr}s_{33}^{tr} & s_{12}^{tr}s_{12}^{tr} & s_{12}^{tr}s_{13}^{tr} & s_{12}^{tr}s_{23}^{tr} \\ s_{13}^{tr}s_{11}^{tr} & s_{13}^{tr}s_{22}^{tr} & s_{13}^{tr}s_{33}^{tr} & s_{13}^{tr}s_{12}^{tr} & s_{13}^{tr}s_{13}^{tr} & s_{13}^{tr}s_{23}^{tr} \\ s_{23}^{tr}s_{11}^{tr} & s_{23}^{tr}s_{22}^{tr} & s_{23}^{tr}s_{33}^{tr} & s_{23}^{tr}s_{12}^{tr} & s_{23}^{tr}s_{13}^{tr} & s_{23}^{tr}s_{23}^{tr} \end{bmatrix}$$

$$-\rho\begin{bmatrix} s_{11}^{tr} & s_{11}^{tr} & s_{11}^{tr} & 0 & 0 & 0 \\ s_{22}^{tr} & s_{22}^{tr} & s_{22}^{tr} & 0 & 0 & 0 \\ s_{33}^{tr} & s_{33}^{tr} & s_{33}^{tr} & 0 & 0 & 0 \\ s_{12}^{tr} & s_{12}^{tr} & s_{12}^{tr} & 0 & 0 & 0 \\ s_{13}^{tr} & s_{13}^{tr} & s_{13}^{tr} & 0 & 0 & 0 \\ s_{23}^{tr} & s_{23}^{tr} & s_{23}^{tr} & 0 & 0 & 0 \end{bmatrix}$$

Fundamental testing of the UMAT on one-element models indicates a perfect agreement between the simulated response and the experimental data for unidirectional tensile and compressive loading, as is shown on Figure 3-21. This figure additionally shows the simulated response under pure shear loading. Upscaling the application of the UMAT to simulate the matrix plasticity in the RVE model did not pose any notable convergence issues.

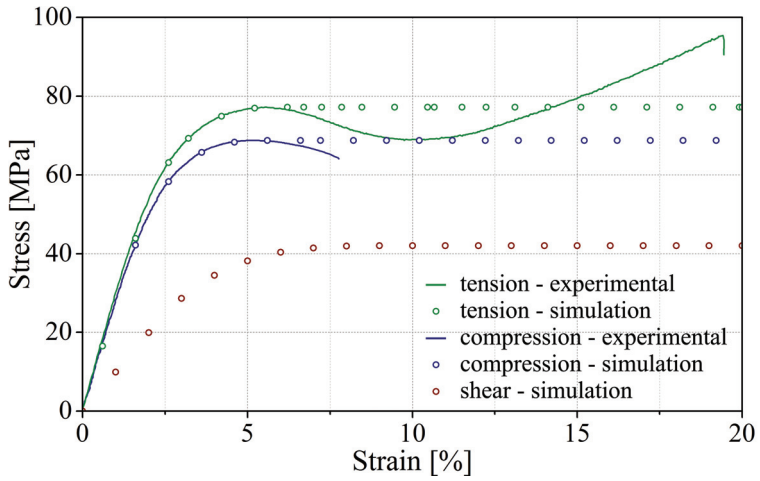


Figure 3-21: Simulated response of a one-element model versus experimental data

### 3.5.3 Results

The results of finite element RVE simulations with elastic-plastic material models for yarns and matrix are shown in Figure 3-22, on a cross section through the crimp region. The RVE model is given complete PBC's, and hence represents an endless stack of plies. A global strain of 0.6% was applied along the warp direction (Figure 3-22.a) and along the weft direction (Figure 3-22.b).

The first two distributions in Figure 3-22 show the matrix plasticity $\gamma$ and the plastic deformations in the load-carrying yarns $\varepsilon_{11}^{p}$. The matrix plasticity is more localized than the yarn plasticity, with strong concentrations around the edges of the transversal yarns. The overall level of plastic deformations in the load-carrying yarns seems to be similar for both loading directions. The matrix plasticity, on the other hand, is much more developed in the weft-oriented configuration.

In the last six distributions in Figure 3-22, the stresses on the fracture plane, i.e. $S_{22}$, $S_{23}$ and $S_{12}$ – or $\sigma_n$, $\tau_{nt}$ and $\tau_{n1}$ – are displayed. Along with the results obtained with elastic-plastic material models for yarns and matrix, the results with purely elastic materials are shown for comparison. It is clear that accounting for the material plasticity generally reduces the stresses in the transversal yarns, but that it does not change the way they are distributed over the yarns. The most critical stress states are still located on the edges of the transversal yarns, rather than on the center. Therefore, even if the non-linear material behavior is accounted for, the RVE model is still unable to predict the observed transversal cracks.

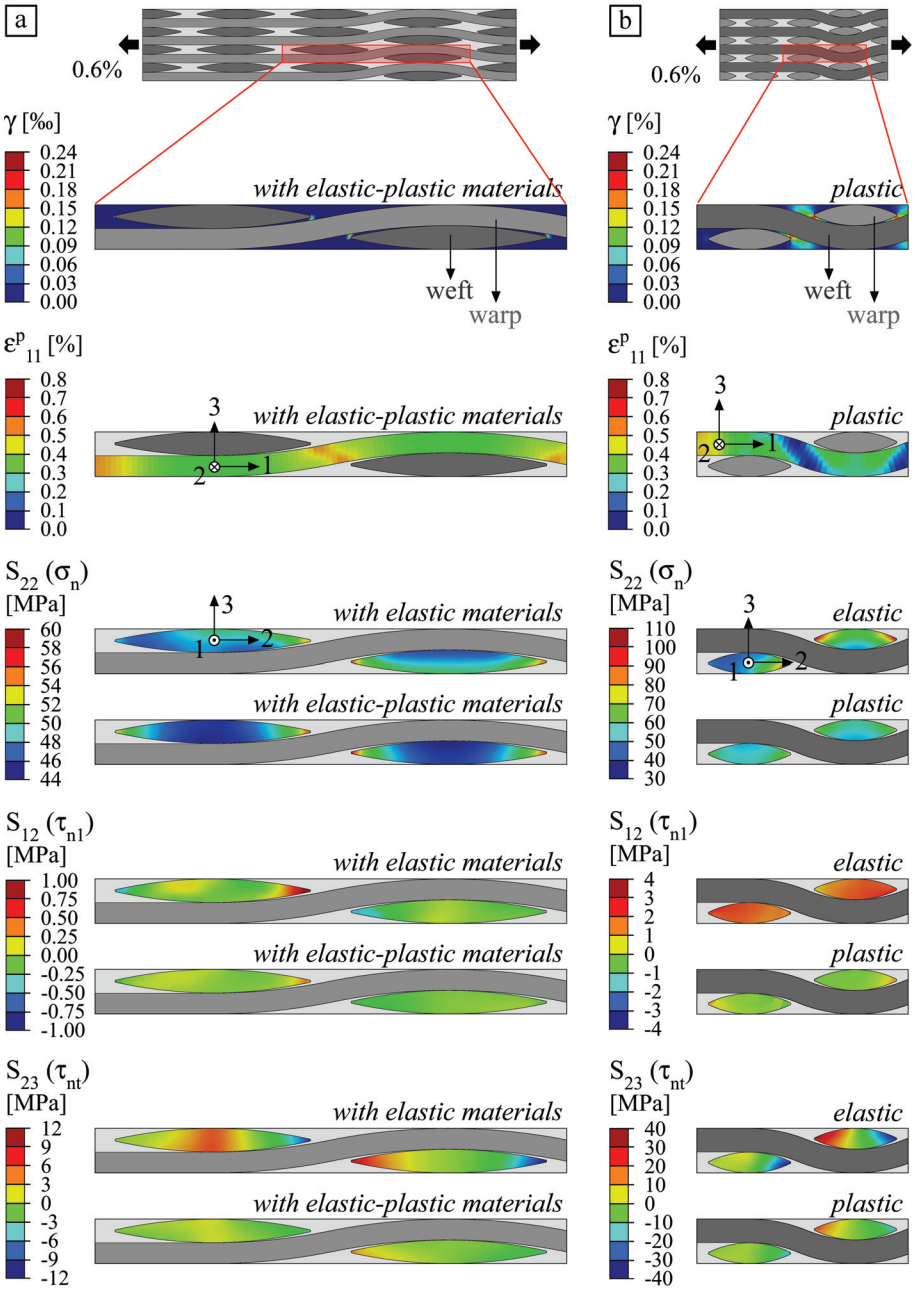


Figure 3-22: FE results in the RVE with plasticity models for yarns and matrix at a global strain of 0.6% along the warp yarns (a) and along the weft yarns (b): matrix plasticity γ, plastic deformations in the load-carrying yarns $\varepsilon^{p}_{11}$, and stresses on the fracture plane $S_{22}$, $S_{12}$, and $S_{23}$ (including the comparison with purely elastic models)

## 3.6 CONCLUSIONS

In this chapter, the most commonly used method in meso-scale modeling was applied to study the mechanics of the stainless steel textile epoxy composite. The method used is known as RVE modeling, because it is based on the assumption that the textile reinforcement can be represented by one representative volume element – or one RVE.

RVE modeling serves two goals: homogenization and localization. The homogenization procedure was performed first, and in two steps. In the first step, the elastic properties of the yarns were deduced through a micro-to-meso homogenization, and in the second step, the laminate properties were determined via a meso-to-macro homogenization. The results were in good agreement with the experimental values that were reported in Chapter 2. The second goal of RVE modeling, localization, is to study the local stresses and strains as a function of the globally applied stress or strain field. Stress and strain localizations are particularly interesting, as they are the key to explaining the transversal damage and the consequent early failure of the composite. The suitability of the RVE model for serving this goal was evaluated by comparing the numerical strain distribution at the surface of the RVE to the experimentally obtained strain field at the surface of a tensile specimen, and by comparing the numerical stress distribution within the RVE to the experimentally observed crack pattern. The RVE model passed neither of both validations, which indicates that the model does not represent all aspects that contribute to the stress and strain localizations within the composite structure.

Two possible shortcomings of the initial RVE representation were put forth in section 3.4.3 of this chapter. The first one was the material non-linearity. This is not an issue in the common, brittle fiber/brittle matrix composites, but it could certainly be important in the ductile fiber/ductile matrix composite at hand. This shortcoming was addressed by refining the RVE model with plasticity models for yarns and matrix. This effort, however, hardly changed the model output. The other shortcoming mentioned was the deficient representation of the geometry of the internal structure. The RVE represents the composite as a perfectly periodic structure, while the real laminates show layer nesting and ply shifting. Furthermore, the yarns are considered homogeneous and perfectly lenticular in the RVE model, while in reality, the fiber density varies over the yarn's cross section, which in turn varies along the yarn's path. This last shortcoming is intrinsic to RVE modeling and can hence not be solved within the framework of the RVE methodology. In the next chapter, the extent of the geometrical imperfections in the composite laminates under study, and their relation to the meso-scale mechanics, will be studied experimentally.

## 3.7 REFERENCES


[1] Hill R. *A self-consistent mechanics of composite materials*. Journal of the Mechanics and Physics of Solids; 13: 213-222. 1965.

[2] Hill R. *Elastic properties of reinforced solids: Some theoretical principles*. Journal of Mechanics and Physics of Solids; 11: 357-372. 1963.

[3] Hashin Z, Rosen BW. *The elastic moduli of fiber-reinforced materials*. ASME Journal of Applied Mechanics; 31: 223-232. 1964.

[4] Hashin Z, Shtrikman S. *A variational approach to the theory of elastic behavior of multiphase materials*. Journal of Mechanics and Physics of Solids; 11: 127-140. 1963.

[5] Eshelby JD. *The Determination of the Elastic Field of an Ellipsoidal Inclusion, and Related Problems*. Proceedings of the Royal Society A: Mathematical, Physical and Engineering Sciences; 241: 376-396. 1957.

[6] Eshelby JD. *Axisymmetric stress field around spheroidal inclusions and cavities in a transversely isotropic material*. Journal of Applied Mechanics; 36. 1969.

[7] Canal LP, Alfano M, Botsis J. *A multi-scale based cohesive zone model for the analysis of thickness scaling effect in fiber bridging*. Composites Science and Technology; 139: 90-98. 2017.

[8] Sodhani D, Reese S, Moreira R, Jockenhoevel S, Mela P, Stapleton SE. *Multi-scale modelling of textile reinforced artificial tubular aortic heart valves*. Meccanica; 52: 677-693. 2016.

[9] Suquet P. *Elements of homogenization theory for inelastic solid mechanics*. Homogenizat!on techniques for composite media: 194-278. 1987.

[10] Voigt W. *Uber die Beziehung zwischen den beiden Elastizitatskonstanten Isotroper Korper*. Wiedmanns Annalen der Physik and Chemie; 38: 573-587. 1889.

[11] Reuss A. *Berechnung der Fließgrenze von Mischkristallen auf Grund der Plastizitätsbedingung für Einkristalle*. Journal of Applied Mathematics and Mechanics; 9: 49-58. 1929.

[12] Hashin Z, Shtrikman S. *Note on a variational approach to the theory of composite elastic materials*. Journal of the Franklin Institute; 271: 336-341. 1961.

[13] Hashin Z. *On some variational principles in anisotropic and nonhomogeneous elasticity*. Journal of the Mechanics and Physics of Solids; 10: 335-342. 1962.

[14] Mori T, Tanaka K. *Average stress in matrix and average elastic energy of materials with misfitting inclusions*. Acta Metallurgica; 21: 571-574. 1973.

[15] Hill R. *Elastic properties of reinforced solids: some theoretical principles*. Journal of the Mechanics and Physics of Solids; 11: 357-372. 1963.

[16] Whitcomb JD, Srirengan K, Chapman DC. *Evaluation of homogenization for global-local stress analysis of textile composites*. Composite Structures; 31: 137-149. 1995.

[17] Whitcomb JD, Srirengan K. *Effect of various approximations on predicted progressive failure in plain weave composites*. Composite Structures; 34: 13-20. 1996.

[18] Richardson RM, Vu VH, Wu L. *An Inscribing Model for Random Polytopes*. Discrete & Computational Geometry; 39: 469-499. 2007.

[19] Temizer I. *Micromechanics - Analysis of Heterogeneous Materials*. Hannover: Leibniz University of Hannover. 2007.

[20] Zohdi TIW, P. *Aspects of the computational testing of the mechanical properties of microheterogeneous material samples*. International Journal for numerical methods in engineering; 50: 2573-2599. 2001.

[21] Xia Z, Zhou C, Yong Q, Wang X. *On selection of repeated unit cell model and application of unified periodic boundary conditions in micro-mechanical analysis of composites*. International Journal of Solids and Structures; 43: 266-278. 2006.

[22] Chapman DC. *Effects of Assumed Tow Architecture on the Predicted Moduli and Stresses in Woven Composites*. NASA Contractor Report 195310. 1994.

[23] Carvelli V, Poggi C. *A homogenization procedure for the numerical analysis of woven fabric composites*. Composites: Part A; 32: 1425-1432. 2001.

[24] Peng X, Cao J. *A dual homogenisation and finite element approach*. Composites: Part B; 33: 45-56. 2002.

[25] Kaminski M, Kleiber M. *Perturbation based stochastic finite element method for homogenization of two-phase elastic composites*. Computers and Structures; 78: 811-826. 2000.

[26] Xia Z, Zhang Y, Ellyin F. *A unified periodical boundary conditions for representative volume elements of composites and applications*. International Journal of Solids and Structures; 40: 1907-1921. 2003.

[27] Li S. *Boundary conditions for unit cells from periodic microstructures and their implications*. Composites Science and Technology; 68: 1962-1974. 2008.

[28] Huet C. *Application of variational concepts to size effects in elastic heterogeneous bodies*. Journal of Mechanics and Physics of Solids; 38: 813-841. 1990.

[29] Hazanov S, Huet C. *Order relationships for boundary conditions effect in heterogeneous bodies smaller than the representative volume*. Journal of Mechanics and Physics of Solids; 42: 1995-2011. 1994.

[30] Sun CT, Vaidya RS. *Prediction of composite properties from a representative volume element*. Composites Science and Technology; 56: 171-179. 1996.

[31] Li S. *On the unit cell for micromechanical analysis of fibre-reinforced composites*. Proceedings of the Royal Society A: Mathematical, Physical and Engineering Sciences; 455: 815-838. 1999.

[32] Li S. *General unit cells for micromechanical analyses of unidirectional composites*. Composites Part A: Applied Science and Manufacturing; 32: 815-826. 2001.

[33] Li S, Wongsto A. *Unit cells for micromechanical analyses of particle-reinforced composites*. Mechanics of Materials; 36: 543-572. 2004.

[34] Li S, Zhou C, Yu H, Li L. *Formulation of a unit cell of a reduced size for plain weave textile composites*. Computational Materials Science; 50: 1770-1780. 2011.
[35] Halpin JC. *The Halpin-Tsai Equations: A Review*. Polymer Engineering & Science; 16: 344-352. 2004.
[36] Chamis CC. *Mechanics of Composite Materials Past, Present and Future*. NASA Contractor Memorandum 100793. 1984.
[37] Allaer K, De Baere I, Lava P, Van Paepegem W, Degrieck J. *On the in-plane mechanical properties of stainless steel fibre reinforced ductile composites*. Composites Science and Technology; 100: 34-43. 2014.
[38] Sabuncuoglu B. *On the high stress concentrations in steel fiber composites under transverse loading*. Journal of Reinforced Plastics and Composites; 33: 1941-1953. 2014.
[39] Jacques S. *Development of a Framework for the Construction of Meso-scale Finite Element Models of Textile Composites*. Ghent, Belgium: Ghent University. Faculty of Engineering and Architecture. 2014.
[40] Knops M. *Puck's action plane fracture criteria* Analysis of Failure in Fiber Polymer Laminates - The Theory of Alfred Puck: Springer-Verlag Berlin Heidelberg. p. 37-115. 2008.
[41] Daggumati S, De Baere I, Van Paepegem W, Degrieck J, Xu J, Lomov SV, et al. *Local damage in a 5-harness satin weave composite under static tension: Part I – Experimental analysis*. Composites Science and Technology; 70: 1926-1933. 2010.
[42] De Carvalho NV, Pinho ST, Robinson P. *An experimental study of failure initiation and propagation in 2D woven composites under compression*. Composites Science and Technology; 71: 1316-1325. 2011.
[43] Daggumati S, Van Paepegem W, Degrieck J, Xu J, Lomov SV, Verpoest I. *Local damage in a 5-harness satin weave composite under static tension: Part II – Meso-FE modelling*. Composites Science and Technology; 70: 1934-1941. 2010.
[44] Dunne F, Petrinic N. *Introduction to Computational Plasticity*. In: Department of Engineering Science OU, editor.: Oxford University Press. 2004.
[45] de Souza Neto EA, Peric D, Owen DRJ. *Computational methods for plasticity*: Wiley. 2008.
[46] Raghava R, Caddell RM. *The macroscopic yield behavior of polymers*. Journal of Materials Science; 8: 225-232. 1973.
[47] Mascarenhas WN, Ahrens CH, Ogliari A. *Design criteria and safety factors for plastic components design*. Materials & Design; 25: 257-261. 2004.
[48] Ghorbel E. *A viscoplastic constitutive model for polymeric materials*. International Journal of Plasticity; 24: 2032-2058. 2008.
[49] Tschoegl NW. *Failure surfaces in principal stress space*. Journal of Polymer Science Part C; 32: 239–267. 1971.
[50] Melro AR. *Analytical and numerical modelling of damage and fracture of advanced composites*. Porto: University of Porto. Faculdade de Engenharia. 2011.

[51] Rolfes R, Ernst G, Vogler M, Hühne C. *Material and Failure Models for Textile Composites*. In: CIMNE, editor. Mechanical Response of Composites: Springer. p. 39. 2008.

[52] Haufe A, Du Bois PA, Kolling S, Feucht M. *A semi-analytical model for polymers subjected to high strain rates*. 5th European LS-DYNA Users Conference. Birmingham, UK. 2005.

[53] Guild FJ, Potter KD, Heinrich J, Adams RD, Winsom MR. *Understanding and control of adhesive crack propagation in bonded joints between carbon fibre composite adherends II. Finite element analysis*. International Journal of Adhesion and Adhesives; 21: 445-453. 2001.

# Chapter 4

# EXPERIMENTAL INVESTIGATION ON THE GEOMETRIC VARIABILITIES OF THE REINFORCEMENT AND ON THE RELATION BETWEEN THE INTERNAL GEOMETRY AND THE MATERIAL MECHANICS

*This chapter presents high-resolution microscopic analyses of the laminate edge in search for the geometric variabilities within the reinforcement structure, and for their relation with the material mechanics. The first section outlines the scope of the investigations. In the second section, the technique that was used to capture the laminate edge on high resolution microscopic images with a large field-of-view is presented. The third section concerns the geometrical variabilities of the reinforcement architecture. An analysis of the strain fields on the laminate edge is performed in the fourth section, and the observed damage on the laminate edge is presented in the fifth section. In the sixth and last section, the conclusions of this chapter are presented.*

## 4.1 SCOPE AND INTRODUCTION

In the previous chapter, the stainless steel 4-harness reinforcement fabric and the corresponding composite laminates were approached as having a periodic internal structure. This abstraction can be a powerful asset when analyzing complex materials with repetitive characteristics, as it brings the problem size down to one representative volume element (RVE). Naturally, one can expect that any deviations from the ideal periodicity will reflect on the accuracy of an RVE analysis. Therefore, it is important to define the geometrical variabilities, and to assess their impact on the material mechanics.

**On the laminate level**, not all reinforcement layers are equivalent. The number of layers in the laminate and their position within the stack will determine the support and the restrictions they receive from surrounding layers. In their study of carbon fiber 5-harness satin weave composites, Daggumati et al. [1] found a difference in the damage behavior between the inner plies and the surface plies of eight-layer laminates. Tensile cracks were observed microscopically in the inner plies starting at a strain of 0.2%, while the surface plies remained undamaged until a strain of 0.6%. Other geometrical aspects on the laminate level are ply shifting and nesting. The textile layers in a laminate are generally not stacked on corresponding horizontal positions, and the shift between plies will determine their boundary conditions. Furthermore, the peaks and valleys in the profiles of neighboring shifted layers will not correspond, and the layers will sink into each other. This phenomenon is known as nesting. Several parameters have been used to quantify nesting. Yurgartis and Morey [2] introduced the term ‘angle match’, i.e. the absolute value of the difference between inclination angles of adjacent yarns, to characterize the nesting in a carbon-carbon composite with plain weave reinforcement. Olave et al. [3] quantified nesting in terms of the thickness reduction it causes. Two types of carbon fiber twill 2/2 weave composite laminates were studied, one with 3K yarns and one with 12K yarns. The architecture with the larger 12K yarns proved more susceptible to layer nesting than the 3K version. Further investigations by these authors on the effects of nesting and ply shifting on the inter-laminar fracture toughness indicated that nesting contributes to the mode I fracture toughness in the 12K laminates, but not in the 3K laminates [4]. The mode II fracture toughness seemed unaffected by the nesting value in either of the laminates [5].

The geometrical characteristics **on the yarn level** include the cross-sectional aspects and the aspects of the yarn path. As is the case for the phenomenon of nesting, there is little uniformity in the terminology and the parameters that are being used to study the yarn geometry. Yurgartis and Morey [2] studied the yarn path in terms of inclination angle and crimp angle. Olave et al. [3] analyzed the cross section of the yarns in terms of width, thickness and total area. The total area is an especially

important characteristic, as it directly relates to the fiber volume fraction of the yarn. The cross-sectional parameters differ from yarn to yarn, but they also vary along the yarn path. Other parameters studied by Olave and coworkers were the yarn crimp, the misalignment of the yarns and the spacing between yarns. Similar analyses have been performed by Karahan et al. [6] on the internal geometry of a carbon fiber composite reinforced with non-crimp 3D orthogonal woven fabric. In all of the investigations just mentioned, the yarn geometry was studied on microscopic images of the edge of a laminate. A three-dimensional view on the reinforcement geometry can be obtained through X-ray micro-computed tomography. Bale et al. [7] used micro-CT data of ceramic-matrix textile composites to decompose the spatial variations of yarn characteristics into non-stochastic periodic trends and non-periodic stochastic fluctuations. This procedure was later termed the 'reference period collation' method, and it was used by Vanaerschot et al. [8] to investigate the internal geometry of a seven-ply 2/2 twill woven carbon-epoxy composite. The yarn characteristics analyzed consisted of the coordinates of the centroid, the area, the aspect ratio, and the orientation of the cross-section. It was observed that the yarn characteristics correlate most strongly with the cross-over points within a ply, while the differences between plies proved to be minor.

**On the fiber level**, a source of variability is in the distribution of the fibers within the yarns. Intra-yarn variations in the fiber volume fractions make for inhomogeneities in the stiffness and strength properties within the yarns, and one can expect that the distribution of these properties will reflect on the mechanical behavior – especially the damage behavior. Karahan et al. [6] performed fiber counts on rectangular details within the yarns to calculate the local fiber volume fractions. The selected details all had the same area, but the number of fibers within them ranged from 257 to 329, corresponding to a fiber volume fraction ranging from 58% to 74%. Using a similar method, Olave et al. [3] found local fiber densities between 20% and 70%, with the lowest values typically located on the yarn boundaries.

In this chapter, the geometrical variabilities within the steel fiber fabric reinforced four-layer laminates are quantified, and the relationships between the reinforcement geometry and the strain and damage phenomena are analyzed. In section 2, the 3D image stitching technique that was used to capture the laminate edges will be explained. Then, the resulting high-resolution images will be used as input for analyses on geometric characteristics in section 3. The results on the laminate level will be presented first, followed by those on the yarn paths and on the yarn cross sections. Finally, the intra-yarn inhomogeneity in fiber volume fraction will be discussed. In a pursuit to automate the processing of the images and the parameter calculations as much as possible, some new methodologies were developed. These will be presented in the course of the third section, along with the results. The fourth section presents the strain fields obtained from experiments using the digital image

correlation technique on the laminate edge. Special attention is paid to how the reinforcement geometry affects the strain distribution. In the fifth section, two methods will be discussed to capture the initiation, the propagation, and the morphology of damage on the laminate edge, and the relation between the damage morphology and the reinforcement architecture will be analyzed. The chapter is finally closed with some conclusions.

## 4.2 THE 3D MICROSCOPIC IMAGE STITCHING TECHNIQUE

The edge of a laminate holds a lot of information about the internal geometry of the composite. When the laminate is cut along the warp yarns, its edge shows the undulations of the warp yarns and the cross sections of the weft yarns (Figure 4-1.a), and when it is cut along the weft yarns, the undulations of the weft yarns and the cross sections of the warp yarns can be studied (Figure 4-1.b). From here on, a yarn that runs along the polished edge will be referred to as 'longitudinal', and one that is perpendicular to the polished edge as 'transversal', regardless whether it concerns a warp yarn or a weft yarn.

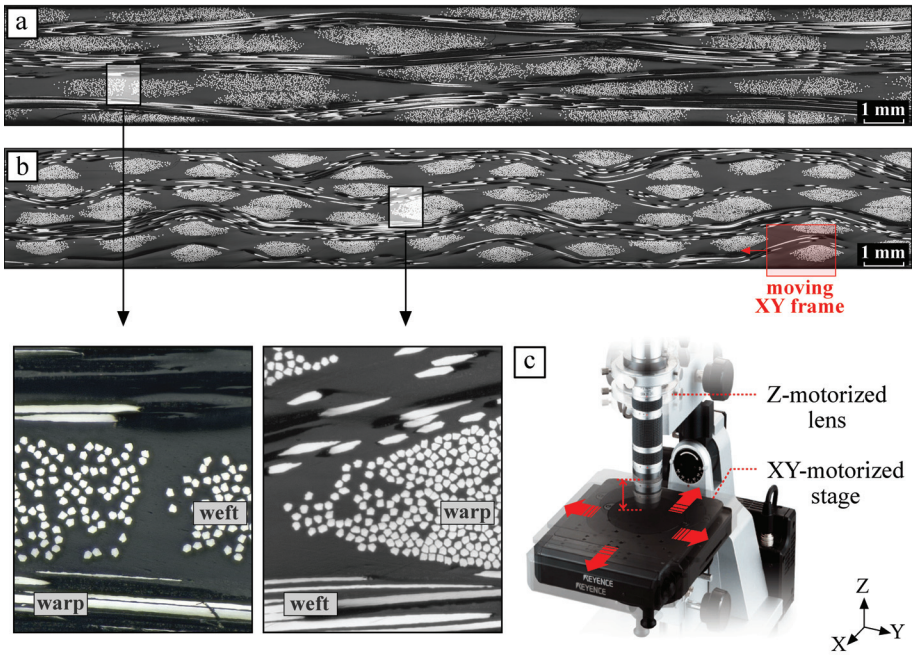


Figure 4-1: Specimen edge along the warp yarns (a), specimen edge along the weft yarns (b), and the 3D motorized control of the Keyence VHX-2000 microscope

The images in Figure 4-1.a-b were taken with a Keyence VHX-2000 microscope (Figure 4-1.c) through 3D image stitching. This microscope has an XY-motorized stage, as well as a Z-motorized autofocusing lens. When a specimen is put on the stage of the microscope, the region under the lens is scanned along the Z-direction with a chosen step size and within a chosen range, and the lens is autofocused on every step. This ensures focused images over a nearly unlimited depth-of-field. An image taken this way is 1600 by 1200 pixels. In order to achieve a larger field of view, the motorized stage can move the specimen to an adjacent XY position, where it is again scanned in the Z-direction. This process can be repeated on every XY position within an area of interest up to 40 mm by 40 mm. When the whole specimen is scanned, the separate images are stitched together by the machine's software, up to an image size of 20000 by 20000 pixels. The images are taken at a resolution of 461 pixels per mm when a magnification of 100x is applied, and proportionally, 691.5 or 922 pixels per mm for a magnification of 150x or 200x, respectively. This means that a steel fiber with an equivalent diameter of 30 μm is covered by 338 pixels at a magnification of 150x. This is a sufficient resolution to study geometrical features on the intra-yarn level.

## 4.3 MICROSCOPIC STUDIES ON THE GEOMETRICAL CHARACTERISTICS OF THE REINFORCEMENT

The microscopic analyses presented in this chapter are performed on the specimens shown in Figure 4-1.a-b. These specimens were first grinded with SiC foils with a grit size starting at 320, and up to 4000, in order to make the surface sufficiently flat for microscopy. Then, they were polished with diamond abrasive with a grain size of 3 μm, and finally, 1 μm. Images were taken at a magnification of x150, hence at 691.5 pixels per mm, over a length of 48 mm along the laminate edge. This means that the analyses of the warp undulations and the weft cross sections (Figure 4-1.a) were performed over a length of almost 3 unit cells, and on 40 full weft yarns, respectively. The analyses of the weft undulations and the warp cross sections (Figure 4-1.b) were performed over a length of more than 6 unit cells, and on 104 full warp yarns, respectively. Note that Figure 4-1.a and Figure 4-1.b only represent a part of the total image (about 22 mm). For visibility reasons, microscopic procedures and results will most often be shown on a sample of the full images. However, all analyses were performed on the full version.

### 4.3.1 Ply shifts and layer nesting

Layer nesting in textile composites originates during the laminate production process. Textiles have profiled surfaces, and the layer positions usually show some shifting when they are stacked in a mold. This makes every layer sink into the valleys of its neighbors. When the mold is closed, the closing pressure further compacts the stack. This compression merely deforms the yarns, without changing their relative positions [9, 10]. The layer nesting is therefore mostly defined by the relative positions of the layers in the stack – the ply shifts, and by the architecture of the fabric. This should be the case for the steel fiber/epoxy laminates as well, as closing the mold on the four-layer stack of fabric does not require a lot of pressure.

Figure 4-2 illustrates the influence of the ply shifts on the layer nesting. In an unshifted stack (Figure 4-2.a), the valleys and peaks in the profiles of neighboring layers coincide, which prevents them from nesting. When the plies are shifted (Figure 4-2.b), the space in between yarns can be taken in by yarns of a neighboring layer.

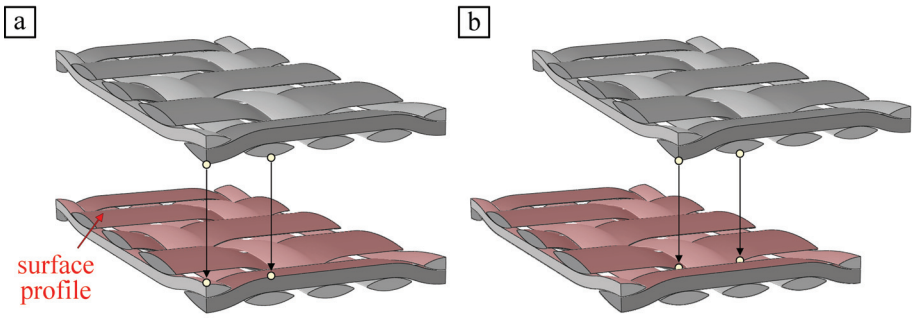


Figure 4-2: Influence of the layer shifts on the geometric nesting of a symmetrical 4-harness satin weave: nesting is prevented if peaks and valleys in the profiles of neighboring plies coincide (a), layers nest if plies are shifted (b)

Nesting can be assessed from a theoretical point of view by defining the surface profiles of the unit cell of the textile layers (Figure 4-2) and seeking for the smallest inter-layer distance that does not cause any overlap between yarns [11-13]. Parameter studies using this strategy revealed some relationships between the characteristics of the fabric architecture and the tendency for nesting:

- Looseness of the fabric promotes nesting, because it makes for larger inter-yarn gaps [11]. This is certainly the case for the steel fiber reinforcement, as the sum of the yarn widths takes only about 80% of the unit cell dimensions. In comparison, the carbon fiber 2/2 twill weave that was analyzed for nesting by Olave et al. [3] has virtually no gaps in between yarns. Furthermore, the looser the fabric, the more pliable the layers are, hence the more they comply to their surroundings.

- Nesting is hindered when the textile has long floats, because this leaves fewer valleys on the textile surface [11]. This is the case for a 4-harness satin weave.
- The tendency for nesting only slightly depends on the yarn shape – provided that the yarns are considered incompressible [11], but it increases considerably with yarn size [3]. Despite the substantially lower fiber count, the steel fiber warp yarns are larger than the 'small' 3K carbon fiber yarns mentioned in the study by Olave et al. [3] (0.40 mm², compared to 0.19 mm²), while the weft yarns are even larger than the 'large' 12K carbon fiber yarns (1.07 mm², compared to 0.80 mm²).

In conclusion, the looseness of the steel fiber fabric and the substantial yarn sizes promote layer nesting, while the long floats counteract.

A 2D visualization of the ply shifts and the layer nesting in the symmetrical four-layer steel fiber 4-harness satin weave laminates is shown on Figure 4-3.a and Figure 4-3.b, on cross sections parallel to the warp and weft yarns, respectively. The transversal yarns of the separate layers are colored for clarity, and the crimp yarns in every layer are marked with a 'C'. The nesting is most clear on the edge in Figure 4-3.a, where the crimp yarns from the inner layers lie next to each other, on apparently the same height. Despite the ply shifts and the layer nesting, the laminate edge still shows periodicity to some extent. This is best seen on Figure 4-3.b, because the fabric unit cell is smallest along the weft direction.

Layer nesting is often quantified by means of the thickness reduction it causes [11, 12]. Olave et al. [3] proposed the following definition for the nesting percentage $N_e$:

$$N_e = \frac{n \cdot t_{nom}}{t} \tag{4-1}$$

In this definition, n is the number of layers, $t_{nom}$ is the nominal thickness of the textile, and t is the laminate thickness. The stainless steel 4-harness satin weave has a nominal thickness of 0.8 mm, hence the nesting percentage of a four-layer laminate with a thickness of 3 mm equals 106,7%. This value holds a direct indication of the effect of the nesting on the fiber volume fraction. In this case, it means that the fiber volume fraction of the real, nested four-layer laminate is 6.7% higher than that of a hypothetical, unnested laminate.

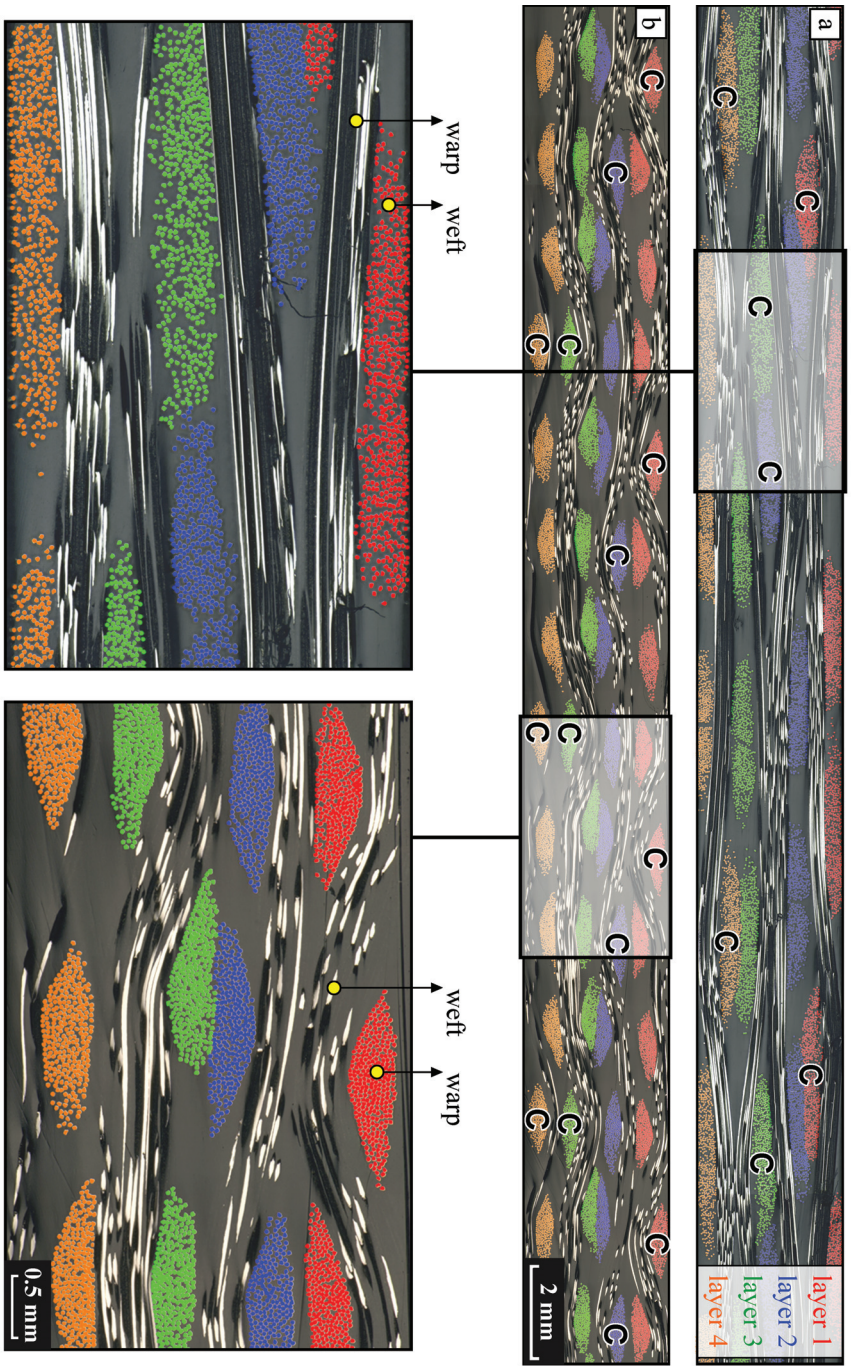


Figure 4-3: Layer nesting in the four-layer laminates on a cross section parallel to the warp yarns (a) and on a cross section parallel to the weft yarns (b)

### 4.3.2 Yarn undulations

The undulations of a yarn can be analyzed on an edge of a laminate which is cut parallel to this yarn. In that case, the yarn under investigation is a longitudinal yarn on the microscopic images. The undulations of the warp yarns are investigated on Figure 4-4.a, and those of the weft yarns on Figure 4-4.b.

A crucial first step into interpreting the undulations is to define the geometry of the longitudinal yarns on the microscopic images. Only the longitudinal fibers that run along the polished cut are visible, and as a result, the definition of the yarn borders is not always unbiased. This is especially the case for the weft yarns, because of their low fiber volume fraction. This issue inhibits automatic border detection, and therefore, the yarn borders were drawn manually as spline entities. Most parts of the borders are clear, especially where they run along the specimen surface or along a transversal yarn. Over those stretches where the border definition is not obvious, the border was continued as parallel to the local fiber direction as possible. As is clear on Figure 4-4.b, the bottom fabric layer in the stack was cut on the very edge of the longitudinal weft yarn. In this case, there are not enough clear reference points to define the geometry of the yarn, and therefore, it was not considered for any analyses. The next step into analyzing the undulations is to define the yarn centerline. This operation was performed by reading an image file containing the yarn borders, and calculating the pixel positions of the points on the centerline $(x, y)$ through Python programming.

Yarn undulations are often analyzed in terms of the inclination angle $\theta_i$, i.e. the angle between the tangent of the centerline and the mean yarn direction, as shown in Figure 4-5.c. In order to determine this angle, a least squares linear regression fit was made for every point $(x, y)$ on the centerline. The inclination angle in point $(x, y)$ can then be found as the angle of the linear regression fit, which can be expressed in terms of the variance and covariance of the surrounding data points:

$$\theta_i(x, y) = \frac{\mathrm{Cov}(x, y)}{\mathrm{Var}(x)} \tag{4-2}$$

The amount of surrounding data points – or the distance over which the inclination angle is calculated – must be large enough to rule out noise, yet sufficiently small to capture the global changes in the yarn direction. With this in mind, a range of 0.5 mm along the length of the specimen was chosen. The microscopic images had a length of 48 mm, and they were processed at a resolution of 345.75 pixels per mm. Therefore, one centerline consists of about 16500 pixel points. As the inclination angle was calculated in every point along the 4 warp yarns in Figure 4-4.a, about 66000 values were obtained. Similarly, about 49500 inclination angles were calculated for the three weft yarns in Figure 4-4.b.

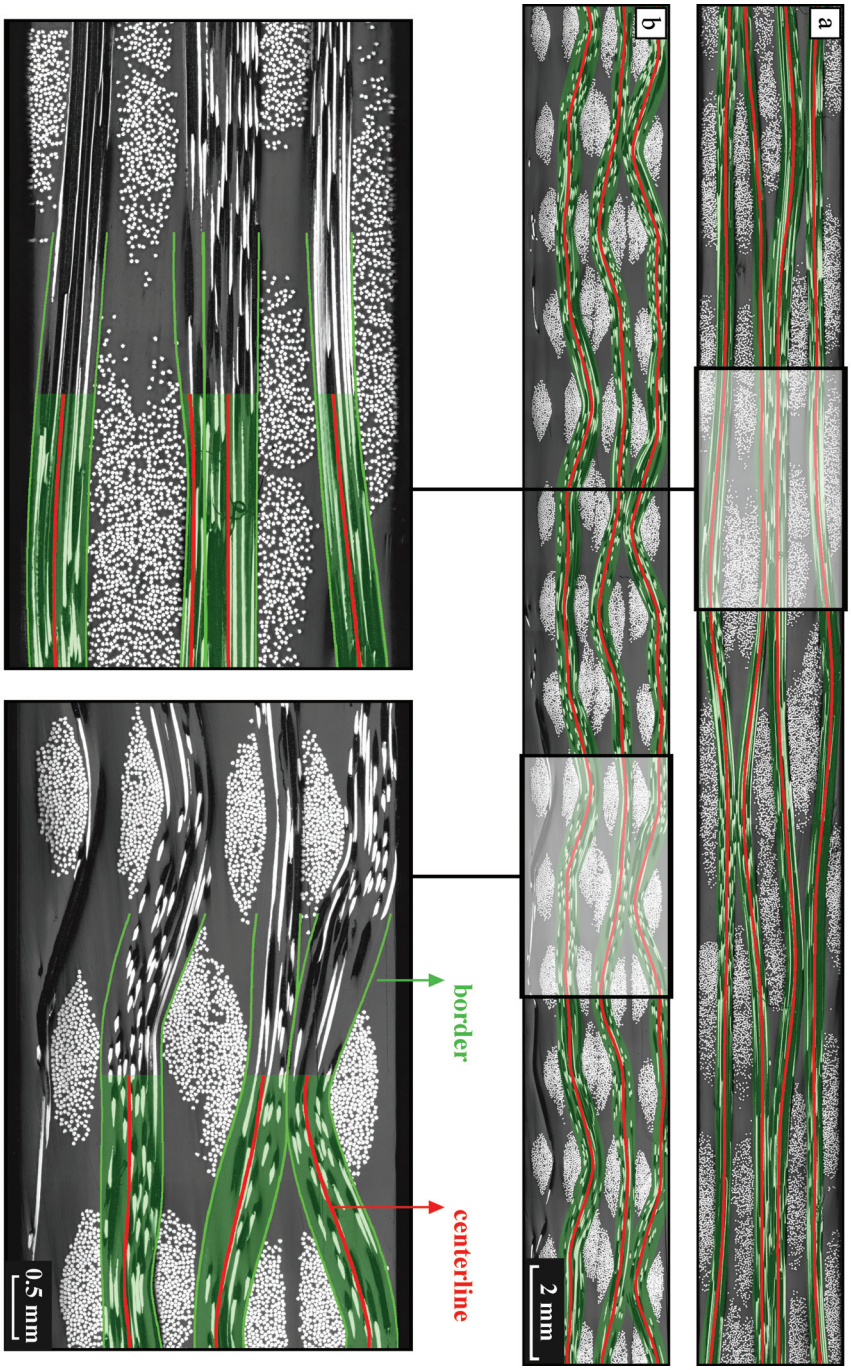


Figure 4-4: Undulations of the warp yarns (a) and the weft yarns (b)

The inclination angles were sorted into bins with a width of one degree in order to visualize their relative distributions, as shown in Figure 4-5.a and Figure 4-5.b for the warp and weft yarns, respectively.

When the inclination angles are known, the angle with the largest absolute value can be withdrawn on every upward and downward slope of the crimp area. This angle is known as the crimp angle $\theta_c$, as illustrated in Figure 4-5.c. The relative distribution of the crimp angles is shown in Figure 4-5.d for both warp and weft yarns.

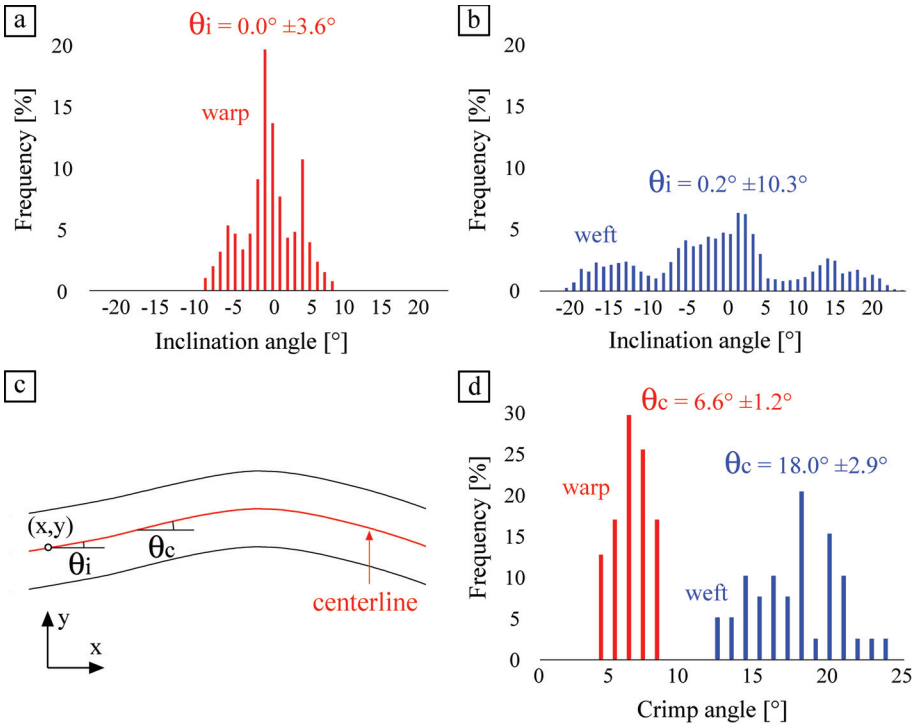


Figure 4-5: Distribution of the inclination angle for the warp yarns (a) and for the weft yarns (b), definition of the inclination angle and the crimp angle (c), and distribution of the crimp angle in warp and weft yarns (d)

The average value for the inclination angle is about zero for both warp and weft yarns. This value is a measure for the mean direction of the yarns, so a large aberration from zero would indicate a misalignment of the input images. The inclination angle distribution is much more narrow in the warp yarns, which indicates that the warp yarns are much straighter than the weft yarns. The distributions of the inclination angles are more or less symmetrical, with a central peak near 0° and secondary peaks on both sides. A central peak in the distribution is typical for a satin weave, because it corresponds to the long floats in between crimp regions. In a plain weave, for instance, the yarns roughly follow a sinusoidal path in going over and under every

yarn they cross. In this weave, the yarns only get parallel to their mean direction at the peaks and valleys of the sine waves they describe, which results in a local minimum at 0° in the inclination angle distributions [2]. The secondary peaks in the distribution plots correspond to the crimp angle. For the warp yarns, an average crimp angle of 6.6° was found, with a standard deviation of 1.2°. As expected, the crimp angle is much larger in the weft yarns, with an average value of 18.0° and a standard deviation of 2.9°. A separate analysis on the yarns in the inner and outer layers of the laminate revealed that the position of the yarn within the laminate does not significantly affect its path. The angle distribution plots for the inner and outer layers separately look very similar as the ones representing all four layers in Figure 4-5.a-b. The difference in crimp angle is negligible as well, with values of 6.7° ± 1.2° and 6.5° ± 1.3° for the warp yarns in the inner and outer layers, and 17.3° ± 2.9° and 18.8° ± 3.9° for the weft yarns in the inner and outer layers, respectively.

### 4.3.3 Yarn cross sections

The cross section of a yarn can be analyzed on an edge of a laminate which is cut perpendicular to this yarn. In that case, the yarns under investigation are the transversal yarns on the microscopic images. The cross sections of the warp yarns are thus analyzed on Figure 4-6.a, and those of the weft yarns on Figure 4-6.b.

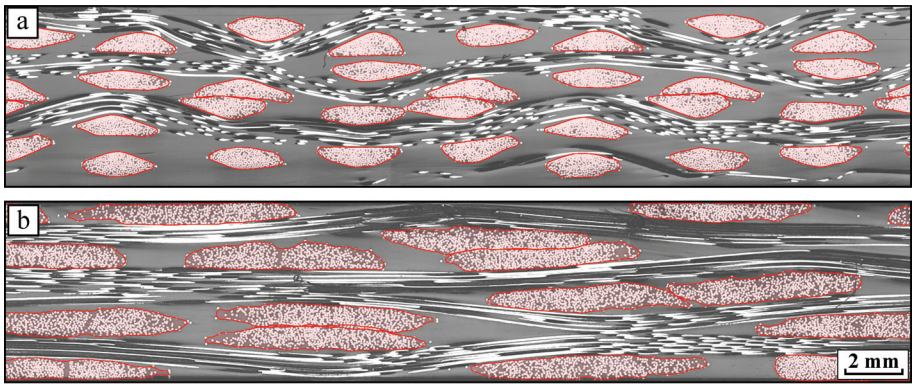


Figure 4-6: Cross sections of the warp yarns (a) and the weft yarns (b)

In order to analyze the cross sections of the yarns, the outlines must first be determined. This was achieved via a semi-automatic selection procedure in Photoshop, as illustrated step by step in Figure 4-7 for the case of the warp yarns.

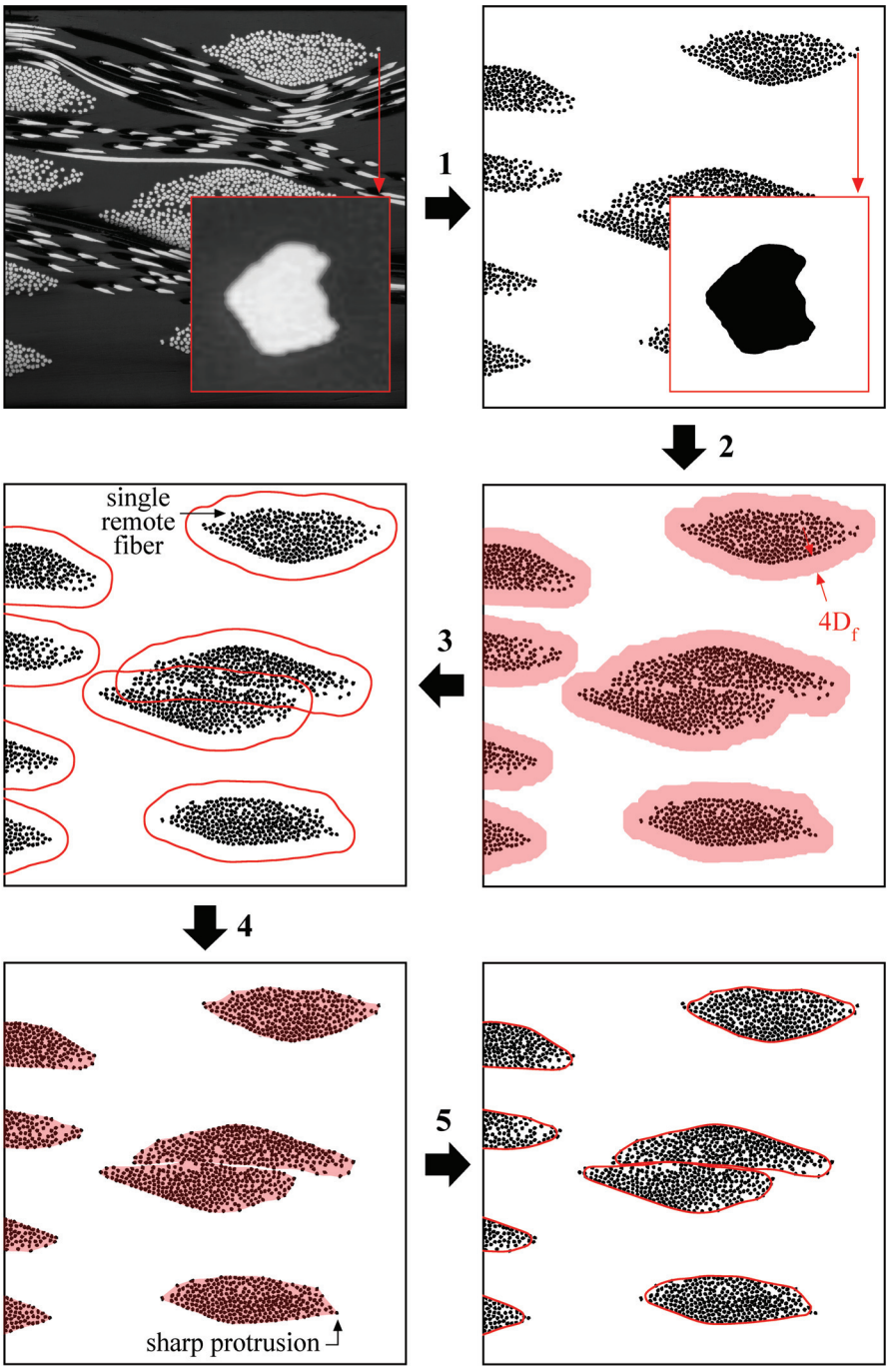


Figure 4-7: Procedure steps for detection of the yarn cross sections

In the first step, the separate warp fibers are abstracted from the microscopic image. The outlines of the fibers are not perfectly sharp, because the shiny steel fiber heads reflect the light, causing them to glow. In order to determine the fiber outlines in a consistent manner, the fibers are selected based on pixel brightness. The threshold is chosen so that the number of pixels in the selection matches the calculated warp fiber area. For instance, one warp yarn consists of 275 fibers, each with an equivalent diameter of 30 µm. This comes down to a total fiber area of 194386 µm² per warp yarn. The microscopic images have a resolution of 691.5 pixels per mm, or 478172.25 pixels per mm². Therefore, one warp yarn should hold 92950 pixels. In the second step, all the fibers are expanded to make them overlap each other, so that their individual borders disappear. This way, the individual fibers are morphed into yarn entities. On the one hand, the fiber expansion must be extensive enough to overcome the largest inter-fiber distances within the yarns, hence to avoid inclusions within the yarn entities. On the other hand, the more extensive the fiber expansion, the more detail is lost on the yarn outline. An expansion over four fiber diameters was found to be a good compromise for this operation. The third step is to smoothen the outlines of the yarn entities. The purpose of this operation is to round off the humps due to single remote fibers, hence to limit their influence on the final yarn shape. A smoothing radius of two fiber diameters was chosen for this operation. The yarn entities are too large at this point. The correct yarn shape is obtained in the fourth step, by contracting the yarn borders over four fiber diameters. The fifth step finalizes the yarn shape by again smoothing the border over two fiber diameters. This operation removes sharp protrusions and it smoothens the final outlines. The cross sections of warp and weft yarns that result from this operation can be seen on Figure 4-6.a and Figure 4-6.b, respectively.

Once the outlines of the cross sections are defined, the geometrical characteristics can be deduced. The sectional area A of a yarn was calculated through the number of pixel points in the yarn. The width w and thickness t of a yarn were calculated from the extreme pixel points with respect to the principal axes of rotation U and V of the yarn, as illustrated in Figure 4-8. The origin of this system is the center of gravity $(u_G, v_G)$ of the yarn:

$$(u_G, v_G) = \left(\frac{\sum_i x_i}{A}, \frac{\sum_i y_i}{A}\right) \tag{4-3}$$

In this, $(x_i, y_i)$ are the coordinates of pixel point i with respect to the global axes X and Y. The principal axes of rotation are the axes amongst which the product of inertia is zero. The angle between the principal axes of rotation and the global axes can hence be found by solving the eigenvalue problem on the moment of inertia tensor:

$$\begin{bmatrix} I_{xx} - \lambda & I_{xy} \\ I_{xy} & I_{yy} - \lambda \end{bmatrix} \begin{bmatrix} \cos(\alpha) \\ \sin(\alpha) \end{bmatrix} = \begin{bmatrix} 0 \\ 0 \end{bmatrix} \tag{4-4}$$

The angle α can now be expressed as a function of the moments of inertia $I_{xx}$ and $I_{yy}$ and the product of inertia $I_{xy}$ by eliminating the eigenvalue λ from the system of equations:

$$\alpha = \frac{1}{2} \operatorname{atan}\left(\frac{2I_{xy}}{I_{xx} - I_{yy}}\right) \tag{4-5}$$

The yarn dimensions w and t were found by transforming all pixel coordinates from the $(x, y)$ to the $(u, v)$ axes system and looking for the pixels that define the bounding box. Finally, the yarn shapes were characterized by their shape factor S, i.e. the ratio between width and thickness.

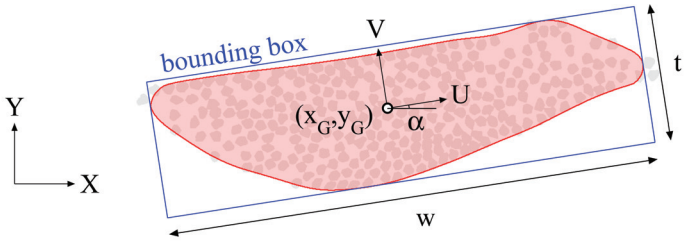


Figure 4-8: Calculation of the yarn dimensions L and H

The calculations of the yarn dimensions w and t, the shape factor S, and the sectional area A were automated through Python programming. The results are listed in Table 4-1, along with the corresponding characteristics as obtained from measurements on micro-CT data of a laminate slice, which were discussed in section 2.4.1.

The yarn widths as calculated from the microscopic images are lower than the values obtained from the micro-CT measurements. The reason is that the calculations on the microscopic images were performed on yarn contours that were determined via the semi-automatic procedure as discussed earlier in this section. These contours do not necessarily contain all the fibers, especially on the edges of the yarns. The width measurements on the micro-CT data, on the other hand, were made between the outer edges of the outermost fibers. The yarn thickness values do comport, because the semi-automatically selected contours do more or less follow the extreme edges of the uppermost and lowermost fibers in the yarns. Consistent with the smaller width, yet similar thickness values, the shape factors obtained from the microscopic analyses are smaller than the ones calculated from the micro-CT measurements. Finally, the sectional area of the warp yarns obtained from microscopic analysis is smaller than the cross section of the idealized lenticular yarn with dimensions as measured on the

micro-CT data. This is again in line with the smaller width value. The sectional area of the weft yarns, on the other hand, is a little larger according to microscopic measurements. This is due to the fact that the real weft yarns have a central region over which the thickness is more or less constant, while the idealization is perfectly lenticular.

Table 4-1: Geometrical characteristics of the yarn cross sections

| | | **Warp yarns** | **Weft yarns** |
|---|---|---|---|
| **Characteristic** | **Obtained from** | | |
| Sectional area A [mm²] | microscopy | 0.36 ± 0.02 | 1.10 ± 0.13 |
| | *micro-CT* | 0.40 | 1.07 |
| Yarn width w [mm] | microscopy | 1.39 ± 0.10 | 3.35 ± 0.29 |
| | *micro-CT* | *1.51 ± 0.12* | *3.58 ± 0.39* |
| Yarn thickness t [mm] | microscopy | 0.37 ± 0.03 | 0.43 ± 0.05 |
| | *micro-CT* | *0.38 ± 0.05* | *0.43 ± 0.06* |
| Shape factor S [-] | microscopy | 3.83 ± 0.51 | 7.91 ± 1.18 |
| | *micro-CT* | *4.07 ± 0.69* | *8.60 ± 1.66* |

The yarn cross section can be expected to vary along the yarn path, and one would expect a certain relationship between the position of the cross section within the textile architecture and its characteristics. Figure 4-9 illustrates the distribution of the sectional area A and the shape factor S on a part of the analyzed specimens. Analysis of Figure 4-9.a reveals no significant pattern in the sectional area of the warp yarns. There is, for instance, no difference between the yarns in the inner and outer layers of the laminate. When it comes to the shape of the warp yarns, however, some trends can be observed. The crimp yarns at the specimen surface (blue arrows), for instance, typically have a low shape factor. The other warp yarns in the outer laminate layers as well are rather compact in shape, with an average shape factor of 3.54. The higher shape factors are concentrated in the innermost layers of the laminate, with an average of 4.11. The weft yarns on Figure 4-9.b show no significant relationship between position and cross section characteristics. Nor the area, nor the shape factor differs significantly between inner and outer layers, and no specific position shows consistently high or low values for either parameter.

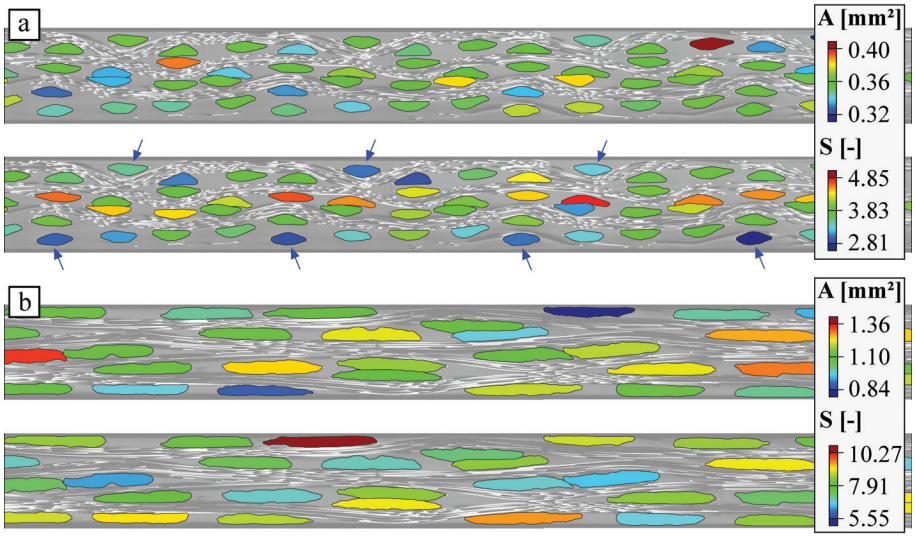


Figure 4-9: Distribution of the cross sectional area A and the shape factor S of the warp yarns (a) and the weft yarns (b)

### 4.3.4 Variability in inter-yarn fiber volume fraction

Because of the inter-yarn differences in sectional area, their fiber volume fractions differ as well. All warp yarns have 275 fibers, but – as discussed in the previous section – they differ in sectional area. As a result, their fiber volume fractions differ as well. Similarly, there is a variability in the sectional area of the weft yarns, but they invariably consist of 550 fibers. Knowing that the steel fibers have an equivalent radius of 15 µm, the fiber volume fraction of yarn i can be calculated by dividing the total area of the steel fibers within the yarn by the sectional area of yarn i:

$$V_{f,i}^{warp} = \frac{275 \cdot (0.015\text{mm})^2 \cdot \pi}{A_i^{warp}} = \frac{0.194386\ \text{mm}^2}{A_i^{warp}}$$
$$V_{f,i}^{warp} = \frac{550 \cdot (0.015\text{mm})^2 \cdot \pi}{A_i^{weft}} = \frac{0.388772\ \text{mm}^2}{A_i^{weft}} \quad (4\text{-}6)$$

The inter-yarn variability in fiber volume fraction that results from these calculations is visualized in Figure 4-10.a for the warp yarns, and in Figure 4-10.b for the weft yarns.

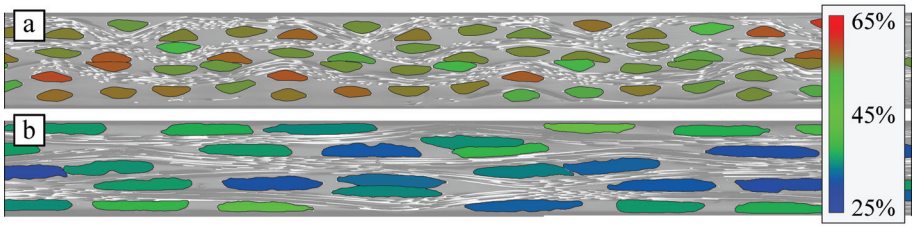


Figure 4-10: Inter-yarn variability in fiber volume fraction in the warp yarns (a) and in the weft yarns (b)

The fiber volume fraction within the warp yarns ranges between 44.1% and 60.8% over the 104 yarns under consideration, with an average of 54.6% and a standard deviation of 2.8%. The fiber volume fraction within the weft yarns ranges between 29.1% and 48.4% over the 40 yarns under study, with an average of 35.9% and a standard deviation of 4.4%. The main reason for the notable difference between warp and weft yarns is the fact that weft yarns are composed of two warp yarns. This halves the number of inter-yarn gaps, which opens up space for the weft yarns to spread wider. Furthermore, the warp yarns are less crimped than the weft yarns, and as a consequence, they do not have the same confining effect on the weft yarn cross section. Finally, the fact that the warp direction accounts for 52.7% of the fiber volume fraction (cf. section 2.4.2) even magnifies the difference.

### 4.3.5 Variability in intra-yarn fiber volume fraction

The fiber volume fraction not only varies from yarn to yarn, it is also inhomogeneous on the scale below, within the yarns. The variability in the intra-yarn fiber volume fraction was assessed via a fully automatic procedure, programmed in Python. The principles are illustrated in Figure 4-11.

First, two images were prepared and read from a file. The first image contains the yarn cross sections, solidly filled in red, green or blue. The outlines of these yarn cross sections were selected according to the procedure explained in section 4.3.3. The second image contains the separate fibers of these same yarns (Figure 4-11.a). The selection procedure for the fibers as well can be found in section 4.3.3. The cross section of a yarn and the corresponding fibers are given the same color, which can be red, green, or blue. The use of three colors allows the automatic procedure to easily distinguish between neighboring yarns, hence neighboring yarns are always assigned with different colors. In a second step, the images were covered with a virtual square grid, as shown in Figure 4-11.b. The calculation of the local fiber volume fraction is performed grid section by grid section. Therefore, the grid size determines the resolution of the calculation. As a compromise between keeping the calculation loops feasible on the one hand, and keeping enough resolution on the other hand, a grid size

of 5 pixels (or about 7 μm) was chosen. In what follows, the calculation of the fiber volume fraction will be illustrated for the special case of a grid section covering two different yarns, i.e. the $i^{th}$ grid section on Figure 4-11.b. In general, if the fiber volume fraction of the grid sections were calculated on the area covered by every grid section itself, most sections would lie either completely outside or completely inside a fiber. The corresponding fiber volume fractions would hence be either 0% or 100%. This is, of course, due to the fact that the grid size is chosen smaller than the fiber diameter. Increasing the grid size is not a proper solution, as this will drastically decrease the resolution. The problem of this method is thus that it inherently links the extent to which the inhomogeneity is taken into account to the resolution of the calculation. A better way is to perform the calculation on a circular region around the grid section under consideration, as shown on Figure 4-11.c. The radius of this region controls the extent to which the inhomogeneity is taken into account – it will be termed the smearing radius $R_s$ from now on – and it can be chosen independently from the grid size. For the demonstration on Figure 4-11, a smearing radius of 120 μm – or four times the fiber diameter $D_f$ – was used. In the next step, the smearing region around every grid section was scanned for fiber pixels and for yarn pixels. For most grid sections, only one color will be encountered in the smearing region. In those cases, the local fiber volume fraction can be calculated by dividing the number of fiber pixels by the number of yarn pixels in the smearing region, and this value can be assigned to the yarn region within the grid section. In the special case of grid section i on Figure 4-11, the same calculation is performed, only color by color. This way, two different fiber volume fractions are obtained – one for the 'blue' yarn, and one for the 'green' yarn (cf. Figure 4-11.d). The proposed procedure does not guarantee conservation of the total fiber volume fraction. Therefore, after processing the whole image, the new overall fiber volume fraction was compared to the original value and a small scaling (less than 1% for all results presented) was applied for all grid sections, in order to maintain the fiber content. As an example, the result of the procedure is shown on Figure 4-11.e for the two yarns that occur in the $i^{th}$ grid section. Three different smearing radii were considered, being 60 μm, 120 μm and 240 μm, or 2 $D_f$, 4 $D_f$, and 8 $D_f$, respectively. Even with the largest smearing radius, the fiber volume fraction ranges from 47% to 70% within the two yarns, with an average value of 58%. As the smearing radius is lowered to 120 μm, and finally, 60 μm, the range of the fiber volume fraction grows, and the distribution pattern becomes more uneven.

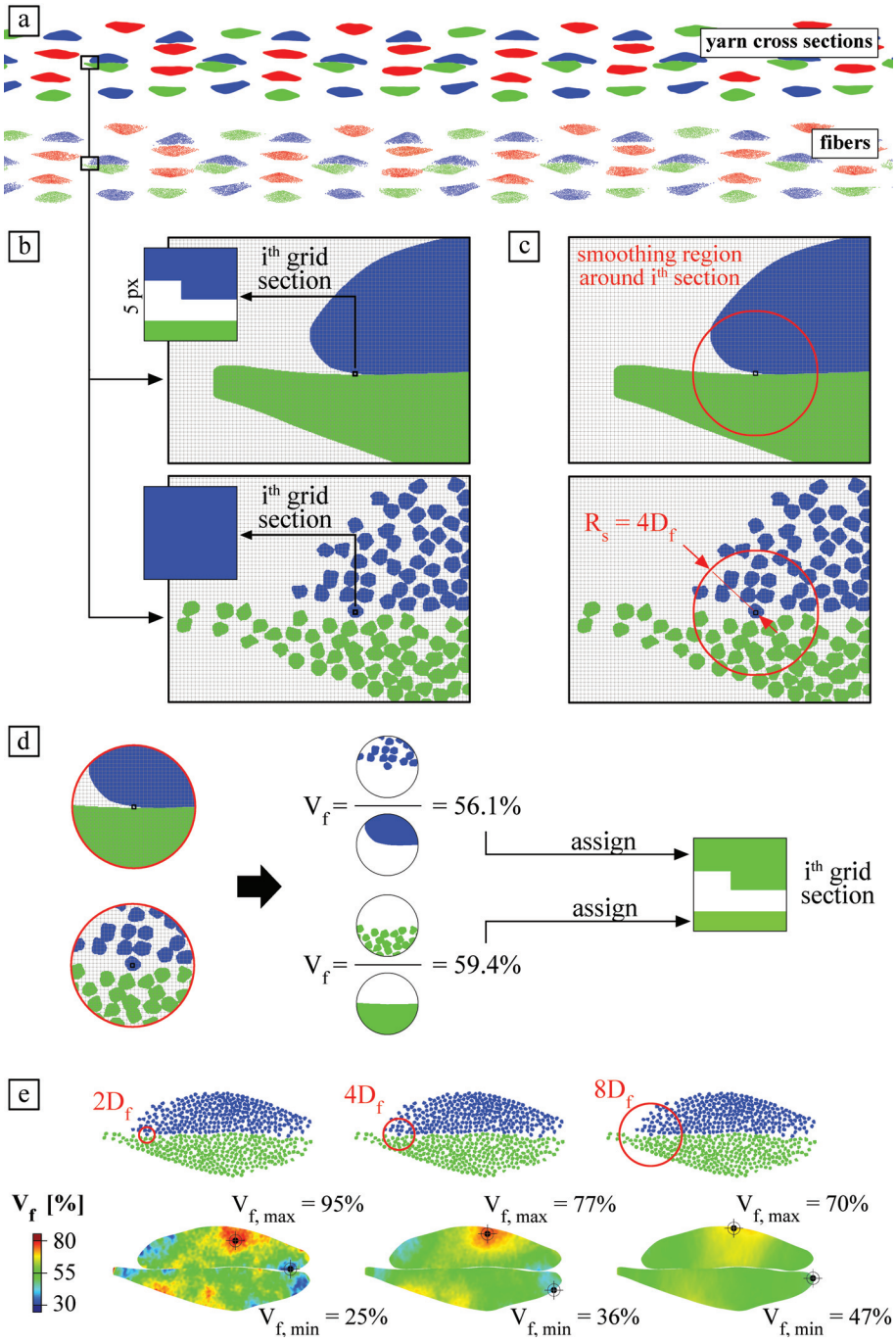


Figure 4-11: Procedure principles for automatic calculation of the intra-yarn distribution of the fiber volume fraction

A global view on the distribution of the fiber volume fraction in the warp yarns that results from the automatic procedure is shown on Figure 4-12. The fiber volume fraction ranges between 0% and 100% when a smoothing radius of $2D_f$ is used. A local value of 0% is found on one yarn of which the outline is in part determined by a single remote fiber. This location is pointed with a blue arrow on Figure 4-12. A local value of 100% is only attained at the very edges of some yarns, in those cases where the smoothing region covers only a small part of the yarn, but a lot of fiber pixels that fall outside the designated yarn outline. These locations are pointed with red arrows on Figure 4-12. The extremes are attenuated when the smoothing radius is raised to $4D_f$, with values ranging between 11% and 80%. The distribution is now less patchy, and more suitable to recognize the global patterns. Elevated fiber volume fractions are typically found at the contact zones with a longitudinal (weft) yarn – often in the crimp region of the longitudinal yarn. Low values are found on unconfined yarn edges. When the highest smoothing radius, $8D_f$, is used, the range in volume fractions further narrows to values between 24% and 72%. The average fiber volume fraction does not depend on the smoothing radius, hence it invariably amounts to 54.6%. The standard deviation decreases with increasing smoothing radius, from 11% for a smoothing radius of $2D_f$, over 8.3% for a smoothing radius of $4D_f$, to 6.1% for a smoothing radius of $8D_f$.

The distribution of the fiber volume fraction in the weft yarns is shown on Figure 4-13. When the smallest smoothing radius of $2D_f$ is applied, the fiber volume fraction varies between 0% and 79%. The locations with a 0% value are much more numerous than in the warp yarns. Many yarns have several voids, both on the edges and in the central region, and both on the outline and internal to the yarn. The voids are indicated for some yarns on Figure 4-13 with blue arrows. The highest values appear mostly in the central regions and often internal to the yarns. Some small local maxima are found on the yarn edges, but this phenomenon is far less important than in the warp yarns. These locations are pointed with red arrows on Figure 4-13. Similar as for the warp yarns, the distribution becomes much smoother when the smoothing radius is increased to $4D_f$, with values ranging between 1.5% and 68%. The strongest minima are clearly located on the unconfined yarn edges again. Additional minima can be found in the center region of some yarns that show a gap due to their double nature. Unlike the warp yarns, the weft yarns do not show a clear pattern when it comes to locations with a high fiber volume fraction. Increasing the smoothing radius to $8D_f$ does not bring more insight either. With this smoothing, a range of 11% to 60% is attained in the fiber volume fractions. The average fiber volume fraction in the weft yarns is 35.9%, and the standard deviation decreases from 11%, over 8.8%, to 7.3%, when the smoothing radius increases from $2D_f$, over $4D_f$, to $8D_f$.

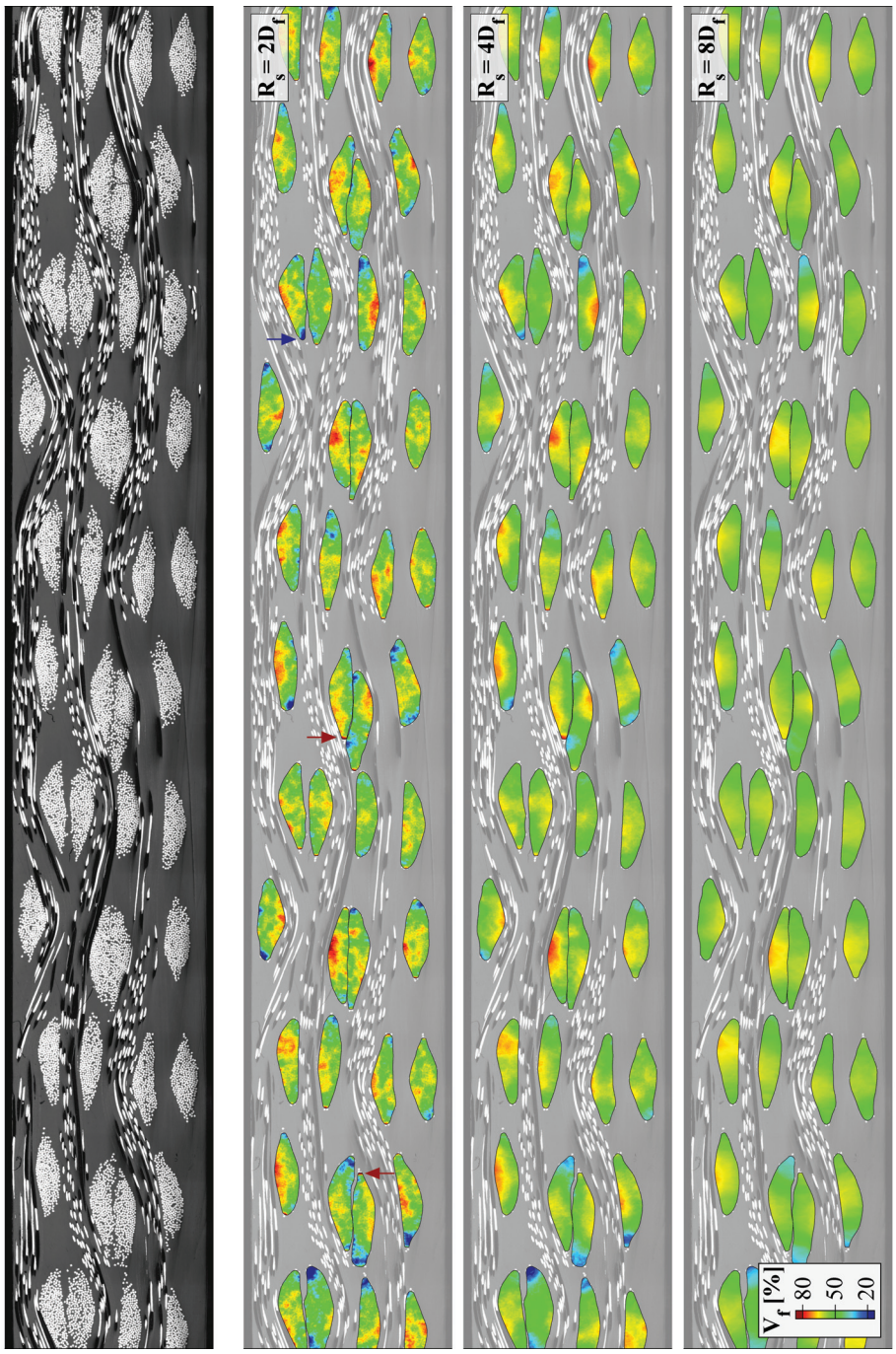


Figure 4-12: Distribution of the fiber volume fraction in the warp yarns, calculated with three different smoothing radii $R_s$ (expressed in terms of fiber diameter $D_f$)

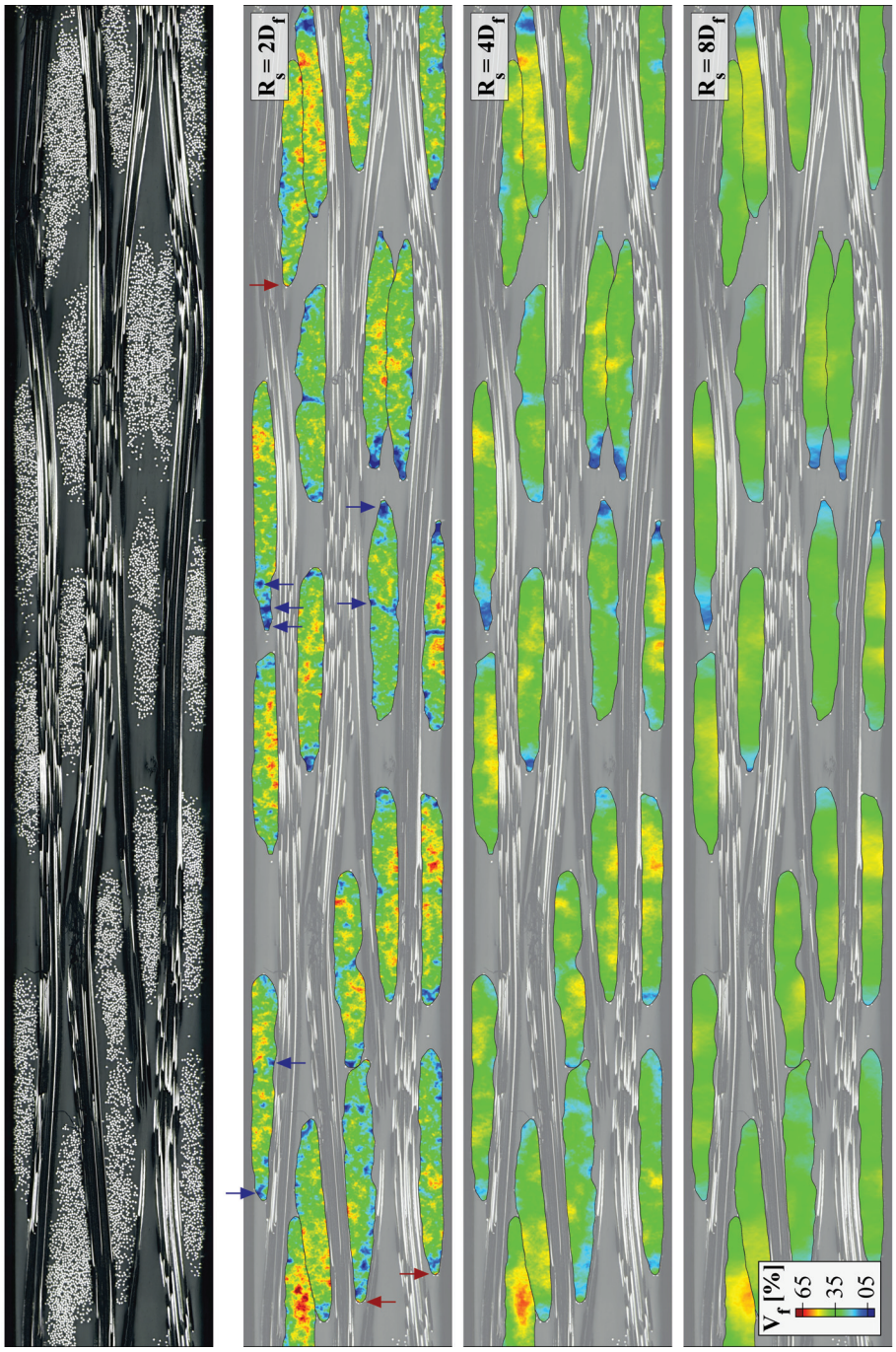


Figure 4-13: Distribution of the fiber volume fraction in the weft yarns, calculated with three different smoothing radii Rs (expressed in terms of fiber diameter Df)

### 4.3.6 Conclusion on the microscopic study of the reinforcement geometry and its variabilities

The microscopic analyses that were performed in this section made it clear that the fabric reinforcement shows strong variabilities on every length scale.

On the ply level, the ply shifts were found to cause severe nesting. Adjacent layers are sometimes sunken into each other so much that some of their yarns are on the same through-thickness coordinate. The nesting percentage was calculated at 106.7%, which means that the fiber volume fraction of the four-layer laminates is 6.7% higher than the value that would be found in an unnested laminate.

The variability on the yarn level was studied in terms of the crimp angle, the cross sectional area, the cross sectional shape, and the fiber volume fraction. For the warp yarns, an average crimp angle of 6.6° ± 1.2° was found, while in the weft yarns, a much larger value of 18.0° ± 2.9° was observed. For the cross sectional area, a value of 0.36 mm² ± 0.02 mm² was found in the warp yarns, and 1.10 mm² ± 0.13 mm in the weft yarns. Consistent with the variability in sectional area, the fiber volume fraction varies from yarn to yarn as well, ranging between 44.1% and 60.8% over the 104 warp yarns under consideration, and between 29.1% and 48.4% over the 40 weft yarns under study. Unlike any of the other geometrical parameters on the yarn level, the shape factor seemed to depend on the position of the yarn within the stack, with typically more compact yarn shapes in the outer laminate layers. This dependency was only observed in the warp yarns, not in the weft yarns.

On the intra-yarn level, severely inhomogeneous fiber distributions were found within the yarns. This variability was quantified with respect to a smoothing radius that defines the circular area over which is averaged. With a smoothing radius of 4 times the fiber diameter $D_f$, for instance, the fiber volume fraction within the warp yarns ranges between 11% and 80%, with an average of 54.6% ± 8.3%. Within the weft yarns, values between 1.5% and 68% were found with the same smoothing radius, with an average of 35.9% ± 8.8%. A smoothing radius of 8 $D_f$ was found to provide just enough resolution to distinguish the global variations. A smoothing radius of 2 $D_f$, on the other hand, merely intensified the solution without yielding more insights.

The remainder of this chapter will be dedicated towards finding the relationship between the imperfect reinforcement geometry on the one hand, and the mechanical behavior on the other hand. In the first section to come, DIC will be performed to capture the surface strain fields on the laminate edge, and the distribution patterns will be compared to the underlying internal structure of the composite. In the subsequent section, the damage on the laminate edge will be studied, with the purpose of finding to what extent the initiation, the propagation and the morphology of the observed damage relate to the internal structure of the composite.

## 4.4 EXPERIMENTAL DETERMINATION OF THE STRAIN FIELDS ON A SPECIMEN EDGE

### 4.4.1 Methodology

The strain distribution on the edge of the composite laminates under static tensile loading was measured using Digital Image Correlation (DIC). Four specimen types were considered for this experiment: warp-A, warp-B, weft-A and weft-B. The first part of the specimen name denotes the loading direction. The second part denotes the layup system, with 'A' being the stacking that has the warp-dominated face of the fabric directed outwards, and 'B' being the stacking with the weft-dominated face directed outwards. The specimen dimensions can be found in Figure 4-14.c.

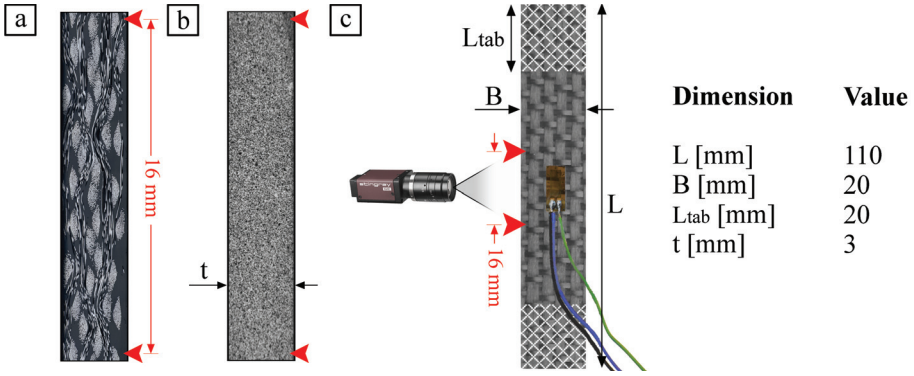


Figure 4-14: Specimen dimensions and instrumentation for DIC experiments

Before instrumenting the specimens for strain measurements, one edge of each test specimen was polished and captured through 3D image stitching with a Keyence VHX-2000 microscope, as illustrated for the weft-B specimen in Figure 4-14.a. Then, the edge was provided with an ultra-fine speckle pattern for DIC, as shown in Figure 4-14.b. The position of the microscopic image was marked on the specimen before applying the speckle pattern. This will make it possible to relate the DIC results to the internal geometry of the laminate. The specimens were additionally instrumented with a longitudinal strain gauge with a working area of 3 x 7 mm², a resistance of 350 Ω and a maximum strain of 5%, as shown on Figure 4-14.c.

The speckle pattern was monitored during loading by a 2 mega-pixel 8-bit CCD AVT Stingray F-201 B1/1.8" camera with extension tube at 5 frames per second and over a length of 16 mm. Correlation of the images and calculation of the surface strain fields were performed with the MatchID software application [14]. The camera setup was calibrated in order to account for intrinsic and extrinsic parameters during the image correlation process. The DIC results were verified by comparing the average

strain along the loading direction to the measurements made by the strain gauge on the specimen surface.

The specimens were subjected to displacement-controlled tension using a servo-hydraulic INSTRON 8801 testing machine with an AlignPRO alignment fixture and a load cell of 50 kN. The crosshead speed was set at 2 mm/min. Force and displacement were given by the FastTrack 8800 digital controller with the same time sampling. Strain gauge measurements were acquired synchronously using Labview data acquisition software. Clamping of the specimens was aided with a self-leveling laser, and the alignment was also checked on the DIC video screen. All four specimens failed within the gauge area, sufficiently far away from the clamping region.

### 4.4.2 Results

The DIC in-plane surface strain fields, along with the distribution of the highest principal strain, are shown in Figure 4-15, Figure 4-16, Figure 4-17 and Figure 4-18, for the warp-A, warp-B, weft-A and weft-B specimen, respectively. Results are shown for a global strain of 0.4% – the strain level at which the first cracks appear, and for a global strain of 0.8%. Results at higher global strains are deemed unreliable, partly because the correlation process is impeded by the numerous cracks that disrupt the speckle patterns, and partly because the images become unfocused due to out-of-plane deformations. The DIC results were projected onto the microscopic images in order to facilitate the comparison between the strain fields and the internal geometry. The region monitored by the DIC camera covers 16 mm along the specimen length, which comes down to almost one fabric unit cell on the warp-oriented specimens, and about two fabric unit cells on the weft-oriented specimens.

Overall, the strain concentrations are weaker in the warp-A specimen in Figure 4-15 than in the warp-B specimen in Figure 4-16. This could be due to the fact that the edge of the warp-A specimen only contains one load-carrying yarn. The section under study will hence not carry a lot of load compared to the sections behind it, and there are not as many strong fluctuations in stiffness between the components in this section. Apart from this difference in intensity, both warp-oriented specimens show similar trends. At a global strain of 0.4%, the strain along the loading direction $\varepsilon_{22}$ shows a treaded pattern, with ridges oriented perpendicular to the loading direction. The ridge tops show no preference in location with respect to the internal geometry of the specimens. The dimensions of the ridges remain unchanged when the global strain is raised to 0.8%, but they are now fewer in number and more intense. Furthermore, all of them are now located on the transversal yarns. As pointed with arrows on Figure 4-15, some of the strongest strain peaks were located on matrix pockets at 0.4% strain. At 0.8% strain, these peaks have all vanished, as indicated by the circles on Figure 4-15. The transverse strain $\varepsilon_{33}$ – the Poisson's effect – is clearly distributed in accordance to the

internal geometry, even at 0.4% strain. The load-bearing yarns and the matrix pockets undergo lateral contraction, while the transversal yarns show lateral expansion. Unidirectional yarns are known to have a positive Poisson's ratio. Therefore, their lateral expansion is unexpected, and could only be explained by mesoscopic mechanical interactions between matrix and reinforcement. The shear strain $\varepsilon_{23}$ is relatively evenly patterned in the warp-A specimen, without discernable relation with the underlying textile architecture. In the warp-B specimen, the distribution of the shear strain $\varepsilon_{23}$ seems to follow the load-bearing yarn on the bottom of the laminate. According to Puck's theory, inter-fiber fracture is governed by the first principal strain $\varepsilon_I$ in a 2D situation. Figure 4-15 and Figure 4-16 clearly show that the strain along the loading direction $\varepsilon_{22}$ is the largest contributor to this criterion.

On the weft-oriented specimens in Figure 4-17 and Figure 4-18, about two fabric unit cells are covered, and the repeating unit cell pattern can also be discerned in the edge surface strain fields. The strain patterns are more distinct than in the warp-oriented specimens, which can be attributed to the larger crimp angles in the weft yarns. The longitudinal strain $\varepsilon_{22}$ again forms ridged patterns at 0.4% strain, and the concentrations again shift towards the transversal yarns if the global strain is raised to 0.8%. The strongest concentrations form periodically repeating, oblique lines across the sides of the specimens. On average, the longitudinal strain in the weft-A specimen in Figure 4-17 appears to be larger on the bottom of the specimen than on the top. This can be due to the geometrical asymmetries within the edge of this specimen – only two load-carrying yarns are fully visible. Another possible cause would be global bending or torsion due to a misalignment of the test setup. This is, however, not likely, as the same test setup and the same clamping procedure was followed for all four experiments. In the weft-B specimen in Figure 4-18, the longitudinal strain is not as obviously periodic at 0.8% strain. In this specimen, a dominant crack has developed on the bottom of the rightmost unit cell. Possibly, this crack is taking a lot of longitudinal strain, which reliefs the leftmost unit cell. The transversal strain $\varepsilon_{33}$ shows the same tendency in the weft-oriented specimens as in the warp-oriented specimens. Negative strains are found on the matrix pockets and on the longitudinal yarns, and positive strains are found on the transversal yarns. When looking at the distributions of the shear strain $\varepsilon_{23}$, two patterns can be discerned. On a larger scale, there are vertical shear bands with alternating signs. The width of these bands fits the periodicity of the specimen geometries. On the smaller scale, the shear distributions are patched. Comparison of the patches and the internal structure of the laminates learns that none of the peaks lie within a transversal yarn. In the weft-A specimen, the patch pattern seems very regularly squared. It was checked that this is not an artifact of any parameter or setting used in the correlation procedure. Like in the warp-oriented specimens, the first principal strain $\varepsilon_I$ is governed by the strain along the loading direction $\varepsilon_{22}$.

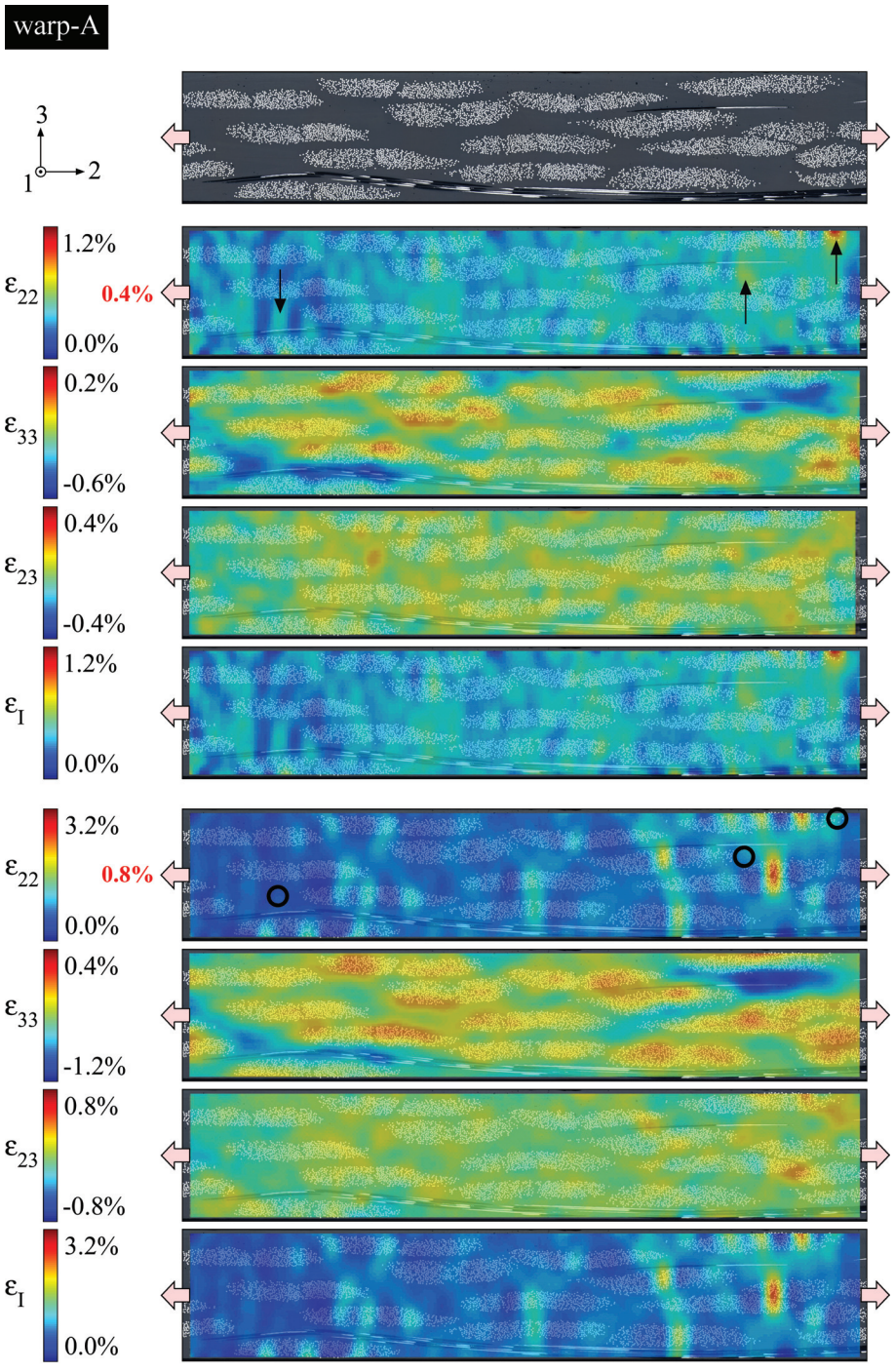


Figure 4-15: DIC surface strain fields on the edge of the warp-A specimen

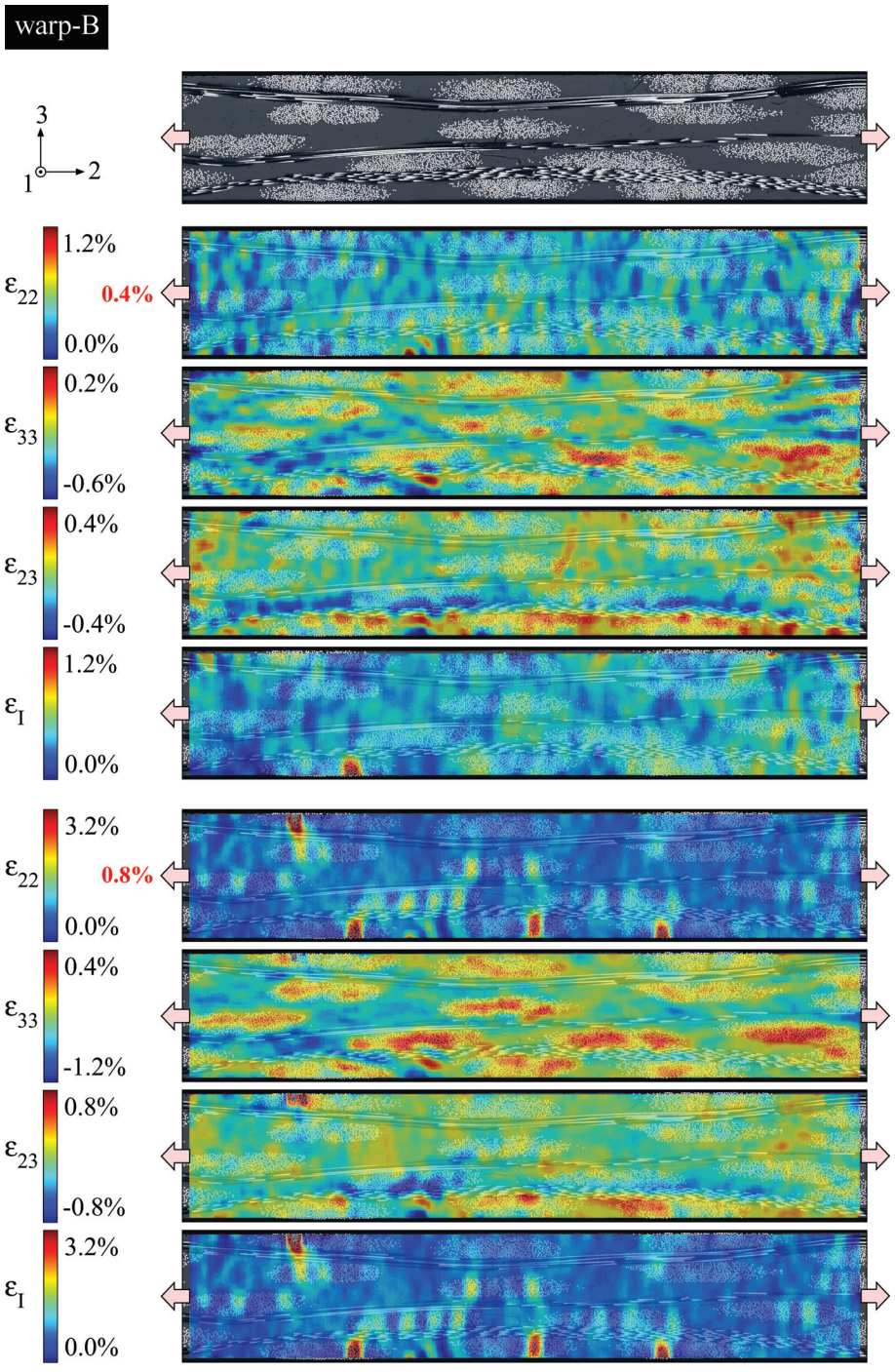


Figure 4-16: DIC surface strain fields on the edge of the warp-B specimen

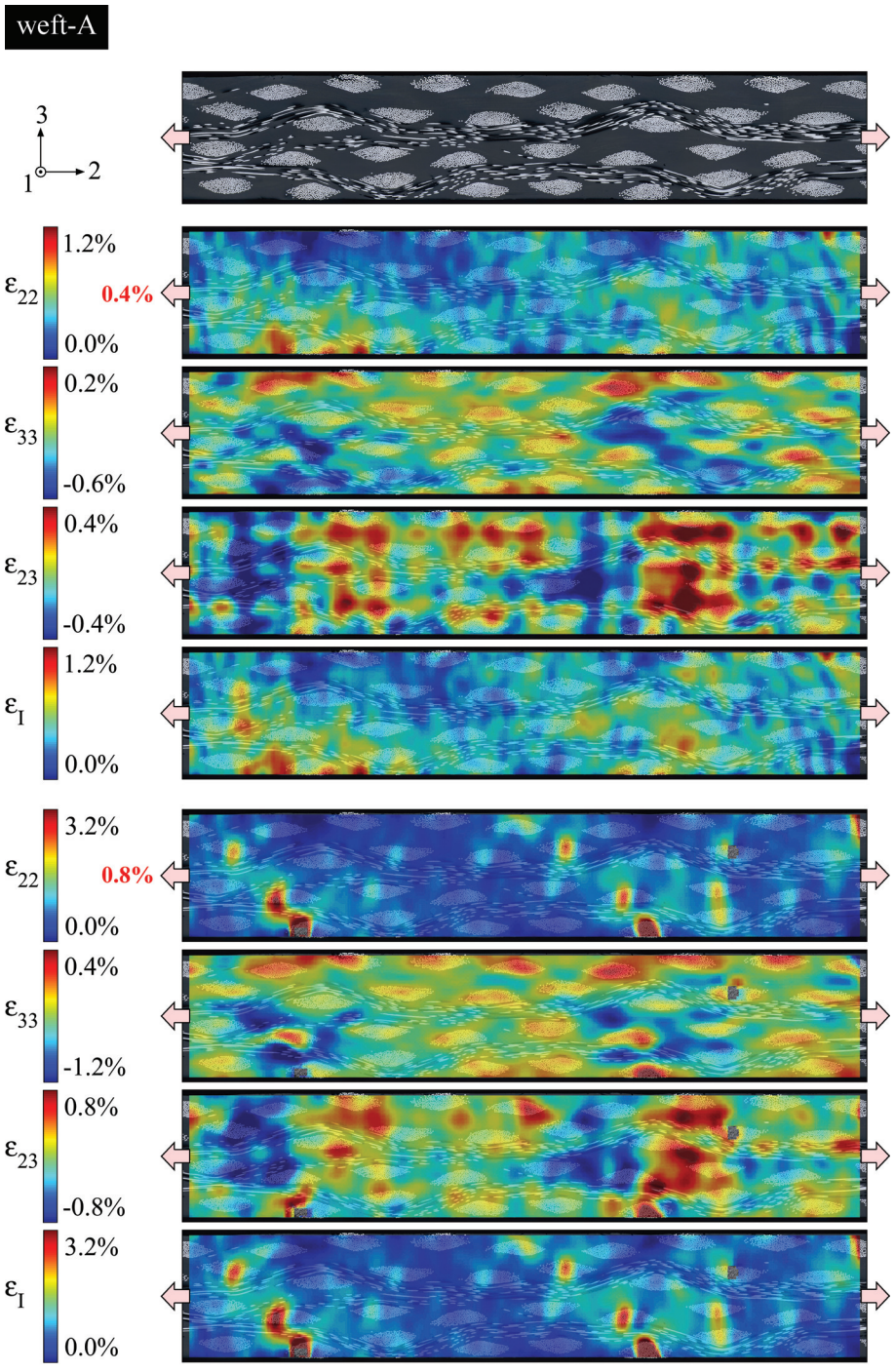


Figure 4-17: DIC surface strain fields on the edge of the weft-A specimen

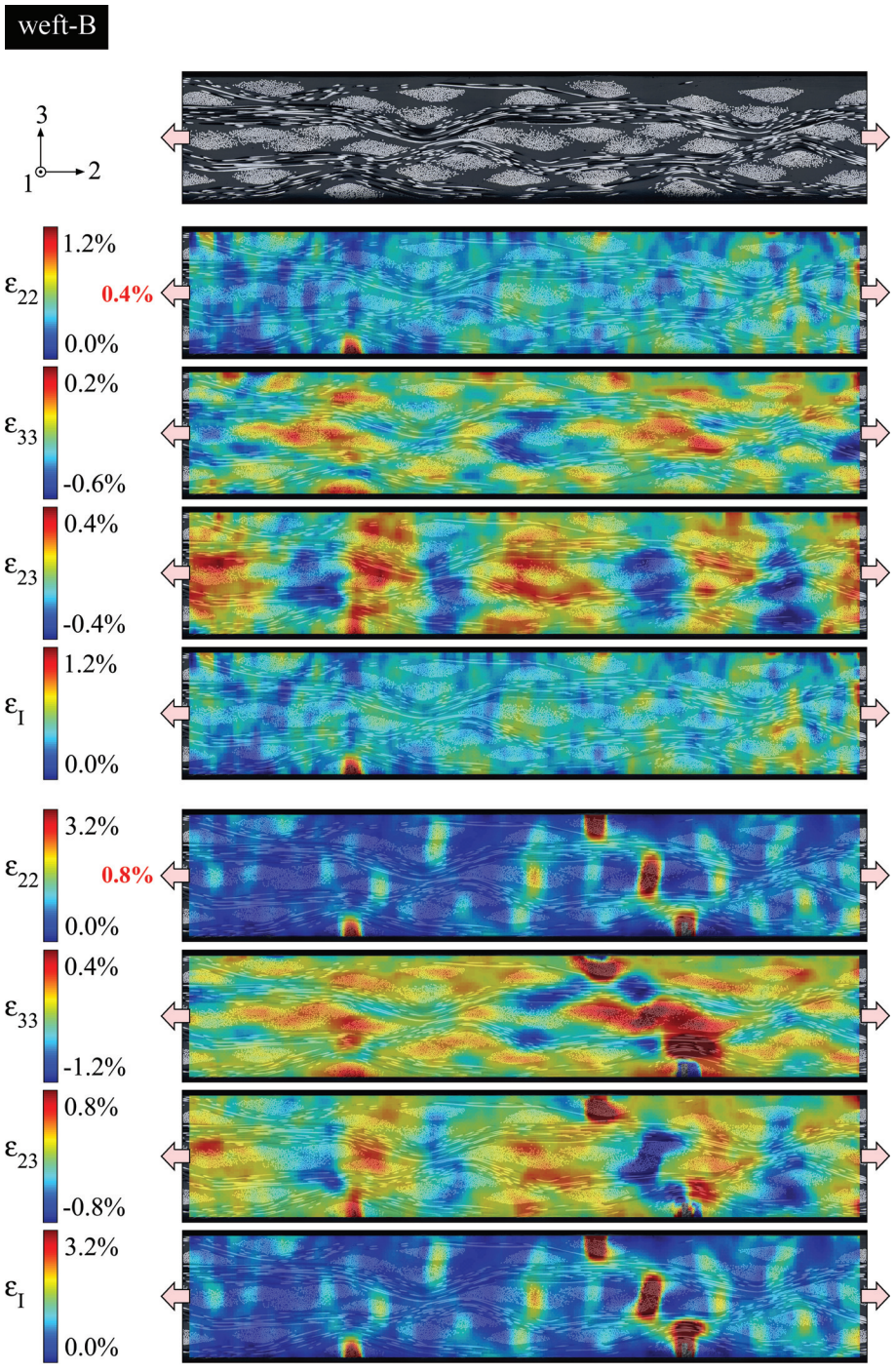


Figure 4-18: DIC surface strain fields on the edge of the weft-B specimen

When a crack on the specimen edge opens up too wide, it disrupts the speckle pattern and thereby inhibits the image correlation process. At a global strain of 0.8%, all but the warp-A specimen have developed at least one such crack, as is clear from the uncorrelated patches on Figure 4-16, Figure 4-17 and Figure 4-18. The crack that seems most dominant is the one on the bottom of the rightmost unit cell of the weft-B specimen in Figure 4-18, especially if it is judged by its influence on the transversal strain and the shear strain. At this point, one would expect for this crack to become fatal. As explained earlier, image correlation was not deemed reliable beyond 0.8% strain. The further development of the experiment can, however, also be appreciated from the raw images of the speckle pattern, as shown in Figure 4-19. The first frame, frame 000, is the reference frame at the beginning of the test. The second frame is the very last frame before the strain gauge ruptured, at a strain of 1.6%. Beyond this point, only the stress level is known. On frame 230, when the stress is still at its maximum, the transversal yarn with the dominant crack is starting to debond from the longitudinal yarn. At frame 281, the stress is dropping, and the debond is growing wider. At this point, the strain is still being increased, so the stress drop is due to fractures. Only two frames – which is 0.5 seconds – later, a very sudden damage event emerges in the leftmost unit cell. This damage includes a transversal crack through the crimp yarn at the specimen surface, as well as a local debonding of this yarn, and it quickly grows through the full thickness of the specimen, causing final rupture. The propagation rate of this damage, in contrast to the rather ductile growth of the cracks in the right unit cell, suggests that this damage had been growing steadily inside the specimen before traveling to the edge at high speed.

In general, the DIC strain fields on the edges of the specimens showed a strong correlation to the corresponding internal laminate structures. This suggests that the edge sections are not heavily affected by the underlying sections when it comes to the distribution of the in-plane strain components at low strain levels. In contrast, the unpredictability of the final rupture of specimen weft-B suggests that damage propagation cannot be approached from a two-dimensional point of view. A more dedicated analysis of the damage on the laminate edge is the subject of the next section.

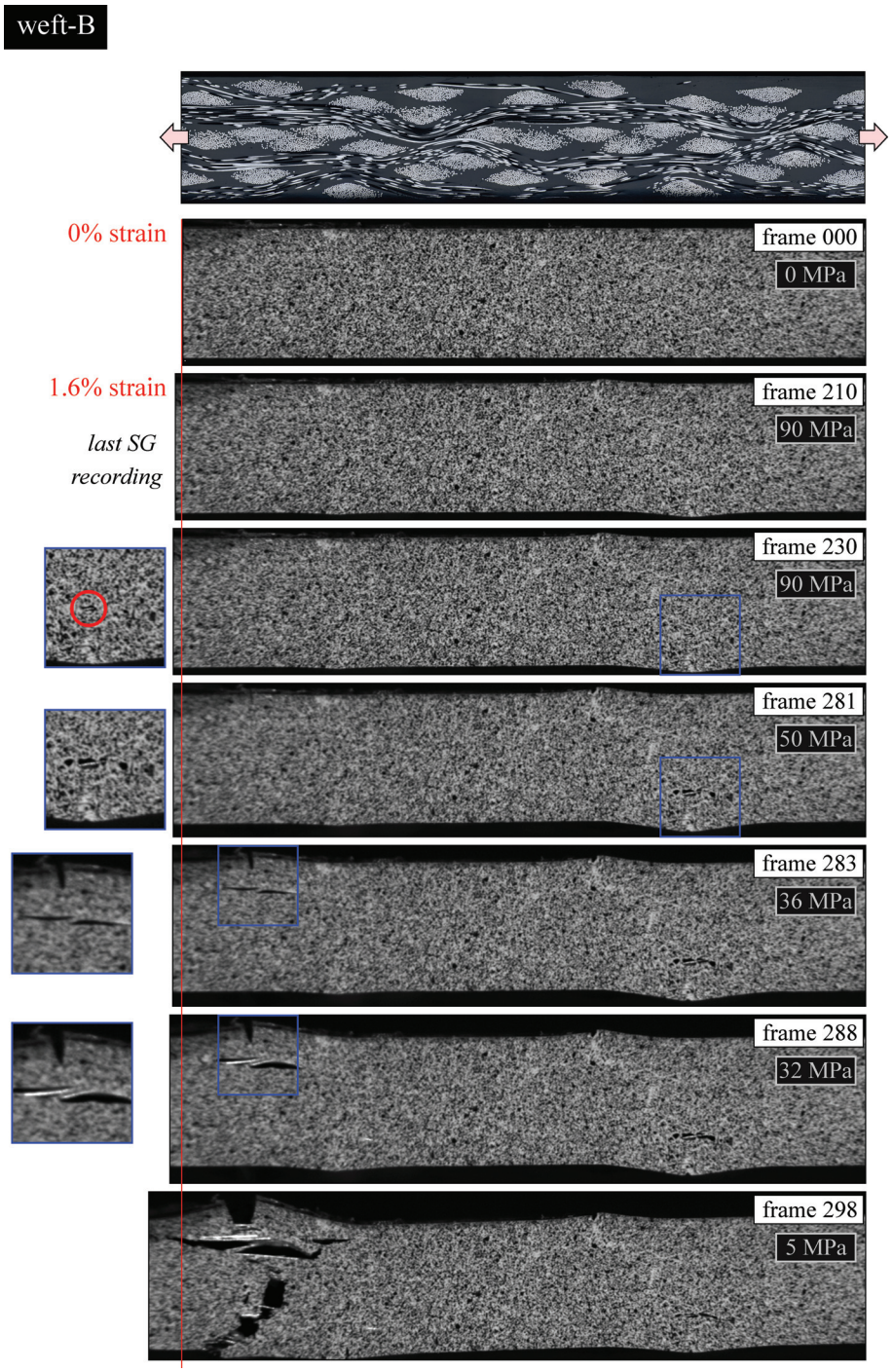


Figure 4-19: Uncorrelated images of the speckle pattern on the weft-B specimen side

## 4.5 EXPERIMENTS ON THE DAMAGE INITIATION, PROPAGATION AND MORPHOLOGY

The damage morphology and propagation were initially studied on microscopic movies made by a USB microscope during tensile loading, as was discussed in section 2.5.6. This approach had the advantage of providing an animated overview on the damage events over a considerable field-of-view, and the movie frames could be situated relative to stress and strain recordings during the experiment. A major drawback was the limited resolution of the footage. Damage was exclusively observed in the form of cracks in the transversal yarns, with an initiation strain between 1.2% and 1.3%. The video frames were, however, not sharp enough to rule out other forms of damage, nor to be certain of the damage initiation strain.

Several concepts and setups were considered in search for a more reliable capture of the initial damage and the details of its propagation. A first attempt was to mount a microscope with camera function on a tripod next to the hydraulic tensile machine. This endeavor failed for several reasons. First of all, the combination of a sufficient magnification and a workable field-of-view appeared unachievable with a common microscope. Preliminary observation of the edge of a failed specimen learned that a magnification of x200 is necessary for some cracks to become visible. At this scale, the field-of-view comprises only a few square millimeters. Second of all, the tolerance on the focal length is small at this high magnification. As a result, the image goes out of focus as the tensile test proceeds, because of the out-of-plane movements of the specimen edge. Any trembling near the camera setup, as well, blurs the image. This makes it impossible to make adjustments on the focal length during the experiment. An additional problem appears when the edge of the specimen deforms unevenly. The steel fiber heads are very reflective, hence a low lighting must be used to capture the surface. If the fiber heads are at some point no longer perfectly perpendicular to the microscope, they reflect the little light away from the lens, resulting in an underexposed image.

In conclusion, the field-of-view and the tolerances on focal length and exposure of a common microscope are too small at the high magnification that is required to properly observe damage. These, in particular, are the issues that are resolved by 3D image stitching. As explained in section 4.2, this technique involves scanning the object under investigation both horizontally – which drastically increases the field of view, and vertically – which ensures focused images, even on uneven or tilted surfaces. The drawback of this technique is that the scanning process takes several minutes. Monitoring the damage will hence require to pause or interrupt the tensile experiment. Two concepts of dealing with this restriction will be elaborated in the next sections. The first concept is to perform the tensile experiment on a small manual

screw bench that fits on the motorized stage of the Keyence microscope. The second concept is to apply the strain with a hydraulic machine, and to intermittently take the specimen out of the clamps to perform microscopy on its edge. Both experimental methods have their own advantages and drawbacks. By applying both, any errors and inaccuracies that may originate from their individual shortcomings can be identified when interpreting the results.

### 4.5.1 Method 1: Tensile experiments on a manual screw bench under the microscope

#### 4.5.1.a Methodology

The idea of the first method is to perform the tensile experiment on a small manual screw bench that fits on the motorized stage of the Keyence microscope, as shown on Figure 4-20.a. This concept allows to perform microscopy on the specimen while it is under strain. Unclamping the specimen could cause possible cracks to close and become invisible, and especially the first damage could be overlooked because of this.

A small manual screw bench was built for this experiment. The device consists of two clamp heads and an encasing bench frame, as depicted on Figure 4-20.b. The whole setup had to stay below 1 kg, which is the weight restriction of the motorized stage of the Keyence microscope. Therefore, both the clamp heads and the frame of the screw bench were made of aluminum. The two-piece clamp heads are bolted together with five M5 hex screws, as shown on Figure 4-20.c. The innermost rows of three screws directly apply the clamping force on the specimen ends. The use of three screws ensures an even spread of the clamping pressure. Furthermore, it reduces the force on the screw threads, which were drilled directly into the aluminum bottom pieces of the clamp heads. The specimens were pierced at their ends (Figure 4-20.d), so that the central screw can pass through. This measure was merely taken in view of applying the clamping pressure as central to the specimen end as possible. Any tension on the end holes would cause premature failure in these weakened sections, hence the clamping is meant to be a pure sandwiching mechanism. Once the specimen is clamped, the bench frame is placed around the clamp heads. The large head is provided with a screw thread for the M10 bolt, which can be tightened to apply a tensile load to the specimen. The small head is kept in place by a long M5 bolt that pierces both the head and the frame, but the tensile load will be solely sustained by the notches in the frame. The device was designed to apply a pulling force of 6 kN. Taking a laminate strength of 100 MPa, a specimen with a width up to 20 mm can be pulled up to failure. The specimens were cut to this maximum width, but a few millimeters were taken off in the polishing process. The maximum distance between the clamp heads is 72 mm, and the gauge length of the specimens was chosen at 64

mm. This leaves a margin of 8 mm to pull the clamp head back, hence to apply a tensile strain.

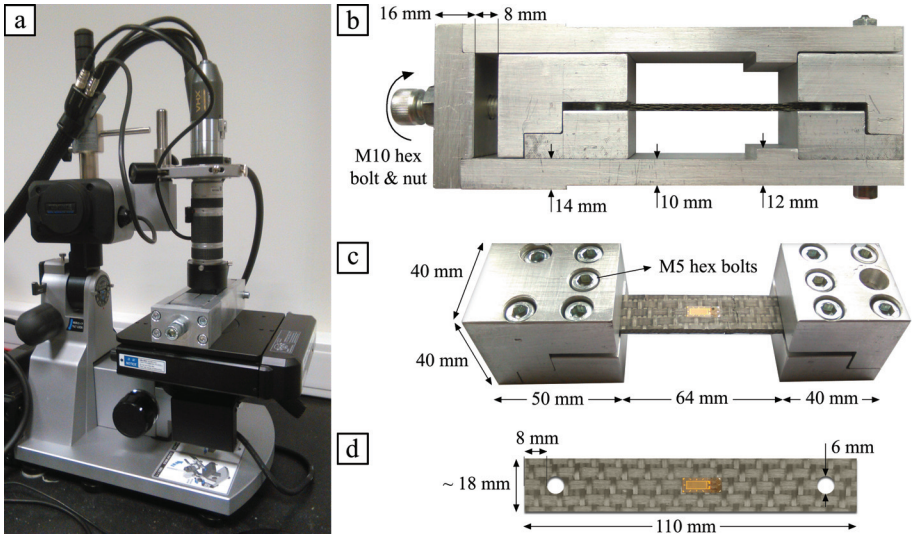


Figure 4-20: Setup for method 1: overview of the tensile experiment (a), manual screw bench (b), clamp head design (c), and specimen preparation and dimensions (d)

The specimen dimensions and the instrumentation are shown on Figure 4-20.d. The ratio between gauge length and specimen width is only about 3.5. This is a small value in view of avoiding bending and torsion due to minor grip eccentricities [15]. Making the gauge length – hence the bench frame – much longer is not possible due to the weight restriction of the motorized stage of the Keyence microscope. Making the specimen narrower is also not an option. The width of 18 mm already covers only one unit cell in the weft-oriented specimens. The specimens were instrumented with a longitudinal strain gauge with a working area of 3 x 7 mm², a resistance of 350 Ω and a maximum strain of 5%. Strain gauge measurements were acquired during the experiments using Labview data acquisition software. These readings were used as a control for the tensile experiment: tension was put on the specimen in steps of about 0.1% strain. After every step, the specimen edge was captured on 3D stitched images over a total length of 40 mm, at a magnification of x200. Prior to finding the first crack, the edge was additionally scanned at a magnification of x500. The whole process of stepwise increasing the strain, followed by microscopy, was pursued until final failure of the specimen.

Four specimens were considered for testing: warp-A, warp-B, weft-A and weft-B. The first part of the specimen name denotes the loading direction. The second part denotes the layup system, with ‘A’ being the stacking that has the warp-dominated face of the fabric directed outwards, and ‘B’ being the stacking with the weft-dominated face

directed outwards. The specimen displayed in Figure 4-20.d, for instance, is the weft-B specimen. Three specimens failed within the gauge region, sufficiently far away from the clamp ends. This proves that the setup is properly aligned. One specimen, the warp-B specimen, broke at 0.93% strain on one of the holes in the clamp ends. This premature failure results from an insufficient clamping force, not from a misalignment. As the homogeneity of the strain field and the strain measurements are not corrupted, the results are presented nonetheless.

#### 4.5.1.b Results

An abstraction of the results of the experiment is shown on Figure 4-21 and Figure 4-22 for the warp-A specimen, and on Figure 4-23 and Figure 4-24 for the warp-B specimen. The stitched images of the specimen edge could not be shown over their full length in one figure, as this would harm their visibility. Therefore, the images are divided over two figures, each covering about 20 mm – or a little more than one unit cell along the specimen length. The unit cell is much smaller along the weft direction – 20 mm covers almost three unit cells. Therefore, one figure suffices to provide an overview on possible repetitions or patterns in the damage phenomena for the weft-oriented specimens. The weft-A specimen can be found in Figure 4-25, and the weft-B specimen is shown in Figure 4-26. All figures display the specimen edge on three different strain levels, and the according frames were referenced to a typical stress-strain graph of the laminates. Note that this is not the curve of the specimen at hand, as stress was not recorded during these experiments. The first frame shows the very first observation of damage, typically between 0.40% and 0.45% strain. The second level was chosen around 0.8% strain in order to give a view on the damage progression. The final image shows the failed specimen. Additionally, some details are highlighted in the enlargements a to c. Damage was marked on the figures for clarity, as a lot of cracks are only visible at the full resolution of 922 pixels per mm. The markings are color-coded according to the initiation strain: red for damage that initiated before point 1 on the stress-strain graph, blue for damage that initiated before point 2, and green for damage that initiated after point 2.

Figure 4-21 and Figure 4-22 depict two consecutive unit cells along the edge of the warp-A specimen. The geometrical equivalence between both figures is clear, even though only one longitudinal yarn is visible on the edge of this specimen. The warp-B specimen is shown in Figure 4-23 and Figure 4-24. Comparison of these two figures reveals a clear periodicity for the three uppermost textile layers. On the bottom layer, the periodicity is off due to a misalignment of this layer: the longitudinal yarn on Figure 4-23 disappears on the very right of the unit cell, and the yarn that appears on the left in Figure 4-24 is a different yarn.

Despite the different stacking systems, the observations on damage are very similar in both specimens:

- The first observations of damage in the warp-A specimen were at 0.39% strain. No damage was seen in the step before, which was at 0.31% strain, so initiation must have taken place between 0.31% and 0.39%. Similar reasoning leads to a damage initiation strain between 0.36% and 0.45% for the warp-B specimen.
- Damage initiates in the form of fiber debondings, as shown on detail 'a' in Figure 4-23. This is not just the case for the very first damage, but also for damage that initiates at higher strain levels. The fiber detachments are typically very well visible, because they are accompanied by matrix cusp marks, i.e. local zones of plastic deformation in the matrix that are characteristic of shear failure [16].
- Damage typically clusters on vertical lines through the transversal yarns. Many occurrences that look like a single crack spanning the full height of a yarn are in fact an assembly of small cracks, cusp marks and single fiber detachments. Examples are shown on details 'a' in Figure 4-22 and Figure 4-24.
- Some damage grows rapidly and merges into wide cracks, while other damage shows no evolution as the strain is increased. An example is shown on Figure 4-22. Details 'b' and 'c' show how one of the very first cracks has hardly grown over the course of the experiment (red markings). In contrast, the wide crack in detail 'c' (the green markings) had not even initiated at 0.8% strain, so this crack must have propagated rapidly.
- Crack propagation seems to be impeded by a large inter-fiber distance. As a result, damage on the unconfined edges of the yarns often remains in the shape of singular cusp marks and fiber detachments, as illustrated on detail 'b' in Figure 4-24.
- Damage keeps initiating as the strain is increased, and it appears well spread along the length of the specimen. The pattern seems – at least to some extent – periodic with respect to the unit cell of the reinforcement.
- Damage initiates inside the transversal yarns (e.g. detail 'a' on Figure 4-21), and then travels to the yarn border. Even in transversal yarns that contact a longitudinal yarn, the cracks initiate inside the yarn, rather than at the interface. Similarly, in transversal yarns at the specimen surface, cracks originate inside the yarns, not at the specimen surface. These phenomena are illustrated on detail 'b' in Figure 4-21 on a transversal yarn that contacts a longitudinal yarn on its bottom side, and the specimen surface at its top side: the cracks do not extend to the interface with the longitudinal yarn, nor to the specimen surface.
- The propagation of a crack after it reaches the yarn border depends on the boundary conditions. Cracks in the surface yarns often travel to the surface, leaving two severe cusp lines under 45°, as shown on detail 'c' in Figure 4-23. When the distance to the neighboring transversal yarn is small enough, cracks can bridge the matrix pocket in between, as shown on detail 'c' in Figure 4-22.

Here as well, two cusp lines under 45° are formed where a crack enters the matrix pocket. Where the transversal yarn touches a longitudinal yarn, some cracks were found to deviate along the interface. In these cases, it is the transversal yarn which detaches from the matrix, not the longitudinal yarn, as is clear on detail 'c' in Figure 4-21. Furthermore, the debonding length is usually very limited, cf. the example on detail 'c' in Figure 4-24.

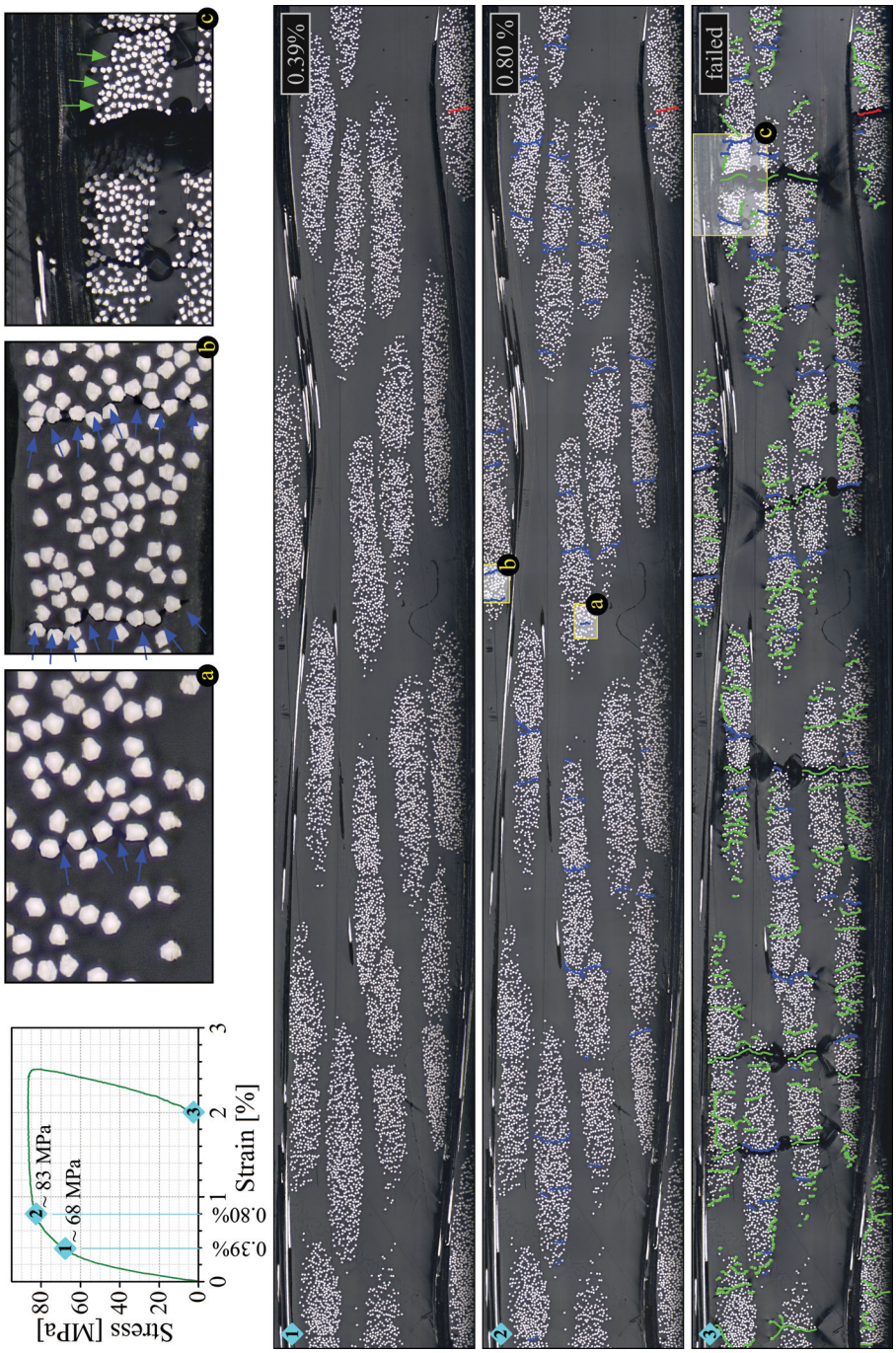


Figure 4-21: Damage initiation and propagation in the warp-A specimen – unit cell 1

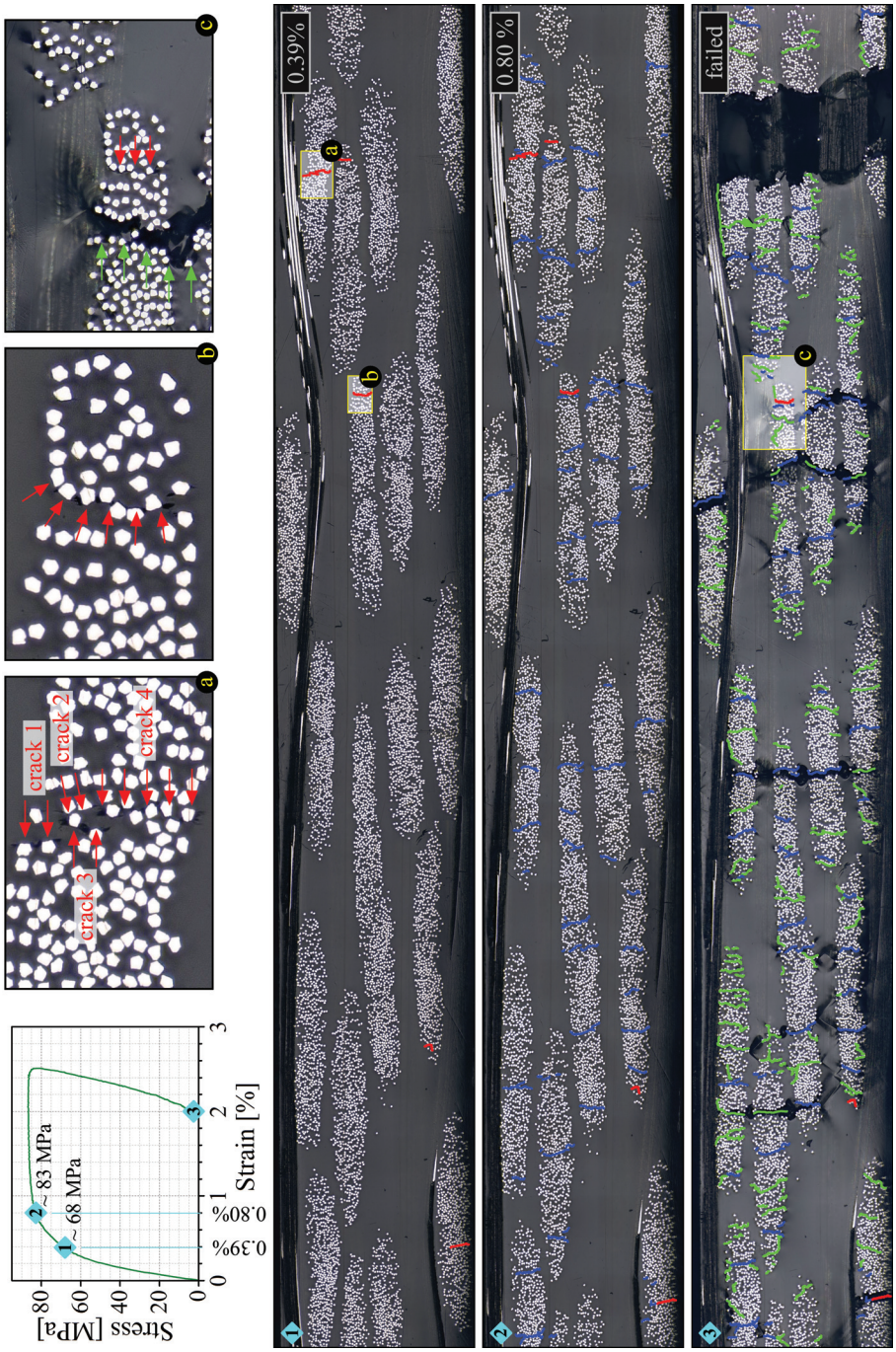


Figure 4-22: Damage initiation and propagation in the warp-A specimen – unit cell 2

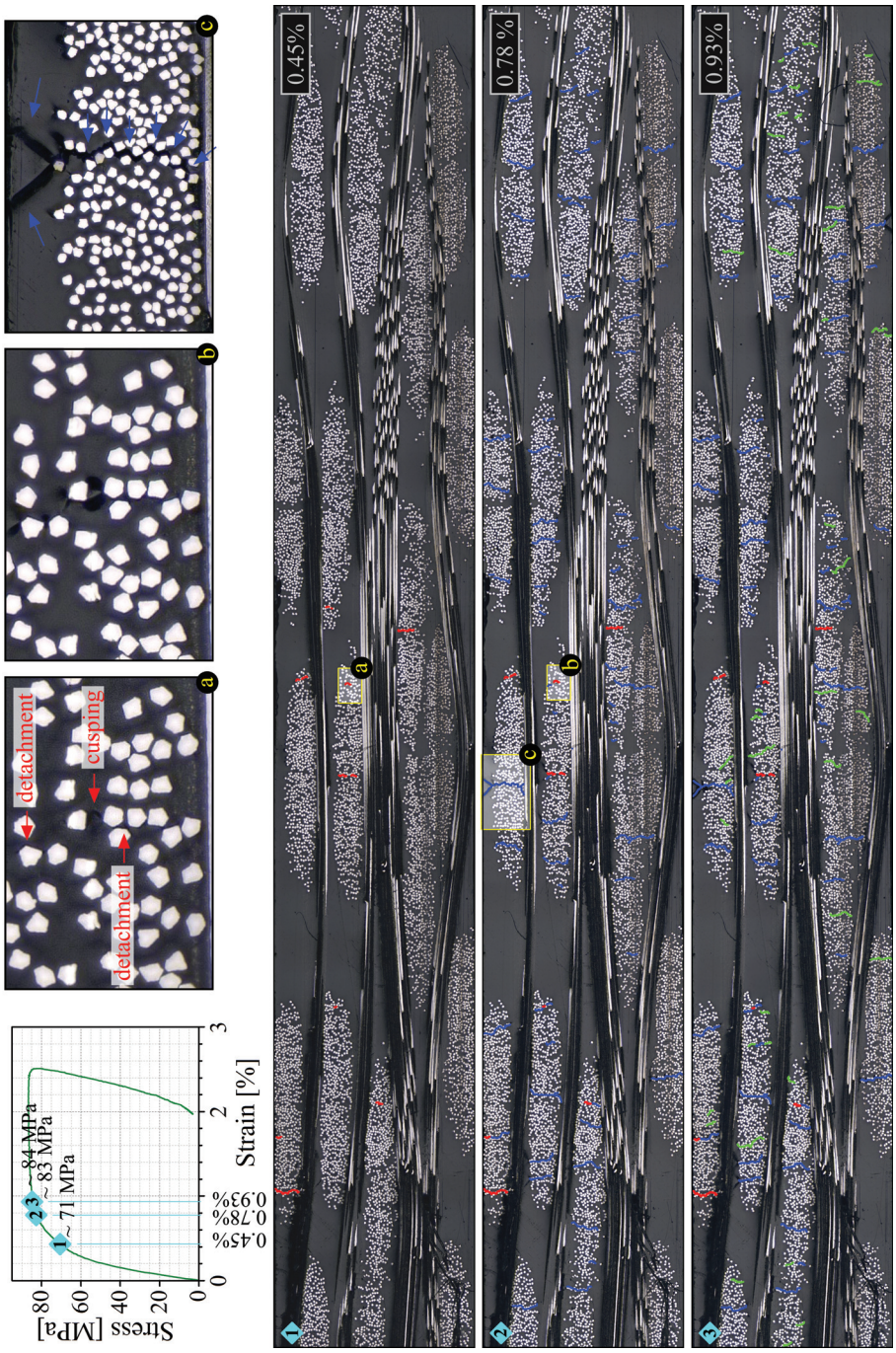


Figure 4-23: Damage initiation and propagation in the warp-B specimen – unit cell 1

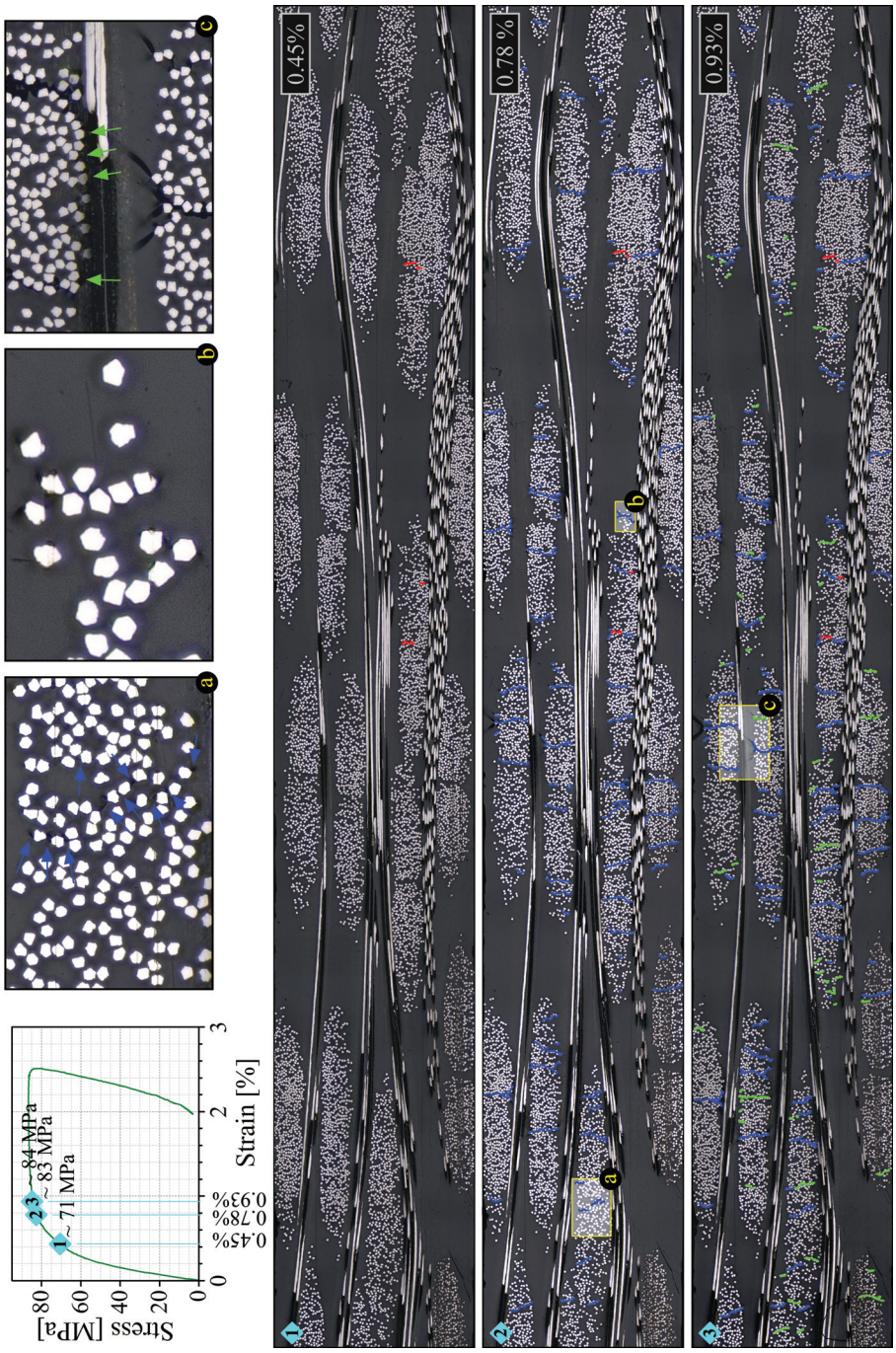


Figure 4-24: Damage initiation and propagation in the warp-B specimen – unit cell 2

Figure 4-25 and Figure 4-26 show the weft-A and the weft-B specimen, respectively, over a length of nearly three unit cells. The observations on the damage patterns in these specimens can be listed as follows:

- The first observations of damage in the weft-A specimen were at 0.43% strain. No damage was seen yet at 0.31% strain, so initiation must have taken place between 0.31% and 0.43%. Similar reasoning leads to a damage initiation strain between 0.34% and 0.44% for the weft-B specimen.
- Damage appears in the form of well-established cracks due to fiber-matrix debonding, most often over the full height of the transversal yarn. An example is shown on detail 'a' in Figure 4-26. The single-fiber detachments and the cusp marks in between single fibers that were observed in the warp-oriented specimens are rarely seen in the weft-oriented specimens.
- The amount and the width of the cracks concentrate in a preferred region in the unit cell, marked as the 'concentration band' on Figure 4-25 and Figure 4-26. The transversal yarns in this region are amongst the first to crack. In the weft-A specimen, the concentration band connects the transversal surface yarns left from the crimp region. In the weft-B specimen, it runs across the surface crimp regions.
- Similar as in the warp-oriented specimens, cracks keep initiating as the strain is increased, and the damage is at all times more or less periodic with respect to the internal geometry and well spread along the length of the specimen.
- Not all cracks propagate at the same rate. The wide crack on detail 'c' in Figure 4-26, for instance, had not initiated yet at 0.78% strain, hence the green markings. This means that it must have opened up rapidly. The crack that is marked in red, on the other hand, was one of the very first cracks. This crack has hardly evolved since initiation. A similar observation was made on the warp-oriented specimens.
- Like in the warp-oriented specimens, damage always seems to initiate inside the transversal yarns.
- The propagation of a crack after it reaches the yarn border is similar as in the warp-oriented specimens. Cracks that travel to the specimen surface leave two cusp lines under an angle of 45°, as shown on detail 'c' in Figure 4-25. Similar cusp marks are seen when cracks encounter a matrix pocket (detail 'b' in Figure 4-25), or bridge the matrix pocket between neighboring yarns (detail 'a' in Figure 4-25). Much more than in the warp-oriented specimens, transversal yarns are debonded over a considerable length along their outer row of fibers. An example of such a delamination is shown on detail 'c' in Figure 4-25.
- The longitudinal yarns of the weft-B specimen show severe splitting, even already at 0.8% strain. All of the splits are located within the concentration bands. The start and end point of the split regions are marked with arrows, and one case is enlarged on detail 'b' in Figure 4-26. This type of damage was not found in the weft-A specimen, nor in the warp-oriented specimens.

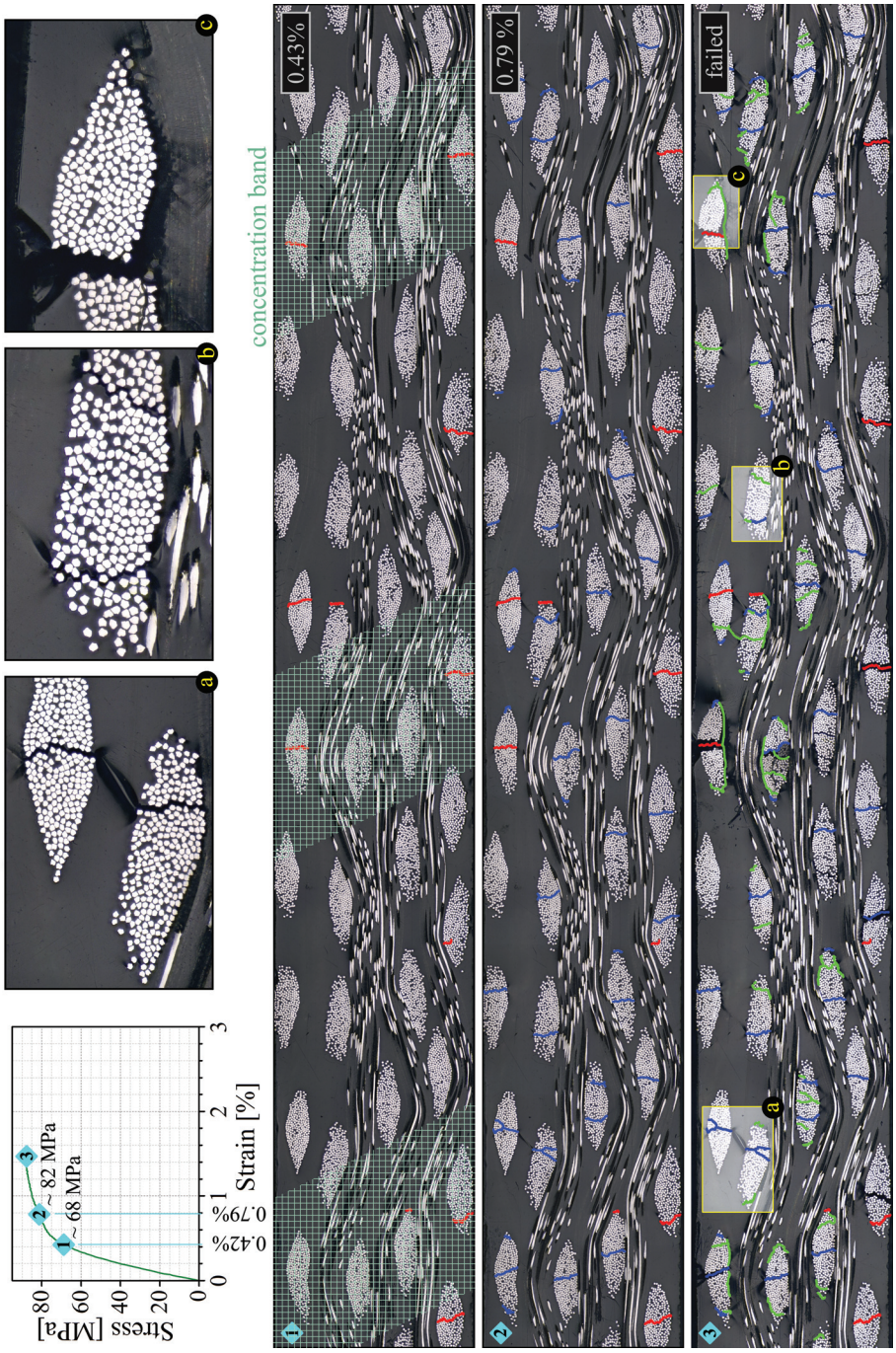


Figure 4-25: Damage initiation and propagation in the weft-A specimen

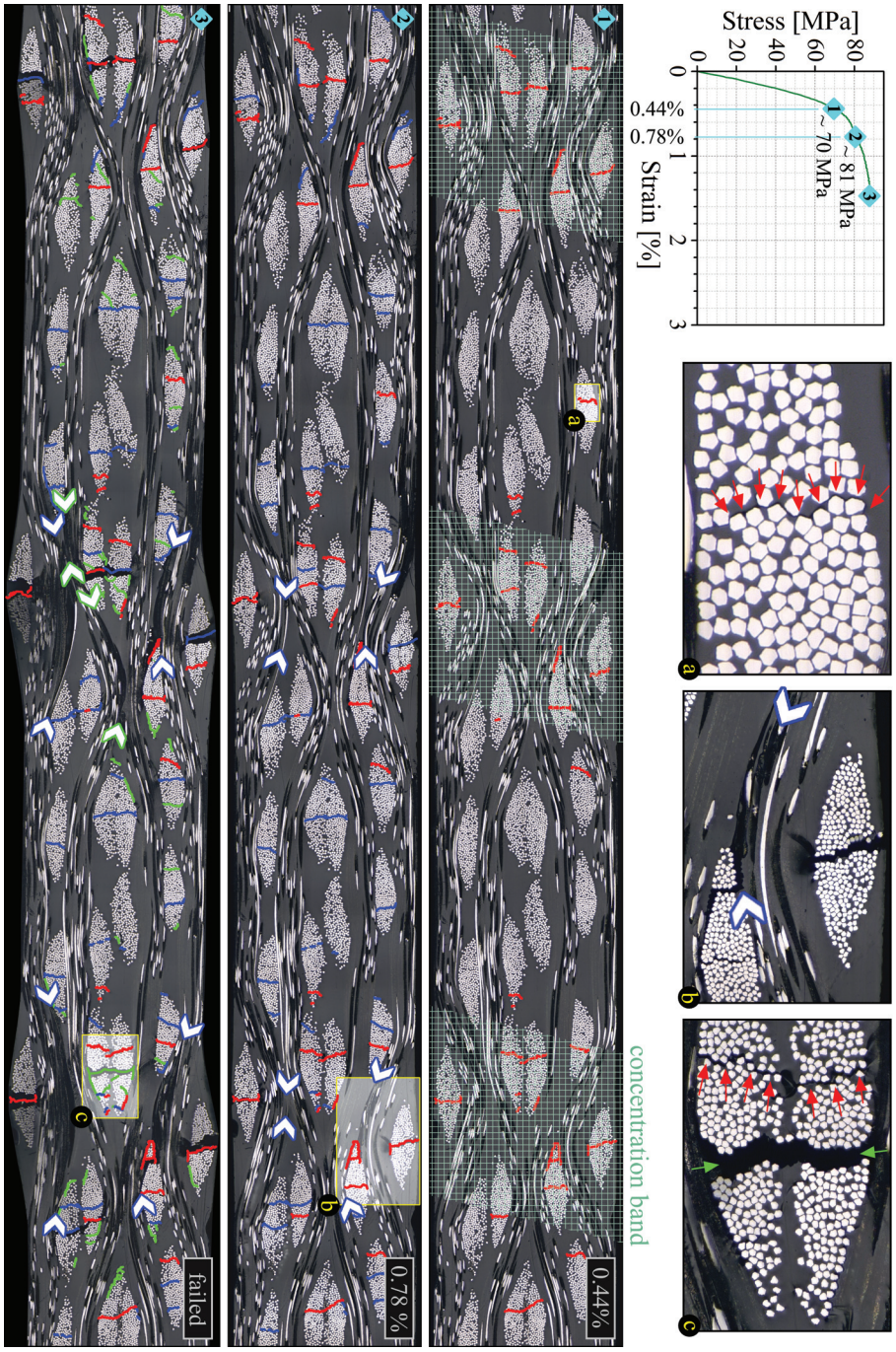


Figure 4-26: Damage initiation and propagation in the weft-B specimen

The main focus of the experimental method proposed in this section was to enable studying the specimen edge while under tension. Taking the tension off could cause cracks to close again and become invisible, and this would lead to an overestimation of the damage initiation strain. The manual screw bench fulfilled this demand, but it has a few drawbacks on other aspects. First, the load was put on manually, without any control over the strain rate. Second, the clamping system is not as reliable as that of an established tensile machine when it comes to rigidity and alignment. The limited length-to-width ratio of the specimens further increases the risk of spurious bending and torsion. The experimental results do not signal any of these shortcomings. Damage initiation was invariably detected around 0.4% strain, the nature of the damage was very similar in the specimens of the same loading direction, and the damage appeared well spread along the length of the specimens, in a more or less periodic pattern with respect to the unit cell of the reinforcement. Nevertheless, a second set of experiments was performed in order to exclude any effects of the shortcomings of the manual screw bench. The method used for these experiments and its results are the subject of the next section.

### 4.5.2 Method 2: Unclamping the specimen from the hydraulic tensile machine to perform microscopy

#### 4.5.2.a Methodology

The aim of this second method is to verify the effects of the shortcomings of method 1, which were the lack of rate-control and the uncertainties on alignment in applying the tension. To this end, the load introduction with this method was performed using a servo-hydraulic INSTRON 8801 testing machine with an AlignPRO alignment fixture, and the length-to-width ratio of the specimens was chosen larger in order to minimize the effects of minor grip eccentricities. The specimens have to be placed on the motorized stage of the Keyence microscope in order to perform 3D image stitching. Therefore, the tension was applied in loading-unloading cycles with increasing amplitude. After every cycle, the specimen was removed from the clamps to perform microscopy.

The amplitude of the loading-unloading cycles was started at 20 MPa, and increased with 5 MPa per cycle. The first three cycles are illustrated on Figure 4-27.a. The tests were displacement-controlled with a constant crosshead speed of 2 mm/min. Force and displacement were given by the FastTrack 8800 digital controller with the same time sampling. After every cycle, the specimen was removed from the clamps and the edge was captured on 3D stitched images over a total length of 40 mm, at a magnification of x200 (Figure 4-27.b). Prior to finding the first crack, the edge was additionally scanned at a magnification of x500. Following every microscopic investigation, the specimen had to be clamped back into the tensile machine for the

next loading cycle. Crucial in this operation is to ensure the alignment of the specimen, and to have the correct gauge length. The first issue was solved by using a self-leveling laser to assist the clamping operation. The second demand was met by placing a thin metal strip in between the grips of the bottom clamp head of the tensile machine for the specimen to stand on prior to closing the clamp. The concept is illustrated on Figure 4-27.c. The thin metal strip ensures that the bottom end of the specimen is clamped over the same length on every loading cycle. As every loading cycle ends at 0 MPa, there will be no change in the specimen length while it is unclamped. Therefore, the top clamp is automatically left on the correct vertical position to clamp the specimen back in for the next loading cycle.

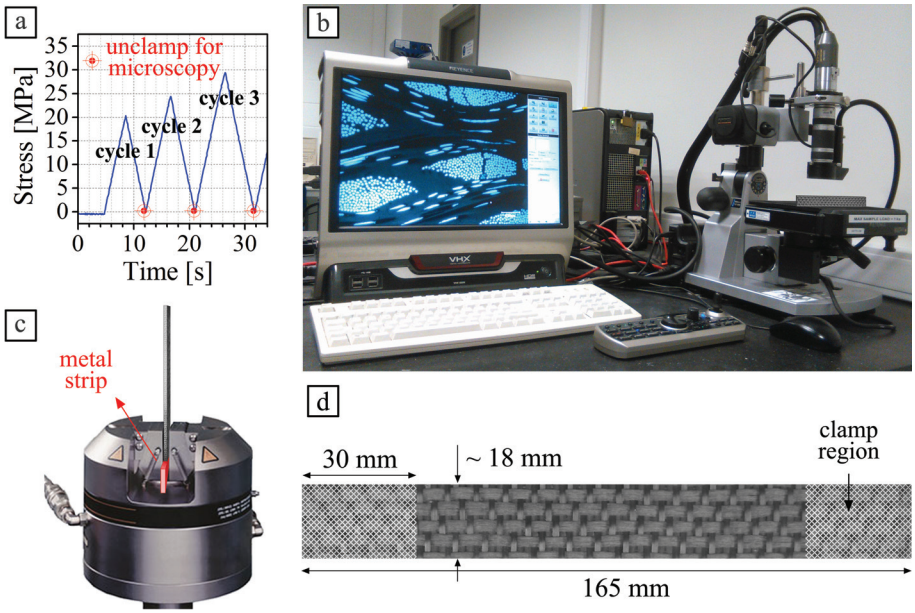


Figure 4-27: First three cycles of the loading-unloading experiment (a), specimen on the motorized stage of the Keyence during 3D image stitching of its edge (b), the clamped specimen, standing on a thin metal strip in order to preserve the clamp length throughout the experiment (c), and the specimen dimensions (d)

Two types of specimens were tested, warp-oriented and weft-oriented, both stacked with the weft-dominated side of the reinforcing fabric facing outward. Following the naming convention that has been used throughout this work, these types will be identified as warp-B and weft-B, respectively. For each of these types, three specimens were tested. The specimen dimensions are shown in Figure 4-27.d. All specimens failed in the gauge area, sufficiently far away from the clamp region.

#### 4.5.2.b Results

The results of the experiments are presented in the same way as was done for method 1 for the ease of comparison. Figure 4-28 and Figure 4-29 depict the results over two consecutive unit cells along the edge of a warp-B specimen. As all three of the warp-B specimens presented similar damage, only one of them is displayed. Two different damage phenomena were seen amongst the weft-B specimens, and therefore, two specimens of this type were displayed, i.e. on Figure 4-30 and on Figure 4-31. All figures display the specimen edge on three different stress levels, and the according frames were referenced to a typical stress-strain graph of the laminates. Note that this is not the curve of the specimen at hand, as the strain was not recorded during these experiments. The mounting-unmounting operations and the handling during microscopy in between cycles would make it complicated to have strain gauges on the specimen surface during the test. Damage was marked on the figures for clarity. Analogously as in the figures of method 1, the markings are color-coded according to the initiation stress.

The warp-B specimen presented in Figure 4-28 and Figure 4-29 showed no signs of damage at a stress of 70 MPa, but several occurrences were spotted at 75 MPa. On the typical stress-strain graph for warp-oriented loading, these stresses correspond to a strain window for damage initiation between about 0.40% and 0.50%. This agrees well with the initiation strain that was measured with method 1 for this specimen type, i.e. between 0.36% and 0.45% (Figure 4-23 and Figure 4-24). Crack-closure after unloading hence seems not to be an issue in this composite material, even though this is a common challenge when studying composites in general. A possible explanation is that the steel fibers deform plastically where they bridge a crack, and hence keep the crack open even after the load is removed. The strong tendency of the matrix to form cusp marks also helps to make any damage permanently visible.

In terms of damage morphology and propagation as well, the results look very similar as those found with method 1. Small separate defects initiate on vertical lines inside the transversal yarns, in the form of fiber detachments and cusp marks in the matrix between fibers. As the stress is increased, some of the separate defects grow and merge into cracks, while others show little evolution. Especially on the unconfined edges of the yarns, where the inter-fiber distance is large, the defects tend to appear and remain in the form of single fiber detachments and local cusp marks. Damage typically initiates inside the transversal yarns, and propagates towards the yarn border. Once the border is reached, the crack is cusped by the matrix. Damage appears well spread along the length of the specimen, and at least some similarities can be observed when comparing the damage patterns on the geometrically equivalent Figure 4-23 and Figure 4-24.

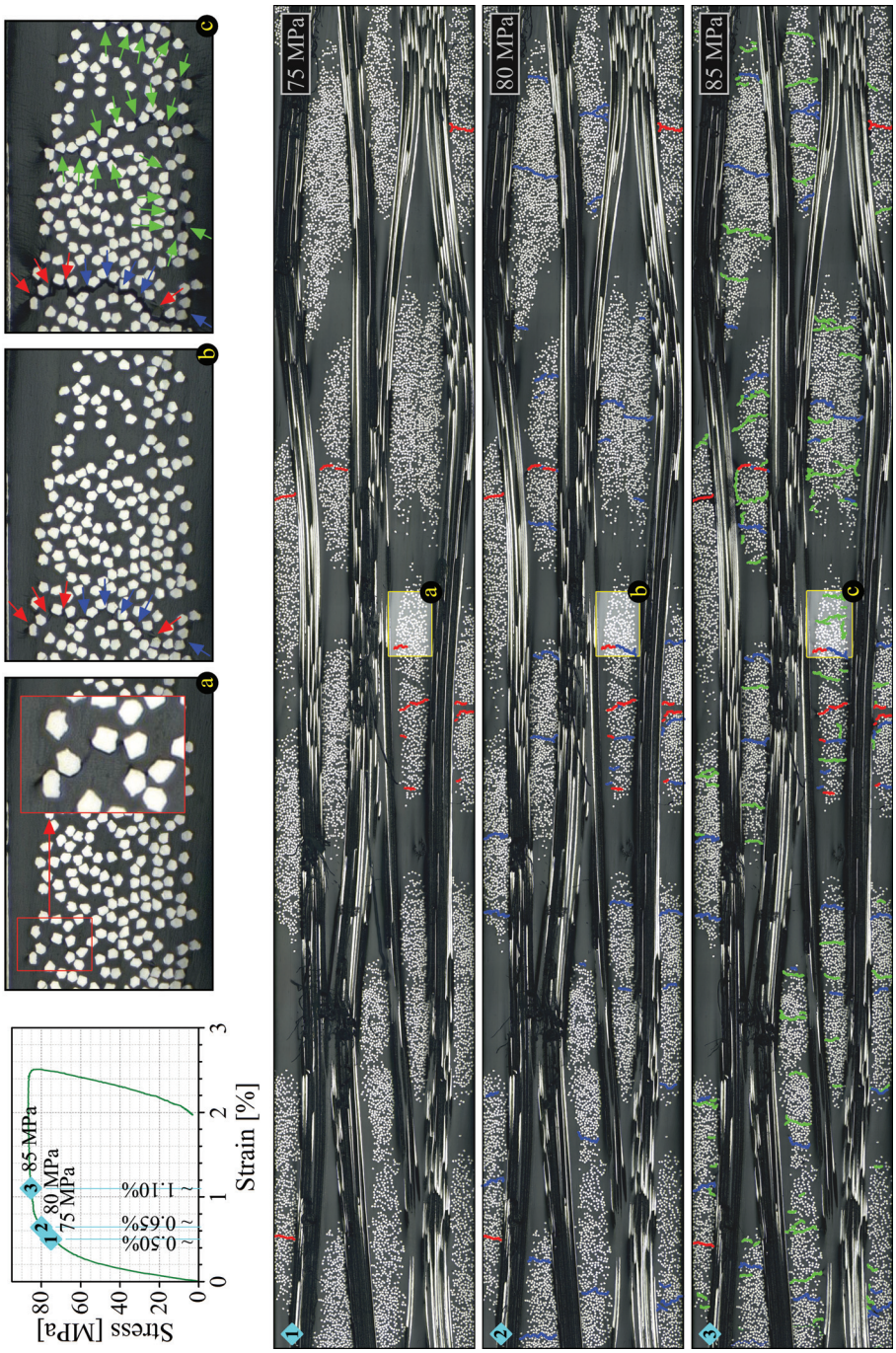


Figure 4-28: Damage initiation and propagation in the warp-B specimen – unit cell 1

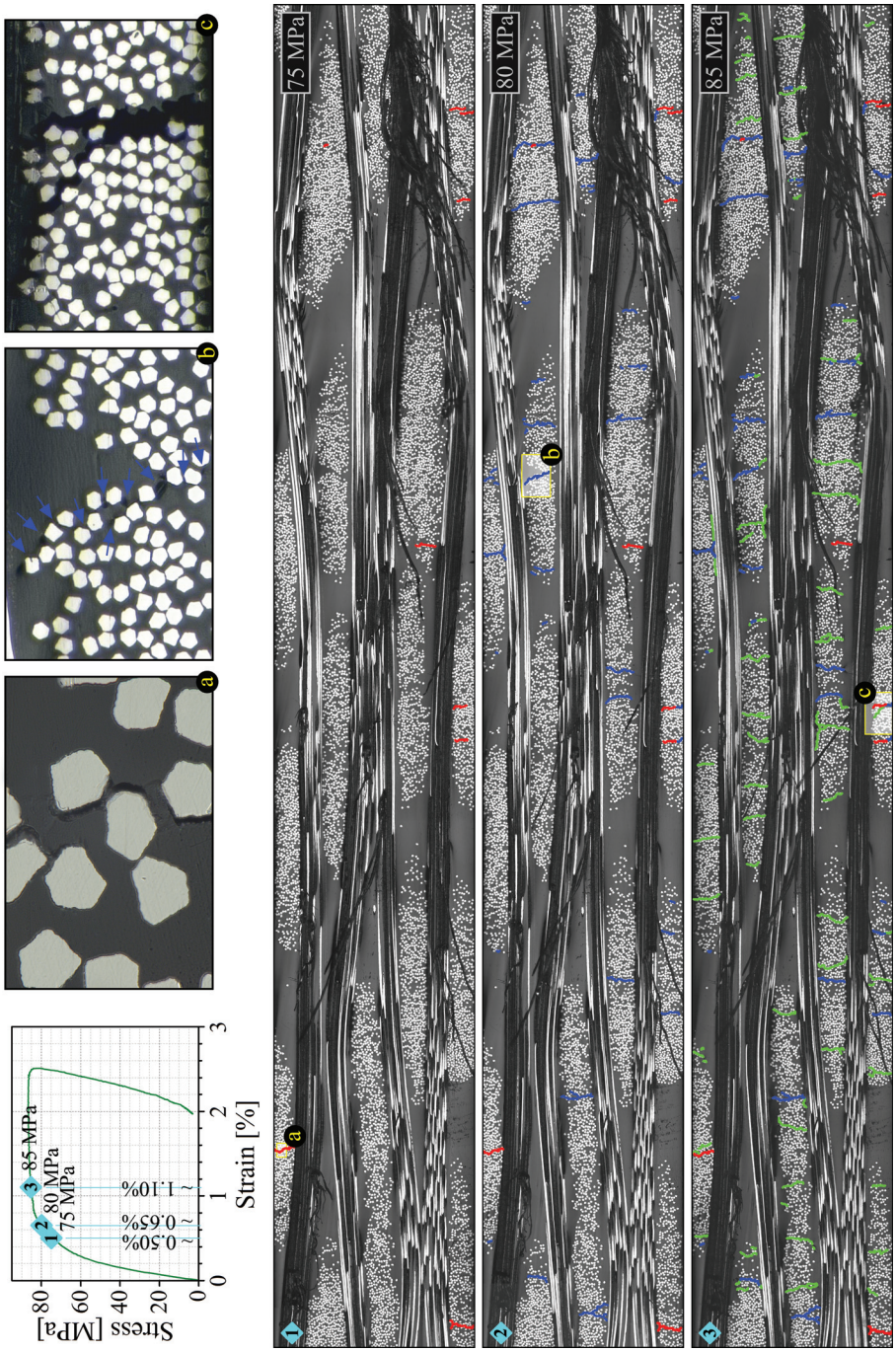


Figure 4-29: Damage initiation and propagation in the warp-B specimen – unit cell 2

The first signs of damage in the weft-B specimens in Figure 4-30 and Figure 4-31 were found at a stress of 70 MPa, which means that initiation must have taken place between 65 MPa and 70 MPa. On the typical stress-strain graph for weft-oriented loading, this corresponds to a strain window for damage initiation between about 0.40% and 0.45%. This agrees well with the initiation strain that was measured with method 1 for this specimen type, i.e. between 0.34% and 0.44% (Figure 4-26). This confirms that crack-closure after unloading is not an issue in this composite. When it comes to the damage morphology and propagation as well, the specimens tested with method 2 show many similarities to those tested with method 1. Damage appears in the form of vertical cracks through the transversal yarns, often spanning the full height of the yarn, as is clear from detail 'a' on Figure 4-30. The cracks initiate inside the transversal yarns due to fiber-matrix debonding, and they are cusped by the matrix when they reach the yarn border, as shown on detail 'a' on Figure 4-31. If the distance to a neighboring transversal yarn or the specimen surface is sufficiently small, cracks can bridge the matrix pocket, as shown on detail 'c' on Figure 4-30. Cracks were also found to redirect along the yarn border, causing the transversal yarn to locally debond from the matrix. A few examples are enlarged on details 'b' and 'c' on Figure 4-31. Damage is at all times well spread along the length of the specimen, and the crack pattern shows some periodicity with respect to the geometry of the reinforcement.

Along with the many parallels between the results from the two experimental methods, some refinements are in order. On both the weft-oriented specimens tested with method 1, cracks were found to concentrate in 'concentration bands'. These oblique, band-like regions typically contained about one quarter of the textile unit cell. Two out of the three weft-B specimens tested with method 2 show similar concentration bands. One of them is shown on Figure 4-30. On the other specimen, shown on Figure 4-31, the amount and the width of the cracks are concentrated over about three quarters of the unit cell. Also atypical is that the quarter with little crack concentration is the band that includes the crimp yarns at the specimen surface. It is important to remember that the three-dimensional nature of the reinforcement cannot be appreciated on the two-dimensional edge section. The material directly behind the edge section can be expected to influence the damage pattern on the edge at least to some extent. Note, for instance, that the specimen on Figure 4-30 did not fail in the concentration band, which clearly indicates that this fatal crack originated from within the bulk of the specimen. Another dissimilarity in the damage patterns when comparing several weft-oriented specimens is the phenomenon of splitting of longitudinal yarns. This was observed in the weft-B specimen tested with method 1, but not in the weft-A specimen. From the three weft-B specimens tested with method 2, only one showed this type of damage, i.e. the specimen on Figure 4-30 (detail 'b'). Due to the three-dimensional nature of the material, this observation again does not necessarily mean that not all specimens have split longitudinal yarns. It is possible that these phenomena do take place in the internal sections of the specimens.

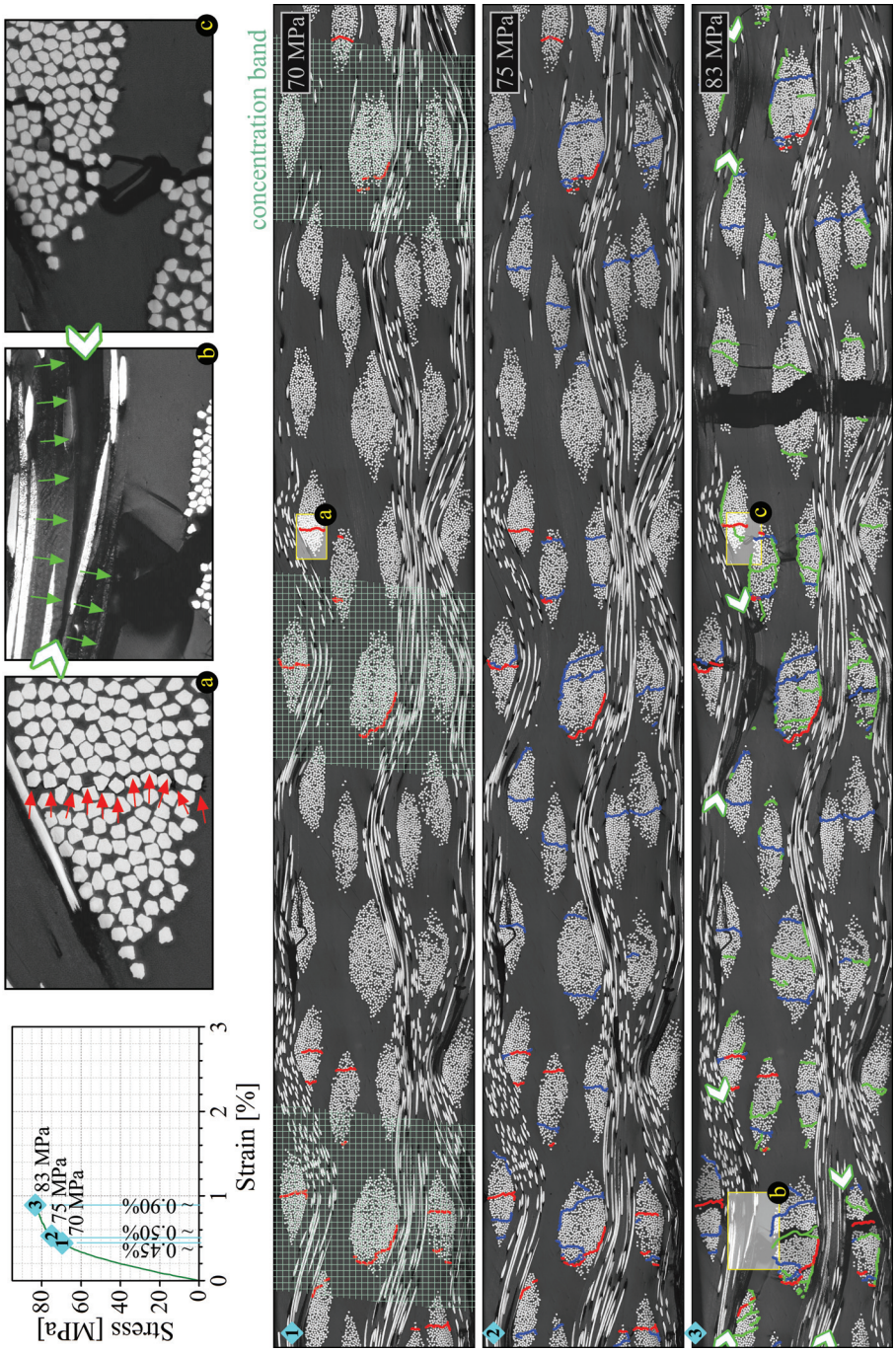


Figure 4-30: Damage initiation and propagation in weft-B specimen number 1

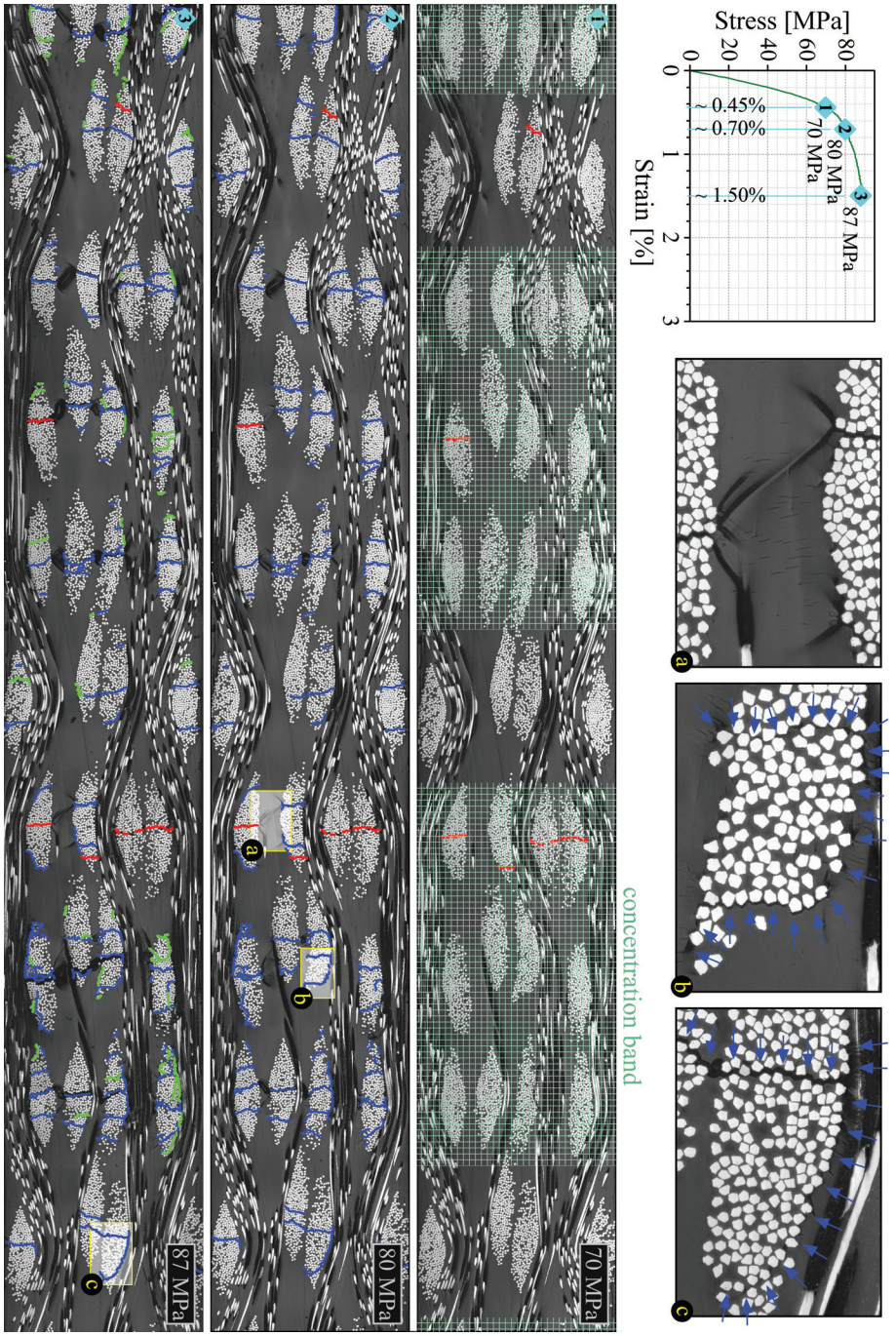


Figure 4-31: Damage initiation and propagation in weft-B specimen number 2

## 4.6 CONCLUSION

In this chapter, the geometrical characteristics of the fabric reinforcement were studied on high resolution microscopic images of a polished edge of the laminates. Several manual, semi-automatic and fully automatic procedures were developed for abstracting aspects of the reinforcement geometry from the images, and for calculating the corresponding characteristics. On the ply level, ply shifts and layer nesting were studied. A nesting percentage of 106.7 % was calculated – this corresponds to an increase in fiber volume fraction of 6.7% due to nesting. Despite the ply shifts and the layer nesting, the laminate edge was found to show periodicity to some extent. On the yarn level, the undulations and the cross sections were studied, and the variabilities were calculated. For the warp yarns, an average crimp angle of 6.6° ± 1.2° was found. As expected, the crimp angle is much larger in the weft yarns, with an average value of 18.0° ± 2.9°. No differences in the undulations were found between yarns in the inner and outer layers of the laminate. The cross sectional area of the warp yarns was determined at 0.36 mm² ± 0.02 mm². The weft yarns are more than double this size, with an area of 1.10 mm² ± 0.13 mm². The sectional area did not seem to vary significantly along the yarn path, but the shape factor (i.e. the width over thickness ratio) of the warp yarns in the inner layers was larger than that in the outer layers. This dependency was not seen in the weft yarns. Consistent with the variability in sectional area, the fiber volume fraction differs from yarn to yarn, ranging between 44.1% and 60.8% over the 104 warp yarns under consideration, with an average of 54.6% ± 2.8%. For the weft yarns, values between 29.1% and 48.4% were found over the 40 yarns under study, with an average of 35.9% ± 4.4%. When it comes to the intra-yarn variability in fiber volume fraction, results depend largely on the area over which is averaged – this was characterized by the smoothing radius. A smoothing radius of 4 times the fiber diameter was found to avoid noise, yet to preserve the important trends in the fiber volume fraction distribution. With this amount of smoothing, values within the warp yarns range between 11% and 80%, with an average of 54.6% ± 8.3%. Within the weft yarns, fiber volume fractions between 1.5% and 68% were found, with an average of 35.9% ± 8.8%.

After studying the characteristics and the variabilities of the reinforcement geometry, its effect on the strain fields and the crack pattern on the polished specimen edge was investigated. In general, the strain fields showed a strong correlation to the corresponding internal laminate structure. This indicates that the edge section is not heavily affected by the underlying sections when it comes to the distribution of the in-plane strain components. At least, this is true at least up to a strain of about 0.8% – or the working range of the DIC method for this application. The location of final rupture could not at all be anticipated by analyzing the DIC results, which shows that a fatal

crack may originate inside the laminate, to only travel to the edge at the very final moment.

The observations on damage initiation, propagation and morphology are consistent with those on the strain distribution. In general, the damage initiation and morphology show a strong relation with the internal architecture. For instance, damage always initiates in the form of fiber detachments inside the transversal yarns at a strain around 0.4%, regardless of the loading direction or the stacking system. When the distance between neighboring fibers is sufficiently small, the detachments grow into cracks. This makes that the loosely packed weft yarns show many singular fiber detachments, while the more densely packed warp yarns tend to be cracked across their full height. Similarly, if the distance to a neighboring transversal yarn or to the specimen surface is small enough, the cracks can bridge the matrix pocket in between, leaving typical cusp marks under an angle of 45°. Damage keeps initiating as the strain is increased, and it appears well spread along the length of the specimen, in a pattern that shows the same periodicity as the reinforcement. Despite the strong relation between the crack initiation and morphology and the internal structure, many of the phenomena, especially regarding crack propagation, are unpredictable. One example is that some of the earliest cracks never open up, while others appear only late, yet grow rapidly. Also, the cracks were found to concentrate in certain bands in some, yet not all of the weft-oriented specimens. Moreover, the location and width of these concentration bands was not constant across all specimens. The section on crack morphology was ended by noting again that cracks can also initiate in sections behind the polished edge under study. Those cracks will also appear in a periodic pattern, as the internal sections are periodic as well, but they will not accord to the reinforcement geometry on the visible edge.

In summary, the reinforcement geometry is imperfect and variable on every length scale, and the observations on damage and strain showed a strong relation with the internal structure of the composite laminates. This certainly explains why the perfectly periodic RVE model from Chapter 3 failed to produce correct stress and strain distributions. In the next chapter, a new modeling approach will be proposed and elaborated. This approach was inspired by the experimental observations that were the subject of the current chapter, especially by the strong agreement between the material mechanics and the reinforcement geometry on the laminate edge.

## 4.7 REFERENCES

[1] Daggumati S, De Baere I, Van Paepegem W, Degrieck J, Xu J, Lomov SV, et al. *Local damage in a 5-harness satin weave composite under static tension: Part I – Experimental analysis*. Composites Science and Technology; 70: 1926-1933. 2010.

[2] Yurgartis SW, Morey K. *Measurement of yarn shape and nesting in plain-weave composites*. Composites Science and Technology; 46: 39-50. 1993.

[3] Olave M, Vanaerschot A, Lomov SV, Vandepitte D. *Internal geometry variability of two woven composites and related variability of the stiffness*. Polymer Composites; 33: 1335-1350. 2012.

[4] Olave M, Vara I, Husabiaga H, Aretxabaleta L, Lomov SV, Vandepitte D. *Nesting effect on the mode I fracture toughness of woven laminates*. Composites Part A: Applied Science and Manufacturing; 74: 166-173. 2015.

[5] Olave M, Vara I, Usabiaga H, Aretxabaleta L, Lomov SV, Vandepitte D. *Nesting effect on the mode II fracture toughness of woven laminates*. Composites: Part A; 74: 174–181. 2015.

[6] Karahan M, Lomov SV, Bogdanovich AE, Mungalov D, Verpoest I. *Internal geometry evaluation of non-crimp 3D orthogonal woven carbon fabric composite*. Composites Part A: Applied Science and Manufacturing; 41: 1301-1311. 2010.

[7] Bale H, Blacklock M, Begley MR, Marshall DB, Cox BN, Ritchie RO, et al. *Characterizing Three-Dimensional Textile Ceramic Composites Using Synchrotron X-Ray Micro-Computed-Tomography*. Journal of the American Ceramic Society; 95: 392-402. 2012.

[8] Vanaerschot A, Cox BN, Lomov SV, Vandepitte D. *Stochastic framework for quantifying the geometrical variability of laminated textile composites using micro-computed tomography*. Composites Part A: Applied Science and Manufacturing; 44: 122-131. 2013.

[9] Jortner J. *Microstructure of cloth-reinforced carbon-carbon laminates*. Carbon; 30: 153-163. 1992.

[10] Saunders RA, Lekakou C, Bader MG. *Compression and microstructure of fibre plain woven cloths in the processing of polymer composites*. Composites Part A: Applied Science and Manufacturing; 29A: 443-454. 1998.

[11] Lomov SV, Verpoest I, Peeters T, Roose D, Zako M. *Nesting in textile laminates: geometrical modelling of the laminate*. Composites Science and Technology; 63: 993-1007. 2003.

[12] Chen B, Chou T-W. *Compaction of woven-fabric preforms: nesting and multi-layer deformation*. Composites Science and Technology; 60: 2223-2231. 2000.

[13] Shady E, Gowayed Y. *Interlaminar Shear Stress Distribution Between Nested Layers of Plain Weave Composites*. Polymer Composites; 31. 2010.

[14] MatchID. *MatchID software*. Available from: http://www.matchid.org/. 2015.

[15] ASTM Standard. D3039/D3039M. *Standard Test Method for Tensile Properties of Polymer Matrix Composite Materials*. West Conshohocken, PA: ASTM International; DOI: 10.1520/D3039_D3039M-14. Available from: www.astm.org. 2014.

[16] Purslow D. *Matrix fractography of fibre-reinforced epoxy composites*. Composites; 17: 289-303. 1986.

# Chapter 5

## NUMERICAL EVALUATION OF GEOMETRICAL VARIABILITIES

*In this chapter, the effect of the geometrical variabilities on the mechanical behavior of the composite laminates is investigated numerically. After introducing the chosen 2D approach in the first section, its validity is checked in the second section, and the modeling methodology is laid out in the third section. Section four presents the numerical results, with the strain fields evaluated with respect to the experimental findings using DIC, and the stresses validated against the observed crack locations. The influence of the intra-yarn variability in fiber volume fraction was assessed in section five. Finally, the chapter is closed with a conclusion in section six.*

## 5.1 INTRODUCTION

In the previous chapter, geometrical variabilities within the composite laminates were reported on every possible length scale. On the macro-scale, the plies are shifted and nested. On the meso-scale, the yarn cross sections and undulations vary from yarn to yarn. On the micro-scale, finally, the fibers are not homogeneously distributed within the yarns. None of these variabilities were accounted for in the RVE model that was presented in Chapter 3. Implementing any local geometrical variations in this type of model is not even an option, as all features are mathematically repeated throughout the material structure by the periodic boundary conditions. Nonetheless, RVE modeling is the common strategy for meso-scale analysis of textile composites, and it has been extensively and successfully used to predict the global elastic properties of composite materials [1-3]. This type of calculation – termed homogenization – does not require precise localizations for stresses and strains, as it is based on volume-averages. When it comes to predicting damage, on the other hand, accurate stress and strain distributions are paramount. Many researchers have pointed out the sensitivity of the predicted localizations on various modeling choices. The need for a correct representation of the yarn geometry, especially when predicting damage initiation, was emphasized by Whitcomb [4]. Concluding his pioneering work on 3D finite element analysis of plain weave composites, he states that 'some of the most severe strain concentrations occur where the weave geometry is most difficult to model with confidence'. The importance of ply shifting and nesting to the damage behavior has been commented on as well, both in experimental [5, 6] and numerical [7] studies. The mismatch between the experimental findings and the numerical stress and strain distributions obtained with the RVE model that was presented and used in Chapter 3 only confirms that some of the non-periodic features need to be represented if a model is expected to produce useful stress and strain distributions.

The most straightforward way to take ply shifting into account is to actually model the whole laminate for several ply configurations, as was performed by Daggumati et al. [7, 8]. An obvious drawback of this approach is the extensive model size. Ivanov et al. [9, 10] addressed this problem by introducing a procedure for analyzing the laminate meso-scale by analytically combining results from boundary value problems on a single unit cell. Aforementioned modeling techniques may account for layer shifting, but they do not cover the nesting phenomenon. During production, the layers of fabric are not only shifted, but also pressed together and pushed into each other. Numerical research on layer nesting is often focused on the compaction phenomenon itself, rather than on its effects on the post-production laminate behavior. Some contributions that aim at constructing a nested geometry are the work by Shady and Gowayed [11] on a 2D representation of nesting and the 3D finite element approach by Lomov et al. [12]. Both come to a nested geometry by stacking shifted layers of

fabric, forcing every layer to sink into the valleys of the neighboring layers. Grail et al. [13] obtained a 3D nested reinforcement geometry by simulating the preforming step and remeshing the resulting geometry. This method is more complex, but the resulting model geometry accounts for the yarn deformations after preforming and compaction. Another way to include more realistic yarn shapes into the analysis was elaborated by Hivet and Boisse [14]. The section shape characteristics were determined based on microscopic images and a schematic yarn shape was set at specific control sections along the trajectory. A complete 3D model of the yarn was obtained through a smooth interpolation between the control sections along the imposed trajectory. Voxel-based methods as well typically reflect realistic yarn shapes, as the geometry is usually extracted from X-ray computed tomography scanning data. A downside is the regular rectangular mesh of voxels without definition of a smooth surface between yarns and matrix. This leads to spurious stress concentrations on the boundaries between components that can only be alleviated by ultra-fine local remeshing [15].

Research that is focused on assessing the influence of geometrical variabilities on the mechanical properties of textile composites has often been directed towards virtual testing. Real experiments on this matter would require large sets of test specimens, and preferably a laminate production process that allows a certain control over the separate geometrical parameters. Blacklock et al. [16] presented a Monte Carlo algorithm based on Markov Chain operators to transform the statistical data measured by Bale and coworkers [17] into virtual composite specimens. The yarn geometry was represented as a concatenation of one-dimensional line elements in three-dimensional space, in accordance with the framework of the Binary Model of textile composites [18]. Rinaldi et al. [19] expanded this method with algorithms for generating solid, three-dimensional yarn representations. Vanaerschot et al. used their own experimental data [20] to build stochastic models in the multi-scale textile software WiseTex [21], and they later proposed a general, multi-scale strategy to develop realistic stochastic replicas of a composite [22].

As models become more realistic, both size and calculation time increase. Moreover, every level of detail makes the process of constructing the model more complex and cumbersome. Experimental validation of the model often lacks, because it is difficult to establish the strain concentrations and the damage morphology inside a test specimen. From the combination of the abovementioned limitations, the idea originated to try a 2D modeling approach on the polished edge of a laminate specimen. The advantages would be ample: (1) the geometry could be constructed more easily based on the high resolution microscopic images of the edge, (2) the possible level of detail would practically be unlimited; variable yarn shapes and nesting would obviously be taken into account, but representing the inhomogeneity in fiber volume fraction in the transversal yarns would also be an option, (3) validation of the stress

and strain patterns would be straightforward, as the polished edge can be monitored during loading, (4) the runtime for a well-meshed 2D model is in the order of minutes. The question remains to what extent an albeit detailed 2D model will be able to capture the mechanics of the complex 3D internal structure of a textile composite. The strong correlation that was discussed in the previous chapter between the visible internal geometry and the strain field on the specimen edge is at least promising. In the next section, the approach will further be validated from a conceptual point of view on a perfectly periodic structure. The method by which the actual laminate specimens were modeled will be explained in section 5.3. In section 5.4, the numerical results will be compared to the experimental findings, and the effect of the variability of the intra-yarn fiber volume fraction will be investigated in section 5.5. Finally, the conclusions will be summarized in section 5.6.

## 5.2 VALIDITY OF 2D MODELING

The concept of the 2D approach was validated using a numerical experiment, as illustrated in Figure 5-1. The goal of the experiment is to investigate to what extent a 2D model can provide a correct distribution of the in-plane stress components. To this end, the results of three 2D plane strain models, representing three slices of the RVE (cf. Figure 5-1.b, "slices", models 1 to 3), were compared to those of the corresponding cross sections through the full 3D RVE model (cf. Figure 5-1.a, sections 1 to 3). The first slice cuts through the center of a weft yarn, the second one is chosen at a quarter distance between weft yarn centers, while the third one is in between weft yarns. Additionally, the stresses on the free edge of the 3D RVE model (cf. Figure 5-1.a, section 4) were compared to those from a 2D plane stress model (cf. Figure 5-1.b, "free edge", model 4). This case would be applicable for a model representing the polished edge of a specimen.

The results on Figure 5-1 are obtained at a strain of 0.4%. The results for the first three cases – the ones representing cross-sections through the RVE – were obtained with in-plane periodic boundary conditions (PBC's) on the 3D RVE. As explained earlier in section 3.4, in-plane PBC's impose periodicity on all the boundaries of the RVE except on the top and bottom plane. Therefore, they make the RVE behave as a single ply, endlessly patterned along both in-plane directions. The corresponding 2D slice models were given periodic boundary conditions along the loading direction, and a plane strain condition perpendicular to the plane of the model. In order to get the stresses on the free edge of the 3D model for case 4, the periodicity conditions between the free edge and its opposite side were removed. This model hence represents a single ply, patterned only along the loading direction. The corresponding 2D model was given the same periodic condition along the loading direction as the other 2D models, but the assumption of plane stress was made for this case.

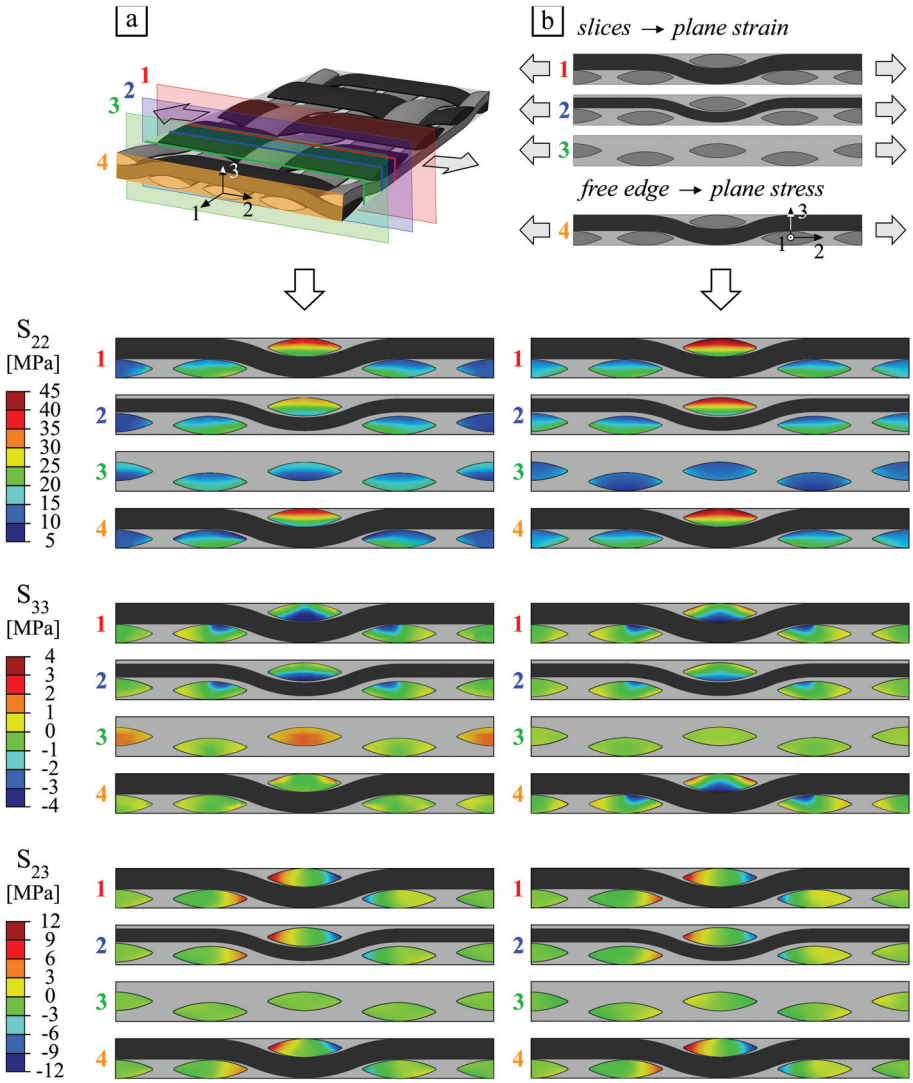


Figure 5-1: Stress distributions in the cross sections (1, 2 and 3) and on the free edge (4) of a 3D RVE model (a), and in the corresponding 2D slice/free edge models (b)

From Figure 5-1, it is clear that the in-plane stress predictions match nearly perfectly for the highly symmetrical section in case 1. If the section moves away from the center of the weft yarn, as in case 2, the direct stresses $S_{22}$ and $S_{33}$ are overestimated by the 2D model, but the distribution patterns are still similar. For the third case, in which the weft yarn is not represented in the 2D model, the stresses do not comport, nor in value, nor in distribution. For the fourth case – the free edge – the $S_{22}$ stress is slightly overestimated by the 2D model, but the pattern is similar. The $S_{33}$ stress is exactly the

same when it comes to the regions under tension, but the prediction by the 2D model has false compression zones in the inside and outside bends of the weft yarn. Note, however, that $S_{33}$ is by far the least relevant stress component, considering its low values. Finally, the match for the shear stress S23 is good, even though the peaks on the edges of the crimp yarn have shifted a little downward in the 2D model. In general, the in-plane stress predictions by a 2D model comport surprisingly well, especially qualitatively, as long as the load-carrying weft yarn is represented. Quantitatively, the 2D model is less accurate as the chosen section is further away from the weft yarn center.

Note that the 2D models of case 1 and 4 produce nearly identical in-plane stress distributions. The only difference between these two is the out-of-plane boundary condition, i.e. plane strain in case 1, and plain stress in case 4. This boundary condition may not affect the in-plane stresses, it still has a fundamental effect on the out-of-plane stress. In case 1, this component takes on a similar pattern as the $S_{22}$ component, but it is about three times smaller in value. In case 4, on the other hand, this component is zero by definition.

The intention behind the 2D modeling concept is to study the composite laminate by analyzing its free edge, which corresponds to case 4 in Figure 5-1. The concept check first of all proves that the predictions by a 2D model are usable for this purpose. In addition, the results indicate that the stress distribution on the free edge of the laminate is very similar to the distribution in the inside sections. Therefore, all findings – both experimental and numerical – on the edge of the laminate can be expected representable for the inside of the laminate as well.

## 5.3 MODELING METHODOLOGY

The 2D models that will be presented in this chapter were constructed by the methodology that is explained step by step in Figure 5-2.

The first step is to abstract the outlines of the reinforcement geometry from a high resolution microscopic image of the laminate edge, to construct the centerlines of the longitudinal yarns, and to draw the bounding box of the model. The bounding box is a simple rectangle that marks the edges of the region to be modeled. The outlines of the reinforcement geometry and the centerlines can be obtained by the methods that were explained throughout section 4.3. More specifically, the method for drawing the outlines of the longitudinal yarns was explained in section 4.3.2, along with the automatic construction of the centerlines from the pixel positions of the yarn borders. A semi-automatic abstraction procedure for the transversal yarns was set forth in section 4.3.3. The second step of the method is to convert the image file with the outlines, the centerlines, and the bounding box (TIF format) into a DXF file, and to

import this DXF into Abaqus as a sketch containing a cloud of points. The imported points are connected with splines in the sketch module, and the blank 2D model is partitioned into regions of warp, weft, and matrix. The file conversion from TIF to DXF does not retain scale or position. This is why the bounding box must be imported along with the outlines of the reinforcement, i.e. to serve as a reference frame. The third step is to assign the correct elasticity constants to the respective regions in the model. The isotropic properties of the matrix can be found in Table 3-1. For the transversal yarns, the elastic constants were calculated yarn by yarn with the analytical homogenization formulas by Chamis [23] (cf. section 3.2.1), in accordance with the fiber volume fraction of each yarn. The volume fractions were determined automatically from the image file, as explained in section 4.3.4. The different material models were then automatically generated and assigned to the correct transversal yarn by direct scripting on the Abaqus input file. Ideally, the material properties of the longitudinal yarns as well would vary from yarn to yarn, and even along the length of the yarns, in accordance with the amount of fibers in the sections in and just behind the visible edge. This is, however, impossible to achieve based on microscopic images. Fibers that are in the section just behind the edge will not be visible, but they will contribute just as much to the stiffness. Other fibers that actually were showing, on the other hand, may have been ripped out during polishing. Therefore, the longitudinal yarns were assumed to be homogeneous, and they were given the transversely isotropic material properties that were determined through numerical micro-to-meso homogenization in section 3.2.2, as reported in Table 3-4. Note that the longitudinal yarns will merely serve as a boundary condition for the transversal structure of matrix and fibers; they will not be the subject of detailed investigations on stress and strain distributions themselves. The fourth step of the method is to assign the correct material directions to the transversely isotropic yarns. For the transversal yarns, the global coordinate system can be employed, provided that the constitutive matrix is transformed to this system. For the longitudinal yarns, the centerline can be selected to define a discrete vector field. In the fifth and final step, the model is meshed. The geometry was seeded with a global element size of 15 μm. A hex-dominated free meshing technique was used on the matrix and the transversal yarns, while the longitudinal yarns were meshed through sweep meshing with hexahedra only.

The most straightforward way to apply a load to the models is to impose a displacement on the right edge of the model, while keeping the left edge fixed with respect to the loading direction. Both edges were left free to deform transversely to the loading direction, but one point of the model was restrained in this direction in order to make the problem well-defined. These boundary conditions are not the natural boundary conditions, as they force the edges of the model to remain perfectly straight at all times. In order to avoid any boundary effects, all the 2D models were cut back over at least 3 mm – the thickness of the model – before presenting the results.

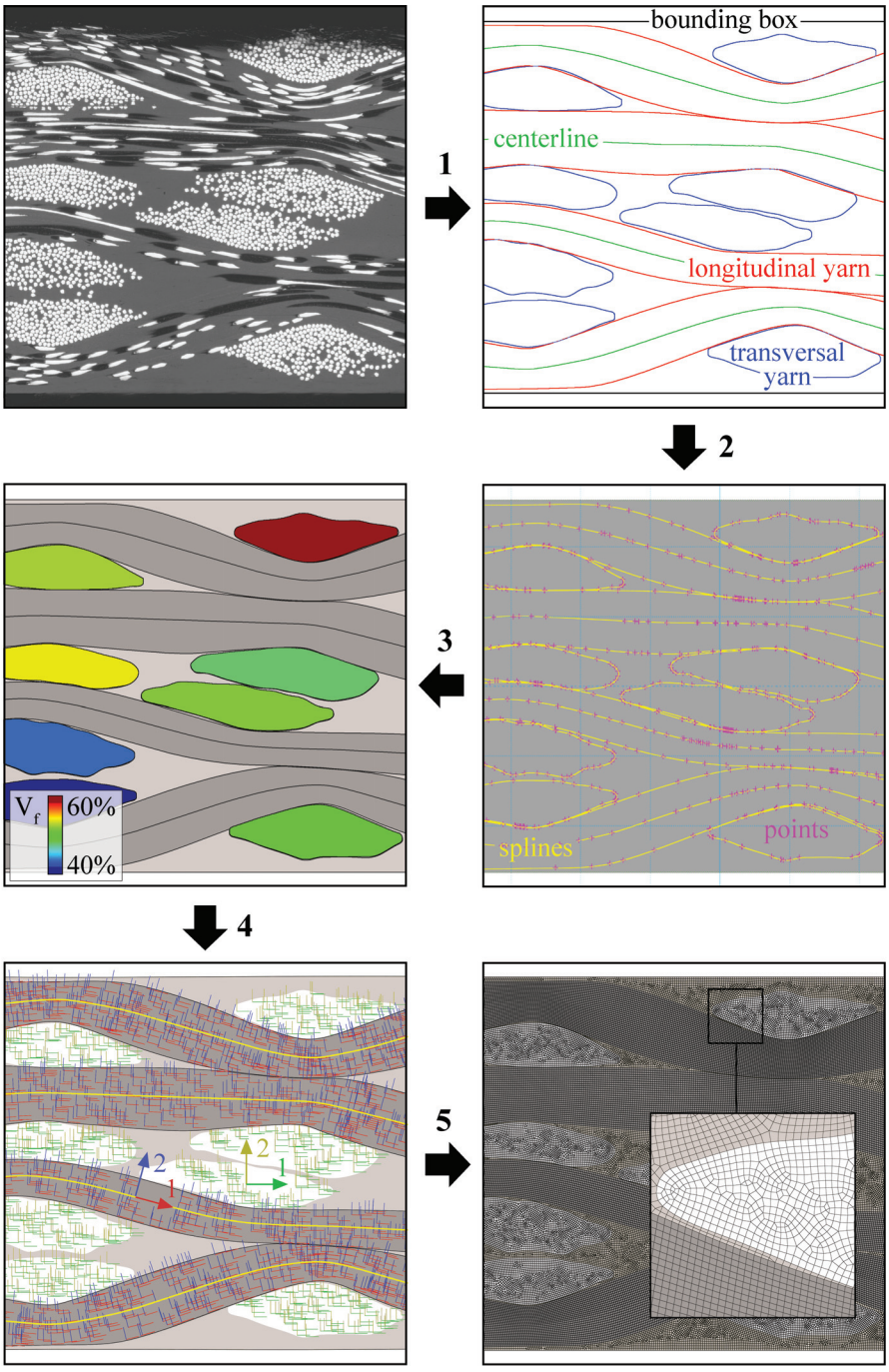


Figure 5-2: Modeling methodology for the detailed 2D models of the laminate edge

## 5.4 NUMERICAL STRAINS AND STRESSES VERSUS EXPERIMENTAL OBSERVATIONS

### 5.4.1 Numerical strain distribution versus DIC strain fields

The weft-B specimen that was presented in section 4.4 of the previous chapter has all four of the longitudinal yarns visible over nearly the full specimen length. Therefore, it qualifies for 2D modeling. The numerical strain fields for this specimen at a global tensile strain of 0.4% are presented in Figure 5-3, along with the experimental results, obtained through DIC. About halfway through the region on which the DIC camera was focused, one of the longitudinal yarns disappears from the specimen edge. For this reason, the model and the DIC results do not fully overlap. In order to facilitate the comparison, the DIC results are patterned beyond the actual measurement area.

The numerical and experimental strain patterns are generally very similar in value. The strain along the loading direction $\varepsilon_{22}$ is in both patterns mildly elevated in the crimp region on the specimen surface. The exact location, however, is not the same. The experimental result shows the highest peak central to one of the outer crimp yarns, while the FE model predicts that this strain is predominantly absorbed by the thin layer of matrix around the transversal yarns. Note that the numerical yarns have a homogeneous stiffness, which is higher than the matrix stiffness. Therefore, it makes perfect sense that the numerical strain concentrates in the matrix. The real yarns, on the other hand, are an alternation of stiff fibers in a compliant matrix, hence the yarns as well contain compliant regions for the strain to concentrate in. It is very well possible that the experimental peak signals one of the first cracks. Cracks were indeed observed to initiate at about 0.4% strain, and when it comes to the outer crimp yarns, they were typically found in a more or less central location. The FE model is not suited to simulate damage propagation, but it can give some insights on the mechanics within the yarn architecture. The longitudinal yarns can achieve the 0.4% global strain either by straightening or by straining. The numerical strain pattern points towards a combination of both. The straightening can be perceived through the elevated strain in and around the transversal crimp yarns. Apart from the crimp yarn, the longitudinal yarn as well is strained in the crimp region, especially where the crimp angle is at its highest. Here, the stiffness of the yarn is at its lowest with respect to the loading direction, so these are indeed the most compliant regions along the length of the longitudinal yarn.

The transverse strain $\varepsilon_{33}$ – the Poisson's effect – is relatively periodic in both the experimental and the numerical pattern. Lateral expansion is found in the oblique regions in between outside crimp yarns. As the load-bearing yarns in the outer layers straighten, they stretch the material in between them. Lateral compaction is found

right next to the crimp regions, where the straightening of the longitudinal yarns has the opposite effect. Although the numerical pattern and the experimental pattern match from a global point of view, one detail does not line up. In the experimental pattern, the positive strain (expansion) concentrates in the transversal yarns. As was already mentioned in section 4.4.2, this is unexpected, as unidirectional yarns are known to have a positive Poisson's ratio. Then, it was suggested that this finding could be the result of mechanical interactions between yarns and matrix on the meso-scale. Now, it seems like this hypothesis is not supported by the FE results. Indeed, the numerical pattern predicts that the expansion is above all taken up by the softer matrix.

The resemblance in the numerical and experimental patterns for the shear strain $\varepsilon_{23}$ is very good. On a larger scale, there are vertical shear bands with alternating signs. On the smaller scale, the distributions are patched such that the transversal yarns are least sheared. Both in the experimental and the numerical results, the maximum principal strain $\varepsilon_I$ is very similar, yet generally a little higher in value, than the strain along the loading direction $\varepsilon_{22}$.

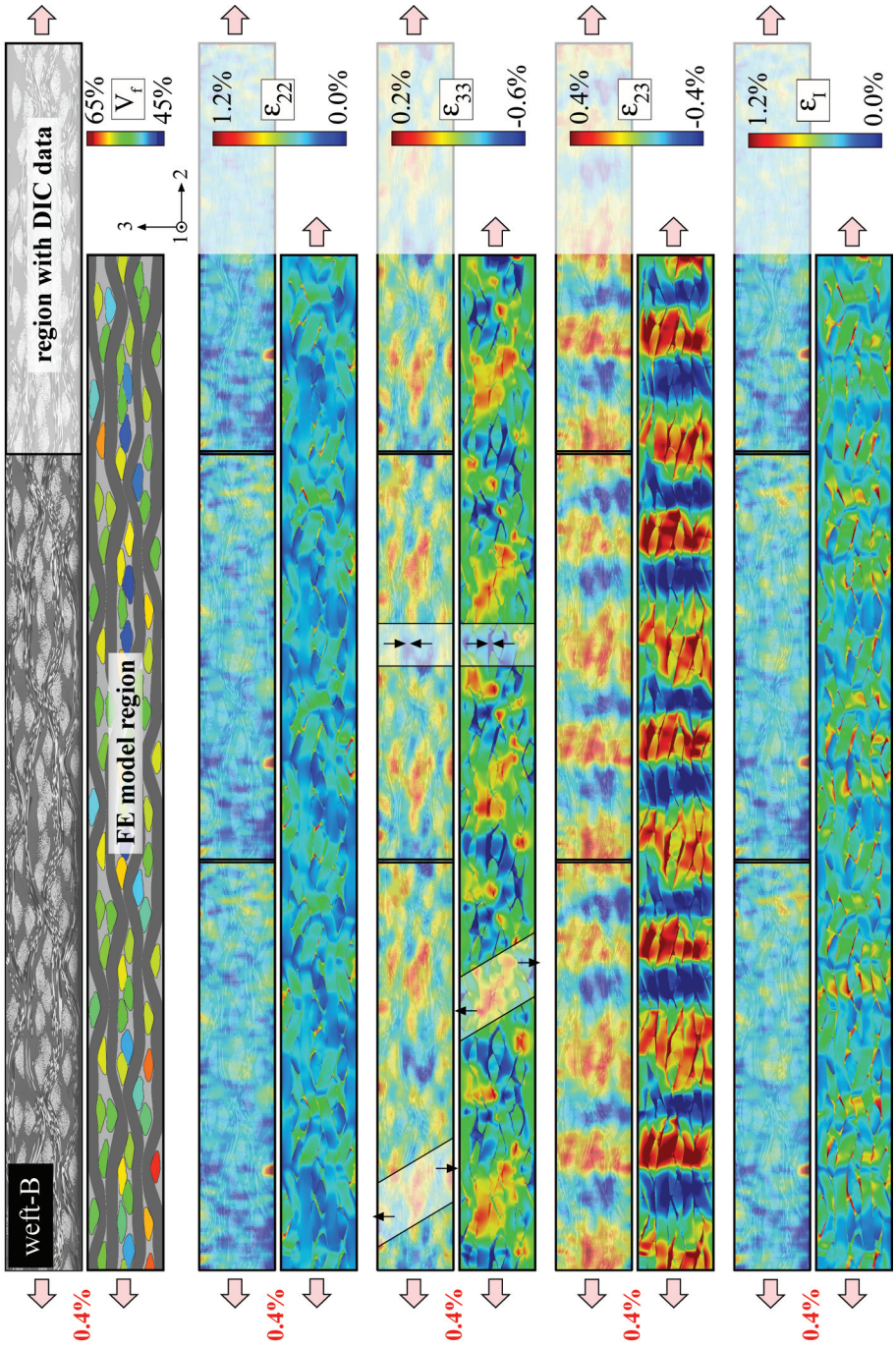


Figure 5-3: Validation of the numerical strain fields in the weft-B specimen against the experimental DIC data at a global tensile strain of 0.4%

On the warp-B specimen from section 4.4 of the previous chapter, only three out of four longitudinal yarns are showing on the polished surface. Modeling this specimen will hence give an idea of the importance of having all four load-bearing yarns represented. The numerical strain fields for this specimen at a global tensile strain of 0.4% are presented in Figure 5-3, along with the experimental results, obtained through DIC.

It seems from the numerical results that the absence of one of the load-bearing yarns renders the model asymmetrical, and that this clearly affects its behavior significantly. The numerical strain along the loading direction $\varepsilon_{22}$ is lower on the bottom of the model than on the top. This causes the model to bend when it is strained. Comparison of the other experimental and numerical strain components as well confirms that this model cannot be used to represent the laminate edge.

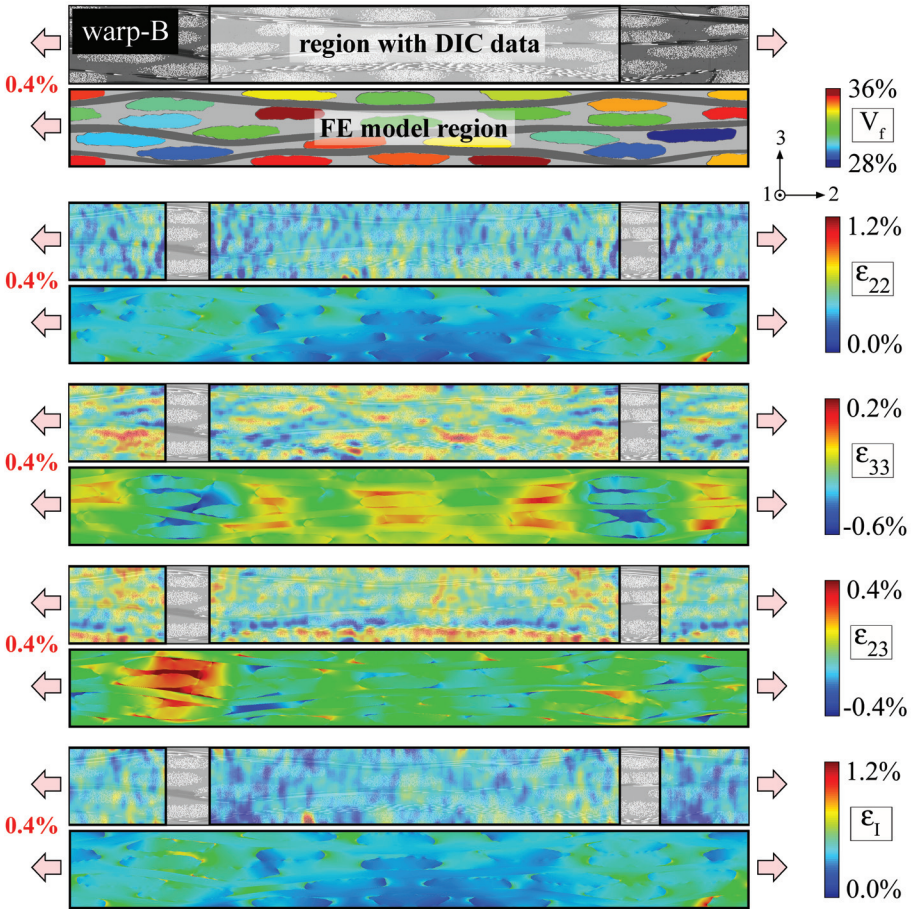


Figure 5-4: Validation of the numerical strain fields in the warp-B specimen against the experimental DIC data at a global tensile strain of 0.4%

### 5.4.2 Numerical stress distribution versus observed damage

The warp-B specimen that was presented in section 4.5.2 of the previous chapter shows all four longitudinal yarns on its polished edge, and therefore, it qualifies to be represented by a 2D model. Figure 5-5 and Figure 5-6 show the stress distribution in the transversal yarns at a global strain of 0.4% and the crack pattern at 0.5% in two consecutive unit cells of the warp-B specimen. The weft-B specimen from section 4.5.2 shows only three yarns on the edge in the section that was presented, but further down the specimen length, there is a section with all four yarns showing. This section was modeled, and Figure 5-7 and Figure 5-8 show the stresses at 0.4% strain and the cracks at 0.45% strain in four consecutive unit cells of this specimen. In general, the stress patterns in Figure 5-5 to Figure 5-8 show the same periodicity as the geometry itself.

According to Puck's theory on inter-fiber fracture [24], fracture within the transversal yarns is governed by three stresses that work on the fracture plane – the normal stress, the shear stress in the plane transversal to the fibers, and the shear stress along the fiber direction. For the case of a perfectly vertical crack in Figure 5-5 to Figure 5-8, for instance, the stress normal to the crack plane would be $S_{22}$, and the shear stress transversal to the fibers would be $S_{23}$. The shear stress parallel to the fibers would be $S_{13}$, but this component is zero by definition in a 2D plane stress model. In the case of unidirectional loading, this stress can indeed be expected to be small and the assumption is justified. If only the stresses in the 23-plane are considered, Puck's criterion reduces to the Coulomb-Mohr theory on brittle fracture of isotropic materials. This theory states that under a 2D stress state, fracture occurs along a plane on which the resultant stress is perpendicular. For any given 2D stress state, two mutually perpendicular planes – the principal planes I and II – can be found on which the resultant stress is a normal stress. These normal stresses are also known as the principal stresses $S_I$ and $S_{II}$:

$$S_I = S_{avg} + R \text{ and } S_{II} = S_{avg} - R,$$
$$\text{with } S_{avg} = \tfrac{1}{2}(S_{22} + S_{33}) \text{ and } R = \sqrt{\left[\tfrac{1}{2}(S_{22} - S_{33})\right]^2 + {S_{23}}^2} \tag{5-1}$$

Under unidirectional tensile loading, the first principal stress is the maximum principal stress, hence the most critical one.

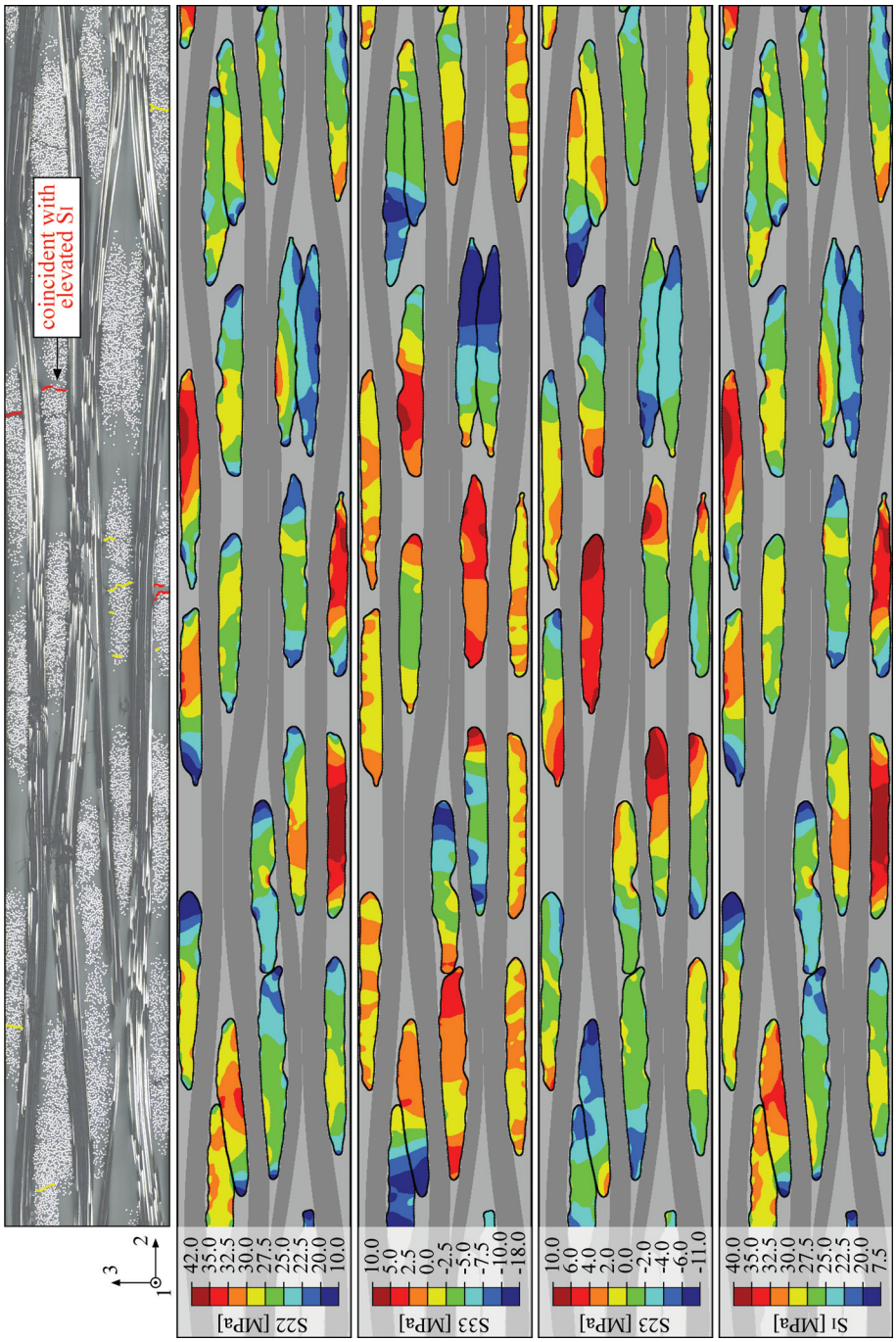


Figure 5-5: Validation of the numerical stress fields at a tensile strain of 0.4% in the warp-B specimen against the experimental crack pattern at 0.5% strain – part 1

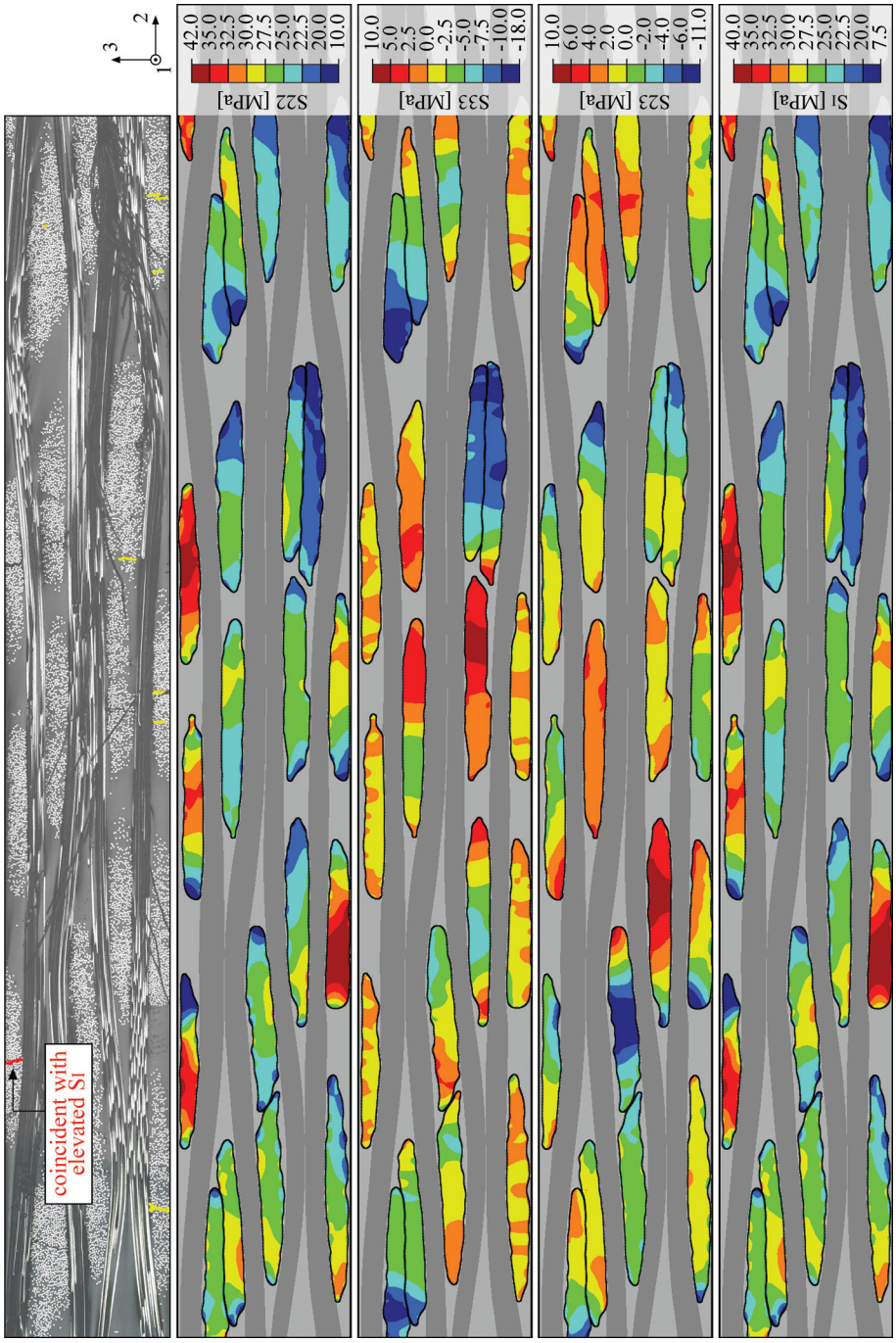


Figure 5-6: Validation of the numerical stress fields at a tensile strain of 0.4% in the warp-B specimen against the experimental crack pattern at 0.5% strain – part 2

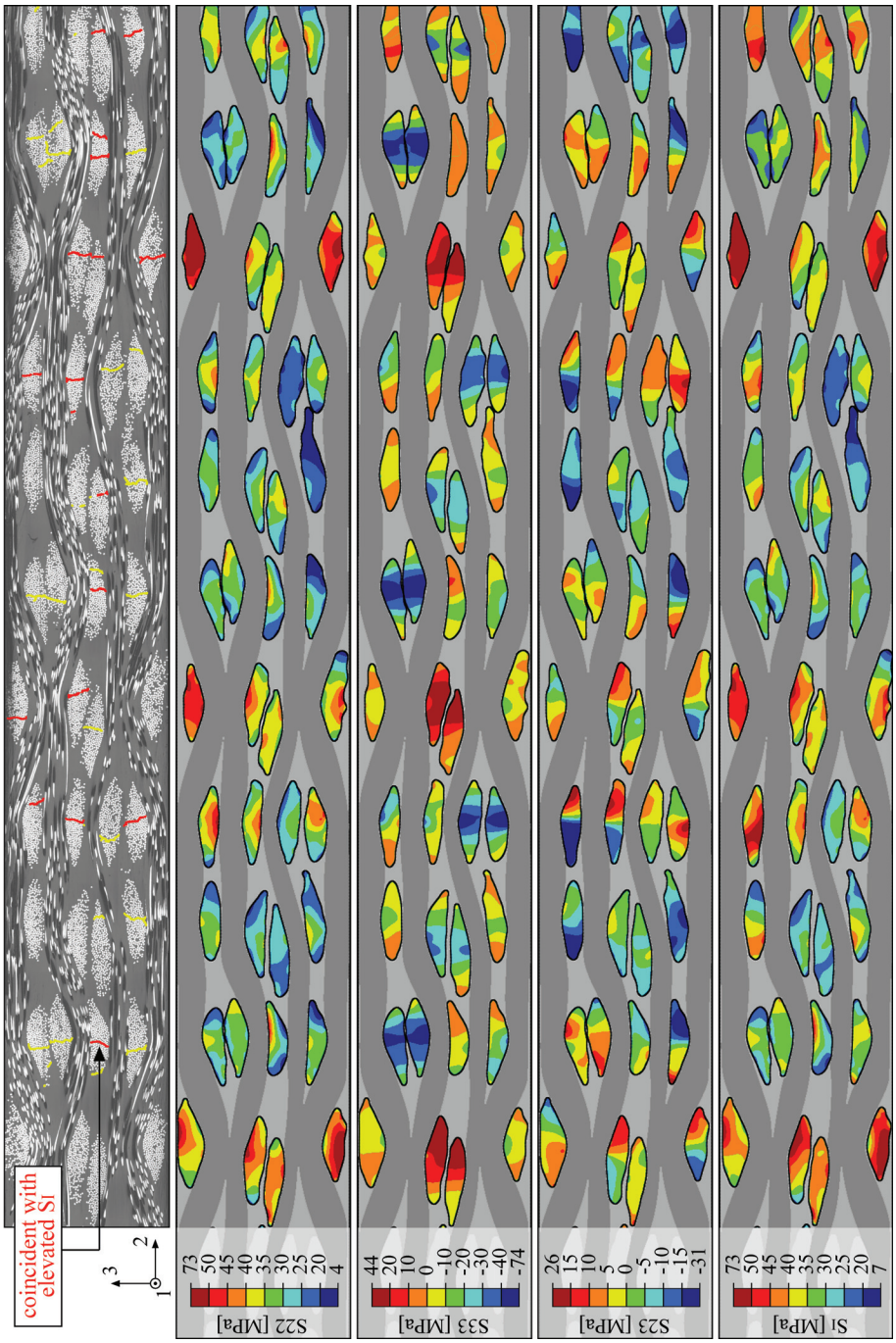


Figure 5-7: Validation of the numerical stress fields at a tensile strain of 0.4% in the weft-B specimen against the experimental crack pattern at 0.45% strain – part 1

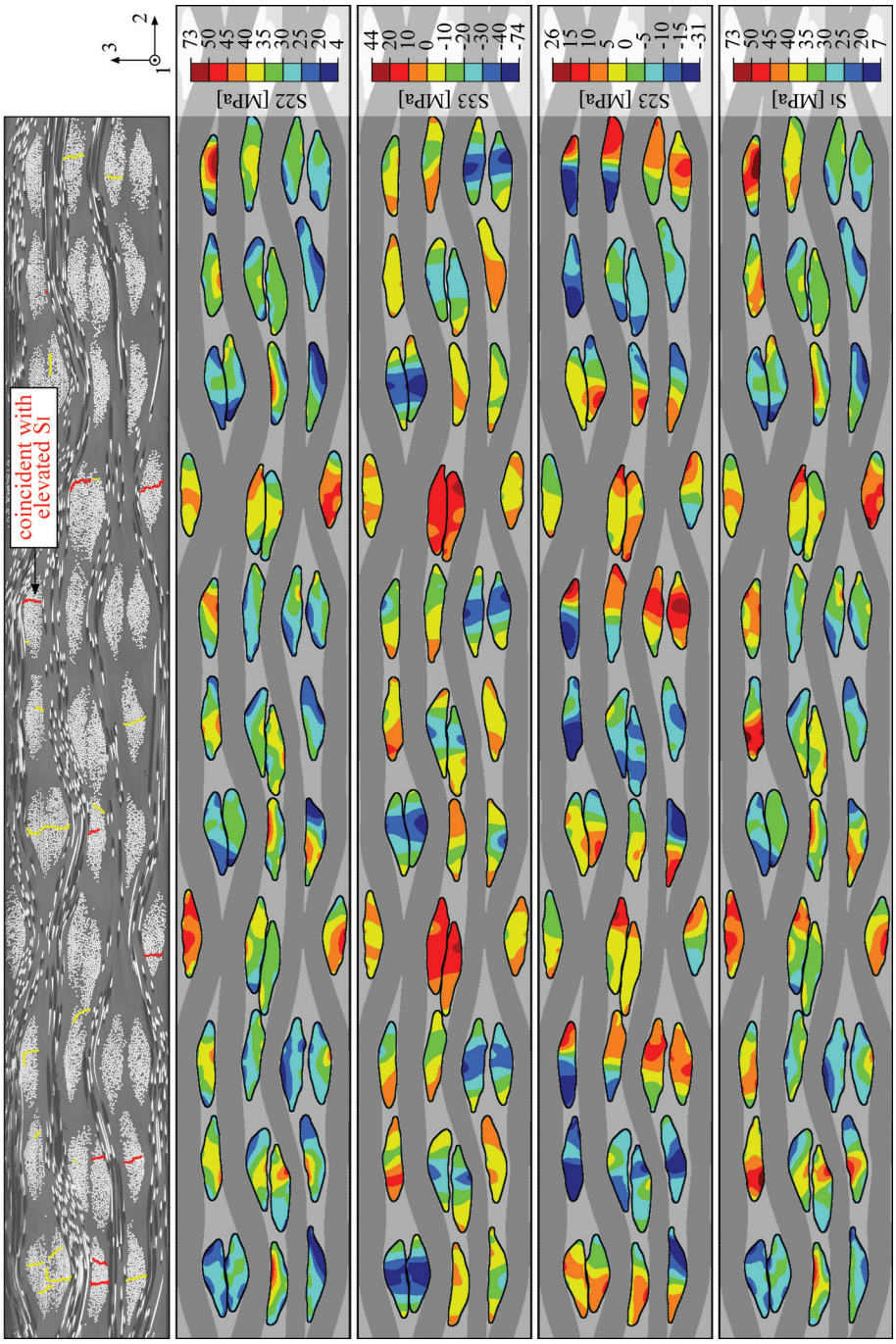


Figure 5-8: Validation of the numerical stress fields at a tensile strain of 0.4% in the weft-B specimen against the experimental crack pattern at 0.45% strain – part 2

The cracks that coincide with a peak in the maximum principal stress $S_I$ are marked in red on Figure 5-5 to Figure 5-8. Note that the principal stress $S_I$ is governed by the direct stress $S_{22}$, which is in line with the predominantly vertical crack direction. Comparison between the maximum principal stress $S_I$ and the crack pattern for the warp-B specimen in Figure 5-5 and Figure 5-6 shows that about one in five cracks can be linked to an elevated stress. The other way around, cracks were found on some of the stress peaks, but certainly not on all of them. For the weft-B specimen in Figure 5-7 and Figure 5-8, almost half of the cracks are predicted by a peak in the numerical $S_I$ pattern. On this specimen, it is apparent that both the cracks and the stress peaks tend to be located inside the bend of one of the load-carrying yarns.

It is important to note that the model can only be expected to predict the initiation of the very first cracks. As soon as damage starts to propagate, the stress patterns will redistribute. Furthermore, some of the cracks may have initiated in a section behind the free edge. These cracks could never be predicted by the 2D model.

## 5.5 INFLUENCE OF VARYING INTRA-YARN FIBER VOLUME FRACTIONS

As reported in section 4.3.5 of the previous chapter, there is a considerable variability in fiber volume fraction within the transversal yarns. Denser regions can be expected to attract more stress, which makes them more prone for crack initiation. Denser regions will also have less matrix in between the fibers, which means less flexibility to strain along with the surrounding material. This even adds to the vulnerability towards damage initiation.

It is common practice in mesoscale modeling to assume homogeneous yarns, as implementing yarn inhomogeneity in a 3D finite element model would be very challenging. With the 2D modeling approach, however, this is a feasible task. An automatic procedure to achieve this will be presented in the first part of this section. The results regarding the strain distribution will be shown in the second part, and the effect on the stress distribution will be discussed in the third part of this section. The final fourth part is a reflection on the difference that was observed between the influence of the yarn inhomogeneity on the strain and on the stress patterns.

### 5.5.1 Methodology

In section 4.3.5 of the previous chapter, a methodology was proposed for assessing the variable intra-yarn fiber volume fractions. The input for the procedure consisted of two image files, one containing the transversal fibers, and one containing the solid transversal yarns. These images were then covered with a virtual grid, and the volume

fraction was calculated for every grid section by dividing the number of fiber pixels by the number of yarn pixels in a circular region around the grid section. The radius of this circular region was termed the 'smearing radius' $R_s$, as it controls the extent to which the inhomogeneity is taken into account. The resolution of the calculation is controlled by the grid size. This methodology can easily be adapted for the problem of getting the variable fiber volume fractions implemented in the 2D model. The key is to have the mesh fulfill the function of the virtual grid, hence to calculate the local fiber volume fraction for every element of the mesh. This is explained in more detail in Figure 5-9.

First, the finite element mesh of the transversal yarns is mapped onto the microscopic images of the fibers and the yarns. More specifically, the gravity center of every element is identified, and its mesh coordinates (x,y) are translated into pixel coordinates (u,v). Now, the exact position of every finite element is known with respect to the microscopic images. Then, for every finite element, a circular smearing region is set around the gravity center. The average fiber volume fraction $V_f$ over this region is calculated by dividing the fiber pixels by the yarn pixels, and this volume fraction is assigned to the element. If neighboring yarns are too close to each other, the smearing region around an element may contain fiber pixels and yarn pixels of the neighboring yarn. The solution to this problem was already explained in section 4.3.5. Three different colors – red, green and blue – are used for the yarns and the fibers in the image files. Fibers are always given the same color as the corresponding yarn, and neighboring yarns are always given different colors. This way, if more than one color shows up in the smearing region, the algorithm can ignore the pixels belonging to the neighboring yarn. For the demonstration on Figure 5-9.a, a smearing radius of 120 μm – or four times the fiber diameter $D_f$ – was used. In total, three smearing radii will be considered, being 240 μm, 120 μm and 60 μm, or $8D_f$, $4D_f$, and $2D_f$, respectively. Figure 5-9.b illustrates the distribution of the fiber volume fraction for these three cases. Even with the largest smearing radius, the fiber volume fraction ranges from 29% to 65% in the example section, with an average value of 50.5%. As the smearing radius is lowered to 120 μm, and finally, 60 μm, the yarn inhomogeneity is reflected more in the model. The proposed procedure does not guarantee conservation of the total fiber volume fraction. Therefore, after processing all elements, the new overall fiber volume fraction was compared to the original value and a small scaling (less than 4% for all models presented) was applied for all finite elements in the transversal yarns, in order to maintain the fiber content in the model. Once the fiber volume fractions of the elements are known, the corresponding elastic properties can be derived from the individual elastic properties of the constituent materials (Table 3-1). The homogenization is performed analytically using the formulas by Chamis [23], as in section 3.2.1. Finally, for every set of elastic constants, a material model is generated and assigned to the correct element by scripting directly on the Abaqus input file.

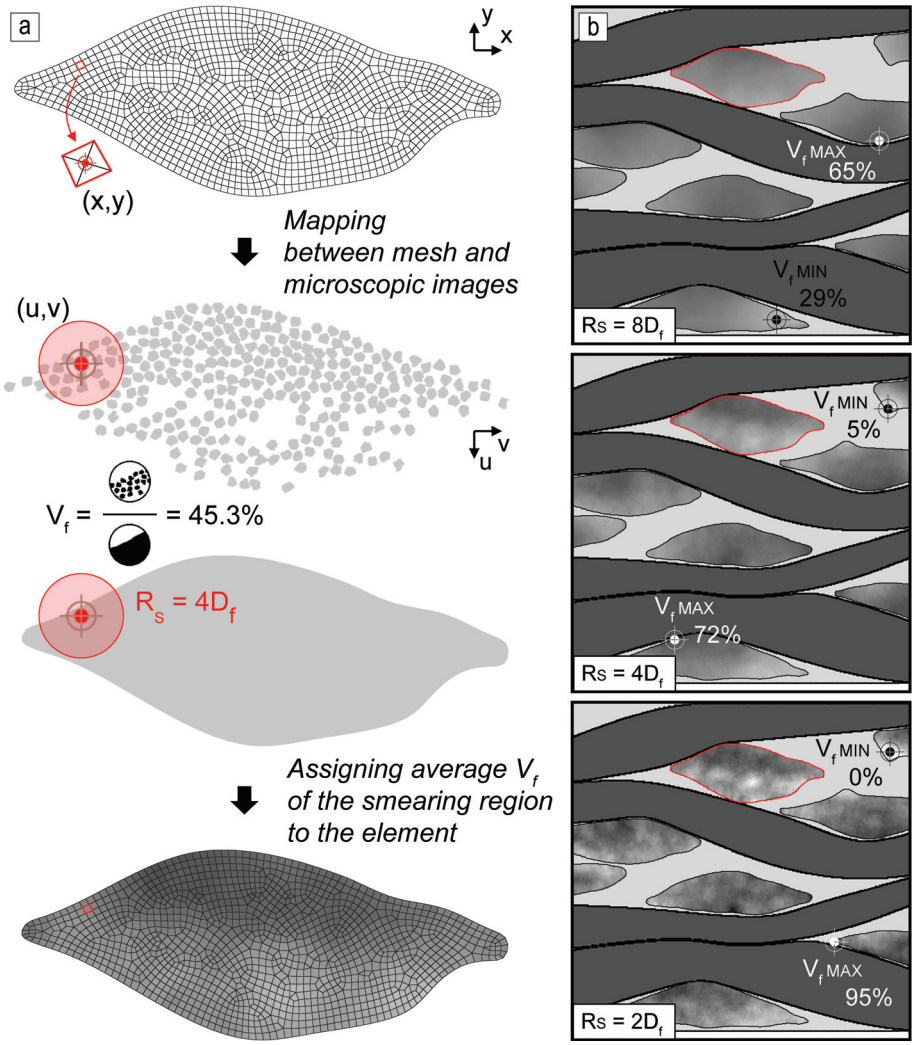


Figure 5-9: Methodology for implementing the inhomogeneity of the transversal yarns in the 2D finite element model

### 5.5.2 Effect of the inhomogeneity of the transversal yarns on the numerical strain distribution

The procedure for incorporating the inhomogeneity of the transversal yarns was applied to the model of the weft-B specimen that was the main subject of section 5.4.1. The three in-plane strain components $\varepsilon_{22}$, $\varepsilon_{33}$, and $\varepsilon_{23}$ at a global tensile strain of 0.4% are shown on Figure 5-10, Figure 5-11, and Figure 5-12, respectively. Four models are presented, i.e. the model with homogeneous transversal yarns, and three models with variable fiber volume fractions within the transversal yarns, calculated with a smearing radius $R_s$ of eight, four, and two times the fiber diameter $D_{f.}$ The corresponding experimental DIC strain field was patterned on an image of the specimen edge beyond the actual measurement area for the ease of comparison.

Figure 5-10 to Figure 5-12 show that the strain patterns become more patchy as the smearing radius decreases. On the strain patterns along the loading direction $\varepsilon_{22}$ on Figure 5-10, a strain concentration appears at the center of one of the outer crimp yarns (marked with a number '1') as the inhomogeneity becomes stronger. This is, however, an exception. In general, simulating the inhomogeneity does not cause real shifts in the distribution of the strain $\varepsilon_{22}$. The transverse strain $\varepsilon_{33}$ tends to lose intensity in the densely packed crimp regions as the inhomogeneity is increased. An example is marked with number '1' in Figure 5-11 for a crimp yarn in compression. In some yarns, e.g. the one marked with number '2', the strain even moves away from the crimp region. On the distributions of the shear strain $\varepsilon_{23}$ on Figure 5-12, no global trends can be discerned with relation to the inhomogeneity of the transversal yarns. Apart from the pattern being more patchy as the smearing radius decreases, there are no differences, nor qualitatively, nor quantitatively.

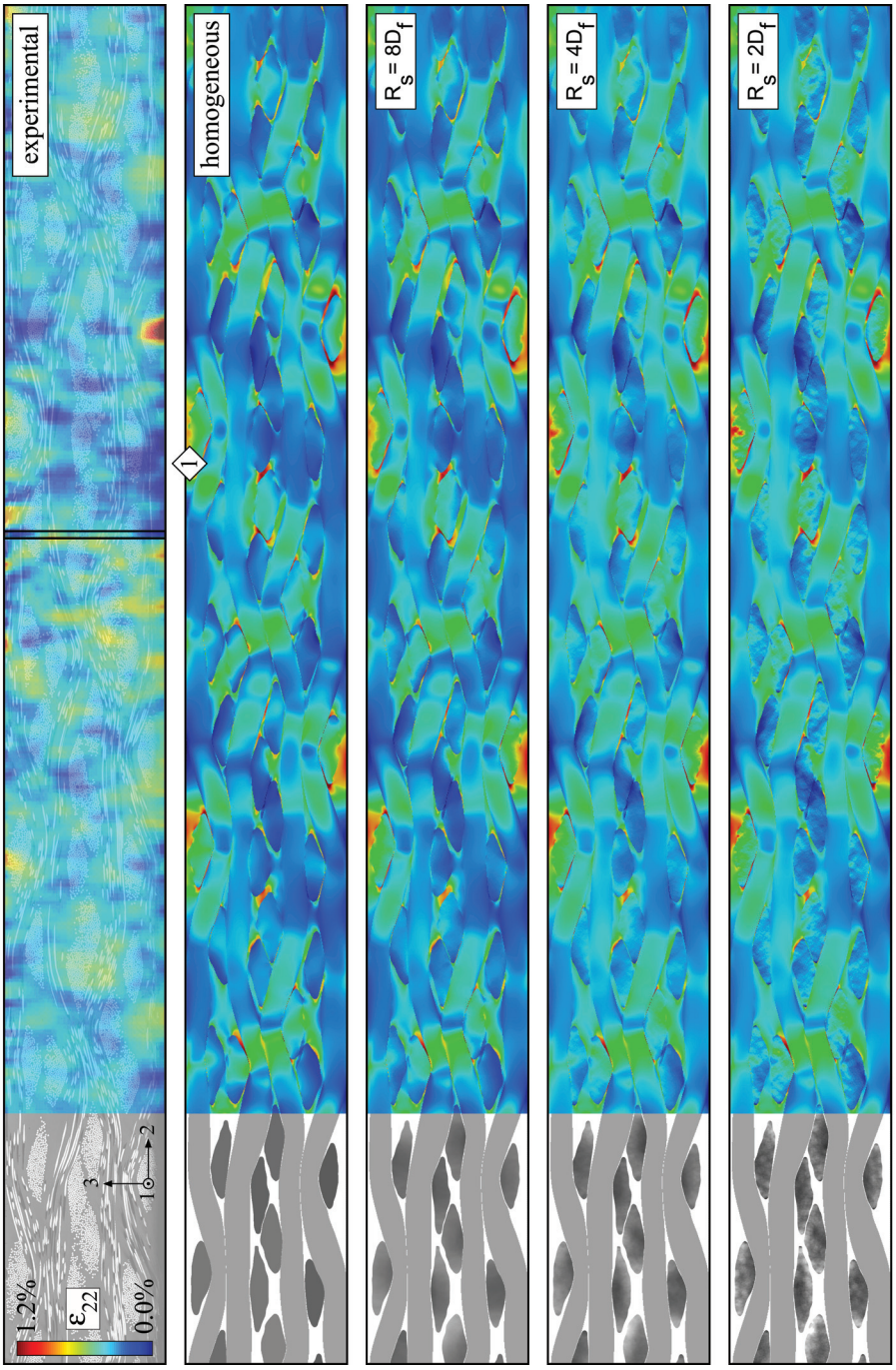


Figure 5-10: Validation for the numerical strain along the loading direction at a global tension of 0.4% in the weft-B specimen against the corresponding DIC strain field

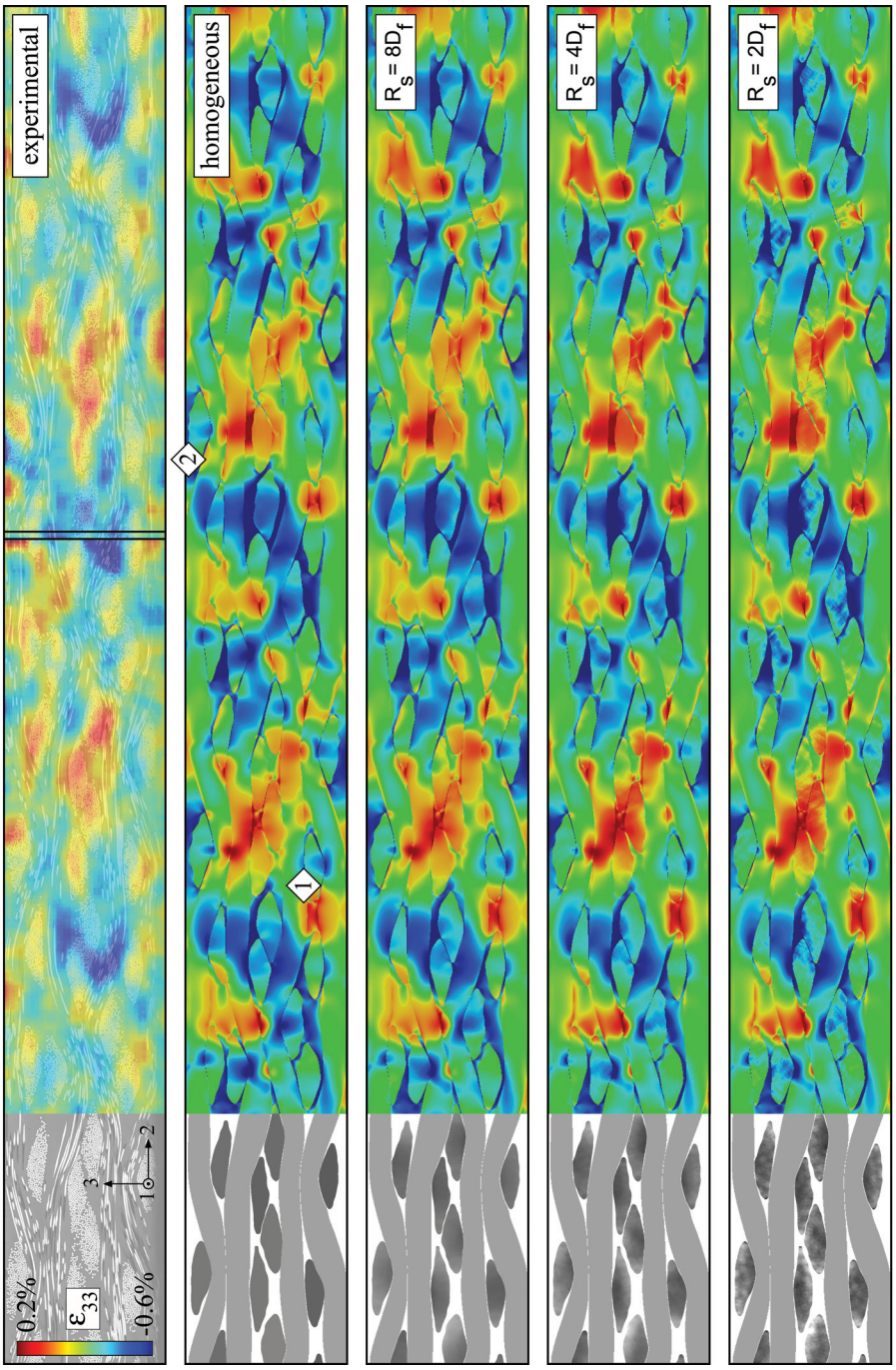


Figure 5-11:Validation for the numerical transverse strain at a global tension of 0.4% in the weft-B specimen against the corresponding DIC strain field

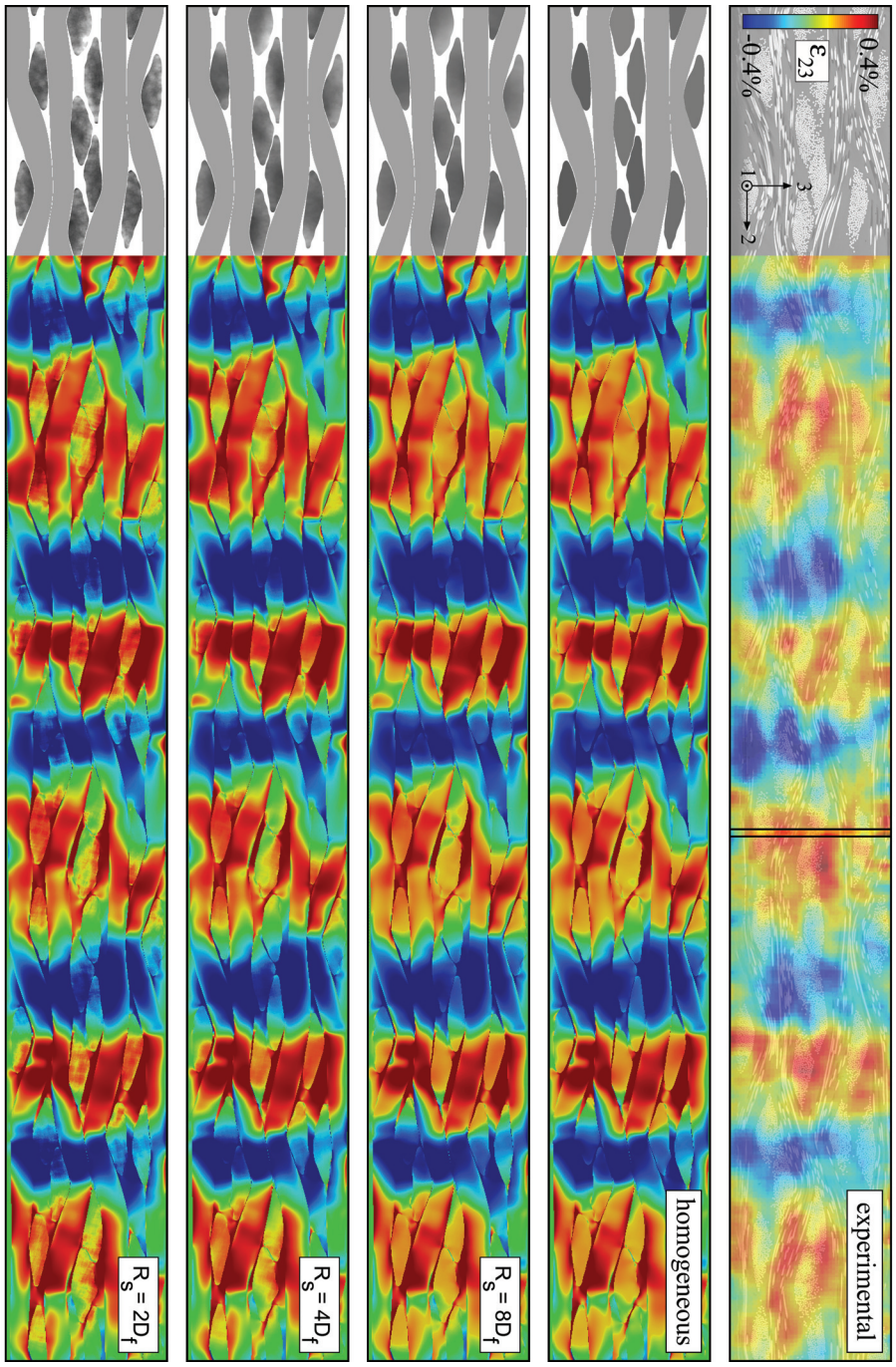


Figure 5-12: Validation for the numerical shear strain at a global tension of 0.4% in the weft-B specimen against the corresponding DIC strain field

### 5.5.3 Effect of the inhomogeneity of the transversal yarns on the numerical stress distribution

The effect of the intra-yarn variability in fiber volume fraction on the numerical stress distribution was investigated on the specimens that were presented in section 5.4.2. The numerical patterns for the first principal stress in the transversal yarns at 0.4% global strain of the warp-B and weft-B specimens are shown in Figure 5-13 and Figure 5-14, respectively, and this for the model with homogeneous transversal yarns, and for the models with variable fiber volume fractions within the transversal yarns, calculated with a smearing radius of eight, four, and two times the fiber diameter. Along with the numerical results, the initial cracks are depicted for comparison, more specifically at 0.5% global strain in Figure 5-13, and at 0.45% global strain in Figure 5-14.

The warp-B specimen in Figure 5-13 is discussed first. Similarly as what was observed for the numerical strain, the stress patterns within the transversal yarns become more patchy as the inhomogeneity is taken more into account. The scales for all four models are the same, only the extreme values differ from model to model. When comparing these extremes, it is clear that the peaks become more severe as the smearing radius decreases. In some of the transversal yarns, the stress pattern has merely intensified. This is, for instance, the case for the yarn marked with number '1' in Figure 5-13. For other yarns, the critical location has shifted. An example of this phenomenon is marked with number '2'. The peak shift from the top of the yarn to the bottom is halfway through when the homogeneity is calculated with a smearing radius of $8D_f$, and it is complete when the smearing radius equals $4D_f$. Lowering the smearing radius further to $2D_f$ does not cause any more major shifts in the peak locations, it only increases the patchiness of the solution.

The weft-B specimen in Figure 5-14 shows very similar effects of the inhomogeneity on the principal stress distribution as the warp-B specimen. The numerical stress pattern again becomes patchier and more intense as the inhomogeneity of the transversal yarns becomes stronger. In some yarns, e.g. the one marked with number '1', the pattern intensifies. In other yarns, e.g. the one marked with number '2', the critical spot shifts to another location. This is notably the case for almost all of the outer crimp yarns, e.g. the yarn marked with number '3'. The model with homogeneous yarns hence predicts crack initiation at the specimen surface for these yarns, while the models with variable fiber volume fractions within the transversal yarns correctly suggest crack initiation within the yarn, close to the crimp region. From the experimental findings in section 4.5, it was indeed clear that cracks initiate inside the transversal yarns, and only later on travel to the surface. The trend that is observed in the outer crimp yarns can be seen throughout the whole model: the stress tends to concentrate more in the crimp regions as the inhomogeneity is more taken

into account. This can be explained with the observations made in section 4.3.5 on the fiber distribution within the yarns. Elevated fiber volume fractions were typically found at the contact zones with a longitudinal yarn – often in the crimp region of the longitudinal yarn. Low values were found on unconfined yarn edges. The denser regions within the yarns have a higher stiffness, and therefore, they attract more stress. When comparing the principal stress pattern obtained with a smearing radius of $4D_f$ to the crack pattern, it is clear that the cracks that were already explained by the model with homogeneous yarns (marked in red) can still be linked to a stress peak. In addition, a few extra cracks (marked in green) – typically ones in the crimp regions – can be matched with a critical stress location for the model with smearing radius $4D_f$. Similar as in the warp-B specimen, decreasing the smearing radius to $2D_f$ does not change the global stress pattern much, it merely intensifies the existing peaks.

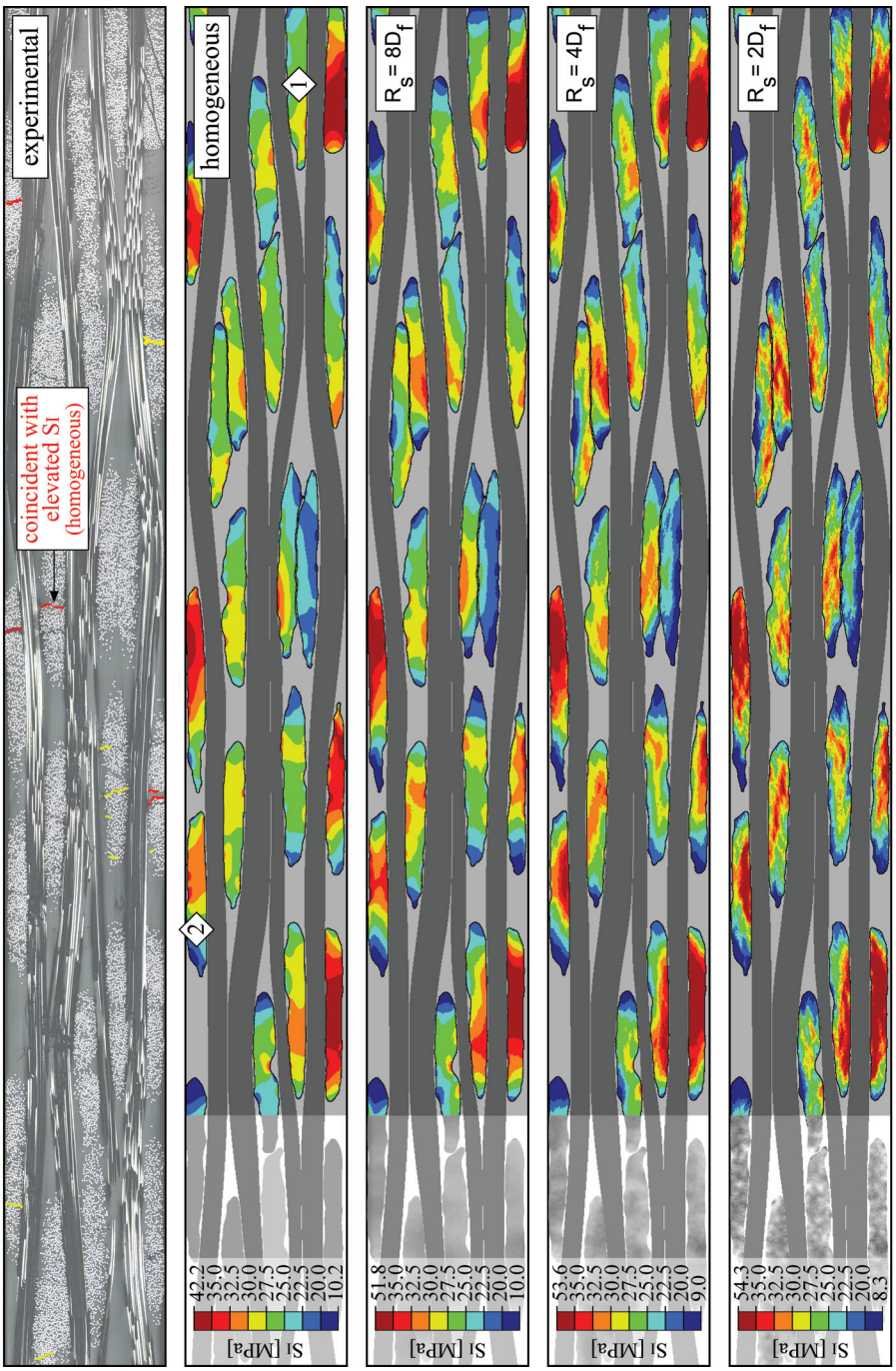


Figure 5-13: Validation for the numerical first principal stress at a tensile strain of 0.4% in the warp-B specimen against the experimental crack pattern at 0.5% strain

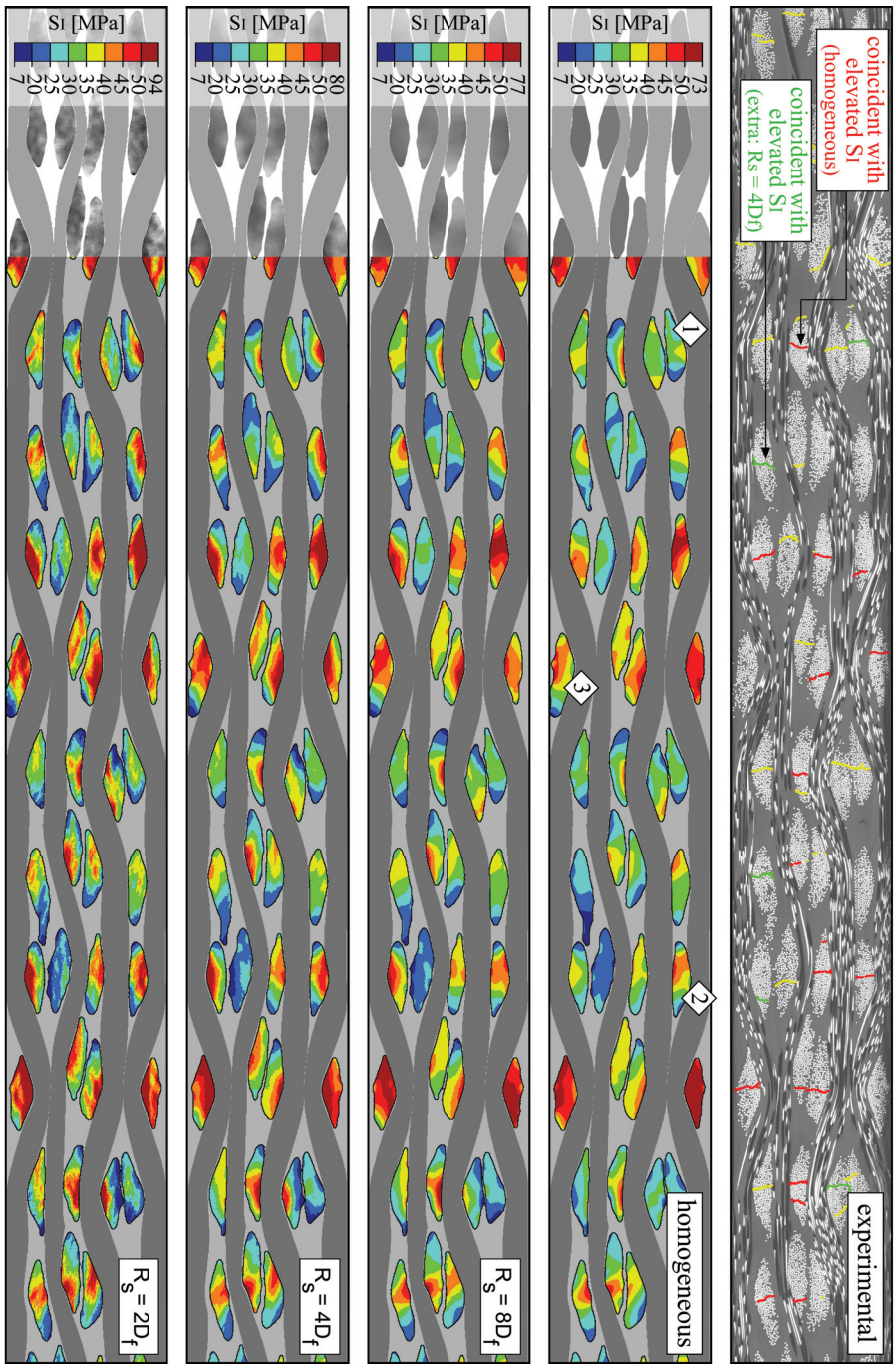


Figure 5-14: Validation for the numerical first principal stress at a tensile strain of 0.4% in the weft-B specimen against the experimental crack pattern at 0.45% strain

### 5.5.4 Reflection on the difference between strains and stresses

The effect of the inhomogeneity is more important in the stress distribution than in the strain distribution. Furthermore, the principal stress was found to concentrate in the densely packed crimp regions, while the strain components either were unaffected, or even moved away from the crimp regions. This difference in conduct between stresses and strains may seem counterintuitive. All the materials in the model are elastic, hence the relationship between stresses and strains should be linear. Indeed, if the model were a homogeneous entity, the stress patterns and the strain patterns would look exactly the same. In the more complex weave architecture, however, the main mechanisms that govern stresses and strains are very different.

This is illustrated in Figure 5-15 on a conceptual 2D plane stress model of a symmetric two-layer laminate. The distributions of the stress and the strain along the loading direction are shown at a global extension of 0.4%. With respect to the stress, the geometry acts as a parallel system of stiff longitudinal yarns, interspersed with a softer transversal structure of transversal yarns and matrix. The stress in the stiff longitudinal yarns is more than 10 times higher than the average stress in the transversal structure. Correspondingly, the longitudinal yarns carry more than 90% of the load. When it comes to the strain along the loading direction, the geometry acts as a serial system. The longitudinal yarns and the neighboring transversal structure are forced to deform together. If a vertical section is stiff on average, the strains will be low in all the materials within that vertical section. The strain will instead concentrate in the softer sections, with an average value up to three times higher than in the stiffest sections.

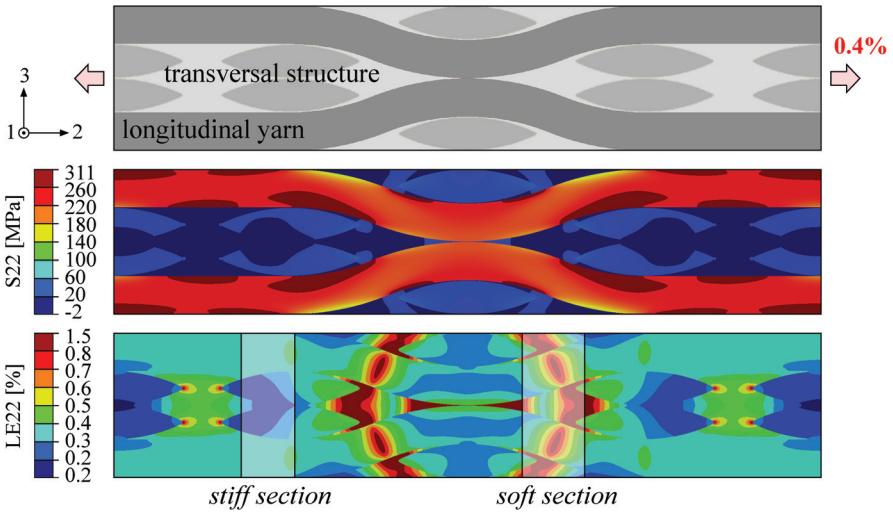


Figure 5-15: Stress and strain along the loading direction in a conceptual 2D model

In summary, the fundamentally different nature of stresses and strains translates into entirely different distributions, and this explains how some details in the internal geometry have a different effect on the stress and strain patterns.

## 5.6 CONCLUSION

The goal of this chapter was to explore the potential of 2D modeling for analyzing the stresses and the strains on the edge of a composite laminate under tension. A 2D model allows to represent the reinforcement geometry and its variabilities in a realistic manner, with a virtually unlimited degree of detail. Moreover, a 2D model of a laminate edge is the best conceivable case for experimental validation.

After the introduction, this chapter was continued with a concept check for the 2D modeling strategy based on the comparison of results from 2D and 3D models of an idealized textile unit cell. Subsequently, a methodology was set forth for constructing a detailed, realistic model of a laminate edge based on high resolution microscopic images. Later on, the methodology was expanded with a procedure for implementing the intra-yarn variability in fiber volume fraction.

Comparison of the numerical and the experimental strain patterns showed a very good correlation, as long as all the longitudinal yarns are visible on the laminate edge that is modeled. This proves that a realistic 2D model is able to capture the relation between the internal mechanics and the internal composite structure. Taking the inhomogeneity of the transversal yarns into account did not have a large effect on the strain distribution. The stress distribution, on the other hand, proved to be very sensitive to the inhomogeneity of the yarns. More cracks can be predicted if the intra-yarn variability in fiber volume fraction is taken into account, and a correct prediction of the point of initiation within the transversal yarns as well depends on the detail beyond the meso-scale.

An obvious limitation of the 2D model is that it is limited to the elastic range. It is certainly expected to lose its accuracy once the first cracks have formed. Cracks can initiate in sections behind the one that is modeled, and then travel through the laminate transversely to the loading direction. The influence of 3D effects may be acceptably low in the elastic range, but this can no longer be presumed once cracks start to disrupt the internal structure. From the point of damage propagation onwards, the material mechanics must hence be studied in a different manner. A pragmatic, yet effective investigation of the damage mechanics will be the subject of the next chapter.

## 5.7 REFERENCES


[1] Carvelli V, Poggi C. *A homogenization procedure for the numerical analysis of woven fabric composites*. Composites: Part A; 32: 1425-1432. 2001.

[2] Chapman DC. *Effects of Assumed Tow Architecture on the Predicted Moduli and Stresses in Woven Composites*. NASA Contractor Report 195310. 1994.

[3] Lomov S, Ivanov D, Verpoest I, Zako M, Kurashiki T, Nakai H, et al. *Meso-FE modelling of textile composites: Road map, data flow and algorithms*. Composites Science and Technology; 67: 1870-1891. 2007.

[4] Whitcomb JD. *Three-Dimensional Stress Analysis of Plain Weave Composites*. NASA Contractor Report 198506. 1989.

[5] Daggumati S, De Baere I, Van Paepegem W, Degrieck J, Xu J, Lomov SV, et al. *Local damage in a 5-harness satin weave composite under static tension: Part I – Experimental analysis*. Composites Science and Technology; 70: 1926-1933. 2010.

[6] De Carvalho NV, Pinho ST, Robinson P. *An experimental study of failure initiation and propagation in 2D woven composites under compression*. Composites Science and Technology; 71: 1316-1325. 2011.

[7] Daggumati S, Van Paepegem W, Degrieck J, Xu J, Lomov SV, Verpoest I. *Local damage in a 5-harness satin weave composite under static tension: Part II – Meso-FE modelling*. Composites Science and Technology; 70: 1934-1941. 2010.

[8] Daggumati S, Van Paepegem W, Degrieck J, Praet T, Verhegghe B, Xu J, et al. *Local strain in a 5-harness satin weave composite under static tension: Part II – Meso-FE analysis*. Composites Science and Technology; 71: 1217-1224. 2011.

[9] Ivanov DS, Lomov SV, Ivanov SG, Verpoest I. *Stress distribution in outer and inner plies of textile laminates and novel boundary conditions for unit cell analysis*. Composites Part A: Applied Science and Manufacturing; 41: 571-580. 2010.

[10] Ivanov DS, Ivanov SG, Lomov SV, Verpoest I. *Unit cell modelling of textile laminates with arbitrary inter-ply shifts*. Composites Science and Technology; 72: 14-20. 2011.

[11] Shady E, Gowayed Y. *Interlaminar Shear Stress Distribution Between Nested Layers of Plain Weave Composites*. Polymer Composites; 31. 2010.

[12] Lomov SV, Verpoest I, Peeters T, Roose D, Zako M. *Nesting in textile laminates: geometrical modelling of the laminate*. Composites Science and Technology; 63: 993-1007. 2003.

[13] Grail G, Hirsekorn M, Wendling A, Hivet G, Hambli R. *Consistent Finite Element mesh generation for meso-scale modeling of textile composites with preformed and compacted reinforcements*. Composites Part A: Applied Science and Manufacturing; 55: 143-151. 2013.

[14] Hivet G, Boisse P. *Consistent 3D geometrical model of fabric elementary cell. Application to a meshing preprocessor for 3D finite element analysis*. Finite Elements in Analysis and Design; 42: 25-49. 2005.

[15] Kim JH, Ryou H, Lee M-G, Chung K, Youn JR, Kang TJ. *Micromechanical modeling of fiber reinforced composites based on elastoplasticity and its application for 3D braided glass/Kevlar composites*. Polymer Composites; 28: 722-732. 2007.

[16] Blacklock M, Bale H, Begley M, Cox B. *Generating virtual textile composite specimens using statistical data from micro-computed tomography: 1D tow representations for the Binary Model*. Journal of the Mechanics and Physics of Solids; 60: 451-470. 2012.

[17] Bale H, Blacklock M, Begley MR, Marshall DB, Cox BN, Ritchie RO, et al. *Characterizing Three-Dimensional Textile Ceramic Composites Using Synchrotron X-Ray Micro-Computed-Tomography*. Journal of the American Ceramic Society; 95: 392-402. 2012.

[18] Cox BN, Carter WC, Fleck NA. *A Binary Model of textile composites .1. Formulation*. Acta Metallurgica et Materialia; 42: 3463-3479. 1994.

[19] Rinaldi RG, Blacklock M, Bale H, Begley MR, Cox BN. *Generating virtual textile composite specimens using statistical data from micro-computed tomography: 3D tow representations*. Journal of the Mechanics and Physics of Solids; 60: 1561-1581. 2012.

[20] Vanaerschot A, Cox BN, Lomov SV, Vandepitte D. *Stochastic framework for quantifying the geometrical variability of laminated textile composites using micro-computed tomography*. Composites Part A: Applied Science and Manufacturing; 44: 122-131. 2013.

[21] Vanaerschot A, Cox BN, Lomov SV, Vandepitte D. *Stochastic multi-scale modelling of textile composites based on internal geometry variability*. Computers & Structures; 122: 55-64. 2013.

[22] Vanaerschot A, Cox BN, Lomov SV, Vandepitte D. *Experimentally validated stochastic geometry description for textile composite reinforcements*. Composites Science and Technology; 122: 122-129. 2016.

[23] Chamis CC. *Mechanics of Composite Materials Past, Present and Future*. NASA Contractor Memorandum 100793. 1984.

[24] Knops M. *Puck's action plane fracture criteria* Analysis of Failure in Fiber Polymer Laminates - The Theory of Alfred Puck: Springer-Verlag Berlin Heidelberg. p. 37-115. 2008.

# Chapter 6

## VARIATION OF THE INTERFACIAL STRENGTH AND THE MATRIX DUCTILITY IN SEARCH FOR THE DAMAGE MECHANISMS

*In this chapter, two important aspects of the composite under study are varied, i.e. the matrix system and the fiber/matrix interface. The aim is to gain more understanding about the failures mechanisms in composite laminates reinforced with a ductile fiber textile. After a short introduction, the variations will be proposed in more detail. Then, the mechanical testing procedure is explained and the stress-strain relation is presented. Subsequently, a more thorough look is taken at the damage morphology and a hypothesis is put forth about the mechanisms that drive failure. The chapter is ended with a conclusion.*

## 6.1 INTRODUCTION

The behavior of a UD fiber reinforced composite material depends on the properties of the fibers, the matrix, and the interface [1]. Altering the toughness of a UD composite with a given fiber reinforcement can hence be done by modifying either the matrix, or the interface.

The **influence of the matrix** is well known for the case of carbon and glass fiber UD composites: a more ductile matrix makes for a tougher composite [2, 3]. This insight incited the relatively recent research topic of toughness enhancement through matrix modification. Ngah et al. [4] and Carolan et al. [5] added core shell rubber and silica nanoparticles to the epoxy matrix of UD glass and carbon fiber composites, respectively, both with a positive effect on the composite toughness. Prasad et al. [6] successfully increased the fracture toughness of a UD carbon fiber composite by blending thermoplastic phases into the epoxy matrix, and by additionally strengthening the matrix with carbon nanotubes. The same relationship between matrix ductility and composite toughness was observed by Callens et al. for the case of ductile stainless steel quasi-UD composites [7]. Two matrix systems were considered, a ductile thermoplastic PA-6 matrix with a failure strain of more than 20%, and a brittle Epikote 828LVEL/Dytek DCH-99 epoxy system with a failure strain of 3.9%. Tensile testing indicated a strain-to-failure of 12.7% for the ductile matrix composite, and only 7.3% for the brittle matrix composite. The authors pointed out correctly that thermoplastic and thermoset matrices have different production processes and a different chemistry, which will most likely cause alterations beyond the matrix ductility. Nevertheless, the results of this study strongly indicate that a tougher matrix makes for a tougher stainless steel quasi-UD composite.

The **role of the interface** in the composite toughness is less straightforward than that of the matrix ductility. There is usually a trade-off between strength and stiffness on the one hand, and toughness on the other hand [8]. Generally speaking, a minimum interfacial strength is needed to ensure the load transfer between the composite phases that is needed to achieve a workable strength and stiffness [9, 10]. If the interface is too strong, on the other hand, the stress concentrations at the fiber/matrix interface intensify, and fiber fracture is promoted at the expense of the energy-absorbing fiber pullout failure mode [11]. Most of the research on the role of the interface applies to brittle fiber composites [12-14]. The case of ductile stainless steel fiber quasi-UD composites was investigated by Callens et al. [15]. An adhesion enhancement was achieved by wet chemical deposition of a silane coupling agent through a procedure that was especially developed for the stainless steel/polymer interface [16-18]. This sizing increased the longitudinal toughness of the composite by about 20%. In summary, the role of the interface is not straightforward, but in the case of a ductile quasi-UD reinforcement, a stronger interface makes for a tougher composite.

The research mentioned so far in this section applied to UD composites. Studies on how the matrix ductility or the interfacial strength influence the toughness of textile composites [19-21] is too scarce to discern trends. The quasi-UD composites with ductile stainless steel fibers could be toughened by choosing a more ductile matrix, or by strengthening the fiber/matrix interface. In a textile composite, however, there is the additional aspect of the architecture of the reinforcement. The macroscopic behavior will in this case be codetermined by the complex mechanics of the internal structure, and the composite can no longer be considered as a sum of its parts. It is clear that a lot can be learned from varying the matrix ductility and the interfacial strength in the ductile textile composite under study. This exercise is the subject of this chapter. In the following section, the variations on the matrix and the interface will be proposed. Then, the experiments on the variations will be discussed, and the observed damage will be analyzed. Finally, the chapter will be ended with a conclusion.

## 6.2 VARIATIONS ON THE MATRIX AND THE INTERFACE

The composite that has been studied throughout this research work has a tough RIM epoxy matrix and an untreated fiber-matrix interface. This composite will be referred to as 'RIM/AR' from here on, with the first part of the name denoting the epoxy system, and the second part referring to the fiber surface being *As Received*. This naming convention is necessary to distinguish from the two variations that will be introduced in this section, i.e. EPON/AR and RIM/GPS. The EPON/AR only differs from the original in its more brittle matrix (EPON epoxy), while the RIM/GPS has a stronger interface (through GPS-treatment of the fiber surface). Apart from the intended variations on the matrix system and the interface, the three composites under consideration were made as similar as possible. All three have the same reinforcement – the stainless steel fiber 4-harness satin weave textile – and the same lay-up system, i.e. a four-layer symmetric lay-up with the weft-oriented side of the fabric directed outwards. Moreover, all three composites were produced in-house using vacuum assisted resin transfer molding (VA-RTM). In the next parts of this section, the intended variations will be explained in more detail.

### 6.2.1 Matrix systems

Two matrix systems were considered in this chapter, one more tough, and one more brittle. The tough matrix is the system that has been used throughout this research work, i.e. EPIKOTE™ MGS™ RIMR 135, cured with EPIKURE™ MGS™ RIMH 137. The brittle matrix system was obtained by combining bisphenol-A resin EPIKOTE™ 828 with a 1,2-diaminocyclohexane curing agent, mixed in a 100:15.2

weight ratio. The resin was obtained from Brenntag N.V., and the curing agent was purchased from Sigma-Aldrich. The brittle matrix was already successfully combined with the stainless steel fibers by Callens et al. [7]. The tensile properties of both epoxies are summarized in Table 6-1. By choosing two thermosetting matrix systems, the differences besides the toughness are kept to a minimum, which will improve the validity of any conclusions.

Table 6-1: Tensile properties of the tough and brittle matrix systems

| **Mechanical property** | **Tough epoxy[a]** | **Brittle epoxy[b]** |
|---|---|---|
| Young's modulus [GPa] | 2.73 ± 0.02 | 2.9 |
| Yield strength [MPa] | 41.4 ± 2.4 | NA |
| Tensile strength [MPa] | 66.1 ± 0.4 | 75 |
| Failure strain [%] | 8.24 ± 0.69 | 4 |

[a] Data obtained from Allaer et al. [22]
[b] Data obtained from Callens et al. [7]

### 6.2.2 Interface modification

An enhancement of the fiber/matrix interface was achieved by introducing a GPS (3-glycidoxypropyltrimethoxysilane) coupling agent to the fiber surface. The GPS molecules act as a covalent chemical bridge between the stainless steel fiber surface and the epoxy matrix, hence increasing the adhesion.

The general structure of monosilanes can be depicted as (Y-R)4−n-Si-Xn, with Y representing an organofunctional group, X a hydrolysable group, R a spacer or linker group and Si a silicon atom. The organofunctional group is chosen to improve reactivity or compatibility with the polymer matrix. The hydrolysable groups are merely intermediates in the formation of silanol groups for bonding to the metal.

The silanes were applied to the fiber surface through a wet chemical deposition procedure that was especially optimized in the framework of the Nanoforce project to improve the bonding between epoxy and stainless steel [17, 18]. First, impurities were removed from the fiber surface. To this end, the fabric was cleaned ultrasonically in ethanol for 15 min. The ethanol was rinsed off with deionized water, and the fabric was dried with clean compressed air. The second step is the hydrolysis of the silanes in a dilute aqueous solution, to form active silanol (Si–OH) groups that can adsorb to the fiber surface (Figure 6-1.a, left). The composition of the solution plays an important role in the amount of self-condensation of the silanol groups prior to deposition (Figure 6-1.a, right). As self-condensation consumes hydroxyl groups that

are necessary for coupling to the fiber surface, it must be kept to a minimum. The silane solution that was used in this study was prepared by adding 2 v% of GPS to a mixture of deionized water (90 v%) and ethanol (10 v%). The pH of the solution was brought down to 5. The third deposition step is to dip the steel fabric reinforcement into the solution, so that hydrogen bonds can form between the silane hydroxyl groups and the metal hydroxyl groups (Figure 6-1.b). A dipping time of 30 s was applied, after which the fabric was rinsed with ethanol for 60 s to remove loosely bound molecules. The last step is to dry the fabric for 90 min at 70 °C to facilitate the condensation reaction. In this step, the silanol groups further covalently bond with the fiber surface and with each other to form, respectively, metal–siloxane (Si–O–M) bonds, and a siloxane network (Si–O–Si) (Figure 6-1.c). The reinforcement was used for laminate production immediately after finishing the deposition process in order to avoid ageing of the coating.

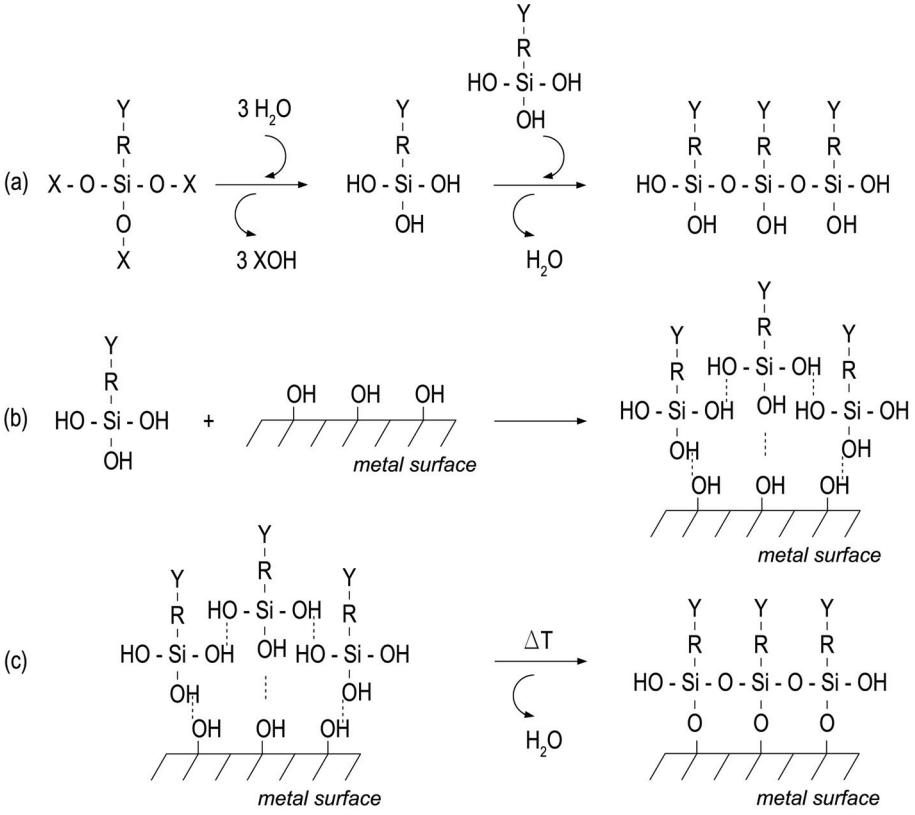


Figure 6-1: Reaction scheme of the wet chemical deposition of a silane surface treatment on the steel fibre surface [18]

## 6.3 MECHANICAL CHARACTERIZATION OF THE RIM/GPS AND EPON/AR COMPOSITES

The static tensile behavior of the RIM/AR composite was discussed in detail in section 2.5. The other two composites will be subjected to the same experiments. Both will be tested along both the loading directions, and in accordance with the ASTM D3039/ D3039M standard [23].

### 6.3.1 Test setup, specimen selection, instrumentation, and data acquisition for the static tensile tests

Like the RIM/AR laminates, the EPON/AR and RIM/GPS laminates were produced as plates with a thickness of 3 mm. For every set of experiments, four rectangular test coupons were cut from the composite plates. The specimen dimensions are summarized in Figure 6-2.a.

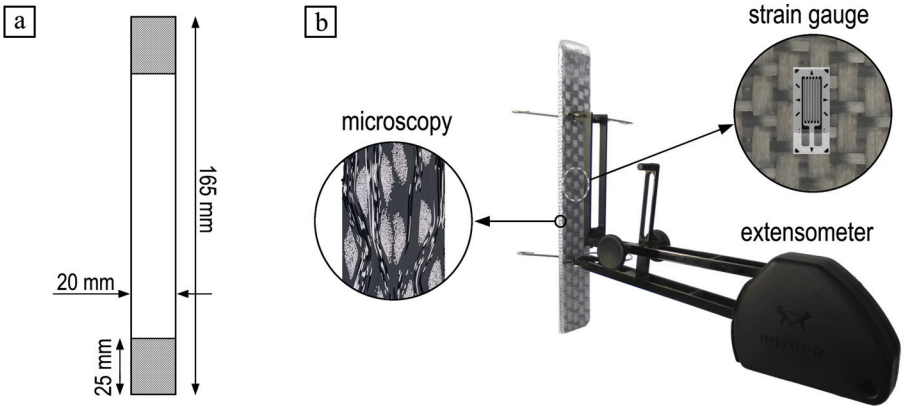


Figure 6-2: Measurements (a) and instrumentation (b) for the RIM/GPS and EPON/AR tensile specimens

The specimen instrumentation is illustrated in Figure 6-2.b. Every coupon was equipped with a strain gauge to monitor the local strain in the gauge area along the loading direction. In order to rule out effects of the measurement procedure as much as possible, the same strain gauges were used as for the tests on the RIM/AR specimens. These strain gauges had a resistance of 350 Ω and a maximum strain of 5%, and their measurement gives the average longitudinal strain over a region of 3 x 7 mm². The specimens were additionally instrumented with an extensometer with a gauge length of 80 mm and a range of 100%. The extensometer serves as a backup in case the strain gauge would reach the limit of its working range, or when it would fail due to brittle surface cracks. Due to the larger gauge length, it also gives a more global

view on the strain in case there would be damage localization. The specimens were polished on one edge, and that edge was captured on high resolution microscopic images before and after testing. These images will be used in section 6.4 to analyze the damage morphology.

The experiments were performed on a servo-hydraulic INSTRON 8801 testing machine with an AlignPRO alignment fixture. The tests were displacement-controlled with a constant crosshead speed of 2 mm/min. Force and displacement were given by the FastTrack 8800 digital controller with the same time sampling. Measurements by the strain gauge and the extensometer were acquired synchronously using Labview data acquisition software. There were no notable problems with improper failure modes, and all the results presented in the next section refer to coupons that failed in the mid-section of the gauge area, sufficiently far away from the clamps.

### 6.3.2 Stress-strain relation and mechanical properties

Figure 6-3.a and Figure 6-3.b show the stress–strain acquisitions for the RIM/GPS and EPON/AR composites tested along the warp direction, along with a photograph of the post-failure specimen surface. In Figure 6-3.c, the according results for the RIM/AR composite from section 2.5 are repeated. Figure 6-3.d, finally, provides an overview with the most representative curve of each composite for comparison. Similarly as for the experiments along the warp direction, Figure 6-4.a and Figure 6-4.b show the stress–strain acquisitions for the RIM/GPS and EPON/AR composite, Figure 6-4.c repeats the results from section 2.5 for the RIM/AR composite, and Figure 6-4.d gives an overview.

The mechanical properties along warp and weft can be found in Table 6-2 and Table 6-3, respectively. All values were derived from the strain gauge measurements unless specified otherwise, and they were all determined in the same manner as was done for the RIM/AR specimens in section 2.5. The yield point was hence calculated as the 0.1% offset value, the ultimate values for stress and strain were the maximum values recorded, and the Young's modulus was calculated as the slope of the least-squares linear regression fit on the stress–strain curve between 0% and 0.15% strain.

A quick view on Figure 6-3.d and Figure 6-4.d reveals that the results are opposite to what was expected based on prior observations on quasi-UD steel fiber reinforced composites. In the quasi-UD steel fiber composite, a more brittle matrix was found to make for a more brittle composite [7], and a better adhesion led to a higher strain-to-failure [15]. The results for the 4-harness satin weave laminates, however, clearly show that the composite with the brittle matrix (EPON/AR) is the most ductile one, while the composite with the improved adhesion (RIM/GPS ) is the most brittle one. In the next section, the stress-strain behavior will be discussed for the three composites one by one, according to the chronology of the experiments.

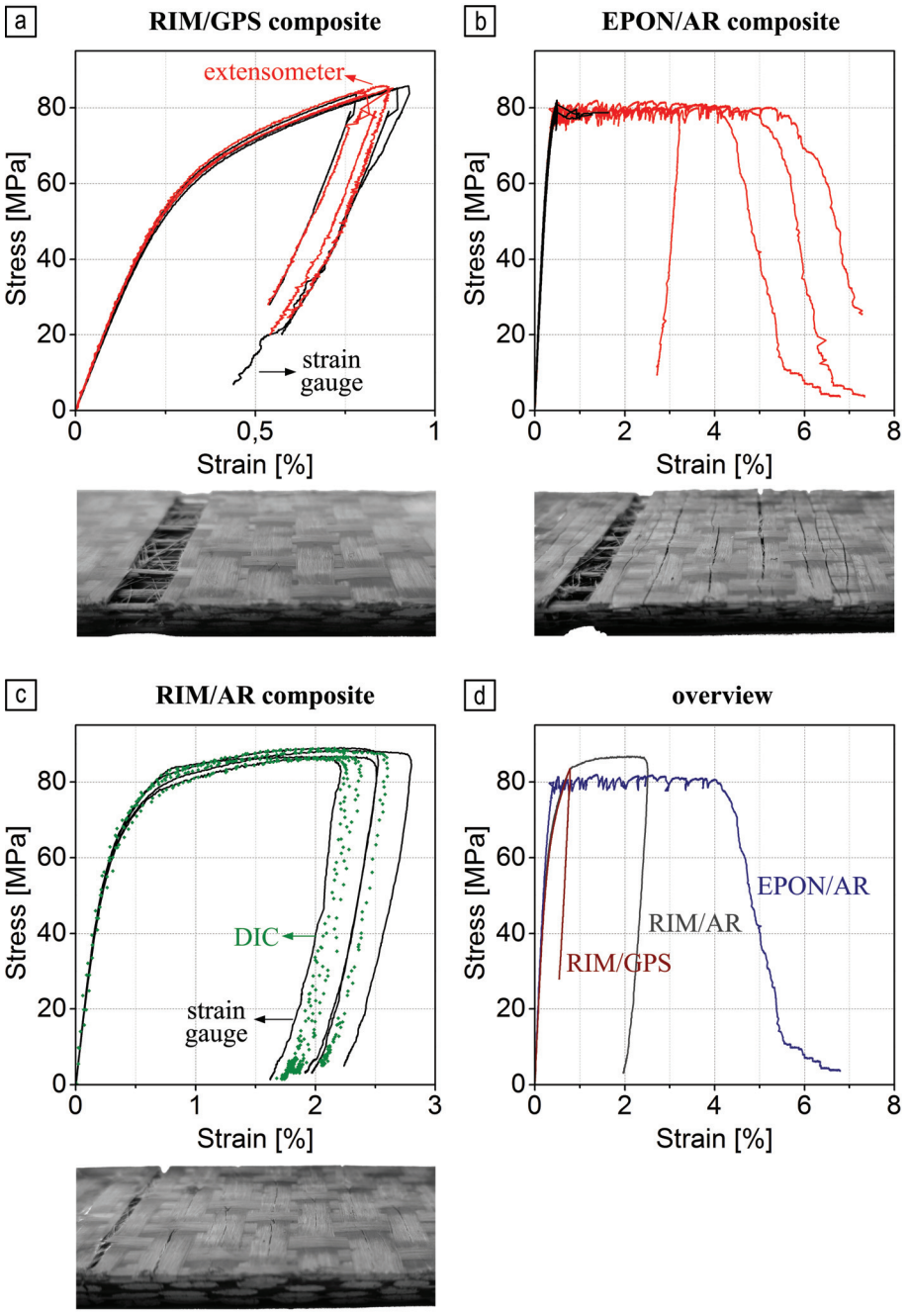


Figure 6-3: Stress-strain response and surface cracks under warp-oriented tensile loading for the RIM/GPS (a), EPON/AR (b) and RIM/AR (c) composite specimens, and a comparative overview of the stress-strain response of all three composites (d)

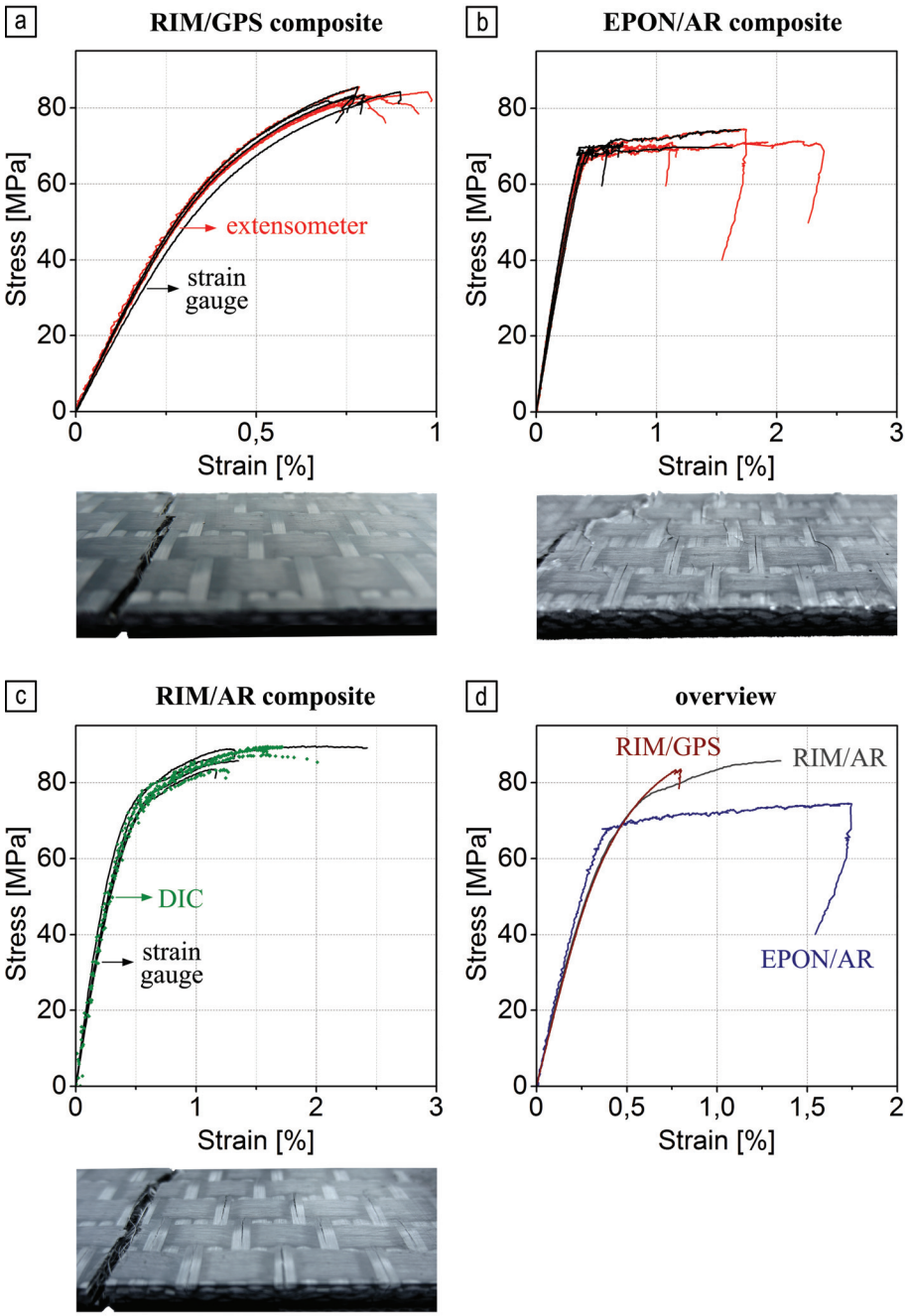


Figure 6-4: Stress-strain response and surface cracks under weft-oriented tensile loading for the RIM/GPS (a), RIM/AR (b) and EPON/AR (c) composite specimens, and a comparative overview of the stress-strain response of all three composites (d)

Table 6-2: Tensile properties along the warp direction of steel fabric composites with brittle (EPON) or tough (RIM) epoxy matrix and with untreated (AR) or enhanced (GPS) interface

| **Mechanical property** | **RIM/GPS** | **RIM/AR** | **EPON/AR** |
|---|---|---|---|
| Young's modulus E [GPa] | 24.5 ± 1.6 | 25.7 ± 0.8 | 25.8 ± 1.5 |
| Yield strength $\sigma_Y$ [MPa] | 65.1 ± 1.5 | 64.6 ± 0.8 | 76.3 ± 0.5 |
| Yield strain $\varepsilon_Y$ [%] | 0.37 ± 0.01 | 0.35 ± 0.01 | 0.40 ± 0.02 |
| Ultimate strength $\sigma_{ult}$ [MPa] | 85.1 ± 1.1 | 87.8 ± 1.2 | 80.9 ± 0.8 |
| Ultimate strain $\varepsilon_{ult}$ [%] | 0.85 ± 0.07 | 2.40 ± 0.31 | 4.81 ± 1.33 [a] |

[a] Maximum strain value with a stress level within 10% of the ultimate stress, as recorded by the extensometer

Table 6-3: Tensile properties along the weft direction of steel fabric composites with brittle (EPON) or tough (RIM) epoxy matrix and with untreated (AR) or enhanced (GPS) interface

| **Mechanical property** | **RIM/GPS** | **RIM/AR** | **EPON/AR** |
|---|---|---|---|
| Young's modulus E [GPa] | 19.0 ± 1.0 | 20.6 ± 1.6 | 20.4 ± 1.5 |
| Yield strength $\sigma_Y$ [MPa] | 67.1 ± 1.4 | 66.0 ± 3.8 | 66.3 ± 0.8 [a] |
| Yield strain $\varepsilon_Y$ [%] | 0.45 ± 0.01 | 0.42 ± 0.02 | 0.37 ± 0.03 [a] |
| Ultimate strength $\sigma_{ult}$ [MPa] | 84.0 ± 1.1 | 86.0 ± 3.1 | 71.8 ± 1.9 |
| Ultimate strain $\varepsilon_{ult}$ [%] | 0.81 ± 0.06 | 1.69 ± 0.63 | 1.61 ± 0.60 [b] |

[a] Offset yield point at 0.1% strain is not available. Last data before first stress drop was reported instead
[b] Maximum strain value with a stress level within 10% of the ultimate stress, as recorded by the extensometer

### 6.3.3 Chronology and analysis of the tensile behavior

The RIM/GPS composite is the most brittle of the three composites, despite the improved interface. Its stress-strain relation hardly depends on the loading direction, as is most clear on the comparative overview in Figure 6-5. Both the blue and the red curve (indicating warp- and weft-oriented loading, respectively) indicate a short, seemingly elastic region, after which a region of increasing softening sets in. At a strain of about 0.85%, one single brittle transversal crack causes a sudden loss of load-bearing capacity. When loading is applied along the warp direction, the crack is

bridged by warp fibers, which continuously ravel out when further straining is applied. This phenomenon is responsible for the downward slope in the stress-strain curves. Crack bridging does not happen along the weft direction, and therefore, the corresponding curves do not have the long downward slope. Regardless of the loading direction, the specimen surface only shows one crack after failure, i.e. the fatal crack.

The original RIM/AR composite ranks in between the other two composites when it comes to ductility. On the overviews in Figure 6-3.d and Figure 6-4.d, it shows that the RIM/AR curves roughly overlap the RIM/GPS curves. The RIM/AR composite can be strained beyond the failure point of the RIM/GPS composite, and for this composite, there is a big difference between the loading directions. The warp-oriented specimens can be strained up to 2.40%, while the weft-oriented specimens only strain up to 1.69%. The damage on the specimen surface, however, is very similar for both the loading directions, and it is in line with the detailed observations on the edge of the laminates as reported on in section 4.5. During the stress plateau, transversal cracks appear on the centers of the transversal weft yarns, evenly spread along the length of the specimen. As more strain is applied, the cracks first open up uniformly, until the deformation starts to localize in one crack zone. When examining the specimen surface after failure, no surface cracks were found that had jumped a crimp region, so all cracks stopped at the crossing point with a warp yarn. Similarly as for the RIM/GPS composites, the curves for warp-oriented loading exhibit a downward slope due to crack bridging, while the curves for weft-oriented specimens are cut off at their peak.

Surprisingly, the toughest behavior is accomplished by the composite with the brittle matrix, i.e. EPON/AR. Figure 6-3.d and Figure 6-4.d show that the EPON/AR curves overlap with the other two curves at first, but they remain steeper after the initial elastic region and they pass much more abruptly into the stress plateau. For the EPON/AR composite, the difference between the loading directions is even more important than for the RIM/AR composite. This is most clear from Figure 6-5. First, the EPON/AR composite is the only one that is significantly stronger along the warp direction than along the weft direction. Second, the strain-to-failure along the warp direction is 4.81%, which means that the EPON/AR composite is almost three times more ductile than the RIM/AR composite, and over five times more ductile than the RIM/GPS composite along the warp direction. Along the weft direction, the EPON/AR composite only strains up to 1.61%, which is about the same level as the RIM/AR composite. A third difference between the loading directions is the damage pattern on the specimen surface. Weft-oriented loading causes a very similar crack pattern as in the RIM/AR specimens, with cracks running through the centers of the surface warp yarns from crimp region to crimp region. The crack pattern caused by warp-oriented loading looks very different. The cracks are much more numerous, they open up wider, and they do not halt at the crimp regions. The easy crack propagation

also shows in the very jagged stress plateau in the stress-strain curves. Every time the tensile strength is reached, a brittle, yet non-fatal crack causes a short fall in the stress–strain curve. Like in the other two composites, fiber bridging was observed during crack localization under warp-oriented loading, but not under weft-oriented loading. Both the loading directions caused rather brittle cracks that broke the resistance wire of the strain gauge when they crossed it. Therefore, only the extensometer captures the full toughness of this material.

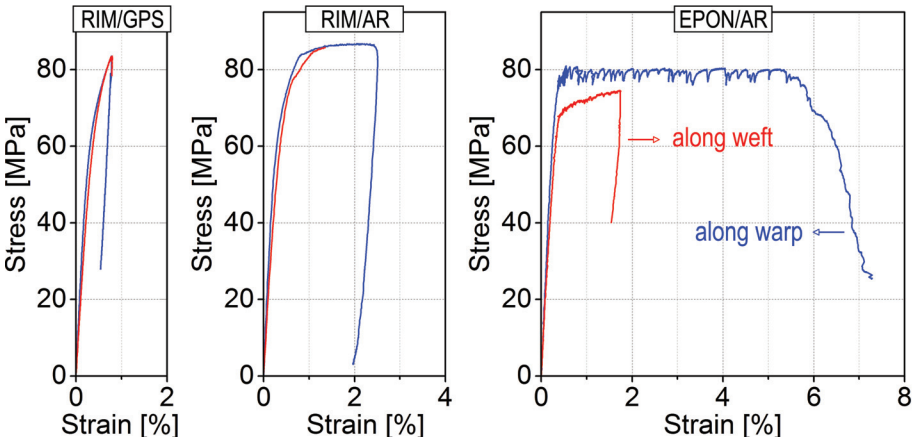


Figure 6-5: Comparative overview between loading directions for the stress-strain response of the RIM/GPS, RIM/AR, and EPON/AR composite

The most notable observations on the stress-strain behavior of the three composites can be summarized as follows:

- Opposite to the expectations, the composite with enhanced adhesion (RIM/GPS) was the most brittle of the three, while the composite with the most brittle matrix (EPON/AR) achieved the highest strain-to-failure.
- Along the warp direction, the three composites were found to vary strongly in toughness, with a failure strain of 0.85, 2.40 and 4.81%, respectively, for the RIM/GPS, RIM/AR and EPON/AR composite. When weft-oriented tension is applied, the tough composites lose a lot of their advantage and the failure strains come closer together: 0.81%, 1.69%, and 1.61%, respectively.

## 6.4 DAMAGE MECHANICS

After the tensile experiments, the polished edges of the damaged specimens were captured over their full length through 3D image stitching with a Keyence VHX-2000 microscope. Analyzing the differences in damage morphology between the three composites may explain the differences in ductility. In addition, dependencies of the

crack pattern on the loading direction may indicate why the RIM/AR, and certainly the EPON/AR composite lose a lot or their ductility when weft-oriented loading is applied.

### 6.4.1 Observations on the specimen edge

Figure 6-6 and Figure 6-7 show the damage morphology of the three composites under warp- and weft-oriented tension, respectively. The comparison of these figures again very clearly shows the considerable differences between warp and weft yarns when it comes to crimp angle (cf. section 4.3.2) and fiber volume fraction (cf. section 4.3.4). In what follows, the nature of the observed damage will be discussed for the three composites separately.

The damage morphology due to static tensile loading in the RIM/AR composites (tough matrix, untreated interface) has been discussed in detail and for three different stages of loading in section 4.5. The observations on the edge of the failed specimen will be briefly readdressed in this paragraph. On Figure 6-6 and Figure 6-7, it is clear that the RIM/AR composite has a lot of cracks after the experiment. The cracks initiate due to debonding of the weak fiber–matrix interface in the transversal yarns. If the distance between neighboring fibers is sufficiently small, the interfacial detachments can bridge through the matrix in between. However, if the matrix zone is wide enough, it will arrest the defect through the formation of a matrix cusp. As marked with arrows on Figure 6-6, there are a lot of singular detachments in the transversal weft yarns, because the inter-fiber distance is relatively large. In the transversal warp yarns on Figure 6-7, the inter-fiber distance is mostly small enough for the detachments to coalesce into well-defined cracks, covering the full height of the yarn. If the distance between neighboring yarns is small, the cracks can jump from one yarn to another. The matrix pocket typically shows severe plastic deformation in this case. Some cracks are found to extend along the boundary of a transversal yarn, especially in the contact zone with a longitudinal yarn. An example of such a defect is marked on the first detail in Figure 6-7. Note that this crack debonds the transversal yarn from the matrix, rather than the longitudinal yarn. Splitting of longitudinal yarns has been observed on some of the RIM/AR specimens under weft-oriented loading, but not on all of them.

The microscopic images of the RIM/GPS composites (tough matrix, enhanced interface) on Figure 6-6 and Figure 6-7 clearly prove the effect of the silane treatment. The stress concentrations around the steel fibers must be considerable, because of the stiffness mismatch between the steel fibers and the epoxy matrix and the angular shape of the fibers. Nevertheless, the RIM/GPS composite edge shows no signs of damage after loading, besides the final crack. Secondary cracks like the one in Figure 6-7 were observed, but only rarely.

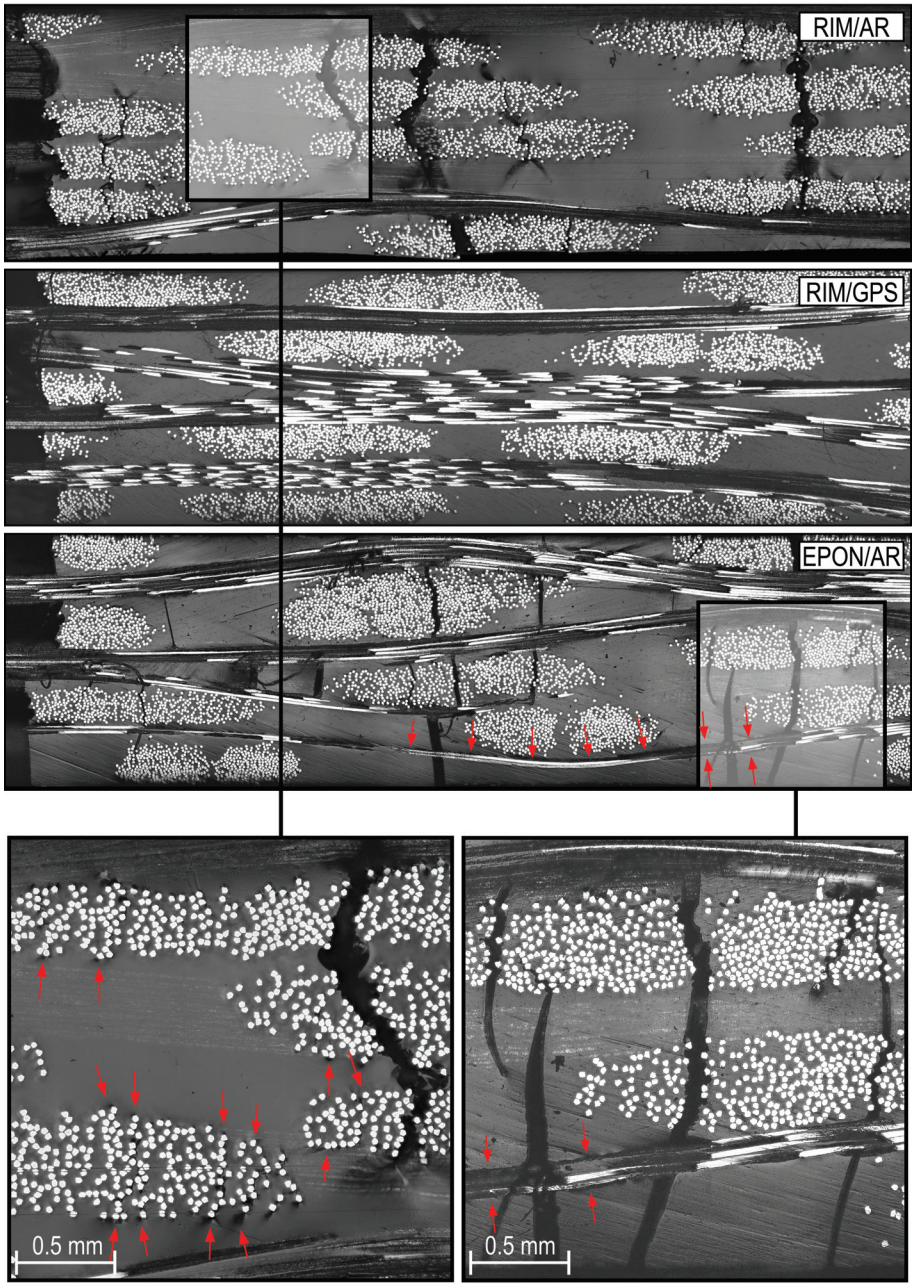


Figure 6-6: Microscopic reconstruction of the RIM/GPS , RIM/AR and EPON/AR composite edge after loading along the warp direction with details of the damage morphology

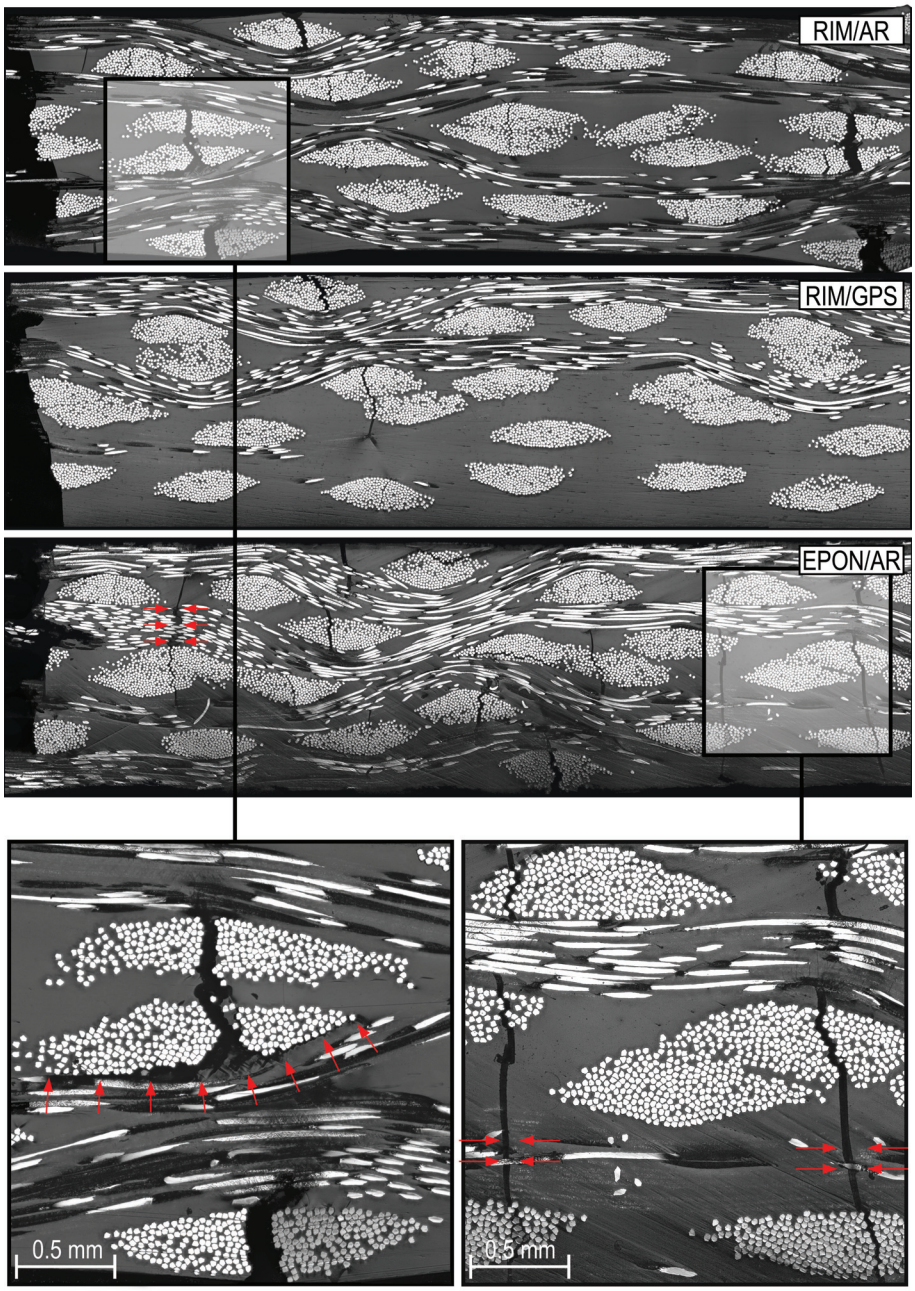


Figure 6-7: Microscopic reconstruction of the RIM/GPS , RIM/AR and EPON/AR composite edge after loading along the weft direction with details of the damage morphology

The EPON/AR composite (brittle matrix, untreated interface) has the same weak fiber/matrix interface as the RIM/AR composite, but the matrix systems is brittle instead of tough. The brittle matrix is unable to stop any defects, which makes that every small flaw grows into a full crack. This is clearly reflected in the crack morphology on Figure 6-6 and Figure 6-7. There are no signs of local fiber detachments or other small defects that are arrested through matrix cusping. Instead, cracks in the EPON/AR composite span the full region between load-bearing yarns. Most of them pass through a transversal yarn, but some run entirely through matrix. This means that the detachment of transversal fibers is not the only source of damage initiation in this composite. The way a crack propagates when it comes across a load-carrying yarn is strongly dependent on the loading direction. If a crack encounters a load-bearing warp yarn, the warp yarn typically debonds from the matrix, as marked on Figure 6-6. The debonding often bridges from one crack to the next, extending over several millimeters. In contrast, if a crack reaches a load-bearing weft yarn, it tends to cross the weft yarn through the matrix, without rupturing or debonding the fibres. This phenomenon is marked on Figure 6-7.

### 6.4.2 Hypothesis on damage mechanisms and failure

The toughness of the three composites relates to the damage morphology through the micro-mechanics that govern the failure strain. First, note that the steel fibers strain to more than 19% before failing. The reason why the composites do not attain such a failure strain is because the load-carrying fibers are fixed within the composite structure. The matrix and the transversal yarns work as a mechanical interlock, forcing the load-bearing fibers to deform along with them. The more rigid this transversal structure and the tighter the fibers are fixed within it, the more it restricts the deformation of the load-bearing fibers. Two types of damages were observed in the composites, and both types can contribute to the failure strain. The principles are illustrated schematically in Figure 6-8. The first type is the transversal damage, ranging from small, local detachments of transversal fibers to fully grown cracks. As long as this damage remains distributed, it softens the transversal structure that interlocks the load-bearing yarns. As soon as it localizes in one section, however, it will onset final failure. The second type of damage is the debonding of load-carrying fibers or yarns. The debonded sections are free to deform to the full plastic potential of the steel fibers, so they can contribute greatly to the deformation capability of the composite. This mechanism cannot occur if the fiber–matrix interface is too strong [8]. Furthermore, it cannot stand alone; it always requires transversal cracks to interrupt the continuity of the transversal structure. The longer the length of the debonding, the more it can contribute to the failure strain by bridging the crack openings. In conclusion, the key to increasing the failure strain of the composites is

to have as much distributed damage as possible before it starts localizing, and to have long debondings on the load-bearing yarns that are able to bridge the fatal crack.

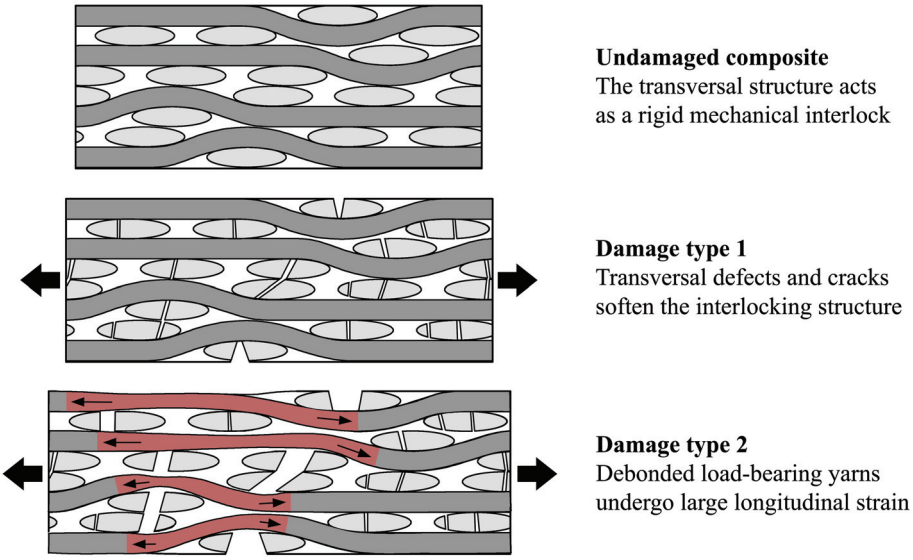


Figure 6-8: Working principles of how the two types of damage contribute to the composite toughness

The principles in Figure 6-8 apply to the composites under investigation. In the most brittle composite, RIM/GPS, no damage is accumulated before failure. The strong fiber–matrix adhesion in this composite makes that the interface bond does not fail until a relatively high stress is reached. Thus, when a local defect finally initiates, the global stress level is high enough to facilitate fast crack propagation. As a result, the first crack leads to catastrophic failure.

The RIM/AR composite has a higher toughness, because there is distributed type 1 damage to soften the material in the transverse direction. The weak fiber/matrix interface in this composite will locally fail at a relatively low global stress level. At that point, the small detachments can easily be cusped by the matrix, because the overall stress is too low to cause sudden rupture. Instead, the cracks open up steadily and a network of cracks arises. There are three arguments for the lower toughness along the weft direction in the RIM/AR composite: (1) the stronger undulation of the weft yarns, (2) the denser fiber packing in the warp yarns, and (3) the lower toughness of the weft fibers. The first argument is obvious: the more undulated the load-bearing yarns, the more severe the stress concentrations they cause within the transversal composite structure. The reasoning behind the second argument, the effect of the fiber volume fraction, is as follows. A densely packed region within the transversal yarns has a higher stiffness and will therefore bear more stress. At the same time, the smaller

inter-fiber distance in these regions will increase the stress concentration factor on the fiber–matrix interface. Indeed, it was mentioned in the previous section that the loosely packed weft yarns often have a lot of singular fiber detachments, while the inter-fiber distances within the more densely packed warp yarns are typically small enough for the detachments to grow into fully developed cracks. The third argument takes the reader back to section 2.2.2, where the stress-strain behavior of the stainless steel weave was discussed. The tensile tests revealed that the textile is about 15% less ductile along the weft direction than along the warp direction, most probably because the weft yarns have undergone cold working during the weaving process. If the weft fibers are less ductile, they cannot strain as much when they are given the space in the damaged interlocking structure, which can only be detrimental for the ductility of the composite.

If a brittle matrix is used instead of a tough matrix, the damage morphology – and therefore, the toughness, strongly depends on the loading direction. The weft-oriented EPON/AR composite is softened by type 1 damage. This damage has a different nature than the type 1 damage in the RIM/AR composite, but its effect on the strain-to-failure seems to be the same. The warp-oriented composite additionally shows type 2 damage. Therefore, the transversal cracks can open up further as they are bridged by load-carrying yarns, and the EPON/AR composite strains almost twice as far along the warp direction as the RIM/AR composite. A possible explanation why the warp yarns debond from the matrix, while the weft yarns break through the matrix, is the difference in fiber volume fraction. The weft yarns can be viewed as a loose collection of separate fibers. If a crack comes across, the fibers act as small separate obstacles that can easily be crossed without changing the crack direction. Because the warp yarns are more compact and have a stronger edge definition, they will act more as one yarn, forcing the cracks to redirect along their boundary. The small distance between the fibers on the yarn border further facilitates debonding.

## 6.5 CONCLUSION

The current chapter reports on the influence of the matrix ductility and the fiber/matrix interfacial strength on the mechanical behavior of the stainless steel 4-harness satin weave composite. The aim was to identify those mechanisms that are characteristic for a reinforcement with a ductile nature and a woven internal structure. Special attention was paid to the mechanisms that contribute to the composite toughness, and to those that lead to failure. After a short specification of the variations on the matrix ductility and the interface, the stress-strain relation of the composites under static tension was presented. Then, the damage morphologies in the composites were compared, and finally, a hypothesis was put forth about the failure mechanisms that govern the composite toughness.

The results of the tensile experiments were in many ways counterintuitive. A more brittle matrix gave rise to a tougher composite, and a stronger interface lowered the toughness. At the same time, the brittle matrix composite was densely packed with transversal cracks after loading, while the composite with the enhanced interface showed no damage but the final rupture. Based on these observations, the hypothesis was put forth that the transversal composite structure acts as a rigid mechanical interlock on the load-carrying yarns. Damage softens the interlock and unbinds the ductile load-bearing yarns, and therefore, it increases the toughness of the composite. Enhancing the fiber/matrix adhesion prevents transversal damage prior to failure, and therefore leads to a brittle composite. A brittle matrix is very prone to develop an evenly distributed transversal crack pattern, and therefore leads to a tough composite.

Besides the matrix and the interface, the reinforcement architecture as well plays an important role in the composite toughness. This is clear from how the behavior depends on the loading direction. In the most brittle composite – the one with the enhanced interface – the warp and weft direction were just as ductile, because damage was observed for neither loading direction. In the other composites, the internal geometry influenced the damage morphology, with a higher ductility along the warp direction as a result.

## 6.6 REFERENCES

[1] Salkind MJ. *The Role of Interfaces in Fiber Composites*. In: Burke JJ, Reed NL, Weiss V, editors. Surfaces and Interfaces II. New York: Syracuse University Press. p. 417-445. 1968.

[2] Vallons KAM, Drozdzak R, Charret M, Lomov SV, Verpoest I. *Assessment of the mechanical behaviour of glass fibre composites with a tough polydicyclopentadiene (PDCPD) matrix*. Composites Part A: Applied Science and Manufacturing; 78: 191-200. 2015.

[3] Compston P, Jar P-YB, Davies P. *Matrix effect on the static and dynamic interlaminar fracture toughness of glass-fibre marine composites*. Composites Part B: Engineering; 29: 505–516. 1998.

[4] Awang Ngah S, Taylor AC. *Toughening performance of glass fibre composites with core–shell rubber and silica nanoparticle modified matrices*. Composites Part A: Applied Science and Manufacturing; 80: 292-303. 2016.

[5] Carolan D, Ivankovic A, Kinloch AJ, Sprenger S, Taylor AC. *Toughened carbon fibre-reinforced polymer composites with nanoparticle-modified epoxy matrices*. Journal of Materials Science; 52: 1767-1788. 2016.

[6] Prasad N, Tola C, Coulaud M, Claes M, Lomov SV, Verpoest I, et al. *Carbon Fiber Composites Based on Multi-Phase Epoxy/PES Matrices with Carbon Nanotubes: Morphology and Interlaminar Fracture Toughness Characterization* Advanced Engineering Materials; 18: 2040-2046. 2016.

[7] Callens MG, Gorbatikh L, Verpoest I. *Ductile steel fibre composites with brittle and ductile matrices*. Composites Part A: Applied Science and Manufacturing; 61: 235-244. 2014.

[8] Wetherhold RC, Bös J. *Ductile reinforcements for enhancing fracture resistance in composite materials*. Theoretical and Applied Fracture Mechanics; 33: 83-91. 2000.

[9] Jiang Z, Zhang H, Zhang Z, Murayama H, Okamoto K. *Improved bonding between PAN-based carbon fibers and fullerene-modified epoxy matrix*. Composites Part A: Applied Science and Manufacturing; 39: 1762-1767. 2008.

[10] Wu G, Ma L, Wang Y, Liu L, Huang Y. *Interfacial properties and impact toughness of methylphenylsilicone resin composites by chemically grafting POSS and tetraethylenepentamine onto carbon fibers*. Composites Part A: Applied Science and Manufacturing; 84: 1-8. 2016.

[11] He H, Li K, Gao F. *Improvement of the bonding between carbon fibers and an epoxy matrix using a simple sizing process with a novolac resin*. Construction and Building Materials; 116: 87-92. 2016.

[12] Downey MA, Drzal LT. *Toughening of carbon fiber-reinforced epoxy polymer composites utilizing fiber surface treatment and sizing*. Composites Part A: Applied Science and Manufacturing; 90: 687-698. 2016.

[13] Feih S, Wei J, Kingshott P, Sørensen BF. *The influence of fibre sizing on the strength and fracture toughness of glass fibre composites*. Composites Part A: Applied Science and Manufacturing; 36: 245-255. 2005.

[14] Liu W, Zhang S, Li B, Yang F, Jiao W, Hao L, et al. *Improvement in interfacial shear strength and fracture toughness for carbon fiber reinforced epoxy composite by fiber sizing*. Polymer Composites; 35: 482-488. 2014.

[15] Callens MG, Gorbatikh L, Bertels E, Goderis B, Smet M, Verpoest I. *Tensile behaviour of stainless steel fibre/epoxy composites with modified adhesion*. Composites Part A: Applied Science and Manufacturing; 69: 208-218. 2015.

[16] Ghosh AK, Bertels E, Goderis B, Smet M, Van Hemelrijck D, Van Mele B. *Optimisation of wet chemical silane deposition to improve the interfacial strength of stainless steel/epoxy*. Applied Surface Science; 324: 134-142. 2015.

[17] Ghosh AK. *The Interphase in Stainless Steel-Polymer Hybrids: Characterisation and Optimisation of Interfacial Interaction via Surface Treatment and Nano-modification of the Polymer*. [PhD Dissertation]. Brussels: Vrije Universiteit Brussel. Department of Materials and Chemistry - MACH. 2015.

[18] Bertels E. *Nano-Engineered Polymer-Steel Hybrids: Chemical and Physical Compatibilization*. [PhD dissertation]. Heverlee: KU Leuven. Department of Chemistry - Polymer Chemistry and Materials Division. 2015.

[19] Karger-Kocsis J, Czigany T. *Interfacial Effects on the Dynamic Mechanical Behavior of Weft-Knitted Glass Fiber Fabric-Reinforced Polypropylene Composites Produced of Commingled Yams. Tensile and Flexural Response* Applied Composite Materials; 4: 209-218. 1997.

[20] Kotaki M, Hamada H. *Effect of interfacial properties and weave structure on mode I interlaminar fracture behaviour of glass satin woven fabric composites*. Composites: Part B; 28: 257-266. 1997.

[21] Vieille B, Casado VM, Bouvet C. *Influence of matrix toughness and ductility on the compression-after-impact behavior of woven-ply thermoplastic- and thermosetting-composites: A comparative study*. Composite Structures; 110: 207-218. 2014.

[22] Allaer K, De Baere I, Lava P, Van Paepegem W, Degrieck J. *On the in-plane mechanical properties of stainless steel fibre reinforced ductile composites*. Composites Science and Technology; 100: 34-43. 2014.

[23] ASTM Standard. D3039/D3039M. *Standard Test Method for Tensile Properties of Polymer Matrix Composite Materials*. West Conshohocken, PA: ASTM International; DOI: 10.1520/D3039_D3039M-14. Available from: www.astm.org. 2014.

# Chapter 7

## CONCLUSIONS

*This last chapter is divided into two parts. The first part summarizes the conclusions of this work. These conclusions start with an assembly of the methodologies and procedures that were set up and used throughout this work into a roadmap to study an imperfect textile composite by analyzing the edge of a laminate. Then, the findings regarding geometrical characteristics and statistics of the steel fiber textile composites are presented, followed by the findings on strain and damage phenomena. Finally, a hypothesis is put forth on why the combination of a ductile reinforcement and a ductile matrix does not necessarily lead to a tough composite. In the second part of this chapter, suggestions for future work are proposed.*

## 7.1 CONCLUSIONS

In this section, the conclusions of this doctoral thesis are summarized. First, a two-step roadmap has been developed to study an imperfect textile composite by analyzing the edge of a laminate, the first step being a geometrical analysis, and the second step being a finite element study. The methodologies and the procedures contained in this roadmap were applied to analyze the steel-fabric reinforced epoxy composite that is the subject of this work, and the findings from each step of the roadmap are presented next. More specifically, the results regarding the geometrical characteristics and statistics are the second item of this section, while the third part concerns the finite element results regarding strain and damage distributions, and their validation with the experimentally observed phenomena. In the final fourth part, a hypothesis is put forth on why the combination of a ductile reinforcement and a ductile matrix does not necessarily lead to a tough composite.

### 7.1.1 Roadmap to analyze an imperfect textile composite through the edge of a laminate

The commonly used RVE (Representative Volume Element) modeling approach that was applied at first proved not to be suited to capture the stress and strain localizations in the composite under study. An RVE model does not represent the imperfections and the variabilities that characterize the internal geometry of the composite, and this shortcoming was identified as the reason behind its inaccuracy. This insight gave rise to the development of a new approach that is especially focused on the details of a realistic reinforcement geometry. More specifically, this work presents a two-step roadmap towards a full geometrical and mechanical analysis of a composite through the edge of a laminate.

**In the first step**, the internal geometry and its variability are characterized and quantified by analyzing high-resolution microscopic images of the edge of a composite laminate. Several methodologies and (semi-) automatic procedures were developed to enable and facilitate this process:

- Method in Photoshop to extract the transversal fibers from a microscopic image while maintaining the fiber volume fraction.
- Method in Photoshop for an unbiased definition of the yarn cross sections starting from fiber bundles.
- Automatic procedure, implemented in Python, to calculate the (statistics on) area, shape factor and fiber volume fraction of the yarns starting from image files of fibers and cross sections.
- Method in Photoshop to reconstruct the longitudinal yarns from a microscopic image.

- Automatic detection procedure through Python scripting to deduce the center lines of the longitudinal yarns, and the statistics of their undulations.
- Fully automatic procedure scripted in Python to quantify and visualize the inhomogeneity of the transversal yarns for a chosen smoothing radius.

The approach of working with microscopic images of a laminate edge allows to characterize the internal geometry of an actual composite laminate in a relatively easy, quick and non-destructive manner. Moreover, the approach is very well suited for in-house analysis, as it does not require advanced equipment such as an X-ray micro-computed tomography scanner. The 2D nature of the method can be overcome by using the statistics to detect possible correlations between a parameter and the position of the corresponding geometrical feature within the laminate structure, or by slicing the sample further down and to study multiple edges.

**The second step** is to develop a finite element model to study the composite from a mechanical point of view. The tools that were developed to analyze the geometrical characteristics are based on an explicit extraction of the geometrical features from the microscopic images. These reconstructed geometrical data are an excellent starting point for building a finite element model. The following methods and procedures were developed in this context:

- Method to translate geometrical data in an image format into an Abaqus part.
- Fully automatic procedure (Python) to map a processed microscopic image onto a finite element mesh, and to translate the local fiber volume fractions into local material properties that are assigned to the proper elements. This procedure was developed both for homogeneous and inhomogeneous transversal yarns.

The advantage of analyzing the mechanical behavior on the edge of a laminate is the possibility of straightforward validation. Numerical results can easily be compared to the observed crack patterns on the specimen edge, or to the strain fields obtained through DIC. Moreover, the models are relatively easy to construct, yet allow for a nearly unlimited geometrical detail. The inhomogeneity of the transversal yarns, for instance, can be taken into account, something which cannot be managed in a 3D model to this day. Due to their 2D nature, finely meshed models can be calculated within minutes, even with a modest computational capacity.

### 7.1.2 Step 1: The geometrical characteristics of the stainless steel fiber 4-harness satin weave epoxy composite

The tools and methods that were summarized as the first step of the roadmap in the previous section were applied to the steel fiber textile epoxy composite that is the subject of this work. The reinforcement under study was a 4-harness satin weave, consisting of ductile stainless steel fibers with a diameter of 30 μm and a strain-to-

failure of 19%. Special about this weave is the large difference between the weft and warp direction. The weft yarns are made of two warp yarns, which causes an especially large difference in crimp angle, and a large difference in fiber volume fraction between them. Another peculiarity is the looseness of the weave. This results in a very low fiber volume fraction of the composite laminates (± 25%), severe nesting of the laminate layers, and strong variations of the inter- and intra-yarn fiber density.

The unusual nature of the reinforcement architecture was very clear from the geometrical analyses on the microscopic images. On the ply level, layer shifting and nesting was observed with a nesting percentage of 106.7%. This corresponds to an increase of the laminate's fiber volume fraction of 6.7% with respect to a hypothetical, unnested laminate. On the yarn level, a large difference in crimp angle was observed between the warp and weft yarns, with values of 6.6 ± 1.2° and 18.0 ± 2.9° for warp and weft yarns, respectively. The cross sections were characterized based on area and shape factor (width over thickness ratio). The weft yarns have exactly twice as many fibers as the warp yarns, but the shape factor of the weft yarns is more than twice that of the warp yarns, i.e. 7.91 ± 1.18 versus 3.83 ± 0.51, and the weft area is more than double the warp area, i.e. 1.10 ± 0.13 mm² versus 0.36 ± 0.02 mm². Accordingly, the fiber volume fraction of the weft yarns is much lower than that of the warp yarns, with 35.9% versus 54.6%. Most of the geometrical parameters on the yarn level did not depend on the position of the yarn within the laminate. On the sub-yarn level, a strong variation of the fiber volume fraction was observed, with denser regions typically located where the yarn touches a perpendicular yarn, especially in the crimp regions of the perpendicular yarn. Low fiber volume fractions were most often observed on the edges of the yarns. The quantification of the intra-yarn fiber volume fraction depends heavily on the smoothing radius, i.e. the radius of the region over which is averaged. A smoothing radius of 4 times the fiber diameter was found to be a good compromise between having enough resolution to capture mesoscopic trends, while filtering out most of the noise.

### 7.1.3 Step 2: Mechanics of the stainless steel fiber 4-harness satin weave epoxy composite: strain and damage

Following the geometrical characterization, the composite was subjected to tensile experiments, and the surface **strain** fields on the edge of a laminate were monitored using Digital Image Correlation (DIC). The measured strain distributions were found to relate strongly to the underlying internal geometry, suggesting that the composite can be studied through the edge of a laminate, not only from a geometrical, but also from a mechanical point of view. This hypothesis was further confirmed with a numerical concept check in section 5.2, which showed that a 2D model of an RVE produces an in-plane stress state that is very similar to that on the edge of the equivalent full 3D RVE model, as long as the 2D model represents an edge on which

all the load-bearing yarns are visible. Finite element models were constructed of the tested laminates according to step 2 of the roadmap. The numerical strain patterns could be directly validated with the DIC results, and a very good correlation was found between them. The inhomogeneity of the transversal yarns did not seem not to affect the numerical strain distribution significantly, which indicates that the strain fields are mainly governed by the geometrical features on the meso-scale.

While the numerical strains on the laminate edge were validated with the experimental DIC strain fields, the numerical stresses were tested against the **damage** that was observed on the laminate edge. Two methodologies were elaborated in order to obtain reliable observations on the initiation strain, the propagation, and the morphology of the damage. Similarly as for the strain, the damage on the edge of a laminate related strongly to the internal geometry:

- *Initiation.* Damage initiates at a strain around 0.4% due to small fiber/matrix detachments inside the transversal yarns, regardless of the loading direction or the stacking system. Damage keeps initiating as the strain is increased and is at all times well spread along the length of the specimen, in a more or less periodic pattern with respect to the geometric periodicity.
- *Propagation.* The separate detachments are initially cusped by the tough matrix, but they coalesce into large cracks if the inter-fiber distances are small enough. The weft yarns are very loosely packed, which makes that many detachments do not grow out to be cracks. In the warp yarns, on the other hand, the inter-fiber distances are smaller, and the detachments typically develop into cracks that span the full height of the yarn. If the distance to a neighboring yarn or to the laminate surface is small enough, cracks can travel across the matrix pockets. On the specimen surface, it was observed that cracks typically extend from crimp region to crimp region. Under warp-oriented loading, the load-carrying yarns bridge the crack when the strain starts to localize, and final rupture is postponed. When loading is applied along the weft yarns, on the other hand, these weft yarns break immediately when a crack starts to open up, which leads to brittle fracture of the laminate at a much smaller strain level. The location of final failure cannot be predicted by monitoring the damage on the laminate edge during loading, because the fatal crack may originate inside the laminate and only travel to the laminate edge at the very final moment.

Finite element models were built for the tested laminates according to the second step of the roadmap, and the earliest cracks were compared to the numerical stress distributions. In general, the models were able to predict some of the observed cracks, but not all of them. The other way around as well, many stress peaks could be linked to an observed crack, yet not all of them. The predictive power of the models was increased by accounting for the inhomogeneity of the transversal yarns, especially when it comes to the exact location of damage within the transversal yarn.

In summary, the strong correlation between the experimental strain pattern and the internal geometry on the edge of the composite laminates was confirmed by the numerical experiments. This shows that the edge section of the laminate is not heavily affected by the underlying inner sections when it comes to the distribution of the in-plane strain components at relatively low strains. Furthermore, it proves that a 2D model that represents the internal geometry of the laminate in a realistic manner qualifies to predict the strain distribution. The correlation between the numerical stresses and the initial damage was less strong, most likely because the cracks that are visible on the laminate edge may have originated inside the laminate. Furthermore, the stress pattern on the laminate edge can be expected to degenerate quickly as cracks start to disrupt the reinforcement structure. This investigation hence shows that the composites can be studied through a 2D analysis on the edge of a laminate, as long as all load-bearing yarns are represented, and as long as the strain level remains low. Damage, especially its propagation, cannot be predicted when merely the edge of the laminate is considered, and can hence also not be studied with a 2D model.

### 7.1.4 Findings on the mechanisms that explain why the combination of a ductile textile with a ductile matrix does not necessarily lead to a tough composite

The idea behind using ductile fibers as a composite reinforcement was to create a tough composite. This expectation was not met. The failure strain of the composite reaches up to 1.5-2.5%, while the matrix can be strained up to 8%, and the fibers up to 19%. In search for more insights on the mechanisms that cause the early failure, an experimental study was performed to investigate the influence of the matrix ductility and the interfacial strength on the composite toughness.

Against the expectations, using a more brittle matrix gave rise to a tougher composite, and strengthening the interface embrittled the composite. An explanation for these findings was found in the damage morphology. The brittle matrix composite showed a lot of damage after failure, with numerous transversal cracks that were evenly spread along the length of the laminate specimen. The composite with the enhanced interface, on the other hand, showed no damage besides the fatal fracture.

This incited the insight that the transversal structure works as a mechanical interlock to the load-bearing yarns. This interlock fixes the ductile load-bearing yarns and prevents them from straining to their full plastic potential. Distributed damage softens the interlocks and gives the ductile fibers a little more space to strain up. Therefore, it is key to have as many evenly spread cracks as possible before the strain starts to localize in one of them. Another mechanism that frees a load-bearing yarn from the interlock is a detachment of this load-bearing yarn from the matrix. The length over

which the yarn is detached is now free to stretch about 19% before failing, which greatly contributes to the strain-to-failure of the composite.

In a tough **matrix** composite, cracks are cusped and halted by the matrix, which hinders them in growing and opening up and really softening the structure. In a brittle matrix composite, on the other hand, every little defect easily grows into a crack that spans the full height of the interlock, which gives the load-bearing yarns a lot of room to stretch. Apart from the distributed damage, the brittle matrix composite exhibited debonding of the load-bearing yarns under warp-oriented loading. Due to this additional mechanism, the toughness of the brittle matrix composite along the warp direction was the highest value observed, with a strain of 4.8% before final rupture.

If the fiber-matrix **interface** is left untreated, fiber detachments start to appear at very low overall stress levels. These detachments steadily propagate through the much stronger matrix pockets, and the cracks that are formed this way soften the interlock. If the interface is enhanced so that its strength is close to the matrix strength, the stress will build up on the interface without causing any damage at first. When a local defect finally initiates, the global stress level is high enough to facilitate fast crack propagation. As a result, the first crack leads to catastrophic failure.

## 7.2 FUTURE WORK

The roadmap that was developed in this work to analyze a composite based on the realistic, visible features on the edge of a laminate should be applicable to any textile reinforced composite. The approach should even be more powerful for traditional composites: these consist of elastic, brittle materials, which should be beneficial to the accuracy of the models, especially near the upper limit of their working range. Application of the new approach to a variety of composites would certainly spark new insights, on the composites and their mechanics, but also on the methodology itself. Some of the procedures may need adjustments for composites with a reinforcement that differs drastically from the one that was used to develop them. For instance, if the fiber volume fraction of the composite under consideration is much higher, it may become difficult to distinguish the contours of neighboring transversal yarns on the laminate edge. On the other hand, a denser packing in the longitudinal yarns would make their contours more visible, maybe even visible enough for automatic detection. These robustness issues can only be addressed through a large-scale application of the proposed approach. This process, in turn, would certainly benefit from a further automation of the separate tools and methods. A next step could be to introduce parametrisable features to the final geometry. Along with the short runtimes of the 2D finite element models, this could make for a very powerful tool to perform parameter studies.

Phenomena concerning damage require a realistic 3D representation of the composite's internal geometry, and material models that correctly account for plasticity and damage. When it comes to the material models, using the explicit solver in Abaqus could already alleviate many of the convergence issues that are typically encountered in Abaqus/Standard. Also other (non-) commercial finite element or finite volume packages could be explored to find solvers that are better suited to deal with material non-linearity. When it comes to building a workable, realistic 3D finite element model of the composite structure, a geometry based on µ-CT data is probably the most promising concept. Unfortunately, the image processing involved is not straightforward. The difficulties involved are illustrated in Figure 7-1, which shows an FE model that was created in the commercial software Simpleware based on micro-CT data of a stainless steel/epoxy composite laminate.

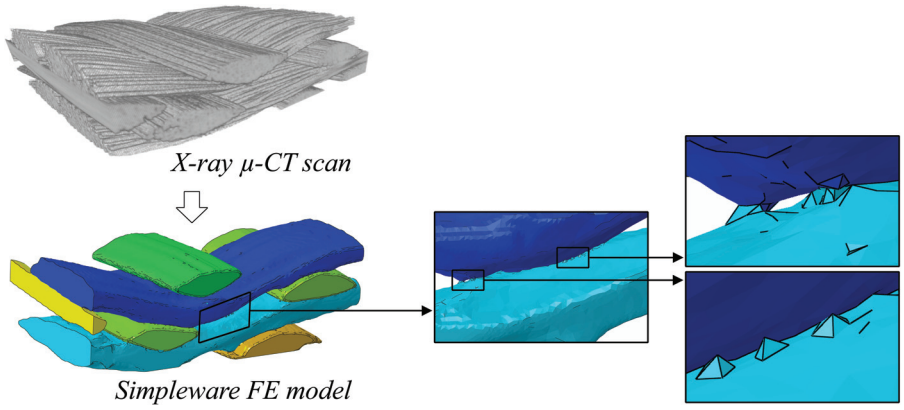


Figure 7-1: FE model constructed from micro-CT data in Simpleware

A prerequisite to building a workable model from µ-CT data is to properly detect the fiber bundles in a way that smooth, separate parts can be generated for yarns and matrix. The first challenge is to define the yarn contours, especially where two yarns are touching. Overlaps are obviously unacceptable, and most often, an artificial layer of matrix is desired in between yarns in order to guarantee a coherent, meshable matrix part. This is not state of the art yet. To obtain the FE model in Figure 7-1, for instance, the borders between yarns and matrix were detected automatically, but yarns were separated manually on their contacting faces. A second challenge is to sufficiently smooth out spurious protrusions without degenerating the yarn shape. Indeed, small protrusions will cause unrealistic stress concentrations in the finite element solution, while larger protrusions will affect the path definition of the yarn. A smoothing algorithm usually drastically improves the outlines of the yarns, again with the exception of the region where two yarns meet. Typical protrusions in these locations are illustrated in the enlargements in Figure 7-1. Once the geometry of all parts is defined, the elastic properties must be abstracted from the µ-CT data. This requires to

detect the fiber volume fraction and the directionality inside the yarns. The most straightforward approach is to consider the yarns as homogeneous entities, with material directions according to the yarn path. This approach is under development, and it will be an important step towards building physically sound 3D models. In a further stage, more realistic approaches could be conceived, with realistic, uneven fiber distributions within the yarns. This is not an obvious advancement, because the variable fiber distribution must be translated to variable material properties in the elements of the mesh. Moreover, a fiber distribution that varies along the yarn path also reflects on the directionality of the constitutive properties. Regardless, even the possibility of building 3D models with homogeneous, yet realistically shaped yarns would contribute tremendously to the scientific developments involving damage in textile composites.